

Science-Driven Optimization of the LSST Observing Strategy

Prepared by the LSST Science Collaborations,

with contributions from the LSST Project.

Contributing Authors

Phil Marshall,¹ Scott Anderson,² Timo Anguita,³ Ruth Angus,⁴ Iair Arcavi,⁵ Humna Awan,⁶ Federica B. Bianco,⁷ Rahul Biswas,⁸ Keaton J. Bell,⁹ Eric C. Bellm,¹⁰ David Bennett,¹¹ Niel Brandt,¹² Chris Britt,¹³ Derek Buzasi,¹⁴ Dana I. Casetti-Dinescu,¹⁵ Laura Chomiuk,¹⁶ Will Clarkson,¹⁷ Chuck Claver,¹⁸ Andy Connolly,¹⁹ Kem Cook,²⁰ James Davenport,²¹ Victor Debattista,²² Seth Digel,²³ Zoheyr Doctor,²⁴ Wen-fai Fong,²⁵ Eric Gawiser,²⁶ Mark Giampapa,²⁷ John E. Gizis,²⁸ Melissa L. Graham,²⁹ Carl Grillmair,³⁰ Zoltan Haiman,³¹ Patrick Hartigan,³² Suzanne Hawley,³³ Željko Ivezić,³⁴ C. Johns-Krull,³⁵ Lynne Jones,³⁶ Shashi Kanbur,³⁷ Vassiliki Kalogera,³⁸ Vinay Kashyap,³⁹ Vishal Kasliwal,⁴⁰ Peter Kurczynski,⁴¹ Michael C. Liu,⁴² Michelle

¹[drphilmarshall](#), SLAC National Accelerator Laboratory, 2575 Sand Hill Road, MS29, Menlo Park, CA 94025, USA

²[ScottAnderson](#), Some Institute, Somewhere, ...

³[tanguita](#), UNAB, Chile, ...

⁴[ruthangus](#), University of Oxford, UK, ...

⁵[arcavi](#), LCOGT, University of California, Santa Barbara, CA ...

⁶[HumnaAwan](#), Rutgers, ...

⁷[fedhere](#), New York University, NY, ...

⁸[rbiswas4](#), University of Washington, ...

⁹[keatomb](#), University of Texas at Austin, ...

¹⁰[ebellm](#), California Institute of Technology, ...

¹¹[davidpbennett](#), NASA Goddard Space Flight Center, ...

¹²[nielbrandt](#), Some Institute, Somewhere, ...

¹³[cbritt4](#), Texas Tech University, ...

¹⁴[derekbuzasi](#), Florida Gulf Coast University, ...

¹⁵[DanaCD](#), Southern Connecticut State University, ..., Yale University, ...

¹⁶[chomiuk](#), Michigan State, ...

¹⁷[willclarkson](#), University of Michigan-Dearborn, ...

¹⁸[cclaver](#), LSST, ...

¹⁹[connolly](#), University of Washington, ...

²⁰[kem0cook](#), Some Institute, Somewhere, ...

²¹[jimdavenport](#), Western Washington University, ...

²²[vpdebattista](#), University of Central Lancashire, UK, ...

²³[sethdigel](#), SLAC National Accelerator Laboratory, 2575 Sand Hill Road, MS29, Menlo Park, CA 94025, USA

²⁴[Doctor](#), NU, ...

²⁵[Fong](#), U of Arizona, ...

²⁶[egawiser](#), Rutgers, ...

²⁷[markgiampapa](#), National Solar Observatory, ...

²⁸[jgizis](#), University of Delaware, ...

²⁹[MelissaGraham](#), University of Washington, ...

³⁰[cgrillmair](#), Some Institute, Somewhere, ...

³¹[Haiman](#), Columbia, ...

³²[phartigan](#), Some Institute, Somewhere, ...

³³[suzannehawley](#), University of Washington, ...

³⁴[ivezic](#), University of Washington, ...

³⁵[CJohnsKrull](#), Some Institute, Somewhere, ...

³⁶[rhiannonlynne](#), University of Washington, ...

³⁷[ShashiKanbur](#), State University of New York at Oswego, ...

³⁸[Kalogera](#), NU, ...

³⁹[vinaykashyap](#), Harvard-Smithsonian Center for Astrophysics, ...

⁴⁰[AstroVPK](#), University of Pennsylvania, ...

⁴¹[pkurczynski](#), Some Institute, Somewhere, ...

⁴²[mliu](#), Institute for Astronomy, Honolulu, HI ...

Lochner,⁴³ Michael B. Lund,⁴⁴ Ashish Mahabal,⁴⁵ Raffaella Margutti,⁴⁶ Peregrine McGehee,⁴⁷ Tom Matheson,⁴⁸ Søren Meibom,⁴⁹ Josh Meyers,⁵⁰ Dave Monet,⁵¹ David Nidever,⁵² Knut Olsen,⁵³ Eric Neilsen,⁵⁴ Matthew T. Penny,⁵⁵ Christina Peters,⁵⁶ Gordon Richards,⁵⁷ Stephen Ridgway,⁵⁸ Jeonghee Rho,⁵⁹ Jason Rhodes,⁶⁰ David Rubin,⁶¹ Samuel Schmidt,⁶² Ohad Shemmer,⁶³ Avi Shporer,⁶⁴ Colin Slater,⁶⁵ Nathan Smith,⁶⁶ Marcelles Soares-Santos,⁶⁷ Jay Strader,⁶⁸ Michael Strauss,⁶⁹ Rachel Street,⁷⁰ Christopher Stubbs,⁷¹ Paula Szkody,⁷² David Trilling,⁷³ Virginia Trimble,⁷⁴ Miguel de Val-Borro,⁷⁵ Stefano Valenti,⁷⁶ Kathy Vivas,⁷⁷ Robert Wagoner,⁷⁸ Lucianne Walkowicz,⁷⁹ Beth Willman,⁸⁰ Peter Yoachim,⁸¹ Bevin Ashley Zauderer,⁸²

⁴³MichelleLochner, UCL, ...

⁴⁴lundmb, Vanderbilt University, ...

⁴⁵AshishMahabal, Some Institute, Somewhere, ...

⁴⁶raffaellamargutti, New York University, NY, ...

⁴⁷pmmcgehee, IPAC, ...

⁴⁸, NOAO, ...

⁴⁹sorenmeibom, Harvard-Smithsonian Center for Astrophysics, ...

⁵⁰jmeye314, Some Institute, Somewhere, ...

⁵¹dgmonet, USNO, ...

⁵²dnidever, LSST, ...

⁵³knutago, NOAO, ...

⁵⁴ehneilsen, Some Institute, Somewhere, ...

⁵⁵mtpenny, Sagan Fellow, Ohio State University, ...

⁵⁶cmp346, Drexel University, ...

⁵⁷GordonRichards, Drexel University, ...

⁵⁸StephenRidgway, NOAO, ...

⁵⁹jhrlsst, SETI Institute, ...

⁶⁰jasondrhodes, JPL, ...

⁶¹rubind, STSci, ...

⁶²SamSchmidt, University of California, Davis, ...

⁶³ohadshemmer, University of North Texas, ...

⁶⁴shporer, JPL, ...

⁶⁵cslater, University of Washington, ...

⁶⁶nathansmith, U of Arizona, ...

⁶⁷soares-santos, Some Institute, Somewhere, ...

⁶⁸caprastro, Michigan State, ...

⁶⁹michaelstrauss, Department of Astrophysical Sciences, Princeton University, Princeton, NJ 08544, USA

⁷⁰, LCOGT, University of California, Santa Barbara, CA ...

⁷¹astrostubbs, Some Institute, Somewhere, ...

⁷²paulaszkody, University of Washington, ...

⁷³davidtrilling, Some Institute, Somewhere, ...

⁷⁴Trimble, Some Institute, Somewhere, ...

⁷⁵miguelvdb, Department of Astrophysical Sciences, Princeton University, Princeton, NJ 08544, USA

⁷⁶svalenti, Some Institute, Somewhere, ...

⁷⁷akvivas, Cerro Tololo Inter-American Observatory, La Serena, Chile

⁷⁸, Physics Department, Stanford University, ...

⁷⁹lmwalkowicz, Adler Planetarium, ...

⁸⁰bethwillman, LSST, ...

⁸¹yoachim, Some Institute, Somewhere, ...

⁸²Zauderer, New York University, NY, ...

Contents

Preface	7
1 Introduction	9
1.1 Synoptic Sky Surveying at Universal Cadence	10
1.2 Evaluation and Optimization of the LSST Observing Strategy	11
1.3 Guidelines for Contributors	12
1.4 Outline of This Paper	14
2 Some Example Observing Strategies	17
2.1 Introduction	17
2.2 The Baseline Observing Strategy	18
2.3 Some Simulated Alternative Observing Strategies	26
2.4 Temporarily Denser Time Sampling: Rolling Cadence	38
2.5 Summary	44
3 Solar System	47
3.1 Introduction	47
3.2 Discovery: Linking Solar System Objects	48
3.3 Discovery of Potentially Hazardous Asteroids	53
3.4 Orbital Accuracy	54
3.5 Detecting Comet Activity	57
3.6 Measuring Asteroid Light Curves and Rotation Periods	60
3.7 Measuring Asteroid Colors	61
3.8 Future Work	62
4 The Milky Way Galaxy	69
4.1 Introduction	69
4.2 Populations in the Milky Way Disk	70
4.3 Astrometry with LSST: Positions, Proper Motions, and Parallax	79
4.4 Future Work	87
5 Variable Objects	103
5.1 Introduction	103
5.2 The Cepheid Mass-Luminosity Relation	104
5.3 Discovery of Multiperiodic, Short-Period Pulsating Variables	109
5.4 Discovery and Characterization of Young Stellar Populations	113
5.5 Future Work	118
6 Transients	127
6.1 Introduction	127
6.2 Realtime Identification of Young Transients	133
6.3 Supernovae as Transients	135
6.4 Gamma-Ray Burst Afterglows	141
6.5 Gravitational Wave Sources	144

Contents

6.6	Future Work	147
7	The Magellanic Clouds	153
7.1	Future Work	155
8	AGN	157
8.1	Introduction	157
8.2	AGN Selection and Census	157
8.3	Disc Intrinsic AGN Variability	160
8.4	AGN Size and Structure with Microlensing	164
8.5	Future Work	167
8.6	Discussion	169
9	Cosmology	171
9.1	Introduction	171
9.2	Large Scale Structure: Testing Dithering Patterns and Timescales to Improve Survey Uniformity	172
9.3	Weak Lensing	173
9.4	Photometric Redshifts	179
9.5	Supernova Cosmology and Physics	184
9.6	Strong Gravitational Lens Time Delays	195
10	Special Surveys	199
10.1	Introduction	199
10.2	Solar System mini-surveys	199
10.3	Short Exposure Surveying	202
10.4	A Mini-Survey of the Old Open Cluster M67	207
11	Synergy with WFIRST	211
11.1	Introduction	211
11.2	Cosmology with the WFIRST HLS and LSST	212
11.3	Supernova Cosmology with WFIRST and LSST	214
11.4	Exoplanetary Microlensing with WFIRST and LSST	215
12	Tensions and Trade-offs	219
12.1	Introduction	219
12.2	Variable Targets - Where Is The Tension?	220
12.3	Static Target Science - Is There Any Tension?	223
12.4	Tension Between Static And Variable Science	224
12.5	Mini-surveys and Main Survey - Tension for Sure	224
12.6	Summary and Conclusion	225
	References	227

Preface

The Large Synoptic Survey Telescope (LSST) is designed to carry out a large synoptic survey. We have a pretty good idea of how we LSST could be deployed: there is a baseline strategy, and a corresponding simulated visit sequence, with which it can be demonstrated that the data required for the promised science can be delivered. However, this baseline strategy may well not be the *best* way to schedule the telescope. Smaller, specialized surveys are likely to provide high scientific value, as is optimizing the pattern of repeated sky coverage. The baseline strategy is not set in stone, and can and will be optimized. Even small changes could result in significant improvements to the overall science yield. How can we design an observing strategy that maximizes the scientific output of the LSST system?

The LSST Observing Strategy community formed in July 2015 to tackle this problem. Composed primarily (but not exclusively) of LSST Science Collaboration and LSST Project members, we are working together to use the Metric Analysis Framework (MAF) provided by the LSST Project to evaluate OPSIM simulations of the LSST survey (also provided by the Project) specifically for the science that we each care most about. Once the baseline visit sequence has been evaluated with a given science case’s metrics, all other proposed visit sequences can be compared against it, automatically. In this way, our goal is to give sustainable quantitative feedback about how any proposed observing strategy would impact the performance of our science cases, and so enable good decisions to be made when the telescope schedule is eventually set up.

This white paper is a compendium of ideas and results generated by the community, assembled so that everyone can follow along with the analysis. It is a living document, whose purpose is to bind together the group of people who are thinking about the LSST observing strategy problem, and facilitate their collective discussion and understanding of that problem (a process we might think of as “cadence diplomacy”). The white paper’s modular design allows pieces of it to be split off and published in a series of snapshot journal papers, as the various metric analyses reach maturity. The white paper itself will be continuously published on [GitHub](#) and advertised periodically on [astro-ph](#). This white paper is large, but we hope that its hyperlinked structure helps you quickly find the science cases that you are most interested in, starting from the [table of contents](#).

The LSST observing strategy evaluation and optimization process will be as open and inclusive as possible. New community members are welcome at any time: we invite all stakeholders to participate, and provide guidance on how to get involved in [Section 1.3](#).

Željko Ivezić, Beth Willman, Phil Marshall

April 24, 2016.

1 Introduction

Chapter editors: *Beth Willman, Andy Connolly, Željko Ivezić, Phil Marshall*.

The Large Synoptic Survey Telescope (LSST) is a dedicated optical telescope with an effective aperture of 6.7 meters, currently under construction on Cerro Pachón in the Chilean Andes. The telescope and camera will have a huge field of view, 9.6 deg², and the étendue, i.e., the product of collecting area and field of view will be significantly larger than any other optical telescope. Thus this telescope is designed for wide-field deep imaging of the sky; its mantra is “Wide-Deep-Fast”, i.e., the ability to cover large swaths of sky (“Wide”) to faint magnitudes (“Deep”) in a short amount of time (“Fast”), allowing it to scan the sky repeatedly. LSST will image in six broad filters, *ugrizy*, spanning the optical band from the atmospheric cutoff in the ultraviolet to the limit of CCD sensitivity in the near-infrared.

The science case for the LSST is based broadly on four science themes:

- Dark energy and dark matter (via measurements of strong and weak lensing, large-scale structure, clusters of galaxies, and supernovae);
- Exploring the transient and variable universe;
- Studying the structure of the Milky Way galaxy and its neighbors via resolved stellar populations;
- An inventory of the Solar System, including Near Earth Asteroids and Potential Hazardous Objects, Main Belt Asteroids, and Kuiper Belt Objects.

These themes, together with *many* other science applications, are described in detail in the [LSST Science Book](#), produced by the LSST Project Team and Science collaborations in 2009. The present white paper represents an important next step in science planning beyond the Science Book. In particular, we now need to quantify how well the LSST (for a given realization of its observing strategy, or “*cadence*”) will be able to carry out its science goals; indeed, we will use this quantification to refine and optimize the cadence itself. To zeroth order, the large étendue of LSST allows it to meet all its science goals with a single dataset with a universal cadence. This document describes the design of the LSST cadence and the various ways in which can be further refined to optimize the science output of the survey. As we describe in detail below, we quantify the effectiveness of a given cadence realization to meet science goals by defining a series of quantitative *metrics*. Any given realization will be more favorable for some science areas, and less so for others; the metrics allow us to quantify this, and optimize the overall cadence for the broadest range of LSST science areas.

In the six years since the Science Book was written, some of the science themes described in there have evolved or become obsolete, while new science opportunities and ideas have arisen. Moreover, our understanding of the capabilities (such as system response and therefore depth, telescope

optics, and so on) have matured considerably. The present document endeavors to explore the principal science themes as described in the Science Book, but is not slaved to them, and where appropriate, we will point out relevant updates to the Science Book.

1.1 Synoptic Sky Surveying at Universal Cadence

The LSST defined a so-called “baseline cadence”, described in the [LSST overview paper](#) and Chapter 3 of the Science Book. This was used to demonstrate that LSST could meet its basic science goals, and indeed the formal [science requirements](#). As described in these references, the default LSST exposure is 15 seconds, and all exposures are taken in pairs, called a “*visit*”, before the telescope is slewed to a neighboring field. Any given field is observed twice on a given night, which allows preliminary trajectories of asteroids to be determined.

The baseline cadence optimizes the amount of sky covered in any given night (subject to the constraint of observing at airmass less than 1.4 throughout), and allows the entire sky visible at any time of the year to be covered in about three nights. The cadence is designed to give uniform coverage at any given time, and reaches survey goals for measuring stellar parallax and proper motion over the ten-year survey. The survey requirements on depth lead to roughly 825 visits (summing over the six filters) in the 10-year LSST survey to any given point on the sky. The resulting Deep-Wide-Fast component of the survey covers roughly 18,000 deg² of high Galactic latitude sky, and requires about 85% of the available observing time.

There are obvious science cases that the Deep-Wide-Fast survey does not address, and thus the remaining 15% of the telescope time in the baseline cadence is devoted to a series of specialized surveys. They are as follows:

- Imaging at low Galactic latitudes. This is currently defined as a wedge which is broader closer to the Galactic Center, corresponding roughly to a locus of constant stellar density. In this region, the number of repeat observations is reduced, given the confusion limit in the stacked LSST data.
- Imaging in the South Celestial Cap. The airmass limit of 1.4 restricts observations to declination $> -75^\circ$, thus missing large fraction of both the Magellanic Clouds. Observations are done in the Cap to cover this region of sky, again to shallower depth.
- Imaging in a series of four *Deep Drilling Fields*, single pointings in which we will obtain roughly 5 times more exposures in all filters in order to go about a magnitude fainter in the stacked data, as well as to get better sampled light curves of variable objects.
- Imaging in the Northern portions of the Ecliptic Plane. The airmass limit of 1.4 restricts us to declination $< +15^\circ$, which means that significant fraction of the Ecliptic Plane is uncovered. By observing with a reduced cadence close to the Ecliptic Plane north of this limit, we will be able to significantly increase the fraction of Near-Earth Asteroids and Main Belt Asteroids for which LSST obtains orbits.

The LSST Project has developed an “Operations Simulator” (OPSIM), which includes a realistic model of telescope operations, including time required for camera readout, slew time, filter exchange, as well as time loss due to clouds. Given a set of so-called “proposals” that set the

priorities of which fields to observe at any given time, OP SIM has developed a series of realizations of the series of observations that make up the ten-year LSST survey. The baseline cadence is a specific realization of the OP SIM output, which meets the LSST survey requirements, following the rules briefly outlined above.

Again, while the baseline cadence demonstrates that the LSST is capable of meeting its stated science goals, it is not optimized for all science, and [Chapter 2](#) of this document describes a series of experiments varying the assumptions in OP SIM. In [Chapter 10](#), we explore additional ideas for future experiments to be done in OP SIM—many of them, we hope, inspired by requests from the community.

Go to: • [the start of this section](#) • [the start of the chapter](#) • [the table of contents](#)

1.2 Evaluation and Optimization of the LSST Observing Strategy

The next step is to quantify how well any given realization of the LSST observing strategy (i.e., an output of OP SIM) supports the (many) science projects that LSST will enable. As the algorithms controlling OP SIM are varied, some projects will benefit, while others may suffer. By quantifying this for each project, we can determine which cadence maximizes the science potential overall of the project.

Therefore, we need a *science-based evaluation of the baseline LSST observing strategy and its variants*. After simulating a sample observing schedule consistent with this strategy (see [Chapter 2](#)), we then need to quantify its value to each science team. This is what the LSST Simulations team’s “Metric Analysis Framework” was designed to enable: science case investigators can now design quantitative evaluations of the outputs of OP SIM, to answer the question, “how good would that observing strategy be, for my science?” These “metrics” can be coded against the MAF API, and shared among the LSST science community at the [sim_maf_contrib](#) online repository. All of the MAF metrics described in this paper can be found there.

Once the fiducial strategy has been evaluated in this way, then any other strategy can be evaluated in the same terms, using the same code. We will then be able to optimize the strategy through iterations between OP SIM and MAF.

With this program in mind, it makes sense to define *one “Figure of Merit” (FoM) per science project*, that captures the value of the observing strategy under consideration to that science team. This FoM will probably be a function of several “diagnostic metrics” that quantify lower-level features of the observing sequence. For Figures of Merit to be directly comparable between disparate science projects, they need to be dimensional, and have the same units.¹

It may not always be straightforward to define a Figure of Merit for some science cases, but the diagnostic metrics that they will likely depend upon will be easier to derive. Writing this white paper is an opportunity to think through the FoM for each science project that we as a community want to carry out, and how that measure of success is likely (or even known) to depend on metrics

¹One natural choice of units for Figures of Merit could be the *information gained* by the science team, in bits. This is a well-defined statistical quantity, albeit not yet one in common use.

that summarize the observing sequence presented to us. We return to the question of FoM design in [Sub-section 1.3.3](#) below.

Thinking about the problem in terms of science projects, each with a Figure of Merit, encourages us to design modular document sections, with one science project and one Figure of Merit per section. These modular sections ought then be easily extracted, combined and edited into publishable articles. They will also naturally lead to the definition of a suite of MAF metrics that can be evaluated on any future OPSIM output database. Tabulating the values of the diagnostic metrics and the FoM, for different cadences, for each science case, will be very helpful for this purpose.

Having laid out the essential features of our science-driven evaluation program, in the next section we translate them into guidance for contributors to this community effort.

Go to: • [the start of this section](#) • [the start of the chapter](#) • [the table of contents](#)

1.3 Guidelines for Contributors

Phil Marshall

Contributions to this community effort are welcome from everyone. In this section we give brief guidelines for how to make a contribution, and how you should structure that contribution.

1.3.1 How to Get Involved

The first thing you should do is browse the current version of the white paper, which you should be able to [view on GitHub](#). You can download the continuously-compiled [latest version of the PDF document](#), which is hyper-linked for easy navigation. You will then be able to provide good feedback, which you should do via the [GitHub issues](#). Please search the existing issues first: there might be a conversation already taking place that you could join. New issues are most welcome: we'd like to make this white paper as comprehensive as possible.

To edit the white paper, you'll need to “fork” its repository. You will then be able to edit the paper in your own fork, and when you are ready, submit a “pull request” explaining what you are doing and the new version that you would like to be accepted. It's a good idea to submit this pull request sooner rather than later, because associated with it will be a discussion thread that the writing community can use to discuss your ideas with you. For help getting started with git and GitHub, please see this [handy guide](#).

1.3.2 Writing Science Cases

For a high-level justification of the following design, please see [Section 1.2](#) above. In short, we're aiming for modular science sections (that are easy to write in parallel, and then re-arrange into other publications later) that are each focused on *one science project each*, and quantified by one (or maybe two) Figures of Merit (which will likely depend on other, lower-level diagnostic metrics).

At the beginning of each science chapter there will be a brief *introduction* that outlines the commonality of the key science projects contained in that chapter. The individual science sections following this introduction will then need to describe the particular discoveries and measurements that are being targeted in each *science case*.

It will be helpful to think of these science cases as investigations that the section leads *actually plan to do*. Thinking this way means that each individual section can follow the tried and tested format of an *observing proposal*: a brief description of the investigation, with references, followed by subsections describing the analysis of its technical feasibility. The latter is where the MAF analysis should go. Like an observing proposal, each section will seek to demonstrate the science performance achievable given various assumptions about the time that could be awarded, or in our case, the survey that could be delivered.

For an example of how all this could look, please see the [lens time delays section](#). While the MAF analysis in this science case is still in progress, the suggested structure of the science case can be seen. Template latex files for the chapters and sections can be found in the [GitHub repository](#).

1.3.3 Metric Quantification

The feasibility of each science case will need to be quantified using the MAF framework, via a set of metrics (a Figure of Merit, and some diagnostic metrics) that need to be computed for any given observing strategy in order to quantify the impact of that cadence on the described science.

In many (or perhaps all) cases, a Figure of Merit will be a *precision* (i.e. a percentage statistical uncertainty) on a astrophysical model parameter, assuming negligible bias in its inference. Precision is usually what we need to forecast in order to convince TAC's to give us telescope time, and so it makes sense to focus on it here too.

Early on in a metric analysis, it may not be possible to compute a science case's Figure of Merit, most likely because to do so would require a large simulation program to capture the response of the parameter measurement to the observing strategy. At this early stage, it makes sense to look for simple *proxies* that scale the same way as model parameter precision. For example, we might expect the precision on a set of luminosity function parameters to scale with the square root of the number of objects in the sample, and so \sqrt{N} could be a sensible proxy for the Figure of Merit. Provided we get the scaling right, we can then compare different observing strategies by looking at the *percentage change in the Figure of Merit*, and arguing that this will correspond approximately to the same percentage change in the ideal case.

Each science section needs to conclude with a discussion of any risks that have been identified, and how these could be mitigated. What does this mean? Each science project will have a threshold acceptable Figure of Merit value, as well as a target (or “design”) value. If an observing strategy gives an FoM value below the threshold, it is very important that we know about it. Optimizing all science cases in such a complex and diverse set is not really the best way of thinking about LSST’s scheduling task: rather than maximizing happiness, what we are really trying to do is minimize global unhappiness. The comparisons between different simulated strategies will help make the case for any changes to the baseline strategy, and in the short term provide motivation for proposed new OPSIM simulation runs.

For some science sections we will have only a metric design, without an implementation. As this white paper evolves, many of these designs will be realized and put into action. At first, though, the discussion of risks to these science cases will necessarily be minimal, containing only predictions for how the Figure of Merit is likely to vary among observing strategies. These “ideas” sections will be presented as sub-sections of a “Future Work” section, on the grounds that the quantitative analysis is still to come. As its MAF-based evaluation and investigation proceeds, a science case will graduate into the main part of the chapter and become a “results” section. The results sections are clearly visible from the Table of Contents. To find a Future Work subsection on any particular topic, you can use the search facility on your PDF viewer.

When does an “ideas” section become a “results” section? *As soon as science performance is quantified using any of the outputs from OPSIM.* There is a learning curve associated with the MAF, but metrics should be able to be designed before the MAF documentation is even opened. And since MAF metrics always work with OPSIM outputs, any quantitative analysis that is focused towards those outputs will have the potential to grow into one of the MAF analyses we need.

1.3.4 Proposing New Simulations

Before we can optimize the LSST observing strategy we must first evaluate its current version for all the science cases we care about. The logical point at which to propose a new OPSIM simulation, capturing a novel aspect of the observing strategy, is *after* evaluating the baseline cadence (and others). The discussion section of your science case is a good place to suggest new OPSIM simulations for further testing by the community; there is also an [online suggestion board](#) for ideas for new simulations to be registered and shared.

Go to: • [the start of this section](#) • [the start of the chapter](#) • [the table of contents](#)

1.4 Outline of This Paper

The rest of this white paper is structured as follows. In [Chapter 2](#) we describe a number of OPSIM simulated observing schedules (“cadences”) explored by the LSST Sims team in summer 2015 in preparation for this paper: they include a “baseline cadence”, and then some small but interesting perturbations to it. Then, we present the science cases considered so far, organised into the following chapters:

- [Chapter 3: Solar System](#)
- [Chapter 4: The Milky Way Galaxy](#)
- [Chapter 5: Variable Objects](#)
- [Chapter 6: Transients](#)
- [Chapter 7: The Magellanic Clouds](#)
- [Chapter 8: AGN](#)
- [Chapter 9: Cosmology](#)

- [Chapter 10: Special Surveys](#)
- [Chapter 11: Synergy with WFIRST](#)

Finally, in [Chapter 12](#) we bring the results of all the science metric analyses together and discuss the tensions between them, and the trade-offs that we can anticipate having to make. This final chapter will serve as this work's set of running conclusions.

Go to: • [the start of this section](#) • [the start of the chapter](#) • [the table of contents](#)

2 Some Example Observing Strategies

Chapter editors: *Željko Ivezić, Peter Yoachim, Lynne Jones.*

Contributing authors: *Kem Cook, Stephen Ridgway, Phil Marshall*

Summary: In this chapter we analyze and compare the performance of a number of simulated LSST observing strategies (“cadences”) which were developed in support of the LSST 2015 Observing Strategy Workshop. A candidate new Baseline Cadence, `minion_1016`, was found adequate and is proposed as a replacement for the previous Baseline Cadence (`opsim3.61`). Simulations that only implemented Universal Cadence proposal imply a “best-case scenario” margin for the number of visits of about 40% relative to the design specifications for the main survey sky coverage (18,000 sq.deg.) and the number of visits per field (825, summed over all bands) from the Science Requirements Document (SRD), and assuming perfect dithering¹. This margin can be used to increase the sky coverage of the main survey, the total number of visits per field, or to enhance special programs, such as deep drilling fields and Galactic plane coverage. Several simulations analyzed here quantitatively explore these strategic options. Additional simulations show that the effects of variations of the visit exposure time in the range 20-60 seconds on surveying efficiency can be predicted using simple efficiency estimates. Various modifications of baseline cadence (e.g. Pan-STARRS-like cadence, no visit pairs, sequences with 3 and 4 visits) indicate a large parameter space for further optimization, especially for time-domain investigations and detailed coverage of special sky regions.

2.1 Introduction

With the release of the latest version of Operations Simulations (hereafter OPSIM) code (version 3.2.1) for simulating LSST deployment, and the active development of Metrics Analysis Framework (MAF, currently version 0.2) for analyzing OPSIM outputs, we can now begin to undertake systematic and massive investigations of various LSST deployment strategies.

The optimization of the ultimate LSST observing strategy will be done with significant input from the community. To facilitate this process, the first of a series of meetings, named “LSST & NOAO Observing Cadences Workshop”, was held during the [LSST 2014 meeting](#) in Phoenix, AZ, August 11-15, 2014. The next workshop, named “LSST Observing Strategy Workshop”, was held [after the LSST 2015 meeting](#) in Bremerton, WA, August 20-22, 2015.

In part as a preparation for the second workshop, the LSST Simulations Team and the Project Science Team have designed, executed and analyzed a number of simulated surveys. The cadence

¹With a fill factor of 0.9 for the 9.6 sq.deg. large field of view, it takes 1.72 million visits to meet the SRD specifications when a perfect redistribution of the field overlap coverage is assumed.

strategies for these surveys, while similar to Baseline Cadence, are modified to study the impact of various strategy variations on the scientific potential of LSST. The cadence set also includes a candidate baseline cadence replacement.

An initial analysis of these [simulated surveys](#) is presented here, and based on [MAF](#) reports.

OPSIM databases investigated in this section (name format: machineName_runNumber):

minion_1016 — <i>The New Baseline Cadence.</i>	18
minion_1012 — <i>Only Universal Cadence, with pairs of visits.</i>	26
minion_1020 — <i>A Pan-STARRS-like observing strategy.</i>	27
minion_1013 — <i>Only Universal Cadence, no visit pairs.</i>	28
kraken_1043 — <i>Baseline Cadence, but with no visit pairs.</i>	30
enigma_1281 — <i>NEO test: triplets of visits.</i>	30
enigma_1282 — <i>NEO test: quads of visits.</i>	31
kraken_1052 — <i>Baseline Cadence, but with 33% shorter exposure time.</i>	32
kraken_1053 — <i>Baseline Cadence, but 100% longer exposure time.</i>	34
kraken_1045 — <i>Baseline Cadence, but with doubled u-band exposure time.</i>	35
kraken_1059 — <i>Baseline Cadence, but with doubled u-band exp. time and Baseline NE Spur.</i>	35
minion_1022 — <i>Only Universal Cadence, with relaxed airmass limit.</i>	36
minion_1017 — <i>Only Universal Cadence, with stringent airmass limit.</i>	37
astro_lsst_01_1004 — <i>Extend Universal Cadence to the Galactic Plane.</i>	37
ops2_1102 — “ <i>Swiss Cheese</i> ” rolling cadence, version 1.	40
enigma_1260 — “ <i>Swiss Cheese</i> ” rolling cadence, version 2.	40
enigma_1261 — “ <i>Swiss Cheese</i> ” rolling cadence, version 3.	40
ops2_1098 — “ <i>Control</i> ” simulation for comparison with the “ <i>Swiss Cheese</i> ” experimental rolling cadence simulations	40

Go to: • [the start of this section](#) • [the start of the chapter](#) • [the table of contents](#)

2.2 The Baseline Observing Strategy

The current “official” (managed by the LSST Change Control Board) Baseline Cadence, `opsim3.61`, was produced with an old version of OPSIM code. We first introduce a candidate replacement simulation that was produced using the latest version (v3.2.1) of OPSIM code, and then proceed with the analysis of other simulations that modify baseline observing strategy in various informative ways. Suggestions for further tool development, and a summary of the main cadence questions addressed here are available at the end of this document.

`minion_1016`

The New Baseline Cadence.

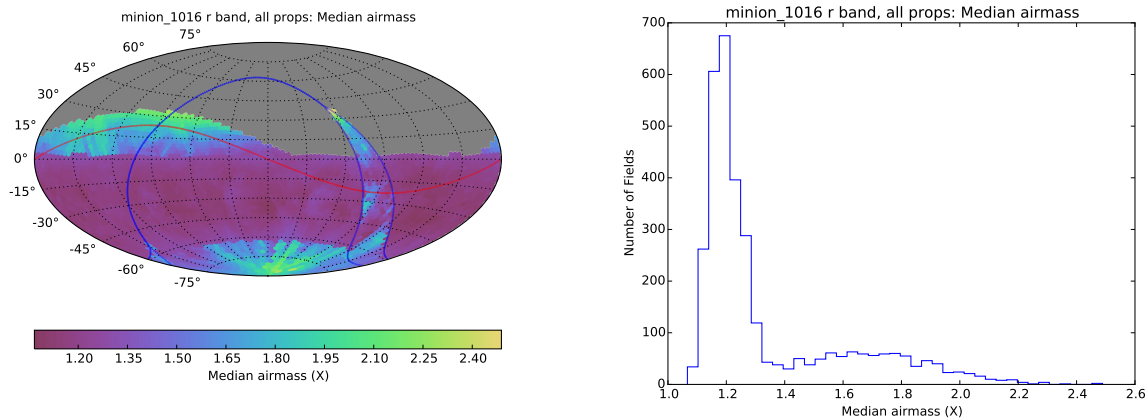


Figure 2.1: The median airmass in the *r* band across the sky for simulated cadence `minion_1016` is shown in Aitoff projection of equatorial coordinates in the left panel. The red line shows the Ecliptic and the blue line shows the Galactic equator (it bifurcates around the so-called “Galactic confusion zone”). The corresponding airmass histogram is shown in the right panel. For the main survey area, the maximum allowed airmass was set to 1.5.

The candidate replacement “Baseline Cadence” candidate, `minion_1016`, has the following basic properties²:

1. The total number of visits is 2,447,931, with 85.1% spent on the Universal proposal (the main wide-fast-deep, WFD, survey), 6.5% on the North Ecliptic proposal, 1.7% on the Galactic plane proposal, 2.2% on the South Celestial pole proposal, and 4.5% on the Deep Drilling cosmology proposal (5 fields).³
2. The median number of visits *per night* is 816, the range is 88 to 1,104, with 3,026 observing nights. The mean slew time is 6.8 seconds (median: 4.8 sec) and the total exposure time is 7.34 Msec. The surveying efficiency, or the median total open shutter time (per night) as a fraction of the observing time (the ratio of the open shutter time and the sum of the open shutter time, readout time and slew time) is 73%.
3. The 25%-75% quartiles for the number of filter changes per night are 2 and 6, with the mean of 4.3. The total number of filter changes is 14,194.
4. In the *r* band, the median effective seeing is 0.93 arcsec (for the more traditional geometric FWHM, the median is 0.81 arcsec), the median airmass is 1.23, and the median 5σ depth for point sources in WFD area (also known as the Universal Cadence area) is 24.16 (using the best current estimate of the fiducial depth at airmass of one, $m_5(r) = 24.39$, defined by the SRD Table 5). The variation of the median airmass for the *r* band observations with the position on the sky is shown in Figure 2.1.
5. The median single-visit depths for WFD fields are (23.14, 24.47, 24.16, 23.40, 22.23, 21.57)

²For MAF output, see <http://ls.st/5ep>

³The community-contributed white papers leading to the deep drilling fields defined in the baseline cadence can be found at <https://lsstcorp.org/content/whitepapers32012>.

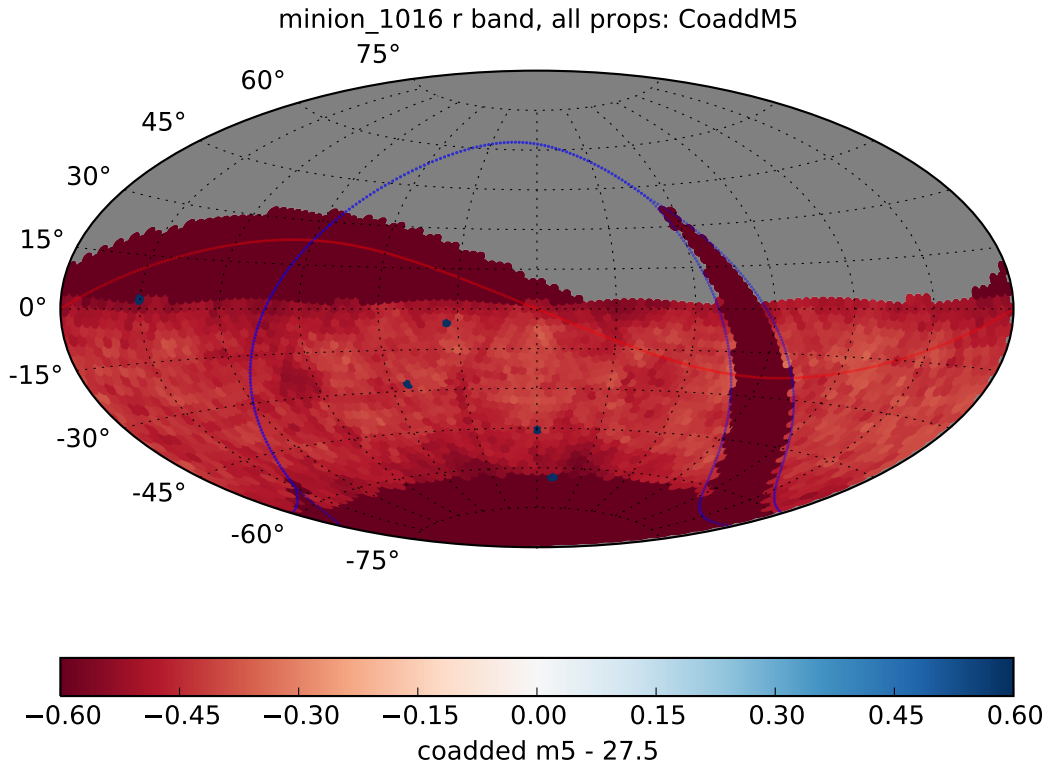


Figure 2.2: The coadded 5σ depth for point sources in the r band across the sky for simulated cadence [minion_1016](#) is shown in Aitoff projection of equatorial coordinates. The red line shows the Ecliptic and the blue line shows the Galactic equator (it bifurcates around the so-called “Galactic confusion zone”). The median value across the Universal Cadence area is 27.1, with RMS scatter of only 0.04 mag. The small dark dots are deep drilling fields, with a median 5σ depth of 28.6.

in the $ugrizy$ bands⁴. These values are shallower than the zenith dark time values for two main reasons: the sky is expected to be brighter for non-dark time and away from zenith, the sky brightness model currently implemented in OPSIM has some shortcomings (a new model will be implemented in version 4), and the moon avoidance is not as aggressive as it could be. As a result, the limiting depths above are biased bright by close to 1 mag in the z and y bands, and a few tenths of a magnitude in the u , g and i bands. The co-added depths are tied to single-visit bands, and suffer from the same bias.

6. For the 2,293 (overlapping) fields from the WFD area, the median number of visits in the $ugrizy$ bands is (62, 88, 199, 201, 180, 180), respectively. Not only do these medians exceed the requested number of visits (design specification from the SRD⁵) of (56, 80, 184, 184, 160, 160) in the $ugrizy$ bands, but the minimum number of visits per field over this area does so,

⁴Note that these values depend on externally supplied values for fiducial single-epoch 5σ depths; the following values were used in analysis described here: (23.62, 24.85, 24.39, 23.94, 23.36, 22.45) in the $ugrizy$ bands, respectively. These values are similar, but not identical, to the values listed in Table 2 from the latest version (v3.1) of the LSST overview paper: (23.68, 24.89, 24.43, 24.00, 23.45, 22.60). This discrepancy is due to continuing improvements in the system performance estimates.

⁵The LSST Science Requirements Document (SRD) is available as <http://ls.st/lpm-17>

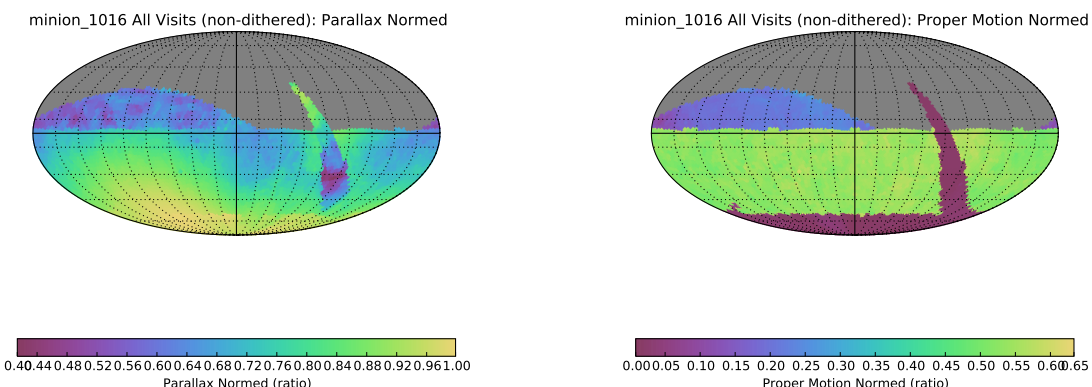


Figure 2.3: The trigonometric parallax errors (left) and proper motion errors (right), normalized by the values for idealized perfectly optimized cadences (parallax: all the observations are taken at maximum parallax factor, resulting in a peak at the South Ecliptic pole; proper motion: a half of all visits are obtained on the first day and the rest on the last day of the survey), obtained for simulated cadence [minion_1016](#) are shown in Aitoff projection of equatorial coordinates.

too. This result is quite encouraging given that only 85% of observing time was spent on the Universal Cadence proposal.

7. The median coadded 5σ depth for point sources in the *ugrizy* bands is (25.4, 27.0, 27.1, 26.4, 25.2, 24.4), respectively, for the Universal Cadence area. The distribution of coadded depth across the sky is fairly uniform, as illustrated in [Figure 2.2](#).
8. For the 2,293 fields from the Universal Cadence area, the median geometric FWHM for seeing is 0.78 arcsec in the *r* band and 0.77 arcsec in the *i* band. The median airmass in the *urz* bands is 1.25, 1.20 and 1.26 (the maximum allowed airmass for the Universal Cadence area was set to 1.5). The median sky brightness in the *ury* bands is 22.0 mag/arcsec², 21.1 mag/arcsec², and 17.3 mag/arcsec², respectively (for comparison, assumed dark sky brightness in the *ury* bands is 23.0, 21.2 and 18.6 mag/arcsec²). The current model sky brightness in the *y* band is biased high by close to 1 mag.
9. Restricted to the Universal Cadence fields, a unique area of 18,000 sq.deg. received at least 888 visits per field (summed over bands; the SRD design value is 825).
10. The median trigonometric parallax and proper motion errors are 0.62 mas and 0.17 mas/yr, respectively, for bright sources (limited by assumed systematic errors in relative astrometry of 10 mas), and 7.9 mas and 2.3 mas/yr for points sources with *r* = 24 (assuming flat spectral energy distribution), over the Universal Cadence fields. The variation of parallax and proper motion errors across the sky is visualized in [Figure 2.3](#).

For comparison, the current Baseline Cadence, `opsim3.61` (obtained with old OpSim code), delivered 2,651,588 visits, or 8.3% more than [minion_1016](#) (this is due to known effects and changes in the code, such as more pre-scheduled down time in the new version). Perhaps the most important (and undesired!) difference between the two simulations is that the new candidate Baseline Cadence spent 6.5% of the observing time on North Ecliptic Spur proposal (vs. 4% spent on the

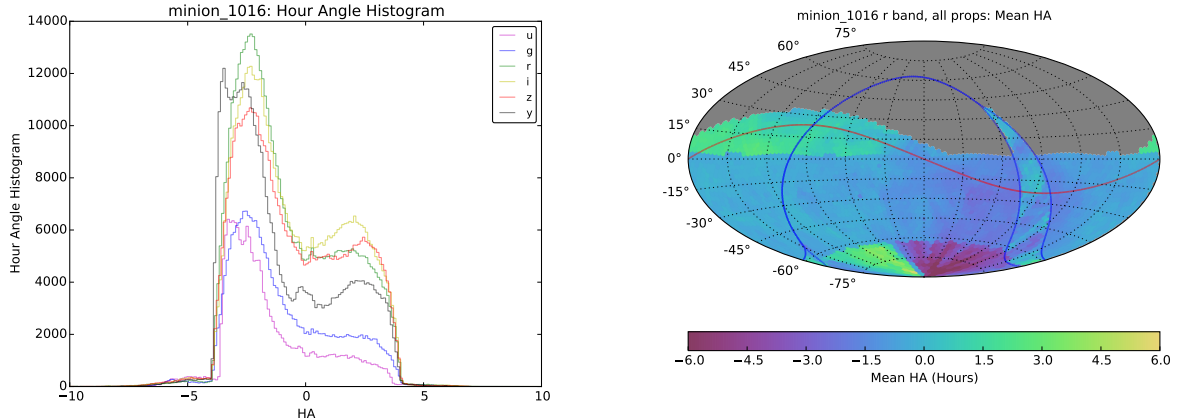


Figure 2.4: Histograms in the left panel show the distribution of hour angles (HA) in 6 bands for all proposals from simulated cadence [minion_1016](#) (the distributions are similar for WFD fields considered alone). Note the bias towards observations west from the meridian. The right panel shows the distribution across the sky of the mean HA for all observations in the r band.

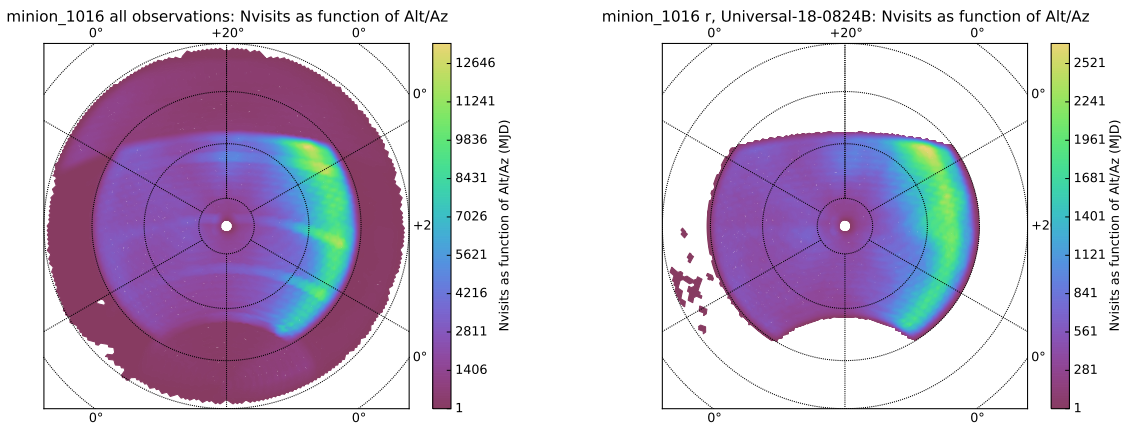


Figure 2.5: The color-coded map in the left panel shows the visit count from Baseline Cadence simulation [minion_1016](#) in the equal-area Lambert projection of the horizontal coordinate system (altitude-azimuth), with north on top and west towards the right, for all six bands and proposals (Universal, Galactic Plane, Deep Drilling fields, North Ecliptic Spur, and South Celestial Pole region). The Universal cadence was limited to airmass below 1.5, while other proposals sampled higher airmass, too (see the histogram in [Figure 2.1](#)). Note the strong propensity of fields for westward observations (the median airmass is about 1.2). The right panel is analogous, but only shows the r band visits for WFD fields.

corresponding Universal North proposal in [opsim3.61](#)), and less than 90% of time on the Universal proposal (the main wide-deep-fast survey).

Analysis of the hour angle distribution, shown in [Figure 2.4](#) and [Figure 2.5](#), reveals a strong bias towards observations west from the meridian for the main survey. *This pattern is not fully understood at this time* and may be caused by specific features of the cost function implemented in the OpSim code.

Another potentially undesirable feature, seen in practically all simulations analyzed here, is that up to about a quarter of visits in the main survey area represents the third, the fourth and sometimes

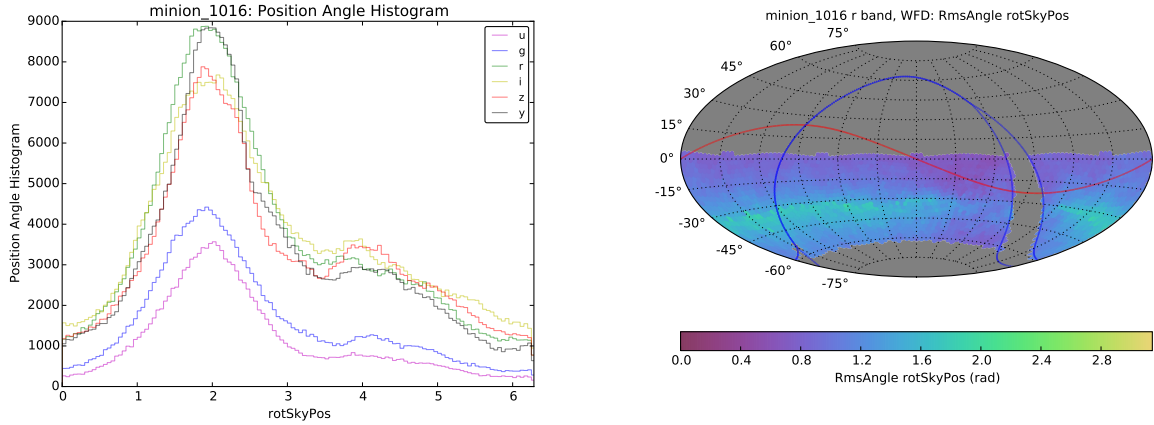


Figure 2.6: The left panel shows the position angle distribution (in radians) in each band for the main survey fields in [minion_1016](#). The position angle is the angle between “up” in the image and North on the sky. The variation of the root-mean-square scatter of the r band distribution across the sky is shown in the right panel.

even the fifth visit to a field in the same night. For a large number of time-domain programs, these visits could be used instead to decrease the field inter-night revisit time. For more details, see [Section 3.2](#). The position angle distributions for this simulation are shown in [Figure 2.6](#).

Time-domain metrics

The analysis of metrics designed for time-domain science has not been performed yet in detail, except for the analysis of asteroid completeness discussed in [Section 3.2](#). MAF already includes several sophisticated metrics, e.g., period recovery for variable stars, which will be described in a later version of this report.

As a brief illustration of time-domain analysis, [Figure 2.7](#) shows the median revisit time distribution when all bands are considered, and [Figure 2.8](#) shows the median revisit time distribution in the band. On average, fields in the main survey get revisited about every 3 days using all filters, and every 15 days when using only r band visits (30 days when using only u band visits is the longest median revisit time). [Figure 2.9](#) shows the maximum inter-night gap, which on average is about 5-6 months.

The temporal sampling for this simulation is sufficient to enable a large recovery fraction for SNe. [Figure 2.10](#) shows that a large fraction of LSST SNe will be detected before their maximum brightness. Similar MAF metrics that explore various quality cuts on SNe light curves (e.g. “detected at least 6 times, at least 3 pre-peak, at least 3 post-peak, with observations in at least 3 filters”).

Intra-night revisit time distribution is discussed in more detail in [Section 3.2](#).

Special Proposals

Regarding the special proposals, here we only provide the basic performance parameters. With the exception of the Deep Drilling proposal, these proposals are essentially strawman placeholders.

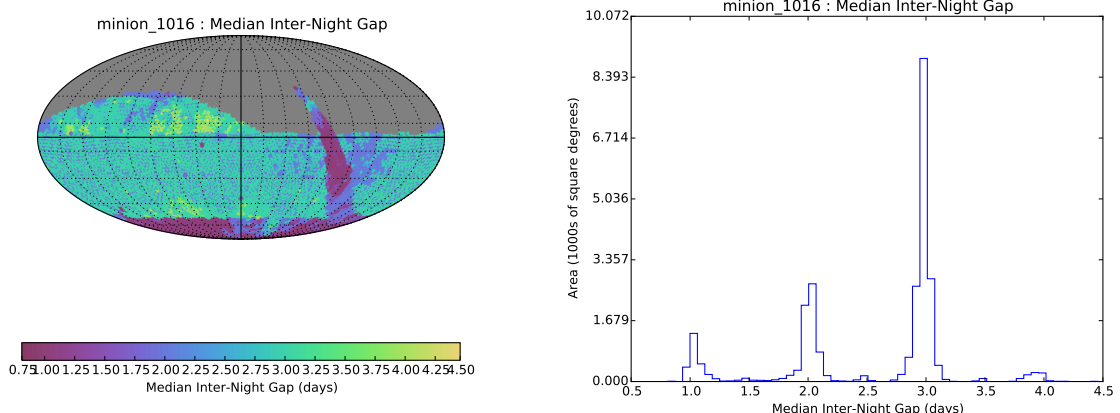


Figure 2.7: The median inter-night gap (or revisit time) is shown in Aitoff projection for all proposals and all filters for candidate Baseline Cadence [minion_1016](#). On average, fields in the main survey get revisited about every 3 days.

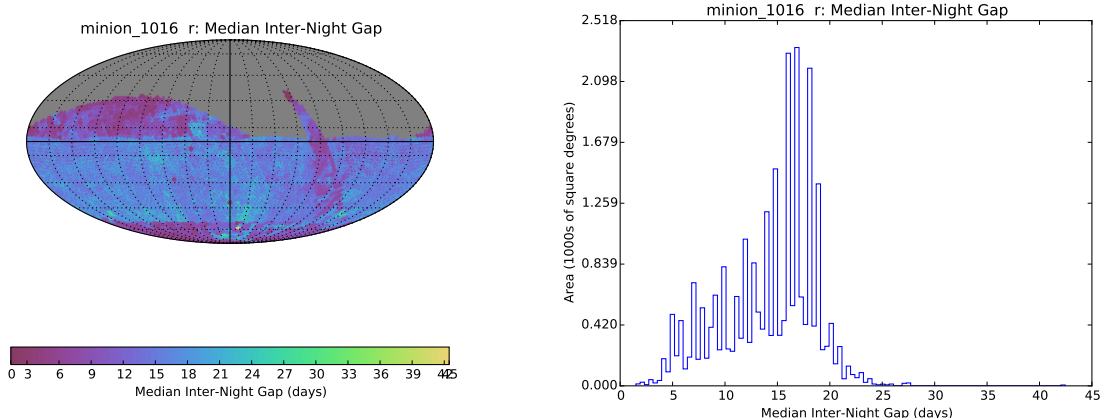


Figure 2.8: The median inter-night gap for r band visits is shown in Aitoff projection for all proposals and all filters for candidate Baseline Cadence [minion_1016](#). On average, fields in the main survey get revisited in the r band about every two weeks.

The North Ecliptic proposal (6.4% of the observing time) obtained an additional 300 visits per field, summed over *griz* bands. These fields are placed along the northern part of the Ecliptic. The Galactic plane proposal (1.7%) obtained 30 visits per band in all six bands, across the region extending in Galactic latitude 10 degrees from the Galactic center, with the boundary approaching the Galactic equator linearly with longitude, and the zone ending at $l = 90$ deg. and at $l = 270$ deg. The South Celestial pole proposal (2.1%) obtained 30 visits per band in all six bands, for fields centers with $\text{Dec} < -62.5$ deg. The Deep Drilling cosmology proposal (4.5%) included 5 fields, with each obtaining several thousand visits per band. The coadded 5σ depths for these fields are much fainter than for the main survey: the median values are (27.8, 28.4, 28.6, 28.0, 27.6, 26.1) in the *ugrizy* bands, respectively.

Conclusions:

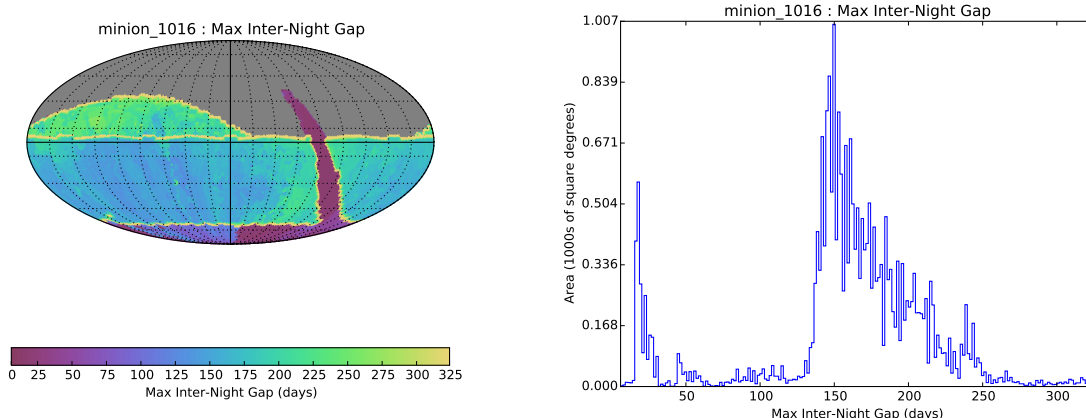


Figure 2.9: The maximum inter-night gap (or revisit time) is shown in Aitoff projection for all proposals and all filters for candidate Baseline Cadence [minion_1016](#).

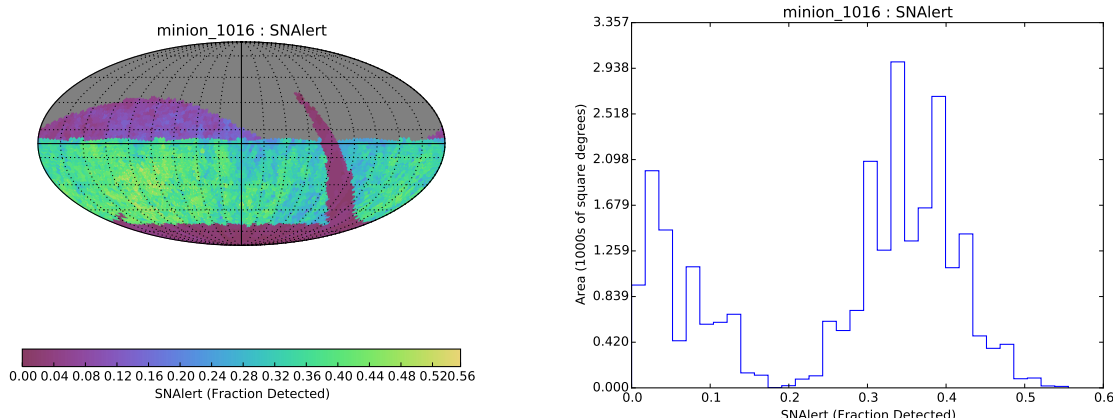


Figure 2.10: The fraction of simulated Type Ia SNe at a redshift of 0.5 detected pre-peak in any filter for candidate Baseline Cadence [minion_1016](#). About 40% of all such SNe from the main survey will be detected before their maximum brightness.

The candidate Baseline Cadence, [minion_1016](#), appears to be an adequate replacement for the current baseline cadence ([opsim3.61](#)). Based on this preliminary analysis, there are no major problems with its performance. While there are patterns which are not fully understood (most notably the observing bias towards west), or undesired (unnecessary revisits of the same field in the same night), [minion_1016](#) is used as a benchmark cadence, and referred to as “Baseline Cadence”, in the rest of this document⁶

An important feature of [minion_1016](#) simulation is that the mean slew time of 6.8 sec (which includes filter change time) is very close to the minimum possible slew time of about 4.5 sec. The implication is that the surveying efficiency, assuming 30 sec exposure time per visit, can be increased by at most about 6% (that is, the total open-shutter time is within about 6% from its possible maximum, given everything else unchanged). Nevertheless, there are other survey

⁶This simulation was proposed by the Project Science Team for adoption as the new Baseline Cadence to the Change Control Board.

aspects, including sky coverage and temporal sampling functions, that can be further optimized, as discussed in [Section 2.3](#) below.

The main remaining known problems with [minion_1016](#) simulation include

- A strong bias towards observations west from the meridian for the main survey, see [Figure 2.5](#). This bias significantly degrades the survey seeing and depth.
- Several proposals complete after only 3-4 years, resulting in regions of sky where the proper motions are poorly constrained due to the short observing baseline. See [Figure 2.11](#).
- The sky brightness model has systematic errors in red bands, resulting in estimates of limit depths (m_5 , both for single visits and coadded depths) that are too shallow by about 0.3 mag in the u band, and 0.5 mag in the z and y bands.
- The moon avoidance angle of 30 deg. allows too many z band observations with elevated sky brightness due to moonshine, resulting in about 0.2-0.3 mag shallower depth.
- There are too many unrequested and unnecessary revisits of the same field in the same night (that is, more than two visits to the same field in the same night).

Go to: • [the start of this section](#) • [the start of the chapter](#) • [the table of contents](#)

2.3 Some Simulated Alternative Observing Strategies

We now describe some alternatives to the Baseline Cadence that were explored. These OPSIM databases are all available for further testing with science-based MAF metrics.

[minion_1012](#)

Only Universal Cadence, with pairs of visits.

Motivation and description: Formally, ~90% of observing time is allocated to the main Universal Cadence program (WFD). The remaining observing time is allocated to other programs, such as “Deep Drilling” programs (see Section 3.4 and Tables 22-26 in the SRD). With this simulation, we wished to find out what would be the effect of ignoring special programs and spending all of the observing time on the main Universal Cadence program.

Expectations: About 2.08 million visits (85% of 2.44 million visits) from Baseline Cadence ([minion_1016](#)) were allocated to WFD cadence. Here we expect that all of these 2.44 million visits will be allocated to WFD cadence.

Analysis Results: This simulated cadence is named [minion_1012](#). Compared to the Baseline Cadence [minion_1016](#):

1. The total number of visits is close to the expected value: 2.42 million. The minimum number of visits per field for the 2,293 WFD fields in Baseline Cadence is 965 for this simulation, compared to 888 for Baseline Cadence.
2. The median number of visits per night and the mean slew time are essentially the same as for Baseline Cadence (807 vs. 816 and 7.2 sec vs. 6.8 sec).
3. The median seeing, sky brightness and airmass in the r and i bands are essentially the same as for WFD fields in Baseline Cadence.
4. The median trigonometric parallax and proper motion errors are improved by about 8%, with improvements commensurate with the increase in the number of visits and the elimination of regions which are not observed for a full 10 years.
5. This simulation also shows observing bias towards west (that is, additional special programs in [minion_1016](#) are not responsible for this bias).

Conclusions: [minion_1012](#), using only uniform cadence proposal, delivered 99.2% of the number of visits obtained by Baseline Cadence. Therefore, *the “filler” aspect of other proposals does not have a major impact on the surveying efficiency*. The minimum number of visits per field for the 2,293 WFD fields in Baseline Cadence is 886 (the SRD design value is 825 and the stretch goal value is 1000). Although the sky coverage of these 2293 fields is about 18,000 sq.deg., their cumulative area is 22,000 sq.deg. With proper dithering, the effective number of visits could be increased to $886 \times 22/18 = 1083$ (or the WFD area increased from 18,000 sq. deg.; see analysis of [minion_1020](#) below). This increase is an improvement of 31% relative to the SRD design specification of 825 visits over 18,000 sq.deg. However, note again that there are no other programs in this simulation (i.e., if other programs were allocated 10% of the observing time, the implied overall “over-performance” in the number of visits would be about 20%).

[minion_1020](#)

A Pan-STARRS-like observing strategy.

Motivation and description: “Pan-STARRS-like cadence” attempts to apply a uniform cadence strategy throughout the survey region, which is maximized and defined by $\text{Dec} < +15$ deg (about 27,400 deg²). The maximum acceptable airmass is kept at its default value of 1.5 (which excludes fields with $\text{Dec} < -78$ deg and $\text{Dec} > +18$ deg. This simulation utilizes uniform cadence and no other proposal, and requires pairs of visits as in Baseline Cadence.

Expectations: The total number of visits should be roughly the same as in Baseline Cadence, but spread over a 42% larger sky area (3,255 fields instead of 2,293), with fewer visits per field.

Analysis Results: This simulated cadence is named [minion_1020](#). Compared to the Baseline Cadence [minion_1016](#):

1. The total number of visits is 2.42 million, and essentially identical to the number of visits in Baseline cadence.

2. The mean number of visits per field is 740, which is 81% of the number of visits for WFD fields obtained by Baseline Cadence (but here the sky area is 42% larger).
3. The median number of visits per night and the mean slew time are essentially the same as for Baseline Cadence.
4. The median seeing, sky brightness and airmass in the r and i bands for WFD fields are essentially the same as in Baseline Cadence.
5. The median trigonometric parallax and proper motion errors show uniform behavior over the entire enlarged area (see [Figure 2.11](#)), with the values similar to those obtained for Baseline Cadence.
6. This simulation also shows observing bias towards west.

Due to increased sky area, which samples regions that can never achieve low airmass, the median coadded depth is about 0.15 mag shallower for this simulation than for Baseline Cadence. As a result, the counts of galaxies per unit area down to a fixed SNR would decrease by about 15-20%. At the same time, the area outside the Galactic plane is increased by about 30%, and thus the total number of galaxies would be increased by about 10%, compared to WFD fields in Baseline Cadence. However, the increased median airmass also results in larger seeing, especially for the borderline regions, as illustrated in [Figure 2.12](#). The increased median seeing would decrease the number of galaxies effectively resolved for weak lensing by about 3-5%. In addition, the additional area has somewhat larger extinction due to interstellar dust which further decreases the galaxy counts (this impact of dust extinction on galaxy counts is not yet implemented in MAF). As a result of these effects, the two strategies result in similar weak lensing galaxy samples.

Conclusions: When only the Universal Cadence proposal is employed, the survey area could be increased by about 40%, while still delivering the mean number of fields at the level of 81% of that in Baseline Cadence (or 90% of the SRD design value of 825). Hence, simulations [minion_1020](#) and [minion_1012](#) demonstrate that the “survey reserve”, relative to the Universal Cadence design specifications from the SRD, can be used to i) increase the number of visits per field over the WFD area, or ii) increase the surveyed area while keeping the number of visits per field statistically unchanged, or iii) increase both area and the number of visits, and/or iv) execute additional programs (the current baseline).

[minion_1013](#)

Only Universal Cadence, no visit pairs.

Motivation and description: The main goal of this simulation was to assess the impact of the requirement for visit pairs on the survey efficiency (Baseline Cadence requests two visits per night to the same field, separated in time by about an hour, and driven by asteroid orbit determination). It is plausible that the removal of this requirement could result in a more efficient survey. In order to allow as simple analysis as possible, only the Universal Cadence proposal is requested. Hence, this simulation should be directly compared to simulation [minion_1012](#).

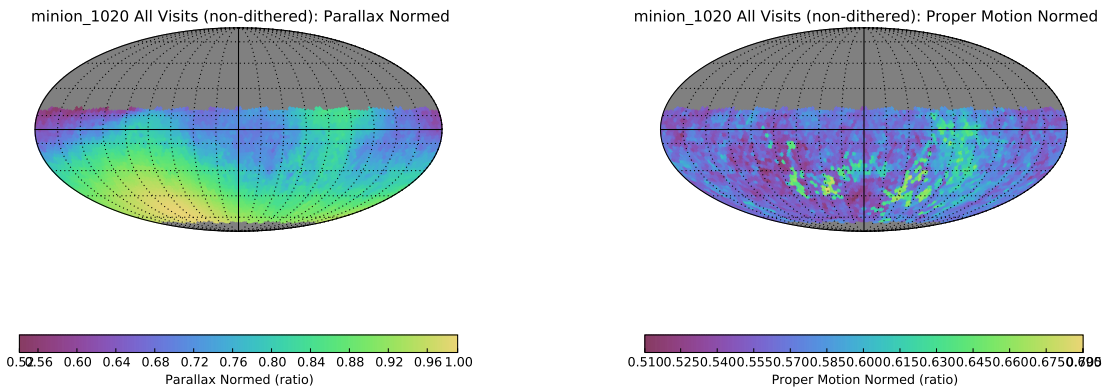


Figure 2.11: The trigonometric parallax errors (left) and proper motion errors (right) for simulated cadence minion_1020 (“Pan-STARRS-like” cadence), normalized by the values for idealized perfectly optimized cadence, are shown in Aitoff projection of equatorial coordinates (compare to Figure 2.3).

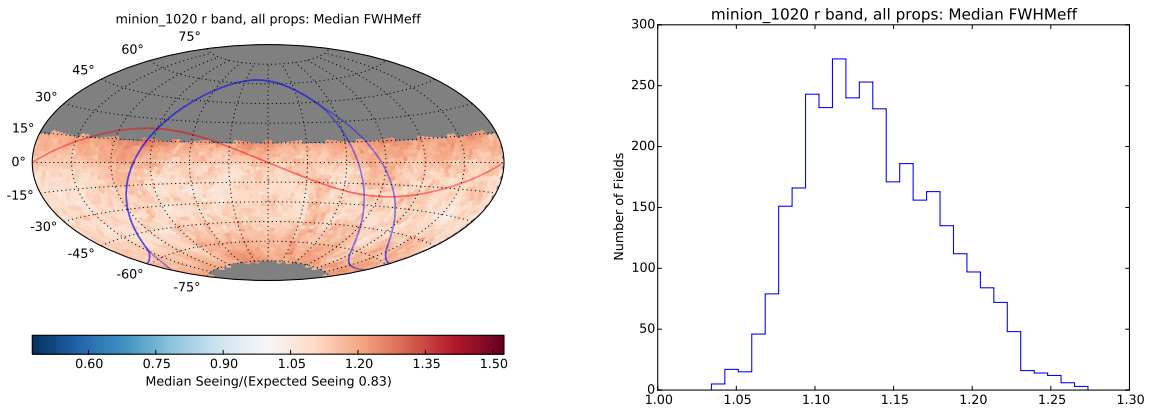


Figure 2.12: The median seeing in r filter, for simulated cadence minion_1020 (“Pan-STARRS-like” cadence), normalized by expected value ($0.83''$). Note that fields with the most positive and most negative declination have on average larger values. For comparison, the median normalized seeing for WFD fields in Baseline Cadence is 1.08, with a negligible fraction of fields with values above 1.18.

Expectations: If the requirement for visit pairs decreases surveying efficiency, then this simulation should deliver more than 2.45 million visits delivered by [minion_1012](#).

Analysis Results: This simulated cadence is named [minion_1013](#). Compared to [minion_1012](#):

1. The total number of visits is 2.42 million, identical to [minion_1012](#).
2. The median slew time, and the median coadded depth and seeing in the r band are essentially identical, too.
3. The median airmass in the r band of 1.25 is a bit higher than 1.18 obtained for [minion_1012](#).
4. The median fraction of revisits faster than 30 minutes of 0.32 is smaller than 0.38 for [minion_1012](#), and is consistent with the absence of pair contributions (that is, such revisits

are due to field edge overlaps, and unintentional revisits, in case of [minion_1013](#)).

Conclusions: The comparison of this simulation and [minion_1012](#) shows that requiring pairs of visits (in a given observing night) does not result in an appreciable loss of surveying efficiency. Indeed, pairs of visits result in a better short-timescale coverage that would enhance many types of time-domain science (and, of course, it's crucial for asteroid science).

`kraken_1043`

Baseline Cadence, but with no visit pairs.

Motivation and description: The main goal of this simulation was to assess the impact of the requirement for visit pairs on the survey efficiency. Instead of the idealized case above which compared only the Universal Cadence proposal fields, in this more realistic case *all proposals from Baseline Cadence are executed*. Hence, this simulation should be compared to Baseline Cadence ([minion_1016](#)).

Expectations: A slight, or no, increase in surveying efficiency and thus the total number of visits is expected when compared to Baseline Cadence.

Analysis Results: This simulated cadence is named [kraken_1043](#). Compared to [minion_1016](#),

1. The total number of visits is 2.51 million, or 2.4% more than in Baseline Cadence.
2. The mean slew time is 5.8 sec, or 15% shorter than for Baseline Cadence. This decrease in the mean slew time implies an efficiency increase of 2.8% and explains the actual 2.4% improvement implied by the total number of visits. Note that this simulation has the shortest mean slew time of all simulations investigated here (the nominal shortest slew and settle time is about 4.5 sec).
3. The median airmass in the r band is slightly larger for this simulation than for Baseline Cadence: 1.29 vs. 1.22.

Conclusions: Unlike the comparison of [minion_1013](#) and [minion_1012](#), here the removal of visit pair requirement results in a 15% shorter mean slew time and consequently in 2.4% more visits.

`enigma_1281`

NEO test: triplets of visits.

enigma_1282

NEO test: quads of visits.

Motivation and description: Many science programs can benefit from having more than a pair of visits in a night; in particular, Solar System science may critically depend on having more than just a pair, depending on the performance of the Moving Object Pipeline Software (MOPS). These two simulations were run to investigate the effects of requiring more than just a pair of visits in each night. The first, [enigma_1281](#), requests sets of three visits (triplets) in each night. The second, [enigma_1282](#), requests sets of four visits (quads) in each night. There is no constraint on the filter chosen for these sets of visits – it may be changed or it may remain the same. These simulations should be compared to the Baseline Cadence, [minion_1016](#), and to the [kraken_1043](#), which all keep the special surveys, but simply vary the sequences requested in the Universal Cadence.

Expectations: The general expectations are that science cases which require many visits on timescales of a few hours will benefit with these runs, while science cases which prefer visits to be spaced more widely over time will see negative impacts.

Analysis Results: First, we emphasize that “requested” is not the same as “delivered”: even the “no pairs” simulation [kraken_1043](#) ends up having multiple visits in a given night to the same fields, and when multiple visits per night are requested, not all fields get to have completed sequences. The statistics of how many fields are combined into sequences of a given number of visits is shown in [Figure 2.13](#). As evident, the highest peak is at the requested number of visits in a sequence, but not all visits are incorporated into requested sequences: some are in both shorter and longer sequences. In particular, even “no pairs” simulation includes multiple visits to some fields, essentially because the current version of the algorithm is not told not to do so. As illustrated in [Figure 2.14](#), such revisits typically happen within 10 minutes from the first visit. This (unintended) behavior implies that the naive expectation above is probably incorrect, or at least softened.

The median inter-night revisit rate is affected by requesting more visits within single night, as expected – there are only so many visits available, and if more occur in a particular night, it is likely (without some kind of rolling cadence) that the result is longer intervals between subsequent nights. This is demonstrated in `autoreffig:internightgapCompare`, where it can be seen that the inter-night revisit rate increases by about 30% from 3 nights to 4 nights if we go from pairs to triplets (or quads).

Details of the impacts on Solar System science is left to ??, in particular the impact on completeness is evaluated in [Section 3.2](#).

The impact of requesting sequences with 3 or 4 visits to the same field on other science programs is not yet analyzed in detail. The impact on static science should be minimal, except perhaps for a bit worse behavior of various systematic errors (because fewer nights, with their observing conditions, are sampled).

Conclusions: The effect of requesting pairs, single visits, triplets or quads, is softened with the current behavior of the scheduler, where it is not uncommon to receive more than the requested number of visits within a night. The inter-night revisit rates are affected, increasing the inter-night

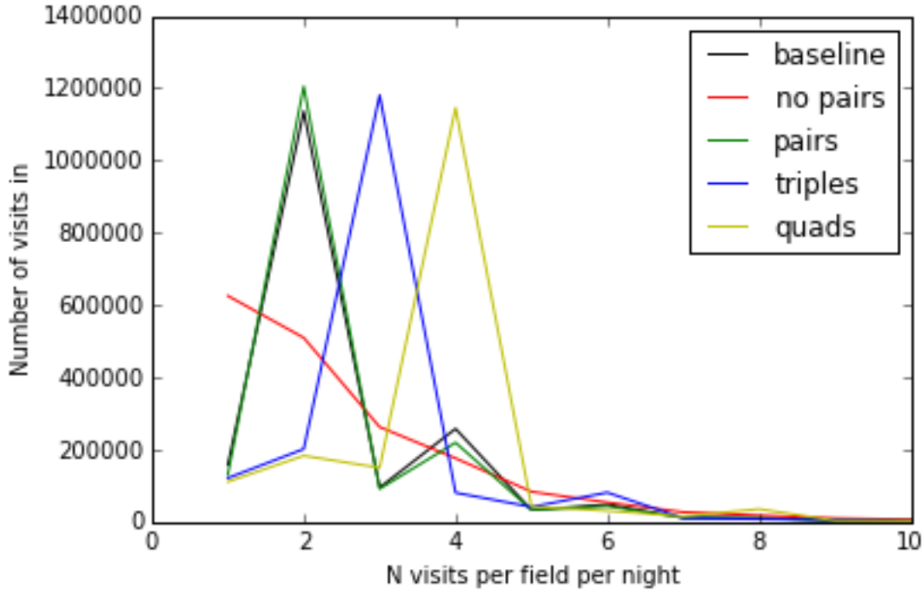


Figure 2.13: The distribution of the number of visits used for nightly sequences of length given on the horizontal axis. Only *griz* bands are used. Note that even “no pairs” simulation (??) includes multiple visits. The highest peak is at the requested number of visits in a sequence.

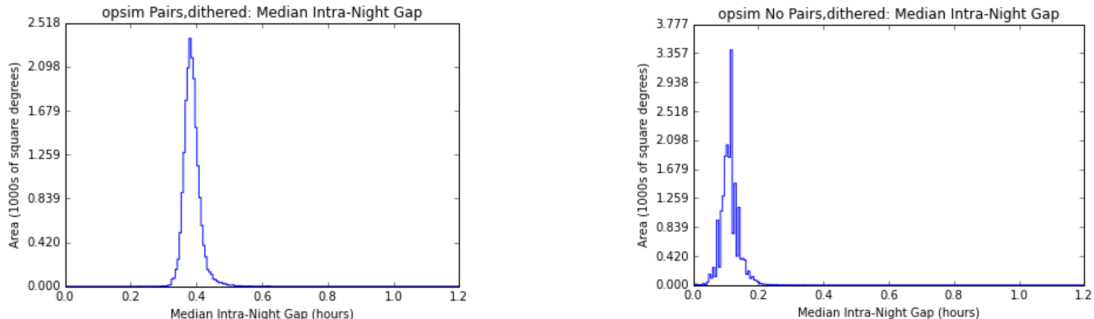


Figure 2.14: The comparison of the median intra-night gap (per field) distributions for Baseline Cadence (left) and simulation [kraken_1043](#), which did not request pairs of visits per night. Despite no need for pairs, simulation [kraken_1043](#) produced them “spontaneously”, as well as longer sequences (see Figure 2.13). The mean field revisit time is much shorter (about 6 minutes, see the right panel) than for Baseline Cadence (22 minutes).

revisit rate by about a night for triplets and quads and reducing the inter-night revisit rate by about a night when no visit pairs are requested (from a baseline value of about 3 nights).

[kraken_1052](#)

Baseline Cadence, but with 33% shorter exposure time.

Motivation and description: The optimal exposure time per visit for the main survey, in the limit of a single value for all bands and at all times, is in the range of about 20–60 seconds (see Section 2.2.2 in the LSST overview paper, arXiv:0805.2366, version 3.1). This simulation investigates the effect of decreasing the exposure time per visit to 20 seconds (from its nominal value

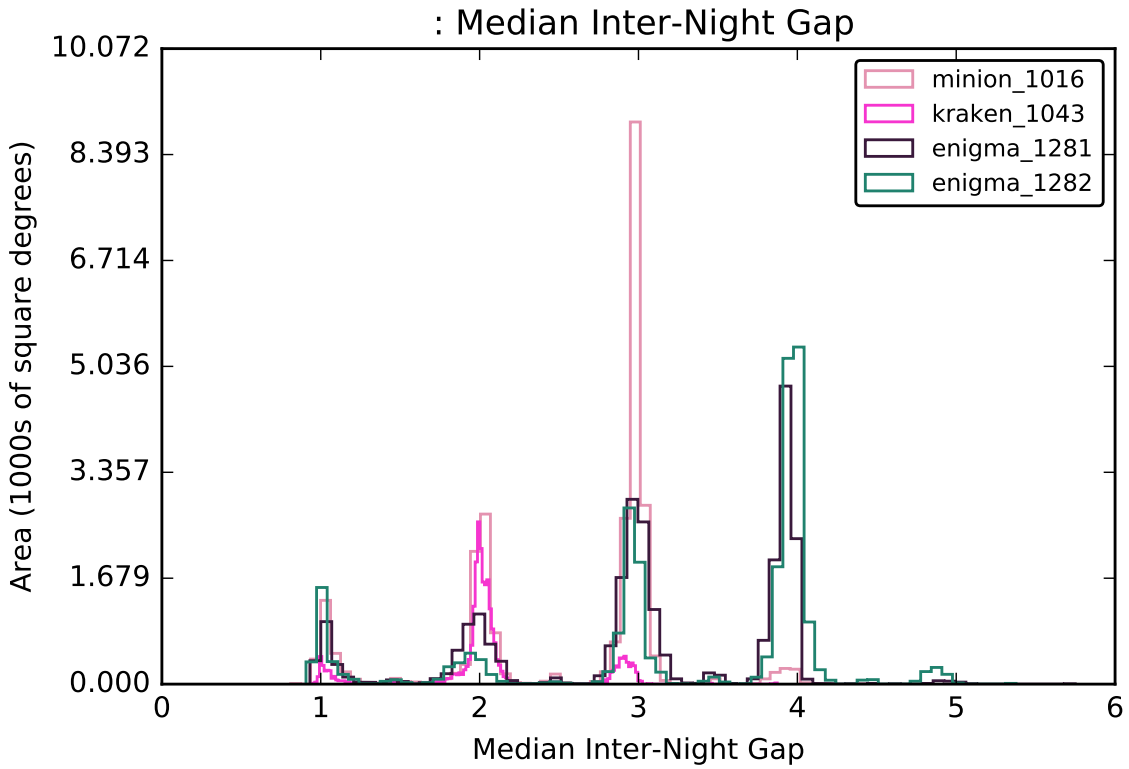


Figure 2.15: Comparison of the median inter-night gap distribution for `minion_1016`, `kraken_1043`, `enigma_1281`, and `enigma_1282`. The peak median inter-night revisit rate (per field) is about 3 days for the baseline cadence, `minion_1016`, about 2 days for `kraken_1043`, and closer to 4 for both `enigma_1281` and `enigma_1282`.

of 30 seconds). The shorter exposure time results in 0.22 mag shallower faint limit per visit (the effect is larger in the *u*-band, see `kraken_1045`).

Expectations: The total number of visits is expected to increase by about 50%, compared to `minion_1016`, to 3.70 million, for the same survey efficiency. However, the shorter exposure time will have a significant impact on the survey efficiency: assuming a slew time of 7 sec, the efficiency drops from 73% to 65% (comparing $30/(30+4+7)$ vs. $20/(20+4+7)$). Therefore, the expected increase in the number of visits is about 32% and the expected number of visits is 3.2 million.

Analysis Results: This simulated cadence is named `kraken_1052`. Compared to Baseline Cadence:

1. The total number of visits is 3.23 million, representing an increase of 31% that is very close to the expected value of 32%.
2. The median number of visits per night is 1079, or about 32% more than for Baseline Cadence. The total open shutter time is 14% smaller for this simulation, and easily understood as due

to expected 11% decrease due to smaller surveying efficiency (the mean slew time is the same as in Baseline Cadence, 6.9 sec).

3. The main survey (WFD, 18,000 sq. deg.) fields received 33% more visits than in Baseline Cadence. The increase in the minimum number of visits over that area is 9% (from 886 to 963). In addition, another 1,000 sq. deg. (6% of the nominal WFD) area has more than 961 visits.
4. Most other performance parameters are essentially unchanged: the fraction of visits spent on the main survey (88% vs. 85%), the median seeing in the r band (0.93 arcsec vs. 0.94 arcsec), and the median airmass (1.23 vs. 1.22).

Conclusions: The comparison of [kraken_1052](#) and [minion_1016](#) simulations demonstrates that the effect of shorter exposures can be easily understood using simple efficiency estimates. With the visit exposure time is decreased from 30 sec to 20 sec, the surveying efficiency and the total open shutter time drops by $\sim 10\%$, while the number of (shorter exposure time) visits (for all proposals) increases by 32%.

[kraken_1053](#)

Baseline Cadence, but 100% longer exposure time.

Motivation and description: This simulation investigates the effect of increasing the exposure time per visit to 60 seconds (from its nominal value of 30 seconds). The longer exposure time results in 0.38 mag deeper faint limit per visit (the effect is larger in the u-band, see [kraken_1045](#)).

Expectations: The total number of visits is expected to decrease by about a factor of 2 in case of no significant impact on the survey efficiency. However, the longer exposure time improves efficiency by a factor of $2 \times (34 + 7)/(64 + 7) - 1 = 15\%$, and thus the expected total number of visits is $0.5 \times 1.15 = 58\%$ of the number of visits in Baseline Cadence (assuming the same mean slew time of 7 seconds).

Analysis Results: This simulated cadence is named [kraken_1053](#). Compared to Baseline Cadence:

1. The total number of visits is 1.42 million or 58% of the visits obtained with Baseline Cadence, and the total open-shutter time is 16% higher than for Baseline Cadence. Both results are in good agreement with above expectations.
2. The median number of visits per night is 467, or 57% of the value obtained with Baseline Cadence. The mean slew time is 0.5 sec longer than that obtained with Baseline Cadence.
3. This simulation has significantly different time allocation per proposal, compared to Baseline Cadence: 74% spent on the Universal proposal (vs. 85%) and 11% spent on the North Ecliptic proposal (vs. 6%) (with smaller and less important differences for other proposals). Because of these differences, *the results of this test may not be very robust*.

Conclusions: Simple estimates of the total number of visits and the improvement in efficiency are in good agreement with delivered values. Of course, the increased efficiency comes at the cost of fewer visits, which is disadvantageous for time-domain science.

kraken_1045

Baseline Cadence, but with doubled u-band exposure time.

Motivation and description: The read-out noise in the u band is not negligible compared to the background noise as in other bands, due to darker u band sky. The current best estimates for survey performance (see Table 2 in the LSST overview paper, arXiv:0805.2366, version 3.1) indicate that the *coadded* depth in the *u* band could be improved by 0.24 mag by increasing the exposure time per visit from 30 seconds to 60 seconds⁷ (assuming the same total exposure time, which implies a decrease in the number of visits by a factor of two). To keep the total exposure time in the *u* band unchanged, the requested number of visits in this simulation is decreased by a factor of 2 relative to Baseline Cadence specification.

Expectations: The total exposure time in the *u* band should remain unchanged. The single visits depth should be 0.38 mag deeper due to twice as long exposure time (the gain of 0.24 mag related to read-out noise effects is not yet implemented in the OPSIM code so MAF outputs may be a bit confusing).

Analysis Results: This simulated cadence is named [kraken_1045](#). Compared to Baseline Cadence ([minion_1016](#)):

1. The total number of visits is 2.32 million or 95% of the Baseline Cadence values. The fraction of time allocated to the main survey is 84% vs. 85% for Baseline Cadence, and for the NE spur proposal 7% vs. 6%.

Conclusions: The *u* band exposure time can be increased from 30 seconds to 60 seconds without a significant impact on the survey efficiency. This change would result in a gain of about 0.2 mag in the coadded depth. However, the number of visits in the *u* band would be decreased by about a factor of two, with a negative impact on time-domain science.

kraken_1059

Baseline Cadence, but with doubled u-band exp. time and Baseline NE Spur.

Motivation and description: This simulation is similar to [kraken_1045](#), which increased the exposure time per visit in the *u*-band from 30 seconds to 60 seconds, with the requested number of visits decreased by a factor of 2. This change resulted in a gain of about 0.24 mag in the coadded

⁷In the background-limited case, a factor of two increase of the exposure time results in 0.38 mag deeper data. Since in the *u* band the read-out noise is not negligible compared to the background noise, the total noise increases by less than a factor of $\sqrt{2}$ and there is an extra depth improvement of 0.24 mag (see eq. 7 and Table 2 the overview paper). Conversely, when exposure time is shorter than 30 seconds, there is an extra penalty of 0.16 mag, in addition to a loss of depth of 0.22 mag due to shorter exposure time in the limit of negligible read-out noise.

depth. Since the number of u band visits in [kraken_1045](#) was decreased by about a factor of two, with a negative impact on time-domain science, this simulation does not change the nominal requested number of visits per field. Hence, the coadded depth in the u band in this simulation would be improved by about 0.6 mag.

Expectations: Given that about 5% of all visits are allocated to the u band, the total number of visits may decrease by up to about 5%, resulting in about 0.03 mag shallower data in bands other than u band.

Analysis Results: This simulated cadence is named [kraken_1059](#). Compared to Baseline Cadence ([minion_1016](#)):

1. The total number of visits is 2.36 million or 95.5% of the Baseline Cadence values. The fraction of time allocated to the main survey is 85% vs. 85% for Baseline Cadence, and for the NE spur proposal 7% vs. 6%.

The median number of visits in the *grizy* filters in the main survey decreases by only around 1-2%. The main survey coadded u is 0.18 mags deeper. The other filters reach the same depth within 1%.

Conclusions: When the u band exposure time is increased from 30 seconds to 60 seconds, and the number of visits is kept unchanged, the single-visit and coadded depths would be improved by 0.6 mag. This improvement would come at the expense of about 1% fewer visits in other bands (with about 0.01 mag shallower coadded depths).

[minion_1022](#)

Only Universal Cadence, with relaxed airmass limit.

Motivation and description: What is the effect of changing the airmass limit from 1.5 to 2.0? To avoid complicated analysis, use only Universal Cadence proposal and thus compare to [minion_1012](#).

Analysis Results: This simulated cadence is named [minion_1022](#). Compared to [minion_1012](#), it collected 99.1% visits. This fraction is identical to the loss of efficiency due to slightly longer mean slew time: 7.2 sec vs. 6.8 sec. In addition, [minion_1022](#) has much worse airmass distributions than [minion_1012](#), extending to the allowed maximum of 2.0. For example, the median for the r band and WFD fields is 1.30, compared to 1.19 for [minion_1012](#).

Conclusions: This simulation confirms that it's a bad idea to relax airmass limit: as a result, the airmass distribution always widens. In addition, relaxed airmass limit tends to result in a longer mean slew time. For a given proposal, the airmass limit has to be as tight as possible, while still allowing observations of all requested fields.

minion_1017

Only Universal Cadence, with stringent airmass limit.

Motivation and description: What is the effect of changing the airmass limit from 1.5 to 1.3? To avoid complicated analysis, we use only the Universal Cadence proposal and thus compare to [minion_1012](#).

Analysis Results: This simulated cadence is named [minion_1017](#). Compared to [minion_1012](#), it collected essentially the same number of visits. The mean slew time is also essentially unchanged (7.4 sec vs. 7.2 sec). The airmass distributions is improved compared to [minion_1012](#). For example, the median for the r band and WFD fields is 1.11, compared to 1.18 for [minion_1012](#). The limiting coadded depth in u and g bands is about 0.1 mag deeper than for Baseline Cadence.

Conclusions: It is possible to achieve the same surveying efficiency with much more stringent airmass limit than 1.5, which was used in most simulations to date. *Given this encouraging behavior, an analogous experiment should be executed for Baseline Cadence (i.e. a simulation like [minion_1016](#), with airmass limit for the main survey set to 1.3) – after the “Western bias” is fixed’.*

astro_lsst_01_1004

Extend Universal Cadence to the Galactic Plane.

Motivation and description: What is the effect of extending the ‘normal’ Universal Cadence and number of exposures to the region of the Galactic Plane within the WFD declination limits? Fields which were previously contained in the Galactic Plane proposal, but which fell within the range of the WFD declination limits, were reassigned to the standard WFD proposal instead of the much more limited Galactic Plane proposal. The remaining proposals were unchanged, and thus we compare this to the Baseline Cadence, [minion_1016](#).

Analysis Results: This simulated cadence is named [astro_lsst_01_1004](#). Compared with the [minion_1016](#), there are small to no changes in proposals other than the WFD and Galactic Plane proposals themselves. The fields which remained in the Galactic Plane proposal obtained the same number of visits as expected (30 in each bandpass). There were differences observed in the overall status of observations taken under the Universal cadence, in the WFD proposal, however. The number of fields included in the WFD proposal increased from 2293 to 2470 ($\sim 8\%$), as 177 fields were moved from the Galactic Plane proposal into the WFD. The total number of observations obtained by the WFD proposal increased from 2085270 to 2116203; an increase of only 1.5%. As a result, the median number of visits per field was reduced in all bands, as well as the corresponding coadded depth; this is shown in table 2.1 below.

Conclusions: In both of these runs, the WFD proposal received about 85% of the total number of visits in the survey. Extending the Universal cadence to the galactic plane, without increasing the overall priority of the Universal proposal, results in slightly fewer visits per field as a result, by about 5%, and a slightly lower coadded depth, by about 0.04 magnitudes. It is worthwhile to note that increasing the priority of the WFD proposal could increase the total fraction of time devoted to WFD, returning the typical number of visits and coadded depth to baseline levels while

Table 2.1: Visits and Coadded Depth in Universal Proposal comparison

Median Number of Visits (per field, per filter)		
	<code>minion_1016</code>	<code>astro_lsst_01_1004</code>
WFD <i>u</i>	62	59
WFD <i>g</i>	88	83
WFD <i>r</i>	201	189
WFD <i>i</i>	200	189
WFD <i>z</i>	180	170
WFD <i>y</i>	181	170
Median Coadded Depth (per field, per filter)		
	<code>minion_1016</code>	<code>astro_lsst_01_1004</code>
WFD <i>u</i>	25.46	25.42
WFD <i>g</i>	26.95	26.91
WFD <i>r</i>	27.07	27.04
WFD <i>i</i>	26.36	26.32
WFD <i>z</i>	25.19	25.17
WFD <i>y</i>	24.43	24.39

decreasing time spent in other proposals. Metrics targeted for specific science cases, explored in later chapters, will help determine whether this is a worthwhile trade.

Go to: • [the start of this section](#) • [the start of the chapter](#) • [the table of contents](#)

2.4 Temporarily Denser Time Sampling: Rolling Cadence

Stephen Ridgway

With a total of ~ 800 visits spaced approximately uniformly over 10 years, and distributed among 6 filters, it is not clear that LSST can offer the sufficiently dense sampling in time for study of transients with typical durations less than or $\simeq 1\text{week}$. This is particularly a concern for key science requiring well-sampled SNIa light curves. Rolling cadences stand out as a general solution that can potentially enhance sampling rates by $2\times$ or more, on some of the sky all of the time and all of the sky some of the time, while maintaining a sufficient uniformity for survey objectives that require it. In this section we provide an introduction to the concept of rolling cadence, and give some examples of ways in which it can be implemented.

2.4.1 The Uniform Cadence

Current schedule simulations allocate visits as pairs separated by 30-60 minutes, for the purposes of identifying asteroids. For most science purposes, the 30-60 minute spacing is too small to reveal temporal information, and a pair will constitute effectively a single epoch of measurement. If the expected 824 (design value) LSST visits are realized as 412 pairs, and distributed uniformly over 10 observing seasons of 6 months each, the typical separation between epochs will be 4 days. The most numerous visits will be in the r and i filters, and the repeat visit rate in either of these will be $\simeq 20$ days.

The possibility is still open that, for asteroid identification, visits might be required as triples or quadrupoles, in which case the universal temporal sampling will be further slowed by 1.5 or $2\times$.

Under a strict universal cadence it is not possible to satisfy a need for more frequent sample epochs. This leads the simulations group to investigate the options opened up by reinterpreting the concept of a universal cadence. Instead of aiming for a strategy which attempts to observe all fields “equally” all the time, it would allow significant deviations from equal coverage during the survey, returning to balance at the end of the survey.

Stronger divergence from a universal cadence, allowing significant inhomogeneities to remain at the end of the survey, is of course possible, but is not under investigation or discussed here.

There is currently considerable interest in the community in strategies that provide enhanced sampling over a selected area of the sky, and rotating the selected area in order to exercise enhanced sampling over all of the survey area part of the time. The class of cadences that provides such intervals of enhanced visits, with the focus region shifting from time to time, is termed here a rolling cadence. As a point of terminology, observing a single sky area with enhanced cadence for a period of time will be described as a “roll”.

2.4.2 Rolling Cadence Basics

Assume a fixed number of observing epochs for each point on the sky, nominally distributed uniformly over the survey duration. A subset of these can be reallocated to provide improved sampling of a sky region. This will have the inevitable effects of: (1) reducing the number of epochs available for that sky region during the rest of the survey, and (2) displace observations of other sky regions during the time of the improved temporal sampling. In short, the cadence outside the enhanced interval will be degraded.

The essential parameters of rolling cadence are: (1) the number of samples taken from the uniform cadence, and (2) the enhancement factor for the observing rate. [LSST document 16370](#), “A Rolling Cadence Strategy for the Operations Simulator”, by K. Cook and S. Ridgway, contains more detailed discussion and analysis.

2.4.3 Some Example Rolling Cadence OPSIM Runs

In this section we describe a set of three experimental “Swiss Cheese” rolling cadence strategies, and a uniform strategy for use as a control.

`ops2_1102`

“Swiss Cheese” rolling cadence, version 1.

`enigma_1260`

“Swiss Cheese” rolling cadence, version 2.

`enigma_1261`

“Swiss Cheese” rolling cadence, version 3.

`ops2_1098`

“Control” simulation for comparison with the “Swiss Cheese” experimental rolling cadence simulations

[Figure 2.16](#) illustrates the difference in how survey depth (characterized by the number of visits) builds up between uniform cadence (`ops2_1098`) and rolling cadence (`enigma_1260`) strategies.

2.4.4 Supernovae and Rolling Cadence

Supernovae as a science topic are addressed elsewhere. In this section, the demands of SN are used to directly constrain or orient the rolling cadence development.

Pending more quantitative guidance, the SN objective for rolling cadence is to obtain multicolor time series significantly longer than the typical SN duration, with a cadence significantly faster than uniform. As an example we discuss the option of a rolling cadence with the regular distribution of filters.

As a simple example, consider improving the cadence by a factor of 2 or 3. If we accept that some regions of the sky will be enhanced every year, and that uniform sky coverage will only arrive at the end of 10 years, then we could use, e.g., 10% of the total epochs in a single roll. If the enhancement is $2\times$, each roll would last for $\simeq 6$ months, with high efficiency for capture of complete SN events. If the enhancement is $4\times$, each roll would last for 2 months, with lower efficiency.

If it is important to achieve survey uniformity after 3 years, the available visits for each roll would be reduced also. With a $2\times$ enhancement of epoch frequency, a roll would last 2 months.

2.4 Temporarily Denser Time Sampling: Rolling Cadence

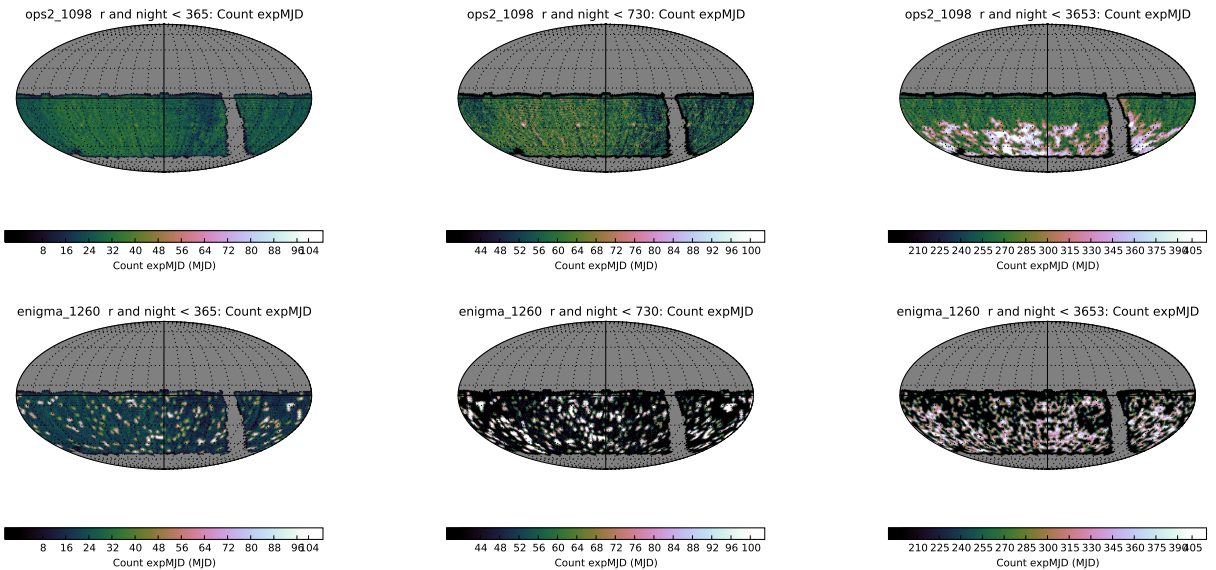


Figure 2.16: Example of a regular uniform survey ([ops2_1098](#), top row) and a rolling cadence survey ([enigma_1260](#), bottom row) after 1, 2, and 10 years in the r filter. For the regular survey, the number of visits for any part of the sky is relatively constant throughout the survey. For the rolling cadence simulation, there are regions with many more exposures in year one which then fade in year two as other parts of the sky are emphasized.

Some leverage would be gained by using more than 10% of the available visits for a single roll. However, this begins to impact the sampling of slow variables reduce schedule flexibility and robustness, and should be approached with caution.

From these examples, it appears that a $2\times$ enhancement with uniformity closure after 10 years is relatively feasible and promising. Much higher gains, or more rapid closure, require additional compromises.

2.4.5 Fast Transients and Rolling Cadence

Fast transients as a science topic are addressed elsewhere. In this section, the demands of fast transients are used to directly constrain or orient the rolling cadence development.

By “fast transients”, we are referring to events that are sufficiently fast that they are not addressed by the rolling cadence designed for SN observations, and slow enough that they are not covered in “deep drilling” type mini-surveys. For higher tempo rolls, it is quite difficult to obtain full color data, because of the constraints on filter selection. For this example, we will examine a rolling cadence utilizing only the r and i filters, as they are used for most visits. They are close in wavelength, and we assume that sufficient color information will be obtained by the “background” uniform survey that continues during a roll.

Again using 10% of the available visits from the full 10 year survey for a single roll, we find that there would be enough epochs for each roll to acquire 1 visit per day for 21 consecutive days, giving an enhancement of $10\times$.

Alternatively, the same epochs could be used to observe a target every 20 minutes for 12 hours during a single night (here it is assumed that visit pairs are not required, doubling the available epochs) for an enhancement of $300\times$.

Several different possible redeployments of portions of a uniform survey have been described, each using 10% of available time. Of course it is possible in principal to implement multiple options, sequentially or maybe in parallel in some cases. This may pose considerable challenges to the scheduling strategy design by introducing incompatible boundary conditions.

While rolling cadences are powerful, they have limitations. For example, sampling events that last longer than $\simeq 1$ day and less than $\simeq 1$ week have the obvious problem of diurnal availability. In this example, intermediate cadences could be implemented in the circumpolar region, where diurnal access is much extended. This is an example of a case in which a mini-survey of a limited number of regions could be considered as an alternative to a rolling cadence applied to the entire main survey.

2.4.6 Constraints, Trades and Compromises for Rolling Cadences

While rolling cadences offer some attractive benefits, it is important to realize that rolling cadences are very highly constrained, and that they do bring disadvantages and compromises.

There are strong arguments against beginning a rolling cadence in the first, or even the second year of the survey. Early in the survey, it is important to obtain for each field/filter combination, an adequate number of good quality photometric images, and at least one image in excellent seeing, to support closure of photometry reductions and to support generation of template images.

Since major science goals require a significant degree of survey homogeneity, it may be advisable to implement a strategy that brings the survey to nominal uniform depth at several times, e.g. after 3 or 5 years. This would strongly constrain rolling cadences.

Some science objectives favor certain distributions of visits. For astrometry, visits early and late in the survey and at large parallax factors, are beneficial. Slow variables may benefit from uniform spacing. Rolling cadences might impact these constraints either favorably or unfavorably.

Many objectives are served by randomization of observing conditions for each field. Some rolling cadences could tend to reduce this randomization, for example by acquiring a large number of observations during a meteorologically favorable or unfavorable season, or during a period of instrument performance variance.

Dithering does not work gracefully with a rolling cadence, reducing temporal coverage at the boundaries of the selected sky region. This is negligible for small dithers, but important for large dithers, which are under consideration.

These cautions illustrate that evaluation of rolling cadences must be based on the full range of schedule performance metrics, and not just those targeted by rolling cadence development.

2.4.7 Directions for Future Work with Rolling Cadences

While preliminary experiments with rolling cadences have been carried out with OpSim, these experiments have significant deficiencies, and are not suited for in-depth study as of this writing. Progress in rolling cadence simulations is expected no sooner than mid to late-2016. Preparatory to that, analysis of cadences described above can guide development of objectives for enhancement by rolling cadence.

Rolling cadences will be required to pass the same metrics as for other cadences, and general requirements such as sky area, depth and visit count must be met. Of particular interest will be metrics that clearly distinguish the gains available with rolling cadences – that is, metrics that measure schedule performance for variable targets, and especially those with strong sampling requirements, or more rapid variability.

Future Rolling Cadence Metrics

The following metrics, based on similar metrics developed for particular science objectives, may be useful in tuning rolling cadence performance:

- Observation Pairs histograms. Visit pairs are simple and easy to quantify. A pair of visits in the same filter describe a brightness change and constrain the rate of change. A visit pair in different filters (probably not coeval) constrain a color. These metrics will describe how rapidly LSST can detect a change in the source fluxes. They will be useful for such science as early discovery of SNe, and identification of interesting galactic microlensing events.
- Observation Triplets histograms. Similar to Pairs, but with closely spaced triplets allowing detection and confirmation of transient events (as described by [Lund et al. 2016](#)).
- Period determination metric. Compute a measure of the period determination accuracy after a given time interval, as a function of period. A complete analysis would allow use of real light curves for various object types with realistic brightness distributions. A simpler approach would use a single example light curve and a fixed measurement error value. A simplest approach would be based on the sampling function and its power spectrum ([Lund et al. 2016](#)). This metric group would rate simulation performance for period determination of periodic variables - mostly stars.
- Sampling of SNe light curves. The most complete metric would count the number of SNe (of various types) light curves that would be well sampled (according to defined criteria), based on analysis of realistic simulated data. A simpler metric would be based on estimated sampling requirements and cadence without considering brightness. The latter could be used initially, pending replacement (or calibration) with more extensive simulations.
- Time series count. For any transient or irregular variable, the optimum observational data will require multiple time and color samples within the duration of the event. Since the category of transients may include discoveries, it is not possible to exhaustively specify the source characteristics. A time series can be defined to consist of a series of samples, over some total duration T , with sampling interval t to tolerance d . The count of time series depends on the total duration, the number of samples, as well as the filter selection, so

the challenge is how to visualize this information, and how to extract useful characteristic summary measures of performance. This type of data can be valuable for identification and study of rapid phenomena such as stellar flares, binary mass transfer events, and exoplanet transits, and for slower events such as AGN reverberation mapping.

Rolling Cadence Recommendations

Based on the analysis presented above, several recommendations for further cadence exploration can be made:

1. Further optimization of the main survey (e.g., exposure time in general, and u band exposure time in particular; fixing western bias; optimizing airmass limit and sky coverage; investigations of variable, perhaps SNR-driven, exposure time).
2. Exploration and optimization of temporal sampling function in general, and of Rolling Cadence in particular.
3. NEO completeness studies: what would it take for LSST to reach 90% completeness for 140m and larger NEOs? Based on previous analysis, directions to explore are deeper visits along the Ecliptic and longer survey duration (about 12 years).
4. Exploration of extending the main survey to the Galactic plane ([Gould 2013a](#)), and further optimization of Galactic plane and Bulge science programs.
5. Optimization of LMC/SMC coverage (and somewhat less importantly, the South Celestial Pole coverage).
6. Deep drilling optimization (detailed analysis of existing proposals; investigation of gains from going to a larger observing time allocation, e.g. 20%).
7. Twilight short-exposure time observing (per internal Stubbs proposal).
8. Planning commissioning observations (e.g. the tension between going wide to enable self-calibration and dense temporal sampling to obtain various light curve templates and fine tune image differencing and multi-epoch data processing and data analysis software tools).
9. Dynamic cadence explorations (the main goal at this time is to answer: are our tools good enough to act and react swiftly and robustly in operations?).

Go to: • [the start of this section](#) • [the start of the chapter](#) • [the table of contents](#)

2.5 Summary

The most important conclusion of this chapter is that the upper limit on possible scheduling efficiency improvements for Baseline Cadence is close to 6%. This conclusion is by and large based on the fact that the mean slew time for (candidate) Baseline Cadence is 6.9 sec, and thus only slightly larger than the design specifications for the system slew and settle time of 4.5 sec. Nevertheless, there are a number of features to understand, and some to fix, and there is substantial

optimization potential in temporal sampling functions and further optimization of the sky area and observing strategy details, that can result in enhanced science even with the same integrated open-shutter time (e.g. by obtaining deeper data through an improved sampling of observing conditions).

The main other questions addressed here are:

1. *By what factor could we exceed the SRD design specification for the number of visits if only Universal Cadence proposal was implemented?*

A simulation that only implemented Universal Cadence proposal exceeded the design specification for the number of visits by about 40% (over the design specification for the sky area of 18,000 sq.deg.)

2. *By what factor could we exceed the SRD design specification for the sky coverage if only Universal Cadence proposal was implemented with the design specification for the number of visits?*

This Pan-STARRS-like strategy results in about 40% larger sky coverage (about 25,000 sq.deg.), with the mean number of visits at 92% of the design specification. The total number of visits is the same as for Baseline Cadence, implying similar surveying efficiency.

Therefore, the available “margin” relative to the SRD design specifications for the main survey is equivalent to about 30-40% larger sky coverage, or about 30-40% more visits per field. The SRD assumes that 10% margin will be available for other programs. The implied “survey reserve”, relative to the Universal Cadence design specifications from the SRD, can be used to:

- a) increase the number of visits per field over the WFD area, or
- b) increase the surveyed area while keeping the number of visits per field statistically unchanged, or
- c) increase both area and the number of visits, and/or
- d) execute additional programs (the current baseline).

3. *What is the effect of auxiliary proposals on surveying efficiency?*

A comparison of simulations which only implemented Universal Cadence proposal to those that included all other programs did not show a significant change of efficiency (older simulations, not analyzed here, showed increases in surveying efficiency of up to about 3% due to shorter slewing time).

4. *What is the effect of visit pairs on surveying efficiency?*

Relinquishing the visit pair requirement results in up to 2-3% improvement of the surveying efficiency. The impact on some time-domain science would be positive, while for NEO and main-belt asteroid science it would be strongly negative.

5. *Can the effects of variations of the visit exposure time on surveying efficiency be predicted using simple efficiency estimates?*

Simple estimates based on comparing exposure (open shutter) and total visit times are in good agreement with simulations. Decreasing the visit exposure time to 20 seconds decreases the total open shutter time by 10%, and increasing it to 60 seconds increases the total open shutter time by 16%, relative to Baseline Cadence and standard exposure time of 30 seconds. The number of visits changes by factors of 1.35 and 0.58.

6. *What are the effects of doubling the exposure time only in the u band?*

The effect of doubling the exposure time only in the u band, while simultaneously halving the number of requested visits, has no significant effect on the survey efficiency.

The effect of doubling the exposure time only in the u band, with the number of requested visits unchanged, is a decrease in the number of visits in other bands by about 6%.

7. *What is the impact of hard airmass limit, $X < 1.5$, on the surveying efficiency?*

It is a very bad idea to relax airmass limit! It is possible to achieve the same surveying efficiency with much more stringent airmass limit than 1.5, which was used in most simulations to date.

Go to: • [the start of this section](#) • [the start of the chapter](#) • [the table of contents](#)

3 Discovering and Characterizing Small Bodies in the Solar System

Chapter editors: *Lynne Jones, David Trilling.*

Contributing authors: *Željko Ivezić, Miguel de Val-Borro.*

3.1 Introduction

LSST has tremendous potential as a discovery and characterization tool for small bodies in the Solar System. With LSST, we have the opportunity to increase our sample sizes of Potentially Hazardous Asteroids (PHAs), Near Earth Objects (NEOs), Main Belt Asteroids (MBAs), Jupiter Trojans, Centaurs, Trans-Neptunian Objects (TNOs), Scattered Disk Objects (SDOs), comets and other small body populations such as Earth mini-moons, irregular satellites, and other planetary Trojan populations, by at least an order of magnitude, often two orders of magnitude or more. In addition to hundreds of astrometric measurements for most objects, LSST will also provide precisely calibrated multiband photometry. With this information, we can also characterize these populations – deriving colors, light curves, rotation periods, spin states, and even shape models where possible.

The motivation behind studying these small body populations is fundamentally to understand planet formation and evolution. The orbital parameters of these populations record traces of the orbital evolution of the giant planets. The migration of Jupiter, Saturn and Neptune in particular have left marks on the orbital distribution of MBAs, Jupiter Trojans, TNOs and SDOs. Rapid migration of Jupiter and Saturn may have emplaced a large number of planetesimals in the Scattered Disk; later slow migration of Neptune will affect the number of TNOs in resonance and the details of their orbital parameters within the resonance. Adding color information provides further insights; colors roughly track composition, indicating formation location and temperature or space weathering history. For example, the color gradient of main belt asteroids, combined with their orbital distribution, suggests that perhaps Jupiter migrated inwards, mixing planetesimals from the outer Solar System into the outer parts of the main belt, before eventually migrating outwards. Studying the size distribution of each of the small body populations themselves provides more constraints on planetesimal formation; this is complicated by the effects of dynamical stirring from the giant planets, which can increase the rate of erosion vs. growth during collisions, and by the existence of the remnants of collisions such as collisional families in the main belt. The presence of binaries and range of spin states and shapes provides further constraints on the history of each population. The location of the planets before migration, the amount of migration, and the size distribution of the small bodies themselves (after detangling the dynamical evolution) all tell a

deeper story about how the planets in the Solar System formed, and how our formation history fits into the range of observed extrasolar planetary systems.

These Solar System populations are unique when compared to other objects which will be investigated by LSST, due to the simple fact that they move across the sky. Metrics to evaluate LSST’s performance for moving objects need to be based on ‘per object’ measurements, rather than at a series of points on the sky or per field pointing. For all metrics discussed in this chapter, the orbit of each object is integrated over the time of the simulated opsim survey and the detections of each object are recorded (using the footprint of the focal plane and including trailing losses and adjusting for the colors of the objects in each filter to generate SNR and likelihood of detection); these series of observations per object are then the basis for metric evaluations.

3.2 Discovery: Linking Solar System Objects

Lynne Jones, David Trilling, Željko Ivezić

Discovering, rather than simply detecting, small objects throughout the Solar System requires unambiguously linking a series of detections together into an orbit. The orbit provides the information necessary to scientifically characterize the object itself and to understand the population as a whole. Without orbits, the detections of Solar System Objects (SSOs) by LSST will be of limited use; objects discovered with other facilities could be followed up by LSST, but almost the entire science benefit to planetary astronomy would be lost. Linking and orbit determination for Solar System objects is similar to source association for non-moving objects; it provides the means to identify multiple detections as coming from a single object.

Therefore, the first concern regarding the Solar System is related to the question “Can we accurately link individual detections of moving objects into orbits?”. This requirement poses varying levels of difficulty as we move from Near Earth Objects (NEOs) through the Main Belt Asteroids (MBAs) and to Trans-Neptunian Objects (TNOs) and Scattered Disk Objects (SDOs), as well as for comets and for other unusual but very interesting populations such as Earth minimoons. Due to their small heliocentric and geocentric distances, NEOs appear to move with relatively high velocities and are distributed over a large fraction of the sky, including regions far from the ecliptic plane. MBAs are densely distributed, primarily within about 30 degrees of the ecliptic. TNOs and SDOs move slowly, however short time intervals between repeat visits in each night may make these difficult to link. Comets and Earth mini-moons may require more complicated orbit fitting to allow for non-gravitational or geocentric orbits. The requirements of accurately linking individual detections into orbits also implies that we do not create false objects by incorrectly linking detections and/or noise.

Much of the answer to this question comes down to the performance of various pieces of LSST Data Management software. In particular, important questions are the rate of false positive detections resulting from difference imaging, possible limitations of the Moving Object Processing System (MOPS) to extend to high apparent velocities, and the capability to unambiguously determine if a linkage is ‘real’ or not via orbit determination (done as part of MOPS). Thus this question includes concerns beyond the limits of the OpSim simulated surveys, although it still bears on the observing strategy requirements for discovering Solar System Objects. An in-depth study of

the performance of difference imaging and MOPS is currently ongoing. However, we can make a range of assumptions on how MOPS will perform and evaluate how many and which objects can be linked under observational cadence, given those assumptions.

3.2.1 Target measurements and discoveries

The criteria for ‘discovery’ with MOPS depends on the number of observations of an object acquired per night within some time window (creating ‘tracklets’), repeated over a number of nights within a window of some days (creating ‘tracks’), which are then linked into an orbit with a threshold on astrometric residuals. The current assumptions are that we can link detections into orbits with 2 detections per night within 90 minutes, repeated for 3 nights within a window of 15 days. The additional assumptions are that with these 6 observations, we will be able to create low-accuracy orbits that will suffice to link additional observations obtained at later (or earlier, in the LSST archive) times, and that the orbit fitting will enable rejection of mislinkages.

We can also use other requirements for discovery. Requiring 4 detections in each night is a fairly common discovery criteria for NEO surveys, as it reduces the number of mislinked tracklets to almost zero. We could also require 4 nights of pairs within a window of 20 days, in order to improve the initial orbit fitting and mislinkage rejection. We can also assume MOPS will perform better than the current assumptions, and evaluate discovery criteria of 3 pairs within a 30 day window.

With these discovery criteria, we can then evaluate the completeness of an LSST simulated survey, for a given population. We can look at this as a function of H magnitude and as a function of orbital parameters.

For PHAs and NEOs there are special considerations in terms of completion that arise from planetary defense concerns. For most other populations, the general desire is simply to have a high level of completeness, with no gaps in completeness that depend strongly on orbital parameters. In particular, the desire is to be able to calibrate any selection effects in discovery so that the survey completeness can be used to debias the underlying population models.

Discovery opportunity, and thus the completeness of the underlying population, is very sensitive to the time interval between observations. Waiting longer between observations within a night means that objects may move beyond a single LSST field of view. Longer times between revisits means that observing in large contiguous blocks (rather than narrow, disconnected strips) within a night becomes more important to make sure that objects are followed between pointings, especially if the time interval is much longer than 30 minutes. Because the objects must be detected on several nights within the window, the inter-night revisit rate for similar large contiguous blocks of sky is important.

An optimal discovery strategy for moving objects could be ensuring a minimum (default: two) number of revisits within a night within a short time window (default: 90 minutes), preferably over a large block of sky, and covering large contiguous amounts of sky several (default: 3) times within a longer time window (default: 15 days). Observations within a single night do not need to be in the same filter, however we will be constrained by the shallower limiting magnitude of the pair; *e.g.* preferably *r* band observations would be paired with *i* rather than *u* observations.

Table 3.1: Solar System Object Differential Completeness Goals

	C_b	H_b	H_f
NEA	80%	18.4	21.9
MBA	90%	19.5	20.2
TNO	90%	7.0	8.1

Finally, the fill factor of the camera is important; in these simulations we have used the LSST focal plane, which has an approximately 92% fill factor.

3.2.2 Metrics

The `DiscoveryChancesMetric` can be used to identify sets of detections of a particular object that meet the defined criteria for discovery: X detections within T minutes in a night, Y nights within a W day window; this describes the number of discovery opportunities for each object. The results from the Discovery Metric can be fed to the `MoCompletenessMetric` summary metric, where if an object achieves a user-defined requirement for the minimum number of discovery opportunities (typically 1), then it is counted as ‘discovered’. The total number of objects discovered at each H magnitude is compared to the total number of objects in the population at that H magnitude, in order to evaluate ‘completeness’ as a function of H. Discovery opportunities can be evaluated as a function of orbital parameters, to look for areas of orbital space that may be missed in a particular survey strategy; completeness, since it marginalizes over the entire population at a particular H value, loses this capability. Completeness can be evaluated as a differential value (completeness @ $H=X$) or integrated over the size distribution (completeness @ $H \leq X$).

The completeness can be parametrized by the completeness (C_b) at some bright absolute magnitude (H_b), combined with the magnitude at which this falls to 50% (H_f). A draft set of requirements for these parameters has been written up in the Solar System Object Specifications document, although these requirements are still quite preliminary. The current goal parameters are described in Table 3.1.

A further simplification of the completeness can be achieved by simply measuring the completeness at a preset absolute magnitude. For example, completeness for PHAs at $H=22$ is an important summary value, and is discussed in its own section, 3.3.

3.2.3 OpSim Analysis

The basic output from the `DiscoveryChancesMetric` is the number of discovery opportunities (e.g. sets of observations that match the required discovery criteria) available. For objects which have at least a given number of discovery opportunities (here, we simply use one required opportunity), then this object can be considered “found” and marked towards the completeness of the population at a given H magnitude with the `MoCompletenessMetric` summary metric. Examining the `minion_1016` Baseline Cadence with these metrics, we find that most objects have many discovery opportunities. This is shown in Figure 3.1.

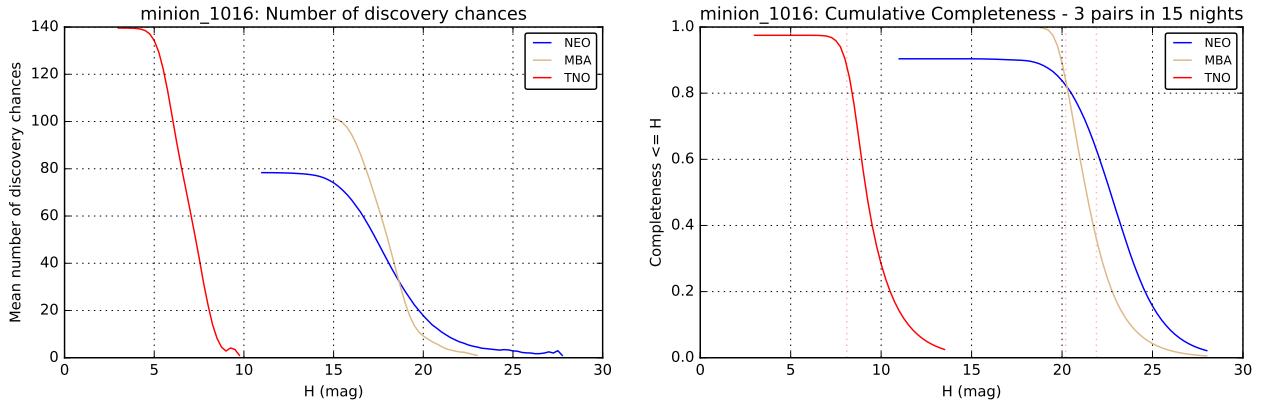


Figure 3.1: Left: Number of discovery chances as a function of H (mean value for all objects at each H value), assuming the minimum criteria for discovery - 2 visits per night within 90 minutes, repeated for 3 nights within 15 days. Right: Resulting cumulative completeness for each population, assuming that only 1 discovery opportunity is required to ‘discover’ each object.

Table 3.2: Solar System Object Differential Completeness in [minion_1016](#)

	C_b	H_b	H_f
NEA	87.5%	18.5	21.5
MBA	89%	19.5	20.2
TNO	96%	7.0	8.3

The runs [minion_1016](#), [kraken_1043](#), [enigma_1281](#), [enigma_1282](#) are particularly interesting to evaluate in light of the different sets of discovery criteria. Because OpSim does not currently require only pairs (or singles, triplets or quads), but instead will sometimes acquire more than the requested number of visits, changing the discovery criteria from pairs within a night to triplets or quads, does not automatically cause the completeness to plummet, although it does decrease. Looking at the raw numbers of discovery chances offers some enlightenment: the number of discovery opportunities does fall dramatically as we go from pairs to quads, however, there are still some times when observations are obtained in triplets or quads, so there are still some discovery chances. This behavior of the scheduler (to frequently acquire more than the requested number of visits) is likely to change in the future and make this effect more pronounced, but the completeness will clearly be very sensitive to how observations are acquired. This effect is shown in Figure 3.2.

Another aspect to consider is to look at how the completeness increases over time. The completeness as a function of time is plotted for particular H values, depending on the population, in Figure 3.3.

3.2.4 Discussion

A large portion of the risk in being able to discover moving objects lies in the currently uncertain performance of the MOPS software. Figure 3.2 clearly shows that with the baseline cadence, if we must have triplets or pairs, or even just require 4 pairs of observations over 20 nights, that the

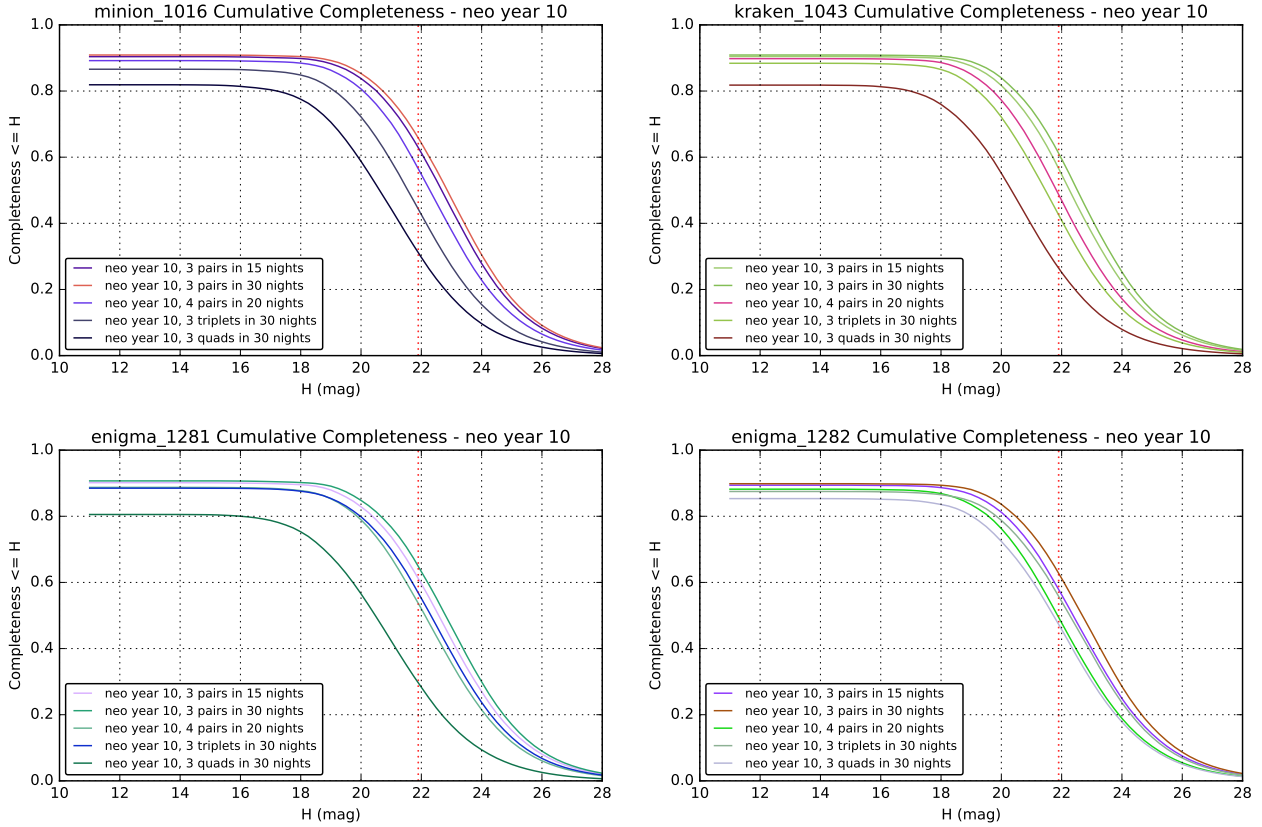


Figure 3.2: Cumulative completeness for an NEO population, given different sets of discovery criteria, for the [minion_1016](#), [kraken_1043](#), [enigma_1281](#), [enigma_1282](#) simulated surveys. The results in the lower right come from a simulated survey, [enigma_1282](#), which attempted to obtain four visits to each field in each night; the results on the upper left, come from the baseline simulated survey, [minion_1016](#), which attempts to obtain pairs of visits.

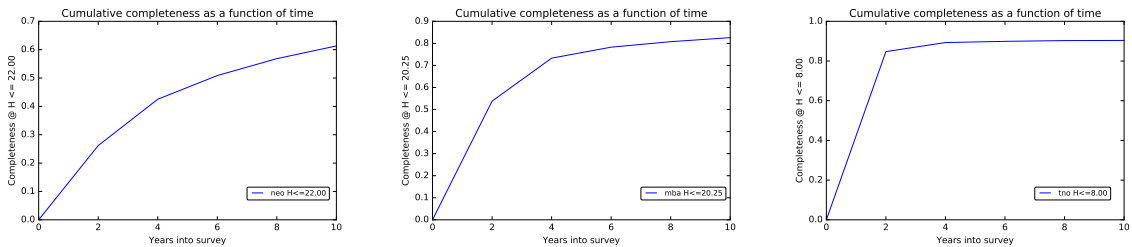


Figure 3.3: Completeness as a function of time, for NEO, MBA and TNO populations. The completeness increases rapidly for the first few years, then increases more slowly. The NEO completeness rises more slowly than other populations, as more NEOs become available to discover due to changing their orbital positioning relative to Earth (becoming closer and brighter, or moving away from sightlines behind the Sun). The TNO completeness rises most rapidly with time, as these objects move slowly; we find most of these objects within the first two years and then improve their characterization over the rest of the survey (measuring better orbits and obtaining lightcurves and colors).

completeness falls. The performance will likely fall even further if the scheduler stops obtaining more than the minimum requested number of observations.

With the expected MOPS discovery requirements, [minion_1016](#) performs adequately for most solar system objects, although completeness falls off more rapidly for faint objects than desired for NEOs. To investigate this effect, more metrics will have to be developed to discover why these fainter NEOs are not being discovered (are they simply missing appropriate sequences of observations due to the cadence or is something more subtle occurring?).

Go to: • [the start of this section](#) • [the start of the chapter](#) • [the table of contents](#)

3.3 Discovery of Potentially Hazardous Asteroids

Željko Ivezić, Lynne Jones.

The U.S. Congress has given a mandate to NASA to implement a Near-Earth Object (NEO) Survey program to detect, track, catalog, and characterize the physical characteristics of near-Earth objects equal to or greater than 140 meters in diameter¹. The goal is to achieve a completeness of 90%. In recent practice, adopted here, the completeness is evaluated for a subset of NEOs called Potentially Hazardous Asteroids² (PHA), with $H \leq 22$, where H is the absolute magnitude³ in the Johnson's V band.

The discovery criteria for PHAs follows the same guidelines and metrics found in the previous section, [3.2](#), but is worth discussing separately to focus on its main figure of merit - completeness for PHAs with $H \leq 22$ magnitudes.

3.3.1 Target measurements and discoveries

Using the same range of discovery criteria as in the previous section, [3.2](#), we can look at the differential and cumulative completeness for a population of PHAs. For this sample of PHAs, we simply pulled the orbits of the brightest ($D > 1$ km) ~ 1500 PHAs from the Minor Planet Center record. These orbits were then cloned over a range of H values to evaluate the chances of discovery for that orbit at each of those H values. The differential completeness as a function of H is then simply the fraction of objects which receive at least one set of observations which meet the discovery criteria during the course of the survey. The cumulative completeness is similar, but integrated over H by assuming an H distribution with a power-law index of $\alpha = 0.3$. Both differential and cumulative completeness are relevant metrics: the former provides more insight in the behavior of a particular simulation, while the latter is a metric given to NASA by the U.S. Congress.

¹See <http://www.gpo.gov/fdsys/pkg/PLAW-109publ1155/pdf/PLAW-109publ1155.pdf>

²Potentially Hazardous Asteroids (PHAs) are defined as asteroids with a minimum orbit intersection distance (MOID) of 0.05 AU or less.

³Absolute magnitude is the magnitude that an asteroid would have at a distance of 1 AU from the Sun and from the Earth, viewed at zero phase angle. This is an impossible configuration, of course, but the definition is motivated by desire to separate asteroid physical characteristics from the observing configuration.

To match the NEO mandate, the cumulative completeness at $H=22$ can be used as a figure of merit.

3.3.2 Metrics

The metrics used here are the same as in [3.2](#), although run with different input populations.

3.3.3 OpSim Analysis

The differential and cumulative completeness for the baseline survey, [minion_1016](#), at a range of years is shown in [Figure 3.4](#). The baseline cadence achieves a cumulative completeness of 73% for $H \leq 22$ PHAs. The differential completeness at $H=22$ for the same survey is 58%, 15% lower due to increasing completeness toward smaller H (larger objects).

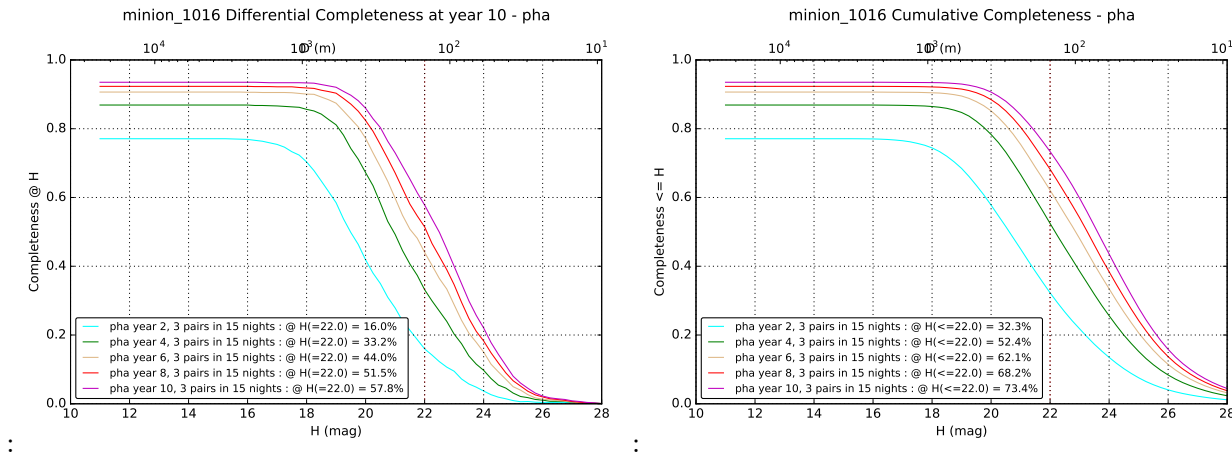


Figure 3.4: The PHA completeness for [minion_1016](#), as a function of the object's absolute visual magnitude H on the horizontal axes (left: differential completeness at a given H ; right: cumulative completeness for all objects brighter than a given H). The cumulative completeness for $H \leq 22$ NEOs (those with diameters larger than 140m) for this simulation is 73% after 10 years.

The differential completeness for a range of discovery criteria, for both the baseline survey and [enigma_1282](#), is shown in [Figure 3.5](#). When the discovery algorithm requires pairs of visits, the runs have fairly similar PHA completeness, with [enigma_1282](#) having a differential completeness about 6% lower than [minion_1016](#). When the discovery algorithm requires 4 detections per night, the simulation with quads achieves a differential completeness of about 15% higher than the baseline cadence (as some quads are unintentionally produced by chance, see [Figure 2.13](#)).

Go to: • [the start of this section](#) • [the start of the chapter](#) • [the table of contents](#)

3.4 Orbital Accuracy

Lynne Jones, David Trilling

Table 3.3: Differential PHA completeness at $H=22$

	<code>minion_1016</code>	<code>kraken_1043</code>	<code>enigma_1281</code>	<code>enigma_1282</code>
3 pairs in 15 nights	58	51	56	52
3 pairs in 30 nights	61	56	59	57
4 pairs in 20 nights	50	41	46	42
3 triplets in 30 nights	35	33	50	48
3 quads in 30 nights	22	18	19	37

Table 3.4: Cumulative PHA completeness at $H=22$

	<code>minion_1016</code>	<code>kraken_1043</code>	<code>enigma_1281</code>	<code>enigma_1282</code>
3 pairs in 15 nights	73	69	71	68
3 pairs in 30 nights	76	73	74	73
4 pairs in 20 nights	68	62	64	61
3 triplets in 30 nights	57	55	66	65
3 quads in 30 nights	42	37	37	55

A vast number of moving objects will appear in LSST images. Multiple observations of a common object will be linked, and a preliminary orbit derived. However, the orbital elements (semi-major axis, eccentricity, etc.) will have some uncertainty. Short arcs — that is, a small amount of time between the first and last observation of a given object — produce orbits with large uncertainties on the orbital elements. As arc length grows, the orbital uncertainties decrease.

A number of science cases require relatively small uncertainties on orbital elements. Perhaps most importantly, small uncertainties can aid in discriminating between Near Earth Objects that might and might not impact the Earth. A more subtle example relates to the libration amplitude distribution for TNOs, which can be compared to predictions from Solar System formation models. Only with small uncertainties on orbital elements can the libration amplitudes be determined to sufficient precision to compare to the predictive models. Finally, during and after the primary LSST survey additional measurements will be desired for further characterization of many objects. Only if the orbital elements are sufficiently well known can objects be studied later with other facilities. For example, to carry out spectroscopy, the position of the object must be known to approximately 1 arcsec (the width of a typical slit). This places strong requirements on the knowledge of the orbital elements.

3.4.1 Target measurements and discoveries

The relevant data here are positions as a function of time for a given object (assuming that the linking of measurements to a given object is satisfactory). Assuming that the accuracy and precision of each measurement are approximately constant (likely, since all will be made by the same observing system), the only significant factor that improves the knowledge of the orbit is extending the observational arc. The observing strategy employed by LSST must therefore have

a cadence in which objects are revisited with the largest possible arcs that still allow linking of observations. In other words, if the observations of a given object are too widely spaced, linking may not be possible, so, even though the arc is long, the linking is poor and the object yield is low. If the observations are made too densely in time, linking is likely to be good, but the arc may not be very long. A middle ground is desired.

3.4.2 Metrics

The best metric here would be to take the actual series of observations of each object, add appropriate astrometric noise to each observation according to its SNR, cull observations which would not be ‘linkable’ to the rest (i.e. observations which occur on a single night far from other nights in the arc, or even a series of observations which occur too many years away from other observations of the same object), and then fit an orbit to the remaining observations and determine the uncertainty in its parameters. This is work for the future however; our first simple proxy uses the `ObsArcMetric` to just look at the time between the first and last observation of an object. For many objects, this will be fairly close to the actual arc length of the linkable observations, as most objects receive many observations clumped together when they are observable, so this simple proxy makes a reasonable starting point.

3.4.3 OpSim Analysis

In [minion_1016](#), the mean observational arc length for NEOs and MBAs is about 8 years for bodies larger than 1 km, and about 6 years for 300 m bodies. With these orbital arcs, the orbits will be quite well known, meaning that the majority of LSST-observed objects will have orbits that are sufficiently well known that the above science cases can be carried out. In some special cases — for example, the case where an NEO’s orbit still presents a significant probability of terrestrial impact — additional non-LSST follow-up may be needed, but this will be a small minority of cases.

3.4.4 Discussion

The simple proxy metric above should be improved to account for potential difficulties in linking observations, and to include actual orbital fitting to determine orbital uncertainties. The timing of observations effects the final orbital accuracy significantly, particularly for TNOs, and having a good distribution on the times of observations can improve orbital accuracy more quickly than would naively be expected from a simple observational arclength scaling.

A figure of merit, including requirements on the orbital accuracy for various classes of objects, should also be developed.

As an intermediate step, we have carried out two anecdotal studies of orbital accuracy. In the first, we took an arbitrary (real) NEO — object 2016 DL — with a six year arc. This is representative and typical of NEOs that will be observed by LSST. The maximum positional uncertainty for this object over the next ten years is 25 arcsec (3σ). This is small enough that essentially any kind of follow-up observation would be possible (presuming that pre-imaging is possible for spectroscopy, for example, to locate the moving object). The orbital uncertainties for the orbital uncertainties

for this object are on the order of 1 part in 10^4 or even smaller. This level of precision should allow all the investigations described above.

In the second experiment, we took an arbitrary (real) TNO — object 2015 SO20 — that has a five year arc. For this object, the maximum positional uncertainty over the next ten year is $\sim 20''$, and its orbital elements are known to around 1 part in 10^5 . Again, this level of precision should enable all of the science investigations described above.

Go to: • [the start of this section](#) • [the start of the chapter](#) • [the table of contents](#)

3.5 Detecting Comet Activity

Lynne Jones, David Trilling, Miguel de Val-Borro

Comets are the remnant building blocks of the Solar System that have been stored at cold temperatures beyond the ice line, either in the Kuiper belt or the Oort cloud, since their formation. Measuring the evolution of cometary activity over a range of heliocentric distances with LSST will allow us to understand the overall comet activity and to link these observations with the physical and chemical conditions in the early solar nebula during planet formation. Comets are classified in two main dynamical families, Jupiter Family comets (JFCs) that have low-inclination orbits with periods less than 20 years, and Long-period comets (LPCs) that originate in the Oort Cloud at a distance of more than 10000 AU and have large orbital eccentricities and nearly isotropic distribution of inclinations. Currently there are over 400 Jupiter-family comets known, most of which are faint compared with the LPCs. LSST will observe about 10^4 individual comets repeatedly including measurements of known objects over its 10-year survey ([Solontoi 2010](#)). The determination of their activity levels at various heliocentric distances will be used to study the time evolution of each object individually and to find the connection between comet families and their formation region in the Solar System.

Several cometary volatiles result in strong emission bands excited by solar radiation that emit by resonant fluorescence at optical and near-ultraviolet wavelengths. The LSST *u* filter peaks near the CN (0–0) emission band at 3880 Å. Although CN is not the most abundant daughter species from cometary volatiles and the OH (0–0) emission band at 3080 Å is generally stronger, CN production rates provide an excellent proxy of the level of overall gas activity in comets. LSST will offer a unique opportunity to produce a large database of CN production rates, vastly increasing our current knowledge (see e.g. [A'Hearn et al. 1995, 2012](#)). Other bands such as *r*, *i*, and *z* will detect continuum brightness that is produced by reflected radiation from dust particles in the coma. Thus, it will be possible to obtain the evolution of the gas-to-dust production ratio at high cadence as a function of heliocentric distance in different comet families. The greatly increased sample size compared with previous catalogs ([A'Hearn et al. 1995](#)) will allow for statistical comparison of the comet families and to link them to other small body populations in the Solar System.

A recently discovered population of main-belt asteroids eject dust and produce coma and tails giving them the appearance of comets ([Jewitt 2012](#)). This so-called main-belt comets or active asteroids have the orbital characteristics of asteroids with $T_J > 3$ and lose mass during part of their orbits. The cometary activity observed in these objects may be driven by primordial water

water ice that is trapped near the surface and sublimates when it is exposed to sunlight. Main-belt comets are important because they may have been able to preserve water ice despite the effect of solar radiation and heating from the decay of short-lived radioactive nuclei. The asteroids in the outer regions of the main belt can therefore have a substantial fraction of water and other volatiles that may have supplied the volatile content of terrestrial planets. Most of the main-belt-comets are faint with very weak comae that are active during part of their orbits. Given the expected flux sensitivity of LSST, the transient cometary activity of main-belt asteroids will be observable including many objects that could be below the detection limits of current photometric surveys. The LSST observations will thus help to understand the overlap between different populations in the Solar System such as the relationship between comets and asteroids.

3.5.1 Target measurements and discoveries

LSST will make an exceptionally large number of comet observations. About 10^4 comets will be observed on average of 50 times by LSST during its main survey, while a few objects will be observed more than 1000 times ([Solontoi 2010](#)). Simulations of characteristic comet orbits have shown that LSST will observe some Jupiter Family comets (JFCs) hundreds of times over their full orbits ([Solontoi 2010](#)). Individual LPCs are predicted to be observed by LSST with dozens of observations as they approach or recede from the center of the Solar System or during their perihelion passage. Thus, these observations will trace the onset of outgassing from quiescence at large heliocentric distances and the decline of activity after perihelion.

Ensuring that any activity or outgassing of a comet or active asteroid is clearly identifiable with LSST DM or contributed Level 3 software is not a solved problem, however there is ongoing work toward this goal (xx ref? Hsieh, other? xx). In the meantime, it does not seem unreasonable to assume that the main requirement, in terms of cadence, is to actually have an observation at a time when activity is visible, as well as at surrounding times to determine the start and end points of that activity.

Cometary activity and outgassing can last for various periods of time, usually on the order of days to weeks. It can be transient, perhaps due to a collision or other resurfacing event, or it can be periodic, such as repeated activity when an object approaches perihelion. Thus, in order to characterize the fraction of active asteroids, or to understand the causes of their activity, or to understand cometary activity as a function of source population (and thus presumably composition) and heliocentric distance, the goal would be to have repeated observations spread throughout the period when the object is visible.

3.5.2 Metrics

A full exploration of the cadence effects on measuring activity rates for comets and active asteroids would include understanding the selection effects of when the object was not observed, as well as the likelihood of detecting activity based on when it was observed. For now, we have focused on the likelihood of being able to detect activity lasting a given amount of time.

The metrics `ActivityOverTimeMetric` and `ActivityOverPeriodMetric` look at when an object was observed (with a detection above a given SNR), and split those observations into bins based

on time or position in the orbit (mean anomaly), respectively. The first is relevant when looking for transient activity that is not expected to repeat at the same point in the orbit, while the second seems more appropriate for activity that would repeat at the same point in the orbit. Each of these metrics takes only a single time or mean anomaly window, distributes the observations of each object into bins based on those windows, and counts the number of bins which received observations. The number of bins with observations, compared to the overall number of bins, determines the calculated likelihood of detecting activity for that object.

To investigate the sensitivity of LSST to activity on a range of timescales and lasting various fractions of the period, we ran these metrics over a range of values and then plot the minimum, mean, and maximum likelihoods of objects at a particular H value, for various populations.

3.5.3 OpSim Analysis

Running these metrics on a sample Main Belt Asteroid population generates results illustrated in Figure 3.7. In the baseline survey [minion_1016](#), the metric results indicate that for bright asteroids with activity lasting more than about 60 days, we have between about 18-60% chance of obtaining at least one observation that captures the event. If the activity is periodic, and lasts around 10% of the orbit, we have between 20-65% chance of observing the activity. If the periods of activity last longer, we have a higher chance of having an observation which captures that activity, as expected.

That the chance of detecting activity is not significantly higher for repeating events than for transient events is interesting. It's not clear if this reflects a characteristic of the observing cadence (e.g. perhaps the observations always are clustered near the same point in the orbit, leaving many "bins" unwatched), but it's seems likely that at the very least, the metric should be tuned to account for the additional likelihood of activity occurring near perihelion.

3.5.4 Discussion

The likelihood of detecting activity depends on if the observing strategy is such that we observe an object when it is active, and the capability to identify this activity in the acquired images.

In terms of observing strategy, if observations are clumped together irregularly in time, we risk missing activity during the times we do not observe the object, although with the possible benefit of being more likely to detect short time-scale activity during the times we have more frequent observations. Balancing these two tensions likely requires more knowledge about the relevant timescales for activity on active asteroids, as only a handful of active asteroids have currently been identified. (comment on cometary activity?)

Go to: • [the start of this section](#) • [the start of the chapter](#) • [the table of contents](#)

3.6 Measuring Asteroid Light Curves and Rotation Periods

Lynne Jones, David Trilling

Two Solar System science projects require a series of photometric measurements. These are (1) measuring lightcurves and therefore shapes of minor bodies and (2) measuring the colors and therefore compositions of minor bodies. This section and the next describe the science and the metrics for these experiments.

3.6.1 Target measurements and discoveries

In general, minor bodies are aspherical, and therefore observations of those bodies produce lightcurves with non-zero amplitudes. Constant monitoring of such a body would reveal the detailed lightcurve, which can be inverted to derive the effective observed shape at that epoch. Observations over multiple epochs allow for observations at different aspects, which can be used to determine the three dimensional shape and pole orientation of the minor body. All of this information can be used to understand, broadly, the orbital and physical evolution of minor bodies in the Solar System.

LSST observations of minor bodies in the Solar System will not, however, necessarily be dense in time (with the exception of observations made in Deep Drilling Fields; see below). Therefore, lightcurves of minor bodies must be combined across arbitrary rotational phase. Without knowing the phase, the amplitude of the lightcurve (a proxy for asteroid shape) can simply be determined. More complicated lightcurve inversion analysis (e.g., [Ďurech et al. 2016](#)) can be carried out, given a sufficient number of points.

3.6.2 Metrics

The general requirement for successful lightcurve inversion is to have a large number of observations, at high SNR, over a wide range of time. A guideline is that \sim 100 measurements of an asteroid over \sim years, calibrated with a photometric accuracy of \sim 5% (SNR=20) or better, is sufficient to generate a coarse shape model. This sparse data inversion gives correct results for both fast (0.2–2 h) and slow ($>$ 24 h) rotators ([Ďurech et al. 2007](#)).

The metric `LightcurveInversionMetric` simply checks to see if the observations of a particular object meet these requirements, and if so, identifies that object as having the potential for lightcurve inversion.

3.6.3 OpSim Analysis

Most solar system objects receive many observations, and bright objects will have high SNR in most of those observations, so it is not surprising that the baseline cadence, [minion_1016](#), performs reasonably well with this metric. Running the same metric on other simulated surveys tends to show similar results, although [enigma_1282](#) demonstrates that a higher fraction of NEOs get suitable observations for lightcurve inversion. This is illustrated in Figure 3.8. More sophisticated metrics or investigation will be required to discover the cause of this, although it seems likely that

with visit quads, there are just more observations of the bright NEOs total, leading to a higher fraction of objects available for lightcurve inversion. The difference between these surveys suggests that it is possible to significantly increase the numbers of NEOs for which we can determine shapes, rotation rates, and spin positions.

3.6.4 Discussion

A risk which is not captured by this simple metric is that the observations included for the lightcurve inversion estimate here, could potentially occur far apart in time such that linking between the observations (to determine that they belong to the same object) is not possible.

Further work needs to be done to understand the necessary final figure of merit, in particular, how many light curve inversion targets are necessary, and how should they be spread among different sizes of objects? Small objects have different shape and rotation distributions than larger objects, so it is interesting scientifically to understand objects at a range of H magnitude. In addition, this metric currently uses observations in any filter; further work should be done to determine if this is sufficient, or if observations must occur in a single filter.

Go to: • [the start of this section](#) • [the start of the chapter](#) • [the table of contents](#)

3.7 Measuring Asteroid Colors

Lynne Jones, David Trilling

The varying compositions of asteroids result in a range of optical colors. Sloan filters in general are sufficiently diagnostic to discriminate among different compositional class (e.g., [Parker et al. 2008](#)). Therefore, when a Solar System minor body is observed in *griz* (Solar System objects are generally quite faint in *u* band and many fewer will be detected), the color can be used to determine the composition and, downstream, composition as a function of asteroid size, family membership, orbital elements, or many other parameters.

One obstacle to determining asteroid colors is that asteroid rotation periods are on the order of 2–20 hours, so that after an initial measurement all further measurements (in the same filter, or other filters) are obtained at an arbitrary rotational phase. Unless the lightcurve is also known (perhaps determined from a large series of measurements in the same bandpass, such as described in the section above), multi-band measurements must occur at closely spaced times in order to minimize the effects of the lightcurve on the measured color.

3.7.1 Target measurements and discoveries

Analysis of existing databases of TNO multi-band measurements indicate that pairs of high SNR measurements ($\text{SNR} > 10$), acquired within a short time period (< 2 hrs) can provide an accurate color measurement ([Peixinho et al. 2015](#)). This is roughly consistent with expectations based on the rotation periods.

3.7.2 Metrics

The metric `ColorDeterminationMetric` searches for pairs of observations, taken within a given number of hours, where the pair contains observations in each of two specified filters above a specified SNR (e.g., g and r band observations taken within 2 hours of each other, with $\text{SNR} > 10$). If an object receives a minimum number of pairs of observations (currently set to just a single pair of observations), then it is considered as having that color “measured.” Thus, this metric can measure the fraction of the sample population which receives an adequate color measurement, for a series of colors.

3.7.3 OpSim Analysis

The timing of repeat visits, and whether or not filter changes occur between these repeat visits, affects the fraction of objects which can receive color measurements with closely spaced observations significantly. This can be seen in the metric results shown in Figure 3.9. The difference is most pronounced in the $r - i$ color measurements. The baseline survey, `minion_1016`, seems to perform rather well — and indeed, the best out of this set of runs.

3.7.4 Discussion

This metric does not yet account for potential linking difficulties related to identifying that these two observations are part of a particular object, and it should be developed further to determine appropriate parameters for objects other than TNOs, as other objects may have different ranges of rotation rates. In particular, the timescales needed when obtaining observations in multiple filters to determine colors need to be explored.

There is some tension between desiring to get observations in the same bandpass on a given night (to maximize detection thresholds instead of being limited by the shallower bandpass) and obtaining color measurements by having observations in multiple bandpasses. The risk here is that without at least some nights with multi-band observations on short timescales, we may not be able to determine accurate colors.

Go to: • [the start of this section](#) • [the start of the chapter](#) • [the table of contents](#)

3.8 Future Work

In this section we provide a short compendium of science cases that are either still being developed, or that are deserving of quantitative MAF analysis at some point in the future.

3.8.1 Deep Drilling Observations

Lynne Jones, David Trilling

Deep drilling observations provide the opportunity, via digital shift-and-stack techniques, to discover Solar System Objects fainter than the individual image limiting magnitude. These fainter objects will be smaller, more distant, or lower albedo (or some combination of these) than the general population found with individual images. Discovering smaller objects is useful for constraining the size distribution to smaller sizes; this provides constraints for collisional models and insights into planetesimal formation. More distant objects are interesting in terms of extending our understanding of each population over a wider range of space; examples would be discovering very distant Sedna-like objects or comets at larger distances from the Sun before the onset of activity. Lower albedo objects may be useful to understand the distribution of albedos, particularly to look for trends with size.

Variations on the basic method of shift-and-stack have been used to detect faint TNOs. Computational limitations on these methods mean that, roughly and in general for images taken at opposition, images taken over the timespan of about an hour can be combined and searched for main belt asteroids, and images taken over the timespan of about 3 days can be combined and searched for more distant objects like TNOs.

With extragalactic deep drilling fields as in the baseline cadence, where observations are taken in a series of filters (g , r , and i would be useful for this purpose) each night, every three or four days, we could use shift-and-stack to coadd the 50 images obtained in gri bandpasses in a single night. This would allow detection of objects about 2 magnitudes fainter than in the regular survey, or approximately $r = 26.5$.

The Solar System Science Collaboration developed a deep drilling proposal specifically targeted to search for very faint Main Belt Asteroids (MBAs), Jupiter Trojans, and TNOs. This proposal can be summarized as follows:

- 9 fields, in a 3x3 contiguous grid block centered on a spot where Jupiter Trojans and Neptune Trojans coincide (if possible, based on timing)
- 8 sequences of ~ 1.5 hour r -band exposures per field, in continuous observing blocks. Each of these blocks would have a coadded limiting magnitude of about $r = 27$, letting us push to smaller sizes than possible with the general extragalactic deep drilling fields.
- These 1.5 hour blocks would be spaced apart in time
 1. Two blocks acquired on two nights, 1.5 months before the fields come to opposition
 2. Two blocks acquired on two nights when the fields are at opposition
 3. Two blocks acquired on two nights, 1.5 months after the fields come to opposition
 4. Two blocks acquired on two nights when the fields are at opposition again, one year later.

- The location of the fields would be adjusted slightly to account for the bulk motion of TNOs in the field, thus letting us follow the majority of these very small objects over the course of a year, providing fairly accurate orbits. Most of the Jupiter Trojans and MBAs would diffuse out of the fields, however we would still have approximate sizes from the magnitude and distance estimates provided by two nights of observations.

This proposal differs from the general extragalactic deep drilling fields in that the field selection, observing cadence, and filter choice is better suited for exploring faint Solar System Objects. More details are available in the Solar System Collaboration Deep Drilling whitepaper, <https://lsstcorp.org/sites/default/files/WP/Becker-solarsystem-01.pdf>.

Go to: • [the start of this section](#) • [the start of the chapter](#) • [the table of contents](#)

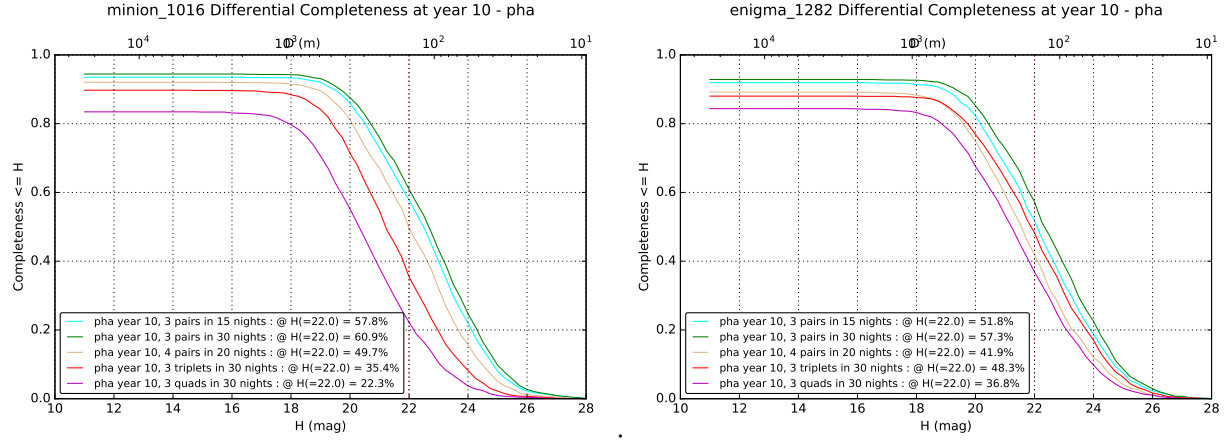


Figure 3.5: Comparison of the differential PHA completeness for the baseline cadence `minion_1016`, requesting two detections per night (left), and `??`, requesting four detections per night (right). With a discovery criteria of 3 pairs within 15 nights, both surveys perform roughly similarly; with a discovery criteria of 3 sets of quad visits within 30 nights, `??` performs better (as expected), although still at a lower completeness level than `minion_1016` did with the pairs criteria.

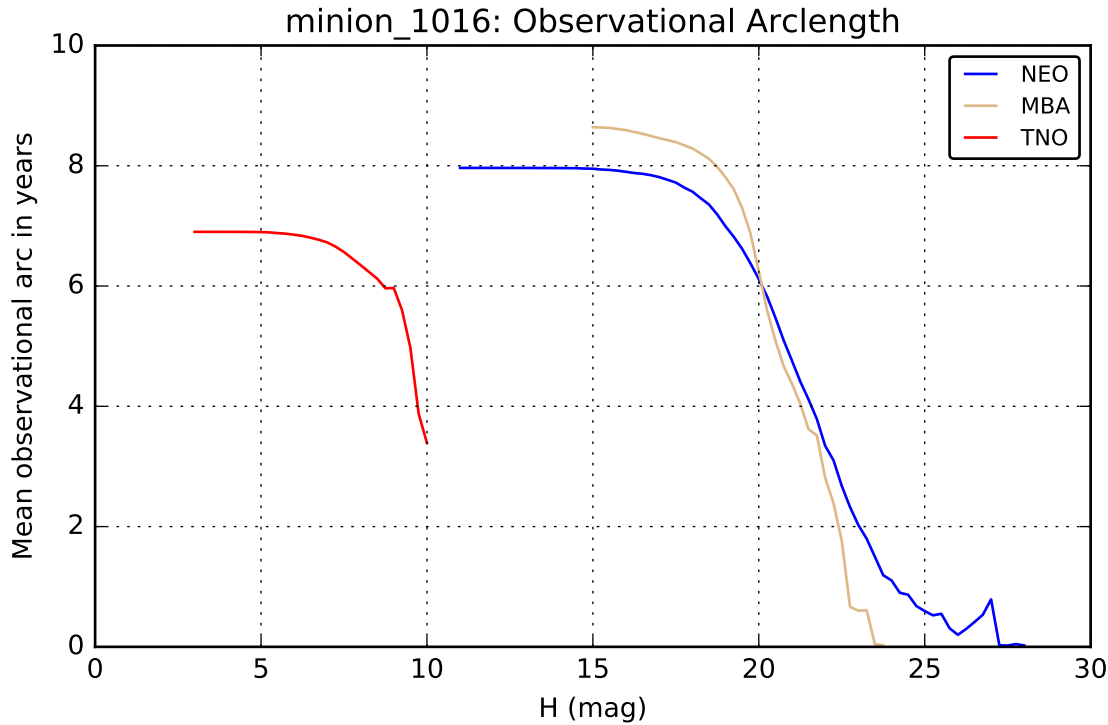


Figure 3.6: Mean observational arc length, in years, for NEO, MBA and TNO populations as a function of H magnitude.

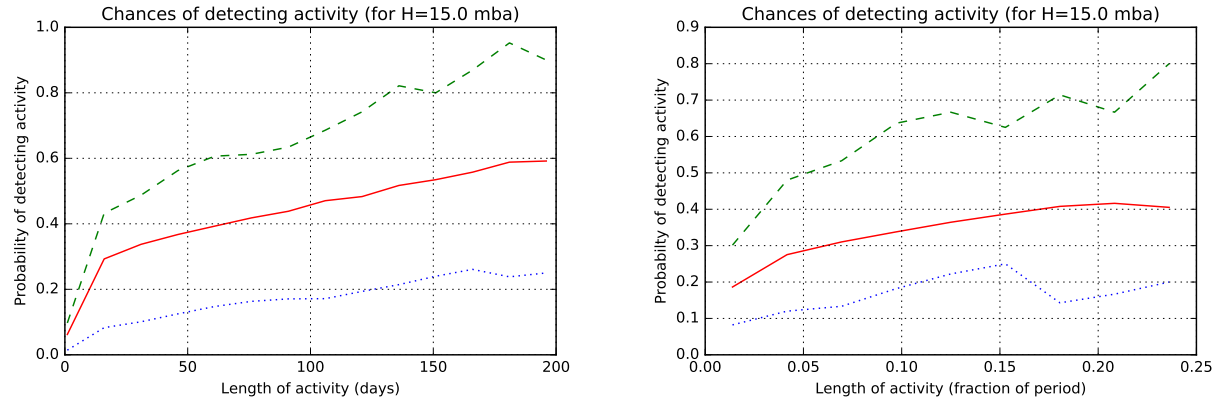


Figure 3.7: Likelihood of detecting activity or outgassing for MBAs, for a single event lasting a given number of days (left) or an event potentially repeating for a given fraction of the period (right).

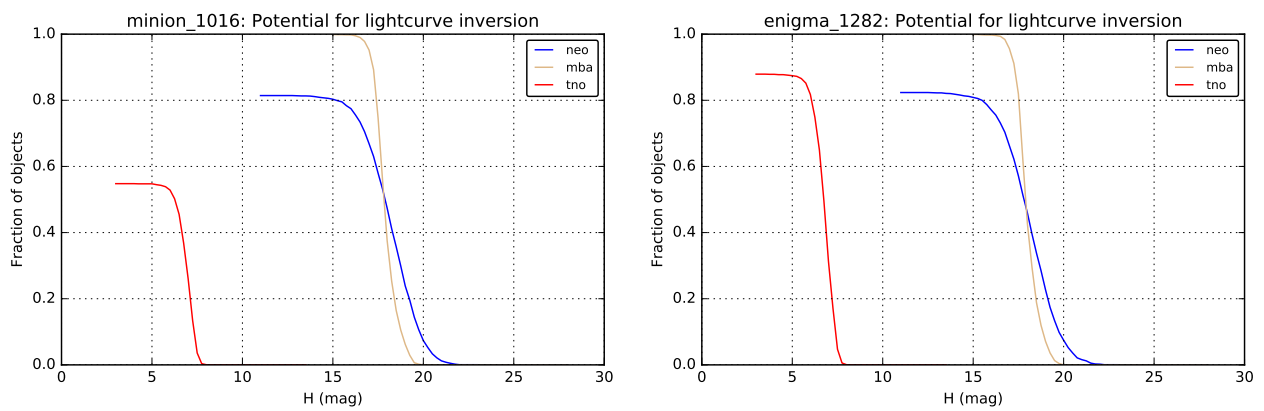


Figure 3.8: Fraction of the sample population with the potential for lightcurve inversion, as a function of H magnitude for NEOs, MBAs and TNOs, for simulated surveys `minion_1016` and `enigma_1282`.

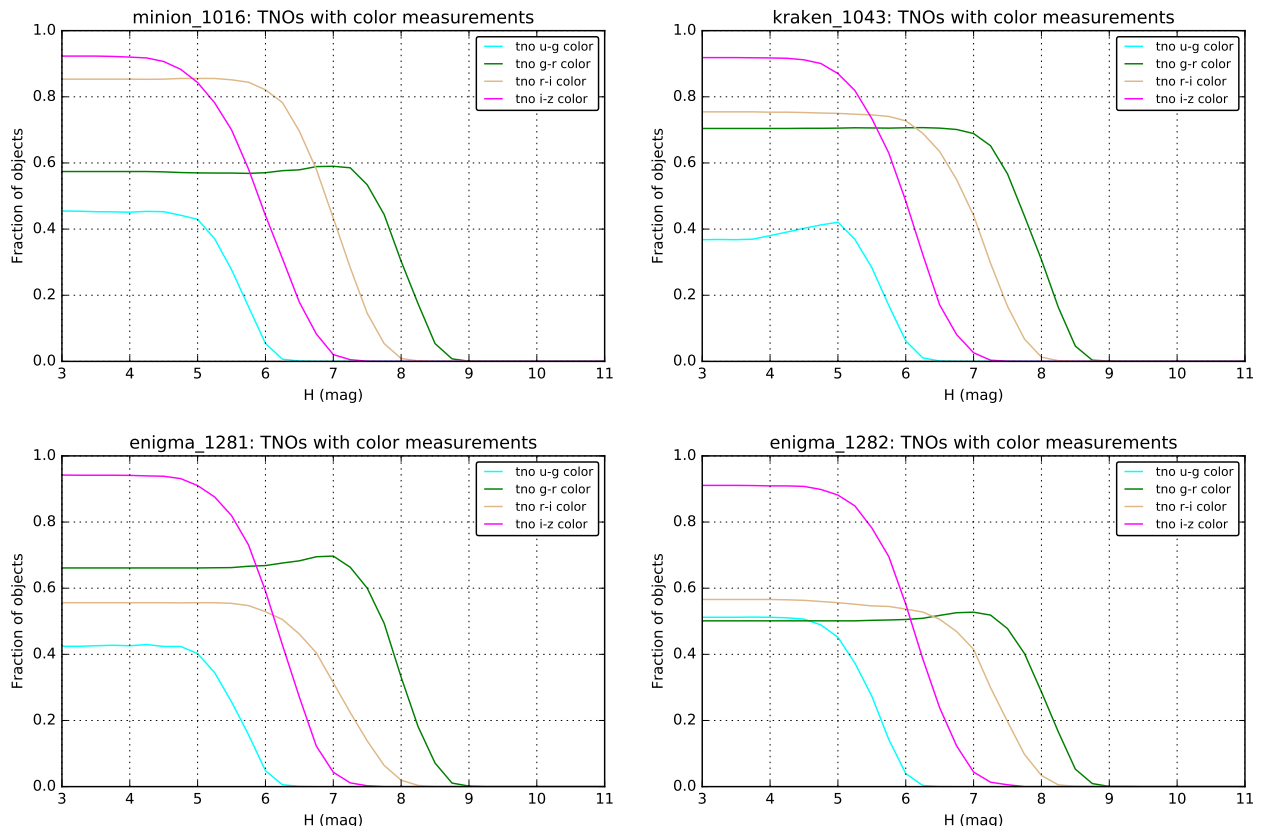


Figure 3.9: Fraction of the sample population with the potential for color measurements in various bands, as a function of H magnitude for TNOs for simulated surveys [minion_1016](#), [kraken_1043](#), [enigma_1281](#) and [enigma_1282](#). The fraction of TNOs which could receive high accuracy color measurements, particularly in $r - i$, bounces around significantly.

4 The Milky Way Galaxy

Chapter editors: [Will Clarkson](#), [Kathy Vivas](#).

Contributing authors: [Beth Willman](#), [David Nidever](#), [Željko Ivezić](#), [Colin Slater](#), [Peregrine McGehee](#), [Chris Britt](#), [Dave Monet](#), [Jay Strader](#), [Dana I. Casetti-Dinescu](#), [John E. Gizis](#), [Michael C. Liu](#), [Victor Debattista](#)

4.1 Introduction

LSST should produce significant contributions to essentially all areas of Galactic astronomy. LSST Milky Way science cases cover lengthscales ranging from a few pc (such as sensitive surveys of low-mass objects in the Solar Neighborhood), up to many tens of kpc (such as surveys for low-mass satellite galaxies of the Milky Way and their post-disruption remnant streams, and beyond this, investigations of resolved stellar populations in the Local Volume). Because the diversity of science cases in the Milky Way is so vast, we make no attempt to be comprehensive. Much more detail about most of the LSST science cases, and specific science questions to be answered, can be found in the LSST Science Book (particularly chapters 6 and 7) and [Ivezic et al. \(2008\)](#), in particular Sections 2.1.4 and 4.4).¹ As with the rest of this whitepaper, we intend to provoke the reader to contribute to the optimization of LSST’s observing strategy.

Concern about observations towards the inner Galactic Plane has for several years been a common theme in feedback on LSST’s observing strategy, as the Baseline survey currently expends relatively little observing time per field at low Galactic latitudes. At the time of writing, observations towards the inner Plane still seem to be compromised further by the way OpSim arranges shorter programs to completion at early times in the simulated survey. This reduces the time baseline available for inner-Plane measurements by a significant factor compared to observations away from the Plane.

Even without the machinery of the Metrics and Figures of Merit, populations only found in scientifically interesting numbers at low Galactic latitudes seem likely to be detected only with low efficiency by LSST under the Baseline strategy. (An example is the probing of the mass function of moderate-separation extrasolar planets via intra-disk planetary microlensing, as argued forcefully in [Gould \(2013b\)](#)). Having stated this, however, our expectation is that the evaluation of the Figures of Merit laid out in this Chapter will, as a by-product, *quantitatively* show how a range of Milky Way science cases will be substantially improved by selecting a strategy with superior Plane coverage, at little cost to the rest of LSST’s scientific investigations.

¹We do however provide motivating details for certain science cases in this Chapter, particularly in [Section 4.2](#), as those cases are not emphasized in the LSST Science Book or the relevant sections of [Ivezic et al. \(2008\)](#)

At the time of writing (April 2016), we plan to explore the scientific impact of shallow Plane observations by comparing Metrics and Figures of Merit evaluated for the Baseline cadence ([minion_1016](#)), for the PanSTARRS-like strategy ([minion_1020](#)) which has essentially uniform depth at all Galactic latitudes observed, and for the `astro_lsst_01_1004` strategy in which the plane is part of the Wide-Fast-Deep survey.

4.1.1 Chapter terminology and structure

To try to tame the diversity of science cases, we have picked representative cases and grouped them within broad scientific areas, devoting one Section of this chapter to each grouping of cases. A small number of Figures of Merit (FoMs) have been described for each case. At present, science cases are grouped in the following way: [Section 4.2](#) assesses the impact of observing strategy on LSST’s ability to map some representative astrophysically important populations that are found mostly or exclusively in the Plane. Several observational challenges for LSST find their sharpest expression in Milky Way science, including (but not limited to) measurements of stellar parallax, absolute astrometry, and proper motions (including the tie-in to the reference frame which will be provided by the *Gaia* mission). For this reason, specific issues relating to precision astrometry are developed in [Section 4.3](#). Finally, [Section 4.4](#) presents descriptions of investigations that are needed to properly determine LSST’s utility for Milky Way science, but which are as yet relatively incompletely developed.

Summary Tables are provided that present the figure of merit for each science case within a given section (one row per figure of merit) evaluated for each tested observing strategy (one column per strategy). This summary information appears in [Table 4.6](#) (the Disk), [Table 4.7](#) (Astrometry).

4.2 Populations in the Milky Way Disk

[Will Clarkson](#), [Jay Strader](#), [Chris Britt](#), [Laura Chomiuk](#)

Many populations of great importance to Astronomy exist predominantly in or near the Galactic Plane, and yet are sufficiently sparsely-distributed (and/or faint enough) that LSST is likely to be the only facility in the foreseeable future that will be able to identify a statistically meaningful sample. Some (such as the novae that allow detailed study of the route to Type Ia Supernovae) offer unique laboratories to study processes of fundamental importance to astrophysics at all scales. Others (like intra-disk microlensing events) offer the *only* probe of important populations.

4.2.1 Target measurements and discoveries

We have identified four science cases within the general area of Milky Way Disk studies, that will have a diversity of dependencies on observing strategy (e.g. slow intrinsic variability vs fast intrinsic variability vs no variability). When the figures of merit have been computed for these science cases, the results will be summarized in a Table in [Sub-section 4.2.4](#).

1. Quantifying the large quiescent compact binary population via variability;

2. New insights into the behavior of Novae and the route to Type Ia Superovae;
3. The next Galactic Supernova;
4. Measuring population parameters of planets outside the Snow Line with Microlensing;

Below we provide more detail on these science cases, including qualitative discussion of the expected impact of the choice of observing strategy, as these science cases are not discussed in detail elsewhere (in the LSST Science Book or the [Ivezic et al. \(2008\)](#) summary paper).

1. Probing quiescent compact binaries via variability: Of the millions of stellar-mass black holes formed through the collapse of massive stars over the lifetime of the Milky Way, only ~ 20 have been dynamically confirmed through spectroscopic measurements (e.g., [Corral-Santana et al. 2015](#)). Many questions central to modern astrophysics can only be answered by enlarging this sample: which stars produce neutron stars and which black holes; whether there is a true gap in mass between neutron stars and black holes; whether supernova explosions result in large black hole kicks.

There is expected to be a large population of black hole binaries in quiescence with low X-ray luminosities from $\sim 10^{30}$ – 10^{33} erg/s. Such systems can be identified as optical variables that show unique, double-humped ellipsoidal variations of typical amplitude ~ 0.2 mag due to the tidal deformation of the secondary star, which can be a giant or main sequence star. In some cases analysis of the light curve alone can point to a high mass ratio between the components, suggesting a black hole primary; in other cases the accretion disk will make a large contribution to the optical light which results in intrinsic, random, and fast variations in the light curve. The disk contribution to optical light can change over time, and several years of data is necessary to properly subtract the accretion disk contribution in order to properly fit ellipsoidal variations ([Cantrell et al. 2010](#)). The brighter sources will be amenable to spectroscopy with the current generation of 4-m to 10-m telescopes to dynamically confirm new black holes; spectroscopy of all candidates should be possible with the forthcoming generation of large telescopes. Thus, LSST would trigger a rich variety of observational investigations of the accretion/outflow process through studies of this large, dark population.

While we have focused above on black hole binaries, we note that LSST would be crucial for investigations of neutron star and white dwarf binaries. For example, the total number of compact binaries is presently poorly understood—Population models of neutron star X-ray binaries diverge by orders of magnitude, largely due to uncertainties in the common envelope phase of binary evolution (e.g., [Pfahl et al. 2003](#); [Kiel & Hurley 2006](#); [van Haaften et al. 2015](#)). This is poorly constrained but has a large impact on, for example, LIGO event rates. A simple test case of common envelope evolution is available in the number of dwarf novae (DNe) (accretion disk instability outbursts around white dwarfs), a population that does not suffer from some of the complicating factors that neutron star and black hole binaries do (e.g. supernova kicks). Theoretical estimates routinely yield a significantly higher number of DNe than are observed in the solar neighborhood. Understanding the true specific frequency of these systems provides a key check on common envelope evolution. LSST will detect dwarf novae, which last at least several days with typical amplitudes of 4–6 mag, out to kpc scales. This will allow a test of not only the number of cataclysmic variables, but also of the 3D distribution within the Galaxy and dependence on metallicity gradients ([Britt et al. 2015](#)).

Response to observing strategy: Since most black hole candidates have been identified near the plane in the inner Milky Way (68%, 92% within $5^\circ, 10^\circ$ of the Plane), this science case *requires* that LSST observe the plane with sufficient cadence to detect the \sim hundreds of quiescent black-hole binaries by virtue of their variability. The natural choice for a survey for low-luminosity black hole binaries would be to extend the Wide-Fast-Deep survey throughout the Plane in the direction of the inner Milky Way. The orbital period of these systems is short (typically < 1 day), so that a rolling cadence for at least parts of the Plane should be considered. For dwarf novae, the cadence of observations is critical in obtaining an accurate measure of the population of cataclysmic variables, as a long baseline is necessary to recover low duty cycle systems while widely-space observations would miss short outbursts.

2. Novae and the route to Type Ia Supernovae: Only ~ 15 novae (explosions on the surfaces of white dwarfs) are discovered in the Milky Way each year, while observations of external galaxies show that the rate should be a factor of ~ 3 higher ([Shafter et al. 2014](#)). Evidently, we are missing 50–75% of novae due to their location in crowded, extinguished regions, where they are not bright enough to be discovered at the magnitude limits of existing transient surveys. Fundamental facts about novae are unknown: how much mass is ejected in typical explosions; whether white dwarfs undergoing novae typically gain or lose mass; whether the binary companion is important in shaping the observed properties of nova explosions. Novae can serve as scaled-down models of supernova explosions that can be tested in detail, e.g., in the interaction of the explosion with circumstellar material (e.g., [Chomiuk et al. 2015](#)). Further, since accreting white dwarfs are prime candidates as progenitors of Type Ia supernovae, only detailed study of novae can reveal whether particular systems are increasing toward the Chandrasekhar mass as necessary in this scenario.

Response to observing strategy: Most novae occur in the Galactic Plane and Bulge, and therefore the inclusion of the Plane in a survey of sufficient cadence to find these events promptly is of paramount importance for this science. These events will trigger multi-wavelength follow-up ranging from the radio to X-ray and γ -rays; these data are necessary for accurate measurements of the ejected mass.

3. The First Galactic Supernova: A supernova in the Milky Way would be among the most important astronomical events of our lifetime, with enormous impacts on stellar astrophysics, compact objects, nucleosynthesis, and neutrino and gravitational wave astronomy. The estimated rate of supernovae (both core-collapse and Type Ia) in the Milky Way is about 1 per 20–25 years ([Adams et al. 2013](#)); hence there is a 40–50% chance that this would occur during the 10-year LSST survey. If fortunate, such an event will be located relatively close to the Sun and will be an easily observed (perhaps even naked-eye) event. However, we must be cognizant of the likelihood that the supernova could go off in the mid-Plane close to the Galactic Center or on the other side of the Milky Way—both regions covered by LSST. While any core-collapse event will produce a substantial neutrino flux, alerting us to its existence, such observations will not offer precise spatial localization. The models of [Adams et al. \(2013\)](#) indicate that LSST is the *only* planned facility that can offer an optical transient alert of nearly all Galactic supernovae.

Response to observing strategy: Even if the supernova is not too faint, LSST will likely be the sole facility with synoptic observations preceding the explosion, providing essential photometric data leading up to the event—but only if LSST covers the Plane at a frequent cadence. Just how frequent is open to exploration at present, but the prospect of high-sensitivity observations of the location of such a supernova *before* it takes place are clearly of enormous scientific value. A secondary issue is the prospect that an easily-observed Milky Way supernova might be too bright

for LSST to measure precisely with its planned exposure time, with a roughly 82% chance of a core-collapse supernova reaching one or two magnitudes brighter than LSST’s nominal saturation limit (with a 1/3 chance that a ccSN would reach $m_V \sim 5$; [Adams et al. 2013](#)). For a Type Ia in the Milky Way, [Adams et al. \(2013\)](#) estimate $m_{V,max} \lesssim 13.5$ in 92% of cases.

4. Population parameters of planets beyond the Snow Line with Microlensing: [Gould \(2013b\)](#) shows that, LSST could contribute a highly valuable survey for intra-disk microlensing (in which disk stars are lensed by other objects in the disk, such as exoplanets, brown dwarfs, or compact objects). The lower stellar density compared to past bulge-focused microlensing surveys would be offset by the larger area covered by LSST. The predicted rate of high magnification microlensing events that are very sensitive to planets would be ~ 25 per year. This survey would be able to detect planets at moderate distances from their host stars, a regime poorly probed by standard Doppler and transit techniques. The LSST data alone would not be sufficient: the detection of a slow (\sim days) timescale increase in brightness of a disk star would need to trigger intensive photometric observations from small (1-m to 2-m class) telescopes that would observe at high cadence for the 1–2 months of the microlensing event. This would represent an excellent synergy between LSST and the wider observing community, and would directly take advantage of the capabilities unique to LSST.

Response to observing strategy: To catch lensing events as they start to brighten, with sufficient fidelity to trigger the intensive follow-up required, the models of [Gould \(2013b\)](#) suggest each field should be observed once every few nights. With sparser coverage, the survey would lose sensitivity to microlensing events in progress. Comparison with a similar sample towards the inner Milky Way would be highly useful, which would argue for observations of the entire visible Plane with similar cadence.

Microlensing is also discussed elsewhere in this document, particularly for relatively the Magellanic Clouds ([Chapter 7](#)), for AGN ([Section 8.4](#)), and in WFIRST fields towards the Bulge ([Section 11.4](#)). There is also some discussion in [Sub-section 5.5.2](#). We note that the WFIRST discussion in [Section 11.4](#) assumes that Bulge fields will be observed even at low cadence (~ 1 observation per day) for the first *eight* years of the survey. This would be compromised by a strategy that puts all the Galactic Plane observations into the first few years of the survey.

4.2.2 Figures of Merit

Here we describe the Figures of Merit (FoMs) we intend to implement and evaluate for the candidate observing strategies of interest. Where these FoM have already been evaluated, we provide the numerical results in [Table 4.6](#). Those FoMs are:

- FoM 1.1 - Fraction of quiescent black hole binaries detectable through ellipsoidal variability;
- FoM 1.2 - Uncertainty on the recurrence time distribution of Dwarf Novae;
- FoM 2.1 - Fraction of Novae detected by LSST (specific and total);
- FoM 2.2 - Fraction of Novae caught early enough by LSST to schedule followup observations;
- FoM 3.1 - Fraction of Galactic supernovae for which LSST would detect variability *before* the main Supernova event;

- FoM 4.1 - Fraction of accurately-triggered Microlens candidates;
- FoM 4.2 - Uncertainty in the mass function of intra-disk microlensed planets.

With the exception of FoM 3.1 above, all these Figures of Merit are likely to be impacted by spatial confusion, as the populations of interest tend to lie at low Galactic latitudes. Metrics for assessing the impact of crowding have been developed (e.g. `CrowdingMetrics.ipynb` in `maf_contrib`), and these should be incorporated into all the FoMs described here. For the present, however, we note that intrinsic source confusion is not a function of observing strategy (assuming the confusion limit is well above the formal limiting magnitude without it). Running the FoMs without accounting for source confusion isolates the impact of strategy alone on the science that can be performed, as FoMs can be compared in a relative sense. Inclusion of crowding will later set the absolute scale for each FoM.

In these FoMs, “uncertainty” can be taken to mean both random and systematic uncertainty, likely recorded as separate numbers for each FoM. We anticipate determining the FoMs that record population parameter-uncertainty in a Monte Carlo sense. This is particularly relevant for FoMs in which the event rate per pointing may be low ($\lesssim 1$ event per pointing per decade) but not so low that only 1-few events are expected over the whole sky over the lifetime of the survey (as is the case for FoM 3.1, the First Galactic Supernova). In very rare-event cases, the FoM can scale with the stellar density and the recovery fraction of that particular transient, and need only be evaluated once for the entire survey.

Since (at the time of writing) evaluating a Metric with relaxed SQL constraints typically takes about 0.5-1.5 hours, we do not expect to perform Monte Carlo simulations initially. In the medium-term, when Monte Carlo experiments in the target populations are desired, the best strategy may be to evaluate the run of a particular metric against a parameter of interest (apparent magnitude, say, which is also expected to lead to a turnover in the importance of confusion error), and the investigator’s preferred Monte Carlo framework for their population of interest can interpolate the stored Metric values at the time of trial-population generation. At the present date (2016-04-26) we have begun investigating the use of these “Vector Metrics” for Figures of Merit. We describe the anticipated FoMs in these cases below.

FoM 1.1 - Fraction of quiescent black hole binaries detectable through ellipsoidal variability: Table 4.1 outlines the steps to evaluate FoM 1.1. Since the lightcurve *shape* matters in addition to the detection (i.e. we expect LSST data to be used to characterize ellipsoidal variations, not just to trigger followup by other observatories) the metric choice for detectability should take the lightcurve shape into account.

The main innovation required before this FoM can be run, is the extension of existing periodic Metrics to cases with a lightcurve shape more complicated than a sine plus noise. The `TransientAsciiMetric` may be a good place to start; or, it might be straightforward to extend `periodicStarFit` to lightcurves with more than one Fourier coefficient. Or, an entirely new metric might be written including more Fourier terms in the fit.

An open question is how best to meaningfully quantify the recovery fraction of a population with a wide range in binary parameters. However, as an initial FoM, evaluating once for an “average” population will allow direct comparison between observing strategies.

Possible higher-order FOM: errors on the population size (mass function?) derived from a survey under a given observing strategy. Can imagine just adding up the “recovered” qLMXB population and comparing it to that simulated. Some white noise component of varying strengths could be added to the light curves to simulate various contributions of the accretion disk to the continuum light. Note that the survey will necessarily be highly incomplete (inclination effects, etc.), it is the likely *uncertainty* on the completeness-correction that would be crucial in this case.

FoM 1.1 - Fraction of quiescent black hole binaries (qLMXB) detectable by LSST through ellipsoidal variability

-
1. Pick a typical binary mass ratio and separation for *qLMXB*
 2. Identify typical ellipsoidal variation amplitude and period
 3. Represent as Fourier terms or ASCII lightcurve
 4. Run a variant of `periodicStarFit.ipynb` that allows the appropriate double-humped lightcurve shape. May be appropriate to modify `mafContrib/periodicStarMetric.py`.
 5. **Arrive at FoM 1.1:** Load the result from 4. and sum over the spatial region (to be determined: Galactic Latitude range? Comparison high-latitude clusters?) where the qLMXBs are expected.
-

Table 4.1: Description of Figure of Merit 1.1.

FoM 1.2 - Uncertainty on the recurrence-time distribution of Dwarf Novae: Table 4.2 illustrates a version of this FoM that could be run in the near future. Dwarf Novae are a heterogeneous class; in the near future we imagine assigning an average lightcurve to a population and determining the recovered vs input recurrence timescale, under the assumption that the spatial distribution of recurrent Dwarf Novae is uniform. This isolates the impact of observing strategy alone due to gaps in coverage. Rather than a full Monte Carlo in Novae populations, initially the investigator might compute the FoM for a representative range of recurrence timescales (since the error on timescale recovery may be expected to scale with the recurrence timescale itself).

FoM 1.2 - Uncertainty in the Dwarf Nova Recurrence timescale

-
1. Pick a typical lightcurve for the Dwarf Nova class of interest;
 2. Assign a recurrence timescale;
 3. Run `TransientMetricASCII` using this lightcurve and recurrence timescale;
 4. Combine the (spatially distributed) results of 3. into a median and formal random uncertainty estimate on the recurrence time estimated from each line of sight;
 5. Compute the offset and its formal error, between the median from 4. and the input recurrence timescale from 2;
 6. **Arrive at FoM 1.2:** The four numbers from steps 4. and 5. are the characterization of the uncertainty in recurrence timescale required.
-

Table 4.2: Description of Figure of Merit 1.2.

Possible higher-order FOM: Uncertainty in LIGO event rates due to uncertainties in common envelope evolution, which drives uncertainties in both LIGO event rates and DN population.

FoMs 2.1 & 2.2 - Fraction of Novae characterized by LSST; and the fraction detected early enough for followup: Since the set of Novae is so heterogeneous, one can imagine a two-stage process. In the near-future, a single run of `TransientMetricASCII` using some sense of an “average” Nova as tracer to enable comparison between observing strategies. We present this in Table 4.3, which includes examples for the specific and total fraction of Novae recovered.

In the longer term, a Monte Carlo simulation could be run on a particular class of Novae depending on the parameters of the overall population whose constraints are desired. This latter effort would likely require further development of the Vector Metrics.

FoMs 2.1 & 2.2 - Novae identified from LSST data

1. Pick a typical lightcurve for the Nova class of interest;
 2. Run `TransientMetricASCII` using this lightcurve;
 3. **Arrive at FoM 2.1a: Specific fraction of Novae discovered:** Sum the result from 2. over the spatial region of interest;
 4. **Arrive at FoM 2.1b:** Multiply the result of 2. by the result of the `Starcounts` metric. Sum this to find the fraction of Novae recovered if their spatial density follows the stellar density in the Milky Way.
 5. From the typical lightcurve and a typical follow-up scenario, determine the time interval before outburst peak that would be required to schedule follow-up observations;
 6. Use these to produce the time interval parameters for the `TripletMetric`;
 7. Run `TripletMetric.py`;
 8. **Arrive at FoM 2.2:** Sum the result of step 6. over the spatial region of interest.
-

Table 4.3: Description of Figures of Merit 2.1. & 2.2.

Possible higher-order metrics: Error on the rate of Type Ia supernovae using LSST data taken under various observing strategies.

FoM 3.1 - Fraction of Galactic supernovae for which LSST would detect variability before the main Supernova event: We have implemented a simple FoM for the Galactic Supernova case, using the parameters of SN2010mc as an example whose pre-SN outburst could be discovered first by LSST. The FoM is defined as the density-weighted average fraction of transient events recovered, where the average is taken over the sight-lines within the simulated strategy:

$$FoM_{preSN} \equiv \frac{\sum_i^{sightlines} f_{var,i} N_{*,i}}{\sum_i^{sightlines} N_{*,i}} \quad (4.1)$$

Here $f_{var,i}$ is the fraction of transient events that LSST would detect for observing strategy including the i 'th sightline, $N_{*,i}$ the number of stars present along the i 'th sightline, and the FoM is normalized by the total number of stars returned by the density model over all sightlines. (For the OpSim runs tested here, `minion_1016` and `minion_1020`, the normalization factors differ by $\sim 2\%$.) FoM values are in the range $0.0 \leq FoM_{preSN} \leq 1.0$.

We assume the Pre-SN variability similar to the pre-SN outburst of SN2010mc ([Ofek et al. 2013](#)). The pre-SN variability is modeled as a sawtooth lightcurve (in apparent magnitude). We assume

this transient event will always reach brightness sufficient for LSST to observe, so opt for a very bright peak apparent magnitude in all filters. We assume that the probability of a supernova going off is proportional to the number of stars along a particular line of sight.

In definition (4.1), a lightly-modified version of `CountMetric` was used to determine $N_{*,i}$ with the output summed over all sight-lines to produce N_* . Module `TransientMetric` was used to determine $f_{var,i}$ for each sight-line.²

FoM 4.1 - Fraction of accurately-triggered Microlens candidates within a spatial region of interest: Table 4.4 lays out a possible FoM for the fraction of microlens candidates that LSST might catch sufficiently early that follow-up observations can be planned for other facilities. This low-level FoM should be straightforward to compute, for a microlens template lightcurve corresponding to some suitable average over the regime of interest.

FoM 4.1 - Fraction of microlens events triggered from LSST observations

1. Decide on the typical microlens scenario of particular interest;
 2. Produce a template ASCII lightcurve for this scenario;
 3. Determine the characteristics for a trigger;
 - e.g. slow rise to 20% flux above baseline at 7σ significance;
 - e.g. must be at most T days after the initial rise to schedule follow-up;
 4. **Arrive at FoM 4.1:** Sum the fraction of detected candidates from 3. spatially over the region of interest.
-

Table 4.4: Description of Figure of Merit 4.1

FoM 4.2 - Uncertainty in the mass function of microlensed planets past the Snow Line: Table 4.5 illustrates a possible FoM for a science case concerning uncertainty in the parameters of a particular planetary population of interest. As with FoM 4.1, in this scenario LSST is used as the initial trigger for follow-up observations by other facilities, but the observing strategy imposes uncertainty and bias on the eventual derived parameters through its removal of parts of the population from further study. The investigator could assume a particular uncertainty imposed on the mass determination from follow-up observations, but this should be fixed for all evaluations of the FoM so that LSST strategies can be compared. Strictly speaking, a Monte Carlo simulation over many realizations of the input planetary population should probably be run. However, formal errors would probably be acceptable in the near-term (i.e. formal errors on the determination of mass function parameters that are determined from the subset of objects that survive LSST's selection function for a particular strategy).

4.2.3 OpSim Analysis

FoM 3.1: the First Galactic Supernova: This FoM is described in Definition (4.1) of Sub-section 4.2.2.

²The notebooks used to evaluate this version of FoM 3.1 can be found in subdirectory `notebooks` of the experimental github repository `lsstScratchWIC`, available at this link: <https://github.com/willclarkson/lsstScratchWIC>

FoM 4.2 - Uncertainty in the mass function for planets beyond the Snoe Line through Microlensing

1. Parameterize the mass function of the population of interest;
2. Parameterize its distribution of lens amplitude and timescale;
3. Parameterize the scaling of event rate with local stellar density;
4. Generate a sample population over the sky;
Scaling from 3. might be used in conjunction with `maf_contrib/starcounts`;
5. Run the transient-recovery metric for this population;
Choice of metric needs to handle spatially varying lightcurve template;
Or, with `TripletMetric` or similar, the time-interval parameters should be allowed to spatially vary;
6. Determine the population of microlens planets that would have been triggered by LSST. Do not sum, but record the indices of the surviving objects;
7. Apply typical measurement uncertainty from a likely followup campaign;
8. Fit the determined mass function from this sample of survivors only;
9. **Arrive at FoM 4.2:** Find the offset (from input) and formal uncertainty on the mass function parameters.

Table 4.5: Description of Figure of Merit 4.2

Parameters used: The lightcurve used has the following parameters: rise slope -2.4 ; time to peak: 20 days; decline slope: 0.08; total transient duration: 80 days. All filters are used in the detections, and 20 evenly-spaced phases are simulated for sensitivity to pathological cases (parameter `nPhaseCheck=20`). Peak apparent magnitudes used: $\{11, 9, 8, 7, 6, 6\}$ in $\{u, g, r, i, z, y\}$. Then, $f_{var,i}$ is taken as the “Sawtooth Alert” quantity returned by `TransientMetric`. For the stellar density metric, distance limits ($10\text{pc} \leq d \leq 80\text{kpc}$) are used to avoid biases in the FoM estimate by the Magellanic Clouds.

Results: $FoM_{preSN}(\text{minion_1016})=0.13$, while $FoM_{preSN}(\text{minion_1020})=0.83$.³ Because `minion_1020` spends no time at all on certain regions of interest (like the South Polar cap and the Northern plane), it might be artificially advantaged over the Baseline survey. A more direct comparison is afforded by the recently-completed (at the time of writing) OpSim run `astro_lsst_01_1004`, which covers the same regions on the sky as `minion_1016` but applies the Wide-Fast-Deep strategy to the inner Galactic Plane. That strategy still shows a strong advantage compared to the Baseline survey, with $FoM_{preSN}(\text{astro_lsst_01_1004})=0.73$, compared to 0.13 for Baseline cadence. See Table 4.6. Figure 4.1 presents a breakdown of this figure of merit across sightlines, for the three observing strategies considered.

³2016-04-25 For comparison, when run on 2015-era OpSim runs `enigma_1189` (Baseline strategy) and `ops2_1092` (PanSTARRS-like strategy) the results were 0.251 (Baseline) and 0.852 (PanSTARRS-like strategy). So the 2016-era OpSim runs show a sharper disadvantage than before to the Baseline cadence for the Galactic Supernova case.

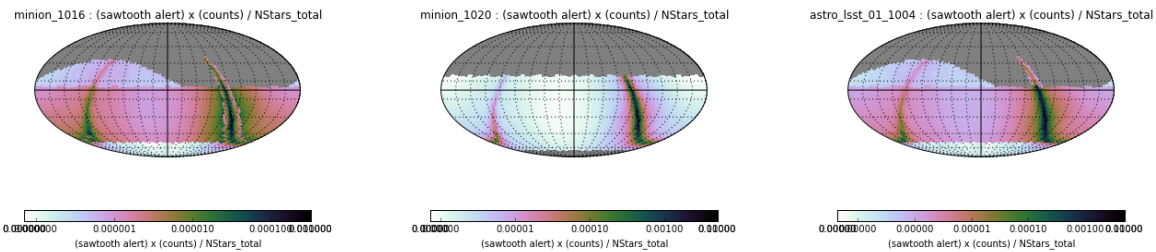


Figure 4.1: Figure of merit FoM_{preSN} describing LSST’s sensitivity to any pre-Supernova outburst for the Galactic Supernova science case, broken down by sightline. FoM_{preSN} is estimated for three OpSim runs (to-date); [minion_1016](#) (left; Baseline cadence), [minion_1020](#) (center; PanSTARRS-like strategy), and [astro_lsst_01_1004](#) (which assigns Wide-Fast-Deep cadence to the inner Galactic Plane). The normalizing factors $N_{*,total}$ are 3.793×10^{10} for both [minion_1016](#) and [astro_lsst_01_1004](#) (that both strategies have the same N_* is not a surprise since both cover the same area) and 3.692×10^{10} for [minion_1020](#). The imprint of reduced sampling towards the inner plane can be clearly seen for [minion_1016](#). Notice the difference in color scale between the panels. See [Sub-section 4.2.3](#)

4.2.4 Discussion

The Figures of Merit listed above must now be implemented within the sims_maf framework and applied to representative science cases. See Table 4.6 at the end of this subsection for initial efforts along these lines. We welcome input and volunteers for this effort.

Qualitatively, however, we can note immediately that the current baseline cadence ([minion_1016](#)) partially excludes the Galactic Plane from the deep-wide-fast survey and instead adopts a nominal 30 visits per filter as part of a special proposal - which also tends to cluster the visits in the inner Plane within the first few years of the survey. This already seriously compromises the time baseline (see Figure 4.4 of [Sub-section 4.3.3](#) for a demonstration applied to proper motions).

Go to: • [the start of this section](#) • [the start of the chapter](#) • [the table of contents](#)

4.3 Astrometry with LSST: Positions, Proper Motions, and Parallax

[Dave Monet](#), [Dana I. Casetti-Dinescu](#), [John E. Gizis](#), [Michael C. Liu](#), [Jay Strader](#), [Will Clarkson](#), [Peter Yoachim](#)

A number of Milky Way science cases of interest to the Astronomical community will depend critically on the astrometric accuracy LSST will deliver. While “astrometry” is not a science case in the framework of this white paper, LSST’s astrometric performance will be sensitive to the particular choice of observing strategy. Hence, the LSST Observing Strategy needs to be examined for systematic trends that might mitigate or even preclude precise measures of stellar positions, proper motions, parallaxes, and perturbations that arise from unseen companions.

[Sub-section 4.3.1](#) highlights two science cases at opposite scales of distance from the Sun that require accurate and precise astrometry and/or proper motion measurements. [Sub-section 4.3.2](#) develops Metrics for LSST’s astrometric performance, and discusses Figures of Merit for the two highlighted science cases. These metrics are applied to two example OpSim runs in [Sub-section 4.3.3](#).

FoM	Brief description	minion_1016	minion_1020	astro_lsst_01_1004	future run 2	Notes
1.1	LMXB ellipsoidal variations	-	-	-	-	-
1.2	Uncertainty in dwarf nova duty cycle	-	-	-	-	LSST as initial trigger
2.1	Fraction of Novae detected	-	-	-	-	-
2.2	Fraction of Nova alerts	-	-	-	-	-
3.1	Galactic Supernova pre-variability	0.13	0.83	0.73	-	Fraction of SN2010mc-like outbursts that LSST would detect; $FoM_{preSN} = f_{var} \times N_*$
4.1	Fraction of LSST-triggered microlens candidates	-	-	-	-	-
4.2	Uncertainty in derived planetary mass function	-	-	-	-	LSST as initial microlens trigger

Table 4.6: Summary of figures-of-merit for the Galactic Disk science cases. The best value of each FoM is indicated in bold. Runs `minion_1016` and `minion_1020` refer to the Baseline and PanSTARRS-like strategies, respectively. Column `astro_lsst_01_1004` refers to a recently-completed OpSim run that includes the Plane in Wide-Fast-Deep observations. See Sub-section 4.2.3.

Finally in Section 4.3.4, the work that is still needed is discussed, both in terms of the Metrics and the Figures of Merit that depend on them.

4.3.1 Target Measurements and Discoveries

1. Identification of Streams in the Galactic Halo using proper motions.
2. A complete sample of stars in the solar neighborhood.

1. Streams in the Galactic halo

Much of the Milky Way’s stellar halo was built by the accretion of smaller galaxies. Given that these galaxies were generally of low mass, their tidal debris should still form coherent structures in phase space, especially in the outer Galaxy where dynamical times are long. The identification of these streams would allow a reconstruction of the accretion history of the Milky Way. Tides also lead to the dissolution of globular clusters, leaving notably thin streams that serve as sensitive tracers both of the Galactic potential and of the presence of dark subhalos.

A relatively small number of streams, originating from both dwarfs and globular clusters, have been identified via photometry of individual stars in large surveys such as SDSS. However, only the highest surface brightness structures can be found in this manner, and it is often difficult to trace the streams over their full extent. LSST will enable streams to be identified by stellar proper motions, and combined with targeted follow-up spectroscopy, will yield full 6-D position

and velocity measurements suitable for dynamical modeling. Further, it will allow the discovery of tidal debris that is no longer spatially coherent but which can be unambiguously identified in phase space.

Finally, streams and other kinematically-distinct halo substructure can be identified and characterized by combining proper motions and photometry in reduced proper-motion diagrams (e.g., [Carlin et al. 2012](#)), and by analyzing proper-motions of tracers such as RR Lyrae and giants over large portions of the sky (e.g., [Casetti-Dinescu et al. 2015](#)).

Response to observing strategy: Most stars in streams will be main-sequence stars, and the old main sequence turnoff is located at $r \sim 24$ at a distance of 100 kpc. The nominal LSST proper motion precision at this magnitude is 1 mas yr⁻¹, corresponding to about 475 km s⁻¹ at this distance. The proper motion measurements will be better for brighter stars, but in general ensembles of stars will be necessary for accurate measurements. To make accurate proper motion measurements for faint stars, several key components are required. First, a zero point must be established, possibly via background galaxies located in each field. Next, the observations must cover a sufficient range of epochs to reliably detect linear proper motions.

To identify streams over their full lengths of many degrees of the sky, relative astrometry over small fields will not be sufficient. Therefore the absolute astrometric frame is important. Matching the optical astrometry to the radio International Celestial Reference System (ICRS) relies on measuring accurate positions for objects visible in both wavelength regimes. These are typically distant QSOs. Unfortunately, many QSOs have detectable optical or radio structures that degrade the positions or suggests a displacement between the location of the sources of the radio and optical radiation. LSST will need to identify a large number of point-like QSOs based on their colors and variability.

Since the number of galaxies is overwhelming toward faint magnitudes, these must be exploited to produce a reliable absolute proper-motion zero point. By using Gaia stars at the bright end as absolute proper-motion calibrators we can quantify the precision and accuracy of background galaxies as a secondary link to an inertial reference system, and thus improve the calibration at the faint end of the survey.

2. A complete sample of stars in the solar neighborhood

The direct solar neighborhood offers our only chance to get make a complete sample of stars, brown dwarfs, and stellar remnants that encompass the entire formation and dynamical history of the Milky Way. While Gaia will offer parallax measurements for perhaps billions of stars, its faint magnitude limit of $G \sim 20$ will limit its measurements of the lowest-mass objects and remnants to nearby objects, much less than the thin disk scale height of ~ 300 pc. For example, Gaia can only measure parallaxes for $0.2M_{\odot}$ M dwarfs to about 100 pc and $0.1M_{\odot}$ M dwarfs to only 10 pc, showing that Gaia is ill-suited for studies of the coolest dwarfs. By contrast, LSST can measure parallaxes for $> 10^5$ M dwarfs and thousands of L/T brown dwarfs (the coolest Y dwarfs are too faint even for LSST; little contribution is likely here beyond the sample provided by WISE). Gaia will likewise be limited to cool white dwarfs within ~ 100 pc with which to estimate the age of the disk, and the thick disk and halo will be out of reach. LSST can directly compare white dwarf luminosity functions to determine precise differential ages for the thin disk, thick disk, and halo.

Response to observing strategy: Successfully completing this project will require parallax measurements much fainter than possible with Gaia as well as a verification that the LSST and Gaia parallax measurements are consistent in the overlapping magnitude range.

The measurement of stellar parallax puts the substantial constraints on the observing cadence. There are two major issues: the need to sample a wide range of parallax factor (related to time of year), and breaking the correlation between differential color refraction and parallax factor.

“Parallax factors” characterize the ellipse of the star’s apparent motion as seen over the course of a year. The shape of the ellipse is given by the Earth’s orbit and is not a free parameter in the astrometric solution. The amplitude of the right ascension parallax factor is close to unity while the amplitude of the declination parallax factor is dominated by the sine of ecliptic latitude. The right ascension parallax factor has maximum amplitude when the star is approximately six hours from the Sun, so the optimum time for parallax observing is when the star is on the meridian near evening or morning twilight. Atmospheric refraction displaces the star’s apparent position in the direction of the zenith by an amount dependent on both the wavelength of the light and the distance to the zenith. Whereas the measured position of star is a function of the total refraction, the measurement of parallax and proper motion depends on the differences in the refraction as a function of the color of each star and the circumstances of the observations. This dependence is called differential color refraction. The combination of parallax factor and differential color refraction leads to two rules:

- 1 Observations need to cover the widest possible range in parallax factor.
- 2 The correlation between parallax factor and hour angle in the observations needs to be minimized.

4.3.2 Metrics and Figures of Merit for LSST’s delivered astrometric accuracy

First we discuss metrics for the observing strategy that affect all of LSST’s astrometric measurements, then discuss figures of merit for the two science cases. (The three general metrics were identified years ago and are already in the suite of MAF utilities, but they should be reviewed prior to making final decisions. For this reason, in addition to the Figures of Merit later in the chapter, we present spatial maps and histograms for the metrics themselves in Section 4.3.3, for representative OpSim strategies.)

- A) For each LSST field, the parallax factors at each epoch of observation need to be computed. The ensemble of these must be checked for sufficient coverage of the parallactic ellipse. In particular, the number of measures with RA parallax factor less than -0.5 and greater than $+0.5$ needs to be tallied because these carry the most weight in the solution for the amplitude (parallax).
- B) For each LSST field, the hour angle of the observation needs to be computed, and the correlation between hour angle and parallax factor needs to be examined for significance. The observing strategy must minimize the number of fields with this correlation.
- C) The epochs of observation for each field must be checked for a reasonable coverage over the duration of the survey and to avoid collections of too many visits during a few short intervals.

For the stream project discussed above, a simple to state (but perhaps complex to implement) figure of merit is the number of streams that can be discovered in LSST via their proper motions. As a first attempt, it would be reasonable to assume about 100 halo streams from old, metal-poor dwarf galaxies with stellar masses $10^5 - 10^7 M_\odot$ distributed as $r^{-3.5}$. The stream widths and internal velocity dispersions can be set from galaxy scaling relations, and their 3-D velocities consistent with a simple Galactic mass model at their radii. Setting the stream lengths is more complicated, but should cover a large range from a few to many kpc. Over a given area, the stream “S/N” can roughly be taken as the number of stream stars (identified via proper motion, color, and magnitude) divided by the square root of the number of field stars. For globular clusters, a similar number of streams could be included, but these should have much smaller widths (10s of pc) and typical masses $10^4 - 10^5 M_\odot$. Eventually it would be desirable to use actual simulated stream parameters taken from cosmological models of the Milky Way (e.g., from the Aquarius simulation).

Solar neighborhood projects will be sensitive to the general parallax and proper motion metrics discussed above. More specific science figures of merit are *required* at this stage. For example, the precision of the differential age measurement between the thin disk and halo, which would depend on the number of white dwarfs that can be isolated from each population.

4.3.3 OpSim Analysis

Here we present initial analysis of LSST’s astrometric performance. Two example strategies are assessed: the current baseline strategy, [minion_1016](#), and the PanSTARRS-like cadence, [minion_1020](#), which greater spatial uniformity and superior coverage of the Galactic Plane.

Metrics: Parallax and proper motion precision

Here we present the expected astrometric performance of LSST as a function of location on-sky, subdivided by elapsed time in the survey (Figures 4.2 - 4.5), and for three extreme choices of filters in which an object is detected (Figures 4.6 - 4.9). Astrometric performance for parallax is quantified using the following metrics:

1. Parallax factor coverage (following metric A of [Sub-section 4.3.2](#)); values farther from 0 are better). See Figures 4.2 & 4.6;
2. Parallax-Hour angle correlation (metric B of [Sub-section 4.3.2](#); values closer to 0 are better). See Figures 4.3 & 4.7;
3. Proper motion error, for a star at apparent magnitude 21.0 in the filter specified (this addresses the distribution of measurement epochs, as recommended in Metric C in [Sub-section 4.3.2](#); smaller values are better). See Figures 4.4 & 4.8;
4. Parallax error, for a star at apparent magnitude 21.0 in the filter specified (smaller values are better). See Figures 4.5 & 4.9.

Limitations of this presentation:

- i. The spatial maps are clipped at 95% in order to keep the color-scale at a sensible range; in some cases this has had the side effect of removing parts of the spatial coverage in the [minion_1016](#) maps.
- ii. No attempt has been made in this subsection to account for spatial confusion in high-density regions. While this confusion would be the same whatever observing strategy was chosen, the numbers for proper motion and parallax uncertainty should be regarded as lower limits.
- iii. The choice of fiducial apparent magnitude $r = u = y = 21.0$ is not terribly well-motivated in this subsection. It would be informative to repeat the analysis for a range of target apparent magnitudes that are better-matched to the specific science cases.
- iv. The comparison between single-filter and *ugrizy* detections likely overestimates the measurement precision for the *u*-only and *y*-only detections, as an object only detected in a single filter may well not be detected in all images taken in that filter. While the comparison between filter subsets for a given strategy may therefore be highly approximate, the comparison between strategies for the same filter should be more reliable.
- v. We have not yet subdivided the samples by a meaningful spatial co-ordinate (galactic latitude would be the obvious choice). A large part of the breadth of the various metric values in [minion_1016](#) as compared to [minion_1020](#) may be due to spatial nonuniformity of the sampling; replotting the histograms coded by galactic latitude would be highly informative in this context.

Indications at this date: Despite these limitations, we note the following:

- I1. Taking snapshots of the survey at various stages of completion (Figures 4.2 - 4.5), the PanSTARRS-like cadence is no worse than [minion_1016](#), and by most measures offers better performance;
- I2. As might be expected, the distribution of metric values for the PanSTARRS-like cadence is narrower than for [minion_1016](#) - thus astrometric survey uniformity is improved;
- I3. For the extremes of object color (objects detected only in the bluest or only in the reddest filter), the differences between strategies is weaker. The histogram of run [minion_1016](#) still shows a population with poorer parallax measures (although this might be due to coverage of difficult-to-observe regions that are not covered at all by the PanSTARRS-like strategy).

Figures of Merit depending on the Metrics

Building on the first-order metrics above, this subsection communicates scientific figures of merit for the cases identified in [Sub-section 4.3.1](#) above.

Table 4.7 summarizes the Figures of Merit (FoMs) for Astrometry science cases. At the time of writing, FoMs have been implemented to summarize the random uncertainty in proper motion and parallax, for two regions experiencing extreme values of these quantities: the inner Plane (conservatively defined in this section as $|b| \lesssim 7^\circ$ and $|l| \lesssim 80^\circ$), and the main survey (excluding the inner plane and the Southern Polar region, taken here as $\delta_{2000.0} < -60.0^\circ$). Figure 4.10 illustrates these selection-regions on the sky. These form FoM 1.1-1.4, and have to-date been

run for the OpSim runs `minion_1016` (Baseline cadence), `??` (similar to PanSTARRS-1), and the recently-completed `astro_lsst_01_1004` (which applies Wide-Fast-Deep cadence to the inner Galactic Plane). From the point of view of parallax and proper motion, the latter two strategies do not negatively impact the non-plane regions, but they *substantially* improve the sampling for proper motions and parallax (again, neglecting the effects of spatial crowding).

At the time of writing, FoMs 2-5 in Table 4.7 are still at the specification stage, and are described in Section 4.3.4.

4.3.4 Topics that will need to be addressed

Here we present suggestions for further work, first on figures of merit for the science cases, and then on additional Metrics for LSST’s astrometric performance.

Further work on science Figures of Merit

At the time of writing, the Figures of Merit for both the highlighted Science cases need to be implemented and applied to OpSim output, preferably in a format that can be summarized in a single Table in this section. These figures of merit are discussed above in Section 4.3.2 (particularly for the Halo Streams science project). Figures of merit for the two science cases might be:

1. Number of streams that LSST can discover via their proper motions;
2. Uncertainty and bias in the thin and thick disk differential age measurement when using white dwarfs from each population as tracers.

Given the diversity of science cases that use local Solar Neighborhood populations as tracers, it may be advantageous to subdivide the Solar Neighborhood projects into further figures of merit. Two further example figures of merit might then be:

3. Uncertainty and bias in the Brown Dwarf mass function using Solar Neighborhood tracers;
4. Uncertainty and bias in the thickness in the main sequence of M-dwarfs within 25pc from the Sun, once variability has been characterized and removed.

Further work on Astrometry Metrics

The MAF metrics presented in Sections 4.3.3 and 4.3.2 are only part of the study of LSST’s predicted astrometric performance. Detailed simulations and studies need to be done in many other areas as part of the prediction and verification of LSST’s astrometric performance. Among the most important are the following.

- How well do galaxies perform as astrometric reference objects? Are certain shapes or colors better than others? What is the surface density of “good” astrometric reference galaxies as a function of filter?
- How well can we identify optically point-like QSOs that will be useful in matching the optical reference frame to the ICRS?

FoM	Brief description	minion_1016	minion_1020	astro_lsst_01_1004	future run 2	Notes
1.1	Median parallax error at $r = 21$ (main survey)	0.69	0.72	0.69	-	See region definitions in Figure 4.10.
1.2.	Median parallax error at $r = 21$ (plane)	2.68	0.91	0.89	-	Smaller values are better.
1.3.	Median proper motion error at $r = 21$ (main survey)	0.19	0.19	0.19	-	
1.4.	Median proper motion error at $r = 21$ (plane)	16.7	0.26	0.25	-	
2.1.	Number of streams LSST can discover via proper motions	-	-	-	-	-
3.1.	Uncertainty and bias in thin- and thick-disk differential age measurement via white dwarfs	-	-	-	-	-
4.1.	Uncertainty and bias in brown dwarf mass function from the Solar Neighborhood	-	-	-	-	Using astrometry metrics for objects detected only in the reddest filter(s)
4.2.	Uncertainty and bias in white dwarf mass function from the Solar Neighborhood	-	-	-	-	Using astrometry metrics for objects detected only in the bluest filter(s)
5.1.	Uncertainty and bias in Solar Neighborhood M-dwarf thickness on the MS	-	-	-	-	-

Table 4.7: Summary of Figures of Merit for the Milky Way Astrometry science cases. The best value of each FoM is indicated in bold. Runs [minion_1016](#) and [minion_1020](#) refer to the Baseline and PanSTARRS-like strategies, respectively. Column `astro_lsst_01_1004` refers to a recently-completed OpSim run that includes the Plane in Wide-Fast-Deep observations. See [Section 4.3](#).

- How does the astrometric performance depend on stellar density? If there are fields in which photometry is only possible via difference imaging, what are the limitations on astrometry in these fields?
- Does the “brighter-wider” effect in the deep-depletion CCDs introduce a magnitude term into the centroid positions?

Go to: • [the start of this section](#) • [the start of the chapter](#) • [the table of contents](#)

4.4 Future Work

In this section we provide a short compendium of science cases that are either still being developed, or that are deserving of quantitative MAF analysis at some point in the future.

4.4.1 Dust in the Milky Way

Peregrine McGehee

As discussed in the LSST Science Book (particularly its Section 7.5), possession of an accurate, three-dimensional dust map is important to many astrophysical studies. The two most significant all-sky maps generated in the past two decades are the SFD98 maps based on IRAS observations, and the recent thermal dust maps derived from Planck submillimeter data. The angular resolutions of both maps are similar - between 4 to 6 arcminutes.

Both of the aforementioned maps are strictly two-dimensional and contain no information about the distribution of dust along the line of sight. A third dimension can be obtained by analysis of accurate stellar photometry which constrains both the reddening $E(B-V)$ and extinction $R_V \equiv A_V/E(B-V)$ towards individual stars. This approach requires determination of the intrinsic stellar colors and the photometric parallax of each star in the presence of an unknown amount and law of extinction. Such maps are necessary to accurately measure the intrinsic luminosities and colors of both Galactic and extragalactic sources. Recent work on 3-D maps include the Bayesian analysis method based on Pan-STARRS-1 (PS1) data ([Green et al. 2015](#)) and an alternative technique using SDSS photometry of M dwarfs (McGehee et al. 2016, in preparation). However, these studies have so far typically been limited to heliocentric distances of $\lesssim 4.5$ kpc. In the full co-added survey, LSST will be able to map dust structures out to distances exceeding 40 kpc, thus revealing a detailed picture of this component of the Milky Way Galaxy.

While the PS1 3-D dust map is a significant advance, it suggests a number of major improvements that LSST will be able to provide. Firstly, the PS1 map covers the region of the sky covered in their 3π survey, and thus excludes a large part of the Galactic Plane towards the South. Secondly, the PS1 map ([Schlafly et al. 2014](#)) saturates at extinctions $E(B-V) > 1.5$ as their tracer stars fall out of the survey catalogs fainter than $g \sim 22$, meaning that this high-fidelity map does not extend uniformly to within a few degrees of the midplane. Thirdly, this map is currently limited to distances $d \lesssim 4.5$ kpc. Deep LSST data will allow this map to be extended to much higher extinctions and larger distances. Owing to the high extinction and the use of blue filters, this project is less affected by crowding than other projects requiring photometry in the Plane.

The SDSS approach is complementary, and makes use of reddening-free colors defined in the SDSS *ugriz* system by [McGehee et al. \(2005\)](#). This approach makes use of M dwarf locus in $(g - r, r - i)$ being nearly perpendicular to the reddening vector in that color-color space. This allows mapping of a reddening-invariant index to the intrinsic stellar $g - i$ color and subsequent determination of the light-of-sight reddening. This approach assumes a set extinction law, i.e $R_V = 3.1$, in order compute the reddening-invariant index from the observed $g - r$ and $r - i$ colors. Given the relative faintness of M dwarfs, this technique is distance limited to ~ 1 kpc when based on SDSS data. With its significantly greater survey depth to M-dwarfs, LSST should revolutionize the use of this technique to probe Interstellar dust.

Target measurements and discoveries

LSST will be in a unique position to measure the changes in the observed reddening vector due to R_V variations due to its superb photometric accuracy. Both of the dust survey techniques mentioned above can be used on LSST data, and perhaps other methods will be developed before the start of survey operations.

When focusing on dust in the ISM (as opposed to time-domain studies, e.g., dust around star-forming regions or young stars), the main drivers of feasibility are coverage of the few degrees around the Plane with sufficient photometric depth and accuracy. This project is less affected by crowding than other projects requiring photometry in the Plane owing to its use of blue filters and the high extinction. Nonetheless, quantitative estimates of the expected photometric accuracy in coadded u and g images at low Galactic latitude are desirable.

Production of a 3-D map of the dust component of the ISM based on LSST photometry will tell us how much dust is present, what type it is, and where it is along the line of sight. The latter concern brings in issues of how to determine stellar photometric parallaxes ($\mu = m - M$) under an unknown reddening. The dust maps that are created will consist of the median and variance of $E(B - V)$ and R_V expressed as functions of μ under a suitable binning scheme. We can create simple Figure of Merit maps that lose the μ dependency by computing the mean and variance of the measured variances in $E(B - V)$ and R_V over the μ bins.

With the possible exception of sightlines towards star formation regions, studies of interstellar dust are insensitive to the distribution in time of the visits. In the case of active star formation regions it is possible that changes in the ISM could be apparent over the lifetime of the survey. Pushing to fainter magnitudes (which means observing these fields with better seeing and longer exposures) will be important, because more stars are required for better statistical constraints on the model, because more stars are required that lie behind the dust. In general, the use of broad band photometry requires attention to the intrinsic SEDs of the background stars in order to correct for heterochromatic variations in the effective reddening law.

Go to: • [the start of this section](#) • [the start of the chapter](#) • [the table of contents](#)

4.4.2 Mapping the Milky Way Halo

[Kathy Vivas](#), [Colin Slater](#), [David Nidever](#), [Beth Willman](#)

The study of the halo of the Milky Way is of the highest importance, not only to understand the formation and early evolution of our own galaxy, but also to test current models of hierarchical galaxy formation. LSST will provide an unprecedented combination of area, depth, wavelength range and long time-baseline for imaging data, allowing detailed studies of the present-day structure of this old Galactic component. More detail on each of these tracer populations, and the general scientific motivations for studies of the Milky Way halo with LSST, can be found in [LSST Science Collaboration et al. \(2009\)](#). Here we focus our attention on halo investigations using three tracer populations. While we anticipate more cases will be developed and compared between strategy choices, we have selected populations here that illustrate many of the most important challenges.. We describe the figures of merit (and the diagnostic metrics on which they depend) that will allow quantitative assessment of the impact of the choice of observing strategy on the constraints LSST will afford. We first briefly discuss the use of three main population tracers to chart the halo population. More detail on each of these tracer populations, and the general scientific motivations for studies of the Milky Way halo with LSST, can be found in [LSST Science Collaboration et al. \(2009\)](#).

1. RR Lyrae stars have been known for several decades as excellent tracers of the halo population. They are not only old stars (> 10 Gyrs) but they are also excellent standard candles that allow construction of three-dimensional maps. RR Lyrae stars have been used to survey Milky Way halo populations extending out to $\sim 60 - 80$ kpc from the Galactic center ([Drake et al. 2013a,b](#); [Zinn et al. 2014](#); [Torrealba et al. 2015](#), among others). Beyond ~ 80 kpc, the halo is mostly uncharted territory.

The RR Lyrae surveys suggest the halo is filled with substructures (clumps of elevated stellar density) which are usually interpreted as debris from destroyed satellite galaxies. This substructure overlies a smooth component in the distribution of RR Lyrae stars, whose number density is well-described by a power law in galactocentric distance, steepening at radii $\gtrsim 30$ kpc ([Zinn et al. 2014](#)). Thus, beyond ~ 60 kpc, few field RR Lyrae stars are expected. However, we presume that any RR Lyrae star beyond this distance may be part of either debris material or distant low-luminosity satellite galaxies that have been escaped detection until now ([Sesar et al. 2014](#); [Baker & Willman 2015](#)). LCDM models predict debris as far as 0.5 Mpc from the galactic center This is the territory that will be explored by LSST.

2. Red giant stars can similarly be used to trace the structure of the halo up to large distances. They have the advantage of being bright and are numerous compared to the RR Lyrae stars.

3. Main sequence stars, although less luminous than RR Lyraes or Red Giants, are so much more numerous that statistical studies can be pursued in a manner not generally possible for those populations. Using the technique of photometric metallicities ([Ivezić et al. 2008](#)), the Sloan Digital Sky Survey (SDSS) provided unprecedented maps of the metallicity distribution up to ~ 10 kpc from the Galactic center, unveiling not only the mean metallicity distribution of the halo but also, sub-structures within the halo. LSST will extend these studies all the way to the outermost parts of the Galaxy.

Target measurements and discoveries

Accurate measurement of these three tracer populations implies the following requirements:

1. RR Lyrae stars: These are bright horizontal-branch variable stars with periods between 0.2 to 1.0 days and large amplitudes, particularly in the bluer bandpasses (g amplitudes 0.5–1.5 mag). [Oluseyi et al. \(2012\)](#) made an intensive search for RR Lyrae stars in simulated LSST data and reached to the conclusion that this type of stars can be recovered to distances ~ 600 kpc. A similar procedure can now be performed using MAF to directly compare LSST cadence scenarios to each other. Chapter 5 discusses the discovery metrics for variable stars including RR Lyrae stars. However, optimal recovery may involve more complex metrics involving the simultaneous use of multi-band time series ([VanderPlas & Ivezić 2015](#); [Vivas et al. 2016](#)). Besides recovery of variable stars, stars, red-wavelength mean magnitudes z and y are particularly valuable since they provide the most accurate distance indicators. ([Cáceres & Catelan 2008](#)).
2. Main sequence stars: lacking any distinguishable variability, the challenge in selecting a large and clean sample of main sequence stars comes from tremendous number of small and nearly-unresolved galaxies present at faint magnitudes. Precise star/galaxy separation is thus the limiting factor on the useful depth of the main sequence sample. In addition to identifying dwarfs, using dwarfs to map the metallicity distribution of the halo requires precise u -band data, since it exhibits the strongest metallicity dependence of the LSST filters.
3. Red Giants: due to their intrinsic luminosity, the Red Giants will sample a far larger volume than main sequence stars at similar apparent magnitudes. However, they must first be identified and separated from the very numerous main sequence stars present in the foreground. A gravity-sensitive photometric index can be used for separating efficiently giants from dwarfs. The u -band magnitude is essential for such an index, so the behavior of the u -band limiting magnitude must therefore be charted under the various observational strategies under consideration. [Figure 4.11](#) shows the distance that can be reached by M-giants of different metallicities assuming limiting magnitude $u = 26.0$.

Metrics

Star-Galaxy Separation: For main sequence stars, the useful depth of the survey will likely not be the photometric detection limit, but will instead be set by the ability to differentiate stars from unresolved background galaxies. Towards faint magnitudes the contamination by galaxies worsens significantly for several reasons: the number of galaxies is rising substantially, the angular size of galaxies is shrinking, and our ability to distinguish stars from marginally resolved galaxies diminishes for faint sources simply due to photon statistics. While the fundamental properties of the contaminant sources are beyond our control, our ability to reject these sources depends on survey parameters which do vary with the choice of observing strategy, such as the distribution of seeing across visits and the depth of these visits.

We are currently in the process of developing a metric that will estimate our ability to separate stars and galaxies for any observation depth and seeing conditions. This requires both an understanding of how images of a source are measured and classified as either a star or galaxy, and how the population of stars and galaxies vary in number and size (for galaxies) with depth. Our model uses the distribution of galaxies in size and number, derived from HST COSMOS observations, along with a fully Bayesian model decision formalism to compute the expected completeness and

contamination in star-galaxy separation. Computationally, for each position in the survey footprint we interpolate the results from that work on a grid in seeing, galaxy size, and coadd depth, then integrate over the distribution of galaxy sizes. This modeling process is currently being verified against existing surveys, and will be incorporated into the observing strategy study at a later date.

Some of the higher-level figures of merit described below will depend on this star/galaxy separation diagnostic metric.

Distance to the farthest RR Lyrae stars: This metric charts our ability to recover an RR Lyrae star from LSST data as a function of its distance. An RR Lyrae star may be considered as recovered if its period and amplitude are within 10% of the intrinsic values. The procedure followed by [Oluseyi et al. \(2012\)](#) is a good example on how this can be achieved. They built a large number of synthetic light curves spanning the properties of known RR Lyrae stars and “observed” them with the cadence given by the OpSim runs available at that time. Anticipated improvements over this previous work include the use of simultaneous multi-band information to recover periods (e.g., [VanderPlas & Ivezić 2015](#); [Vivas et al. 2016](#)).

However, a first look into this problem using MAF can be achieved by simplifying the procedure and only test if a star with period 0.55 days (the mean period for RR Lyrae stars) can be recovered by metrics already available in MAF. Then, distance can be calculated using the mean magnitude of the recovered RR Lyrae stars (in the reddest bands available to LSST) and the interstellar extinction at that point of the sky (maps are available now in MAF). This metric should compute the largest distance that can be measured with a 10% precision at which certain percentage of RR Lyrae stars (eg. 80%) can be recovered by LSST. It is expected that the results of this metric at low galactic latitudes will be largely dependent on the chosen observational strategy (through variations in cadence towards the Plane).

A reasonable Figure of Merit for this sub-project is the volume of the halo within RR Lyrae stars can be recovered. Similarly, another Figure of Merit would be the fraction of the Galactic thick disk’s volume that can be traced by RR Lyrae stars.

Distance to the farthest main sequence stars and giant stars: Since variability is not the signal property for these tracer populations, metrics are somewhat simpler than for the RR Lyrae. Here the distance metric requires the determination of the limiting *u*-band magnitude for which galaxy/star separation is reliable to a certain level. In these cases, distances depend on metallicity. Then, a figure of merit is the volume of the halo mapped with stars within a specified metallicity range.

Go to: • [the start of this section](#) • [the start of the chapter](#) • [the table of contents](#)

4.4.3 Other Ideas

Will Clarkson, Kathy Vivas, Victor Debattista

In this final section we provide an extremely brief list of important science cases that are still in an early stage of development, but that are deserving of quantitative MAF analysis in the future:

- *Formation history of the Bulge and present-day balance of populations:* Sensitivity to metallicity and age distribution of Bulge objects near the Main Sequence Turn-off;

- *Migration and heating in the Milky Way disk:* Error and bias in the determination of components in the (velocity dispersion vs metallicity) diagram, for disk populations along various lines of sight (e.g. Loebman et al. 2016 ApJ 818 L6);
- Fraction of Local-Volume objects discovered as a function of survey strategy.

Go to: • [the start of this section](#) • [the start of the chapter](#) • [the table of contents](#)

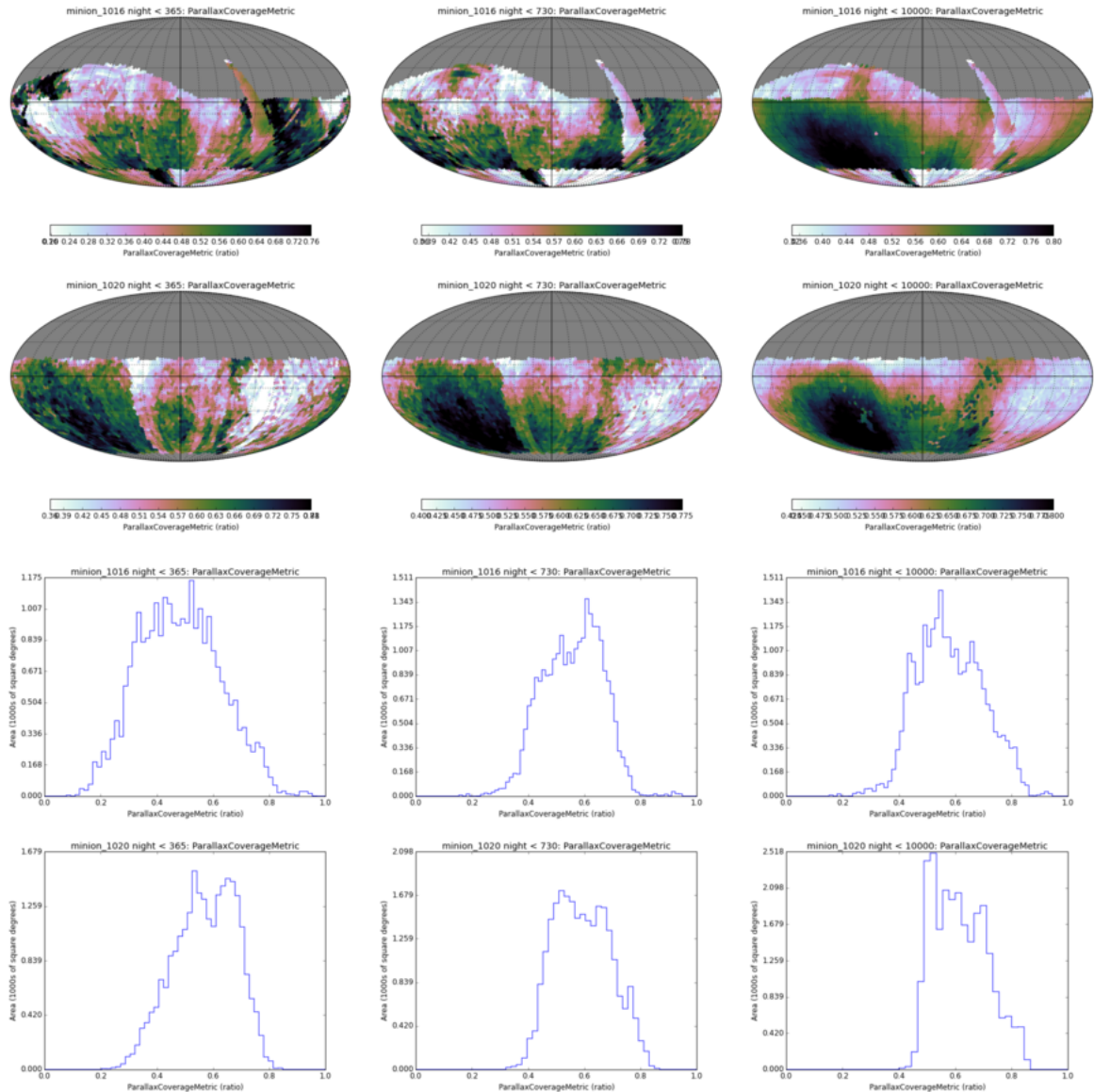


Figure 4.2: Parallax coverage achieved at different epochs within the survey. *Top and Third row:* OpSim run **minion_1016**. *Second and bottom row:* OpSim run **minion_1020** (PanSTARRS-like cadence). Reading left-right, columns represent: *Left column:* all observations within the first 365 days of operation; *Middle column:* first two years; *right column:* the full 10-year survey. Spatial maps are clipped at 95%, with histogram horizontal scale set to ± 1.0 for easy comparison.

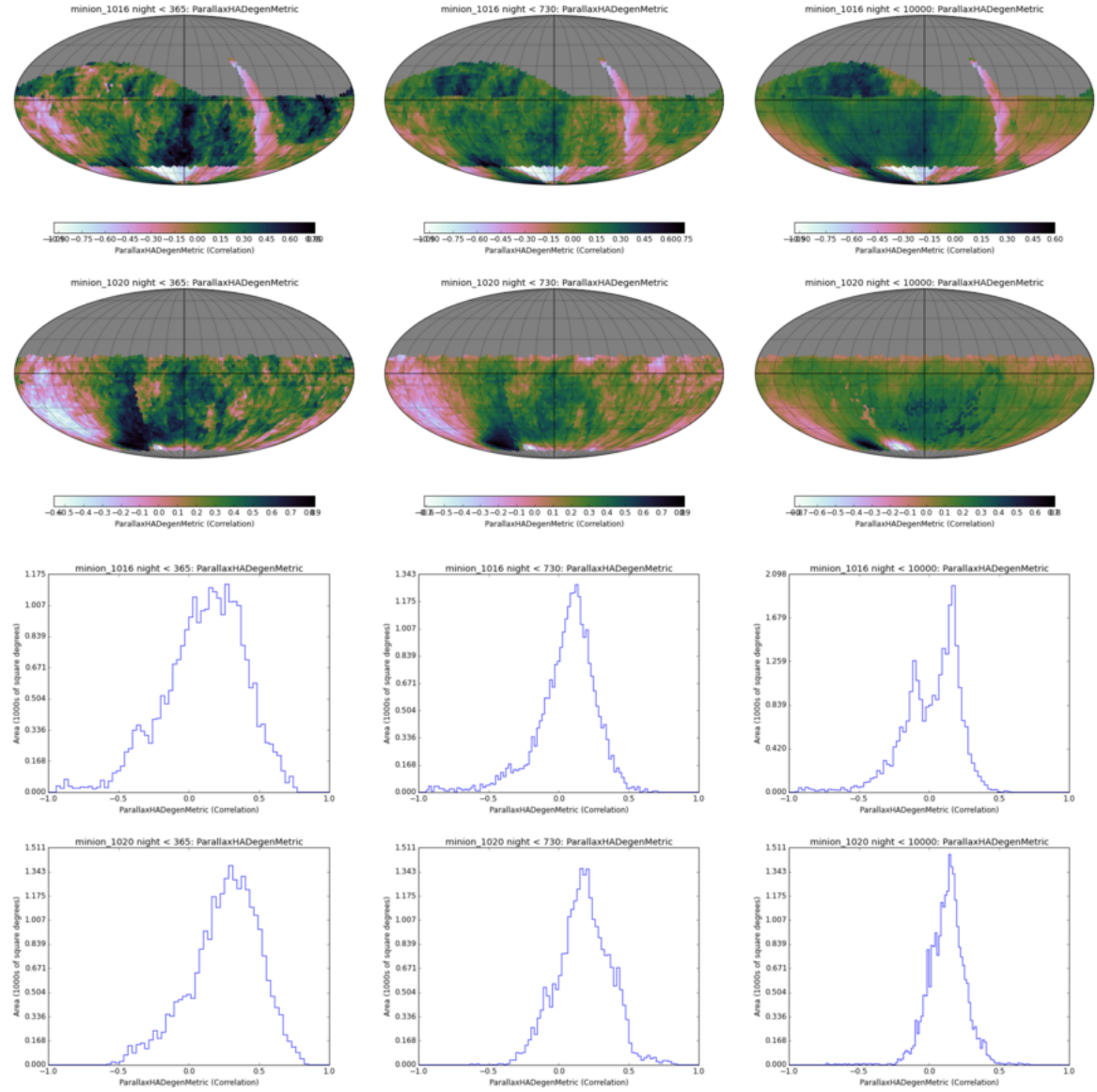


Figure 4.3: Parallax degeneracy with hour angle for different epochs within the survey. *Top and Third row:* OpSim run `minion_1016`. *Second and bottom row:* OpSim run `minion_1020` (PanSTARRS-like cadence). Reading left-right, columns represent: *Left column:* all observations within the first 365 days of operation; *Middle column:* first two years; *right column:* the full 10-year survey. Spatial maps are clipped at 95%, with histogram horizontal scale set to the range 0.0 – 1.0.

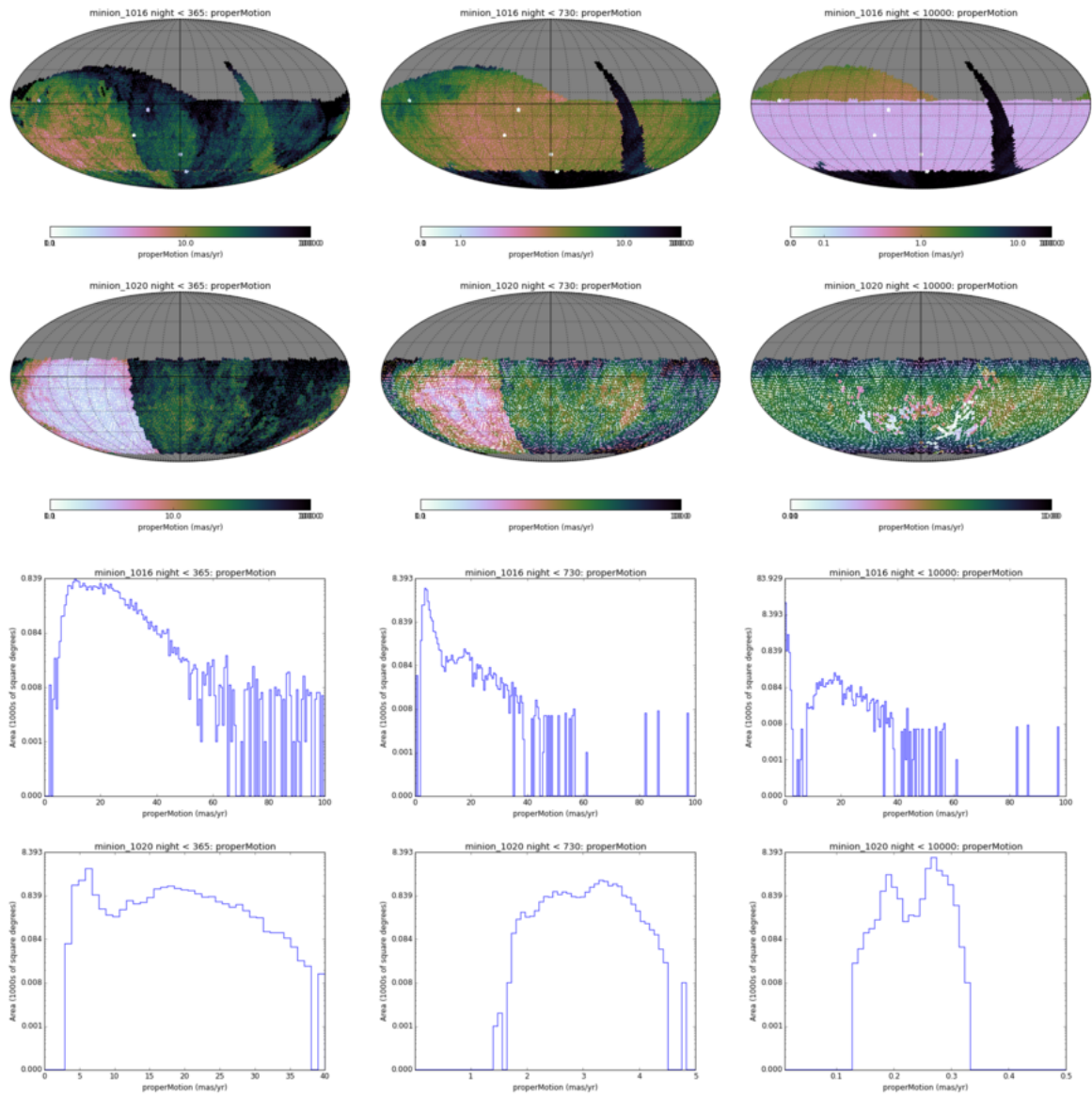


Figure 4.4: Proper motion error for a star at $r = 21.0$, for different epochs within the survey. Crowding errors are ignored. *Top and Third row:* OpSim run [minion_1016](#). *Second and bottom row:* OpSim run [minion_1020](#) (PanSTARRS-like cadence). Reading left-right, columns represent: *Left column:* all observations within the first 365 days of operation; *Middle column:* first two years; *right column:* the full 10-year survey. Spatial maps are clipped at 95% and a log-scale is used for the maps and histograms. NOTE: the horizontal axes in the histograms are different for the two strategies; this is to allow the long tail of the proper motion error distribution in the [minion_1016](#) to be displayed.

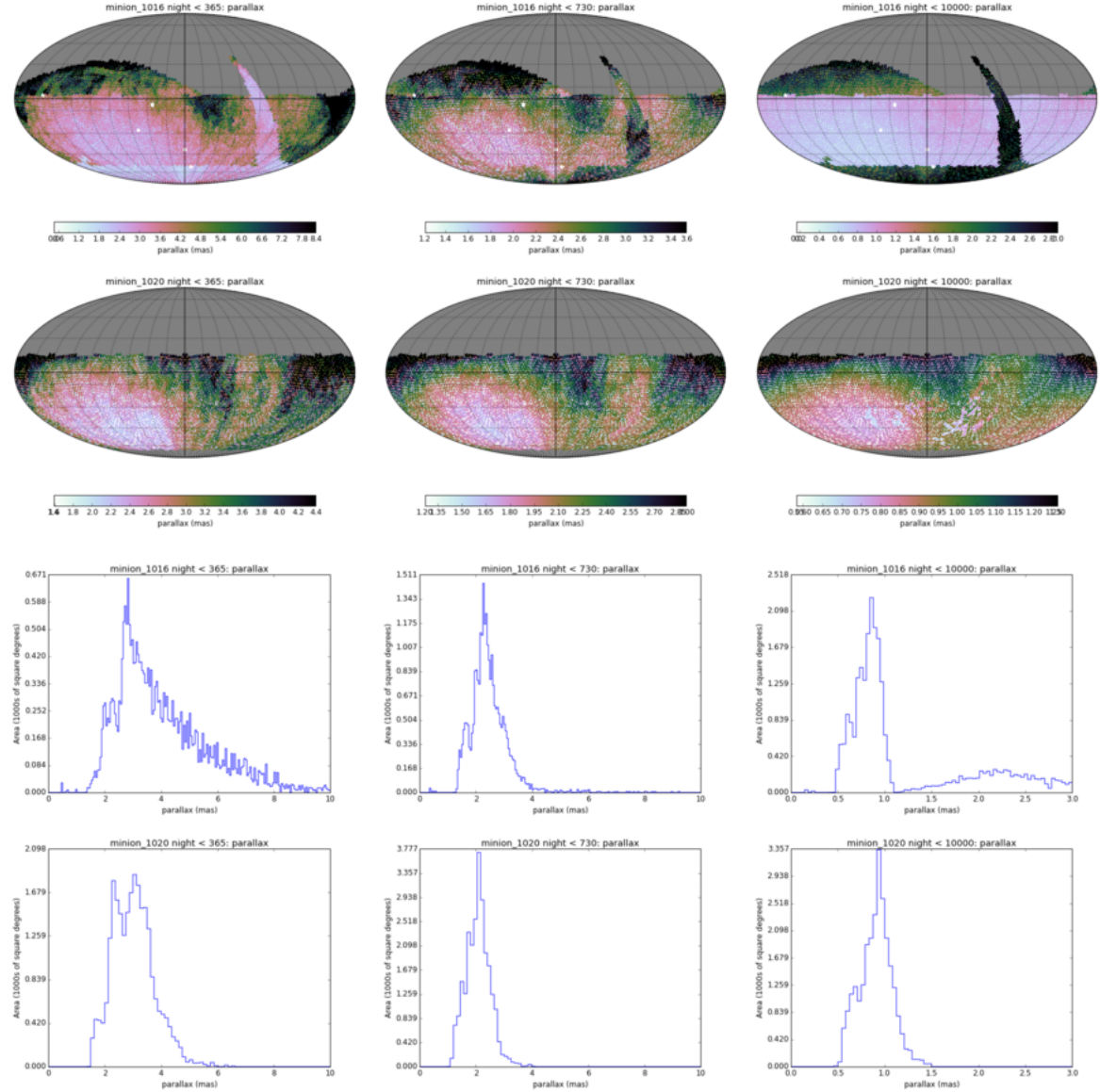


Figure 4.5: Parallax error for a star at $r = 21.0$, for different epochs within the survey. Crowding errors are ignored. *Top and Third row:* OpSim run **minion_1016**. *Second and bottom row:* OpSim run **minion_1020** (PanSTARRS-like cadence). Reading left-right, columns represent: *Left column:* all observations within the first 365 days of operation; *Middle column:* first two years; *right column:* the full 10-year survey. Spatial maps are clipped at 95%.

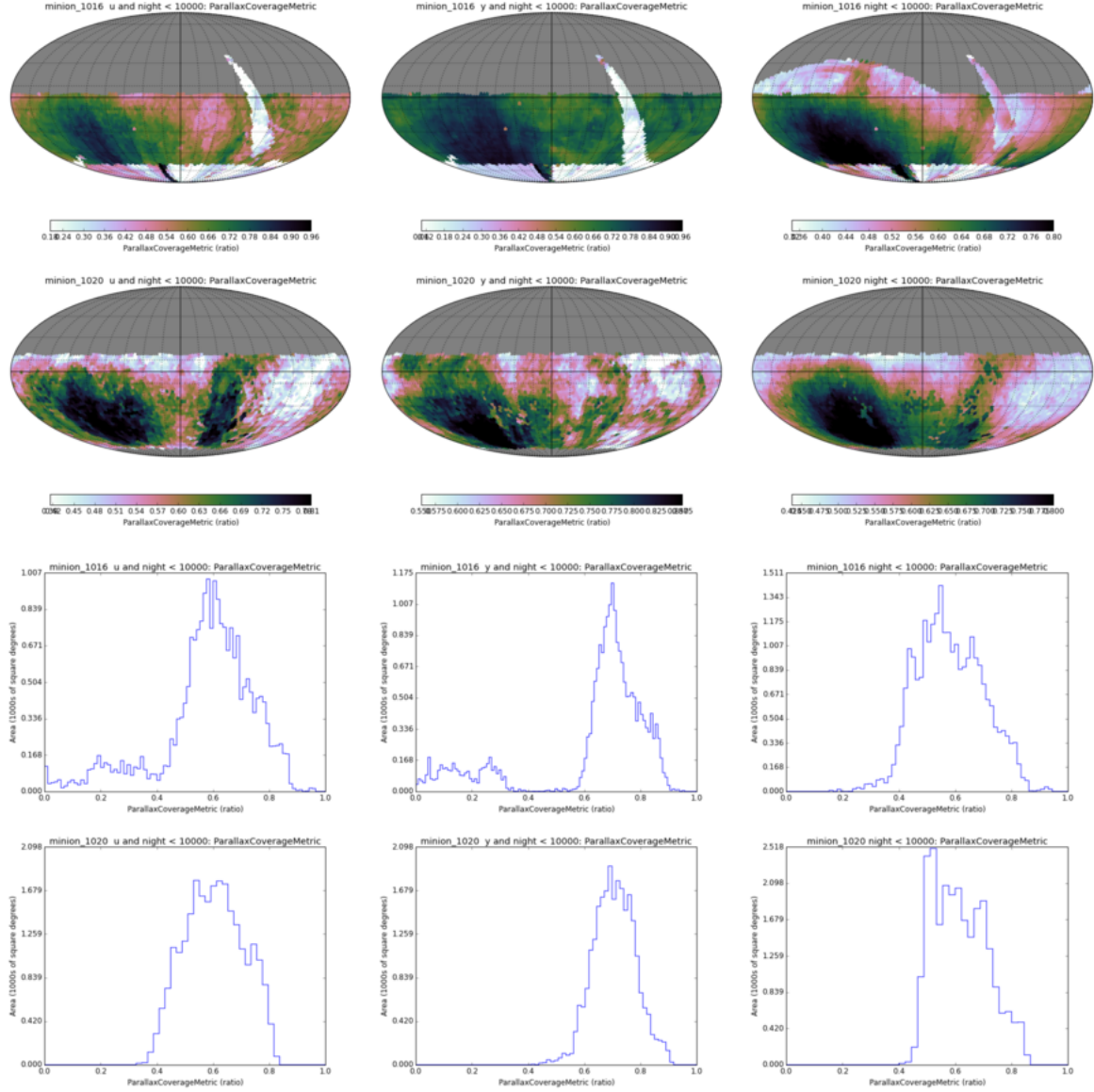


Figure 4.6: Parallax coverage achieved for three extremes of object color, over the full 10-year survey. *Top and Third row:* OpSim run `minion_1016`. *Second and bottom row:* OpSim run `minion_1020` (PanSTARRS-like cadence). Reading left-right, columns represent: *Left column:* Objects detected only in the bluest filter; *Middle column:* objects detected only in the reddest filter; *Right column:* objects detected in all filters. Spatial maps are clipped at 95%, with histogram horizontal scale set to ± 1.0 for easy comparison.

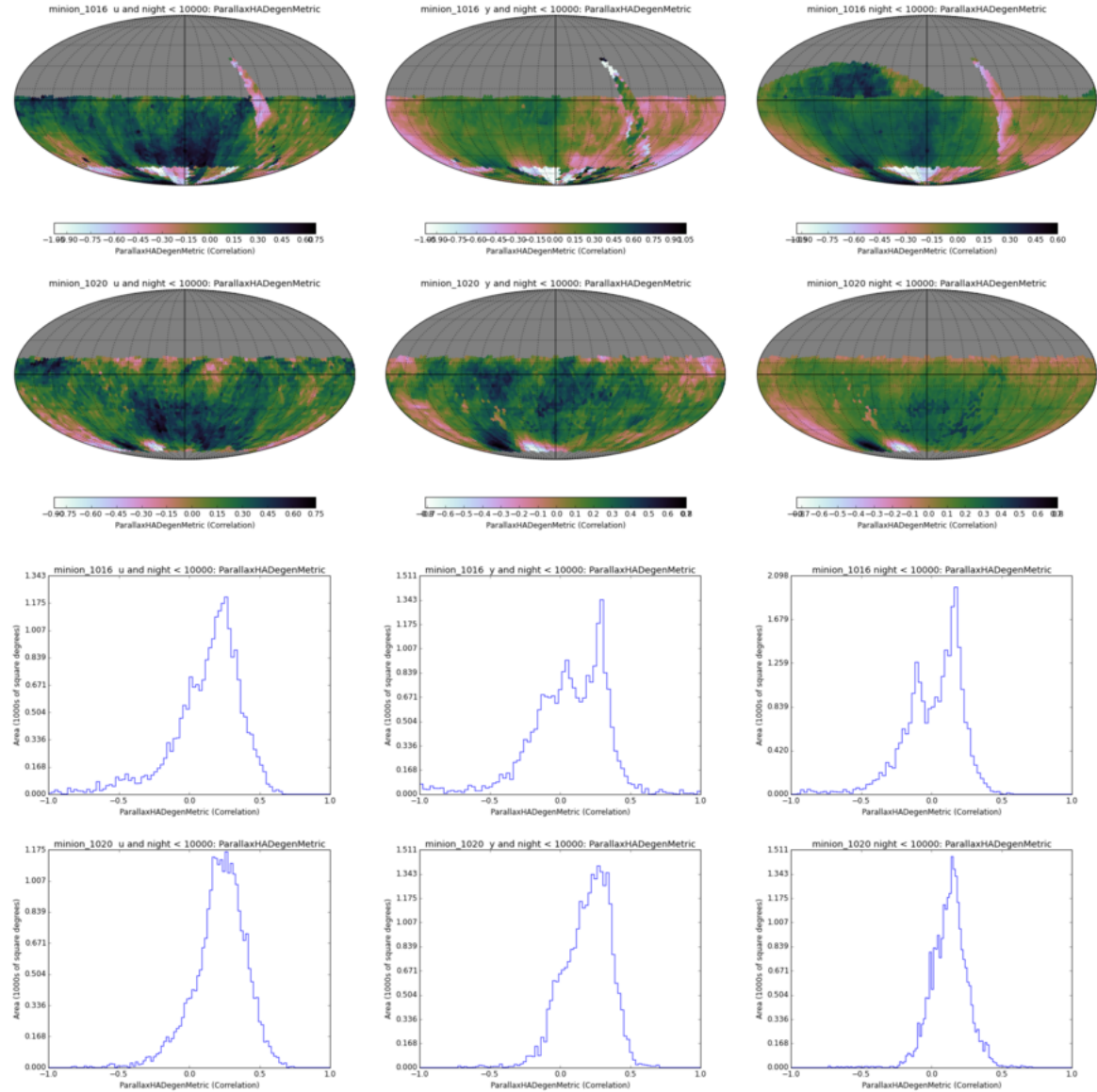


Figure 4.7: Parallax degeneracy with hour angle, selecting filters for three extremes of object color, over the full 10-year survey. *Top and Third row:* OpSim run **minion_1016**. *Second and bottom row:* OpSim run **minion_1020** (PanSTARRS-like cadence). Reading left-right, columns represent: *Left column:* Objects detected only in the bluest filter; *Middle column:* objects detected only in the reddest filter; *Right column:* objects detected in all filters. Spatial maps are clipped at 95%, with histogram horizontal scale set to the range 0.0 – 1.0.

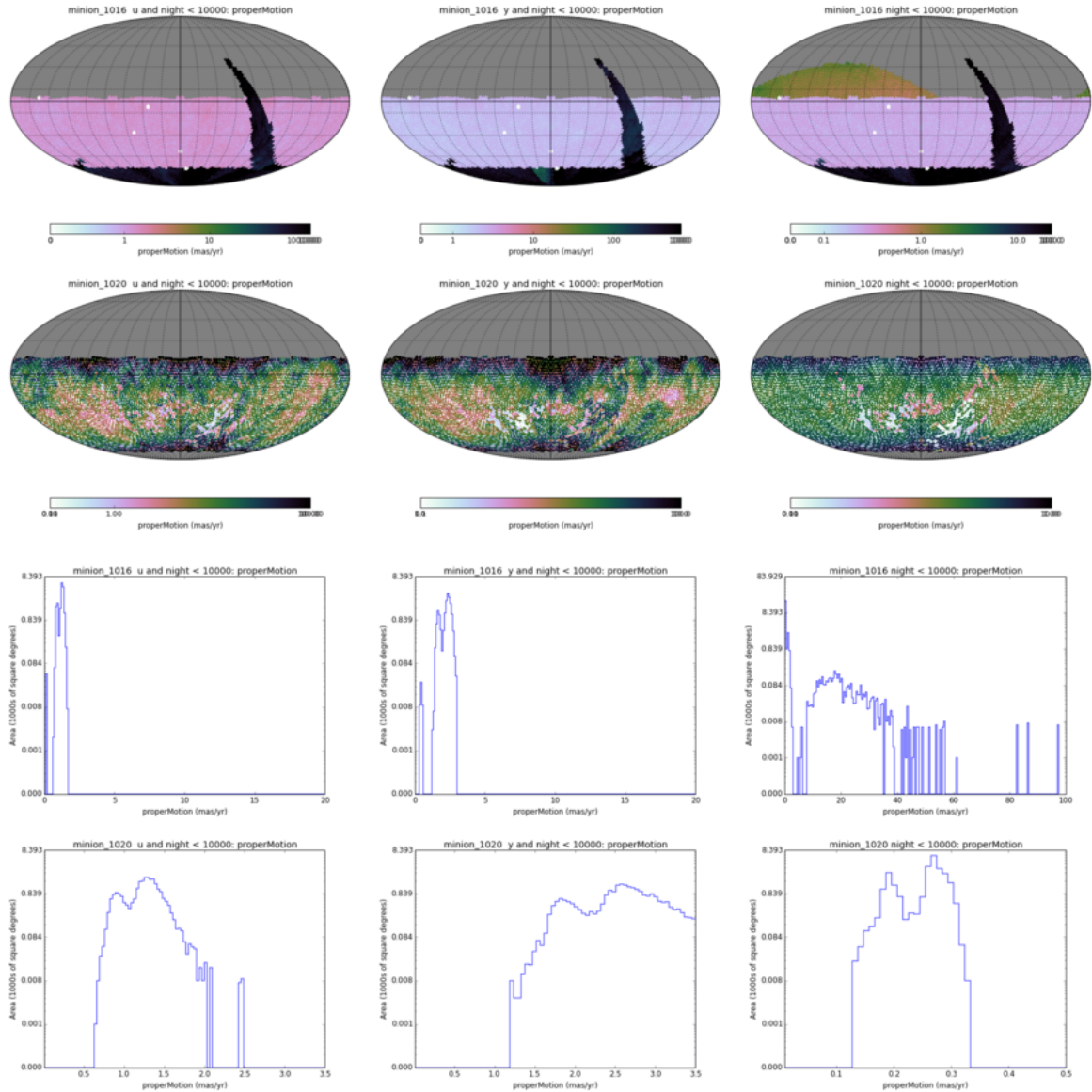


Figure 4.8: Proper motion error for a star at apparent magnitude $m = 21.0$, for three extremes of object color and assessed over the full survey. Crowding errors are ignored. *Top and Third row:* OpSim run [minion_1016](#). *Second and bottom row:* OpSim run [minion_1020](#) (PanSTARRS-like cadence). Reading left-right, columns represent: *Left column:* Objects detected only in the bluest filter; the fiducial object has apparent magnitude $u = 21.0$; *Middle column:* objects detected only in the reddest filter (so $y = 21.0$); *Right column:* objects detected in all filters (using $r = 21.0$ and a “flat” spectrum within `sims_maf`). Spatial maps are clipped at 95% and a log-scale is used for both the spatial maps and histograms. NOTE: the horizontal axes in the histograms are different for the two strategies; this is to allow the long tail of the proper motion error distribution in the [minion_1016](#) to be displayed. Horizontal scales on histograms may need adjusting.

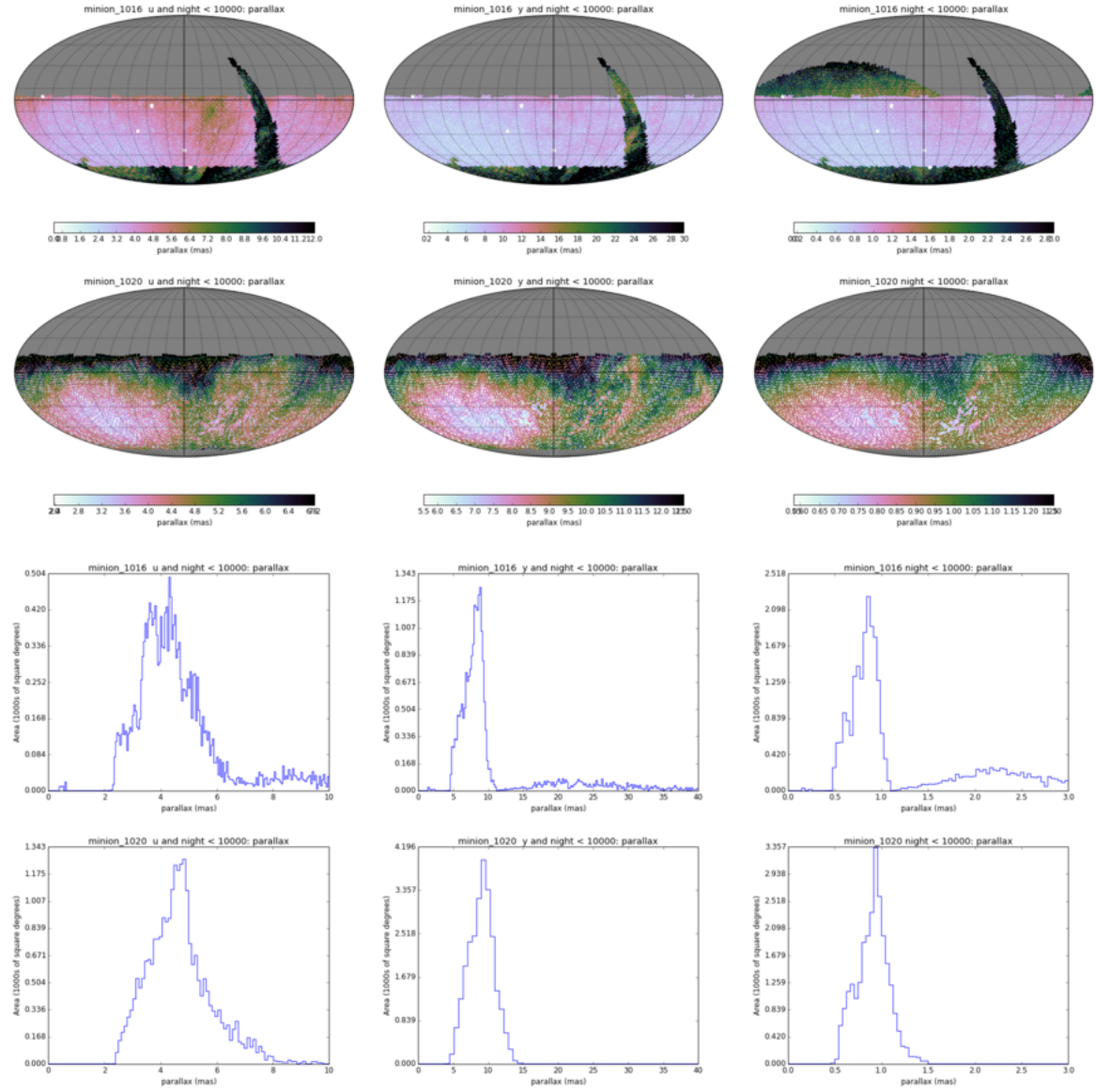


Figure 4.9: Parallax error for a star at apparent magnitude $m = 21.0$, for three extremes of object color and assessed over the full survey. Crowding errors are ignored. *Top and Third row:* OpSim run `minion_1016`. *Second and bottom row:* OpSim run `minion_1020` (PanSTARRS-like cadence). Reading left-right, columns represent: *Left column:* Objects detected only in the bluest filter; the fiducial object has apparent magnitude $u = 21.0$; *Middle column:* objects detected only in the reddest filter (so $y = 21.0$); *Right column:* objects detected in all filters (using $r = 21.0$ and a “flat” spectrum within `sims.maf`). Spatial maps are clipped at 95%.

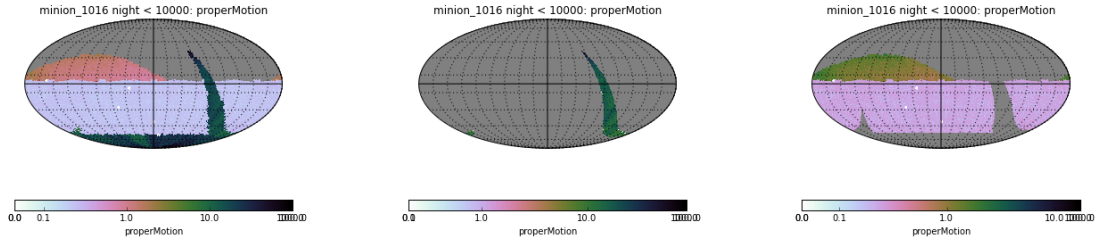


Figure 4.10: Selection regions for the Astrometry Figures of Merit (FoMs) 1.1-1.4. Figures of Merit 1.1 and 1.3 refer to the “main survey” region shown in the middle panel (which for the FoM also avoids the region of the South Galactic Pole). The right panel shows the inner Plane region to which FoMs 1.2 & 1.4 refer. The left-hand panel shows the entire survey region for reference. This example shows run [minion_1016](#). See Table 4.7 and Section 4.3.2.

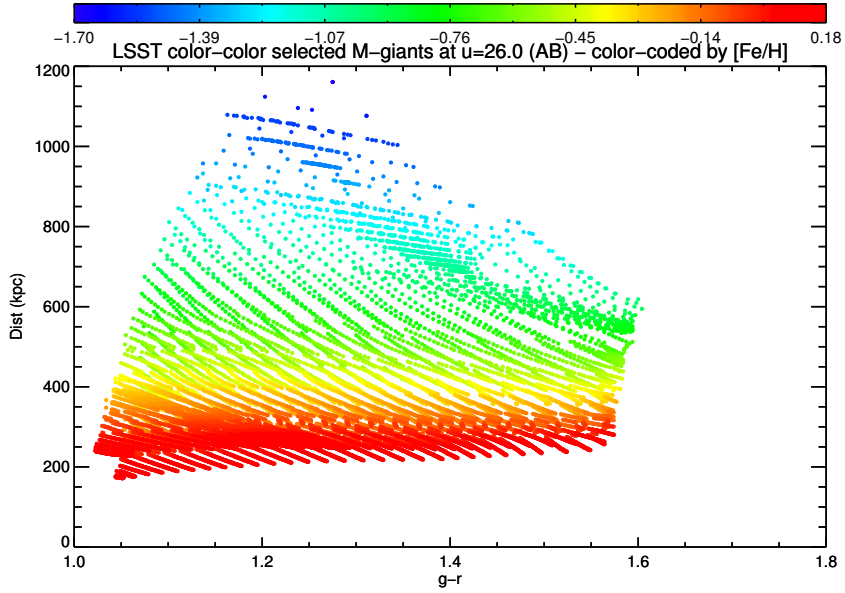


Figure 4.11: Distance to which red giant stars can be identified in the galactic halo assuming a limiting magnitude of $u=26.0$. The color code scales with the metallicity of the stars. More metal-poor stars can be detected to farther distances.

5 Variable Objects

Chapter editors: *Ashish Mahabal, Lucianne Walkowicz*.

Contributing authors: *Michael B. Lund, Stephen Ridgway, Keaton J. Bell, Patrick Hartigan, C. Johns-Krull, Peregrine McGehee, Shashi Kanbur*

5.1 Introduction

Variable objects are defined as those that exhibit brightness changes, either periodic or non-periodic, which are detected in quiescence and non-destructive to the object itself. Variable objects span a wide range in timescale-of-interest (sometimes even within a single class of objects), and so different science cases benefit from different sampling strategies. These strategies may be significantly disparate from one another, sometimes even mutually exclusive; competing objectives described in this chapter and the next are therefore at the heart of LSST observing strategy and cadence design.

Below we develop a number of key science cases for LSST studies of variable objects, associating them with related metrics that can be used within the Metrics Analysis Framework (MAF) to understand the impact of a given survey strategy realization on the scientific results for that case. The science cases outlined are by no means exhaustive, but rather are motivated by providing key quantitative examples of LSST’s performance given any particular deployment of survey strategy. The authors encourage community contribution of similar cases, where the scientific outcome can be quantified using specific metrics.

Periodic Variable Type	Examples of target science	Amplitude	Timescale
RR Lyrae	Galactic structure, distance ladder, RR Lyrae properties	large	day
Cepheids	Distance ladder, cepheid properties	large	day
Long Period Variables	Distance ladder, LPV properties	large	weeks
Short period pulsators	Instability strip, white dwarf interior properties, evolution	small	min
Periodic binaries	Eclipses, physical properties of stars, distances, ages, evolution, apsidal precession, mass transfer induced period changes, Applegate effect	small	hr-day
Rotational Modulation	Gyrochronology, stellar activity	small	days
Young stellar populations	Star and planet formation, accretion physics	small	min-days

5.2 The Cepheid Mass-Luminosity Relation

Classical Cepheids begin to pulsate once they evolve up the giant branch and execute blueward loops on the HR diagram that take them into the Instability Strip. Cepheid masses and luminosities in the instability strip are connected through the Mass-Luminosity (ML) relation. This ML relation is strongly dependent on stellar evolution physics. Canonical/Non-canonical ML relations arise from varying treatments of convective core overshoot and mass loss ([Brocato & Castellani 1992](#); [Bono et al. 2000](#); [Marconi et al. 2013](#)).

Stellar pulsation models adopt a given ML relation and then compute a theoretical light curve for a range of different temperatures and metallicities. This theoretical light curve can then be transformed into LSST wavebands using stellar atmospheres (B20 and references therein) and quantitatively compared to observed LSST light curves through Fourier decomposition of the form

$$V = A_0 + \sum_{k=1}^{k=N} (A_k \cos(k\omega t) + \phi_k),$$

where $\omega = 2\pi/P$, with P the period, N is the order of the fit. The coefficients $R_{k1} = A_k/A_1$ and $\phi_{k1} = \phi_k - k\phi_1$ can be computed for both theoretical and LSST observed light curves. These coefficients are sensitive to the adopted *ML* relation and other global parameters such as metallicity and effective temperature. By utilizing such a decomposition, the multiwavelength light curves that the LSST will produce for both Cepheids and RR Lyraes can rigorously constrain Cepheid and RR Lyrae global stellar parameters such as the *ML* relation. Of course, knowledge of the *ML* relation through this approach can then lead to another “theoretical” distance scale using both Cepheids and RR Lyrae. However, in the case of Cepheids, given good enough cadence in LSST bands and thus an accurate Fourier decomposition with precisely known Fourier parameters, it will be possible to discriminate between canonical and non-canonical *ML* relations and thus provide constraints for stellar evolution physics. *A good Figure of Merit for this science case would be one based on the precision with which we can infer the parameters of these relations.*

[Bhardwaj et al. \(2014\)](#) describes in detail the way the quantitative structure of Cepheid and RR Lyrae light curves vary with period and optical band. Given appropriate cadence, LSST light curves will provide accurate Fourier decompositions at multiple wavelengths that can significantly augment these results and provide an important database with which to connect quantitative aspects of Cepheid and RR Lyrae light curve structure to pulsation envelope physics. Two examples are the following.

- 1) RRab stars found in stripe 82 of the SDSS exhibit a flat PC relation at minimum light at certain SDSS colors but not at others. LSST observations of RRab stars will be able to augment this result and investigate if there are any links to the structural properties of observed light curves.
- 2) Short period ($\log P \leq 0.4$) FU Cepheids in the SMC exhibit a noticeable break in their $(V - I)$ PC relation at certain phases of pulsation phases. At the same period, the Fourier parameter R_{21} displays a strong turnover. LSST data will be important in seeing if this result extends to LSST colors.

Bhardwaj et al. (2014, 2015, and references therein) have clearly demonstrated how Cepheid and RR Lyrae Period-Color(PC)/Period-Luminosity (PL)/ Period-Wesenheit(PW)/Period-Luminosity-Color(PLC) relations vary significantly both as a function pulsation phase and period and observation band. The LSST database on Cepheids and RR Lyraes will provide an excellent database to further investigate the variation of these relations with pulsation phase with a view to understanding pulsation physics and constraining theoretical models. Currently, the literature only discusses these relations at mean light, that is the average over pulsation phase. Yet this averaging process clearly masks some dependencies: there are pulsation phases with very high/low PL/PC dispersion and there are some phases where the relation is highly nonlinear. In the era of precision cosmology, it is important to understand the tools that we use to construct a distance scale. The LSST database on Cepheids and RR Lyraes will be an important database with which to investigate the multiphase properties of PL/PC/PW/PLC relations.

What cadence is required for “accurate multiwavelength Fourier decomposition”? Probably more opsim experiments are required but one way forward is to consider a cadence and then simulate observed light curves with this cadence, Fourier analyze these light curves with errors on Fourier parameters (Petersen 1980) and the compare with a preliminary grid of theoretical model light curves.

5.2.1 Description of Relevant Metrics

Despite the range in scientific motivation for the cases presented in this chapter, there are some common metrics that are widely applicable (or may be combined in a variety of ways with other metrics to suit a variety of applications). [The present science case provides as good a venue as any in which to introduce these common metrics.](#)

Metric	Description
Eclipsing/transiting system discovery	Fraction of discoveries vs fractional duration of eclipse
Lightcurve shape recovery	...
Phase gap	Histogram vs period of the median and maximum phase gaps achieved in all fields
Period determination (period dependent)	Fraction of targets vs survey duration, for which the period can be determined to 5-sigma confidence
Period variability (period dependent)	Fraction of targets vs survey duration, for which a period change of 1% can be determined with 5-sigma confidence

The ability to identify that an object is periodic, and to correctly determine that object’s period, are widely applicable measures of discovery. In the case of regular variables (as outlined below), these two measures together can uniquely identify a population. Other kinds of periodic systems (transiting planets for example) also require a measurement of periodicity, but have a much wider range of relevant periods, and looser requirements on the strictness of that periodicity.

Lund et al. (2015; <http://arxiv.org/pdf/1508.03175.pdf>) discuss three *diagnostic* metrics that have been incorporated into the MAF. Two of these metrics deal explicitly with time variable behavior: a) observational triplets, and b) detection of periodic variability.

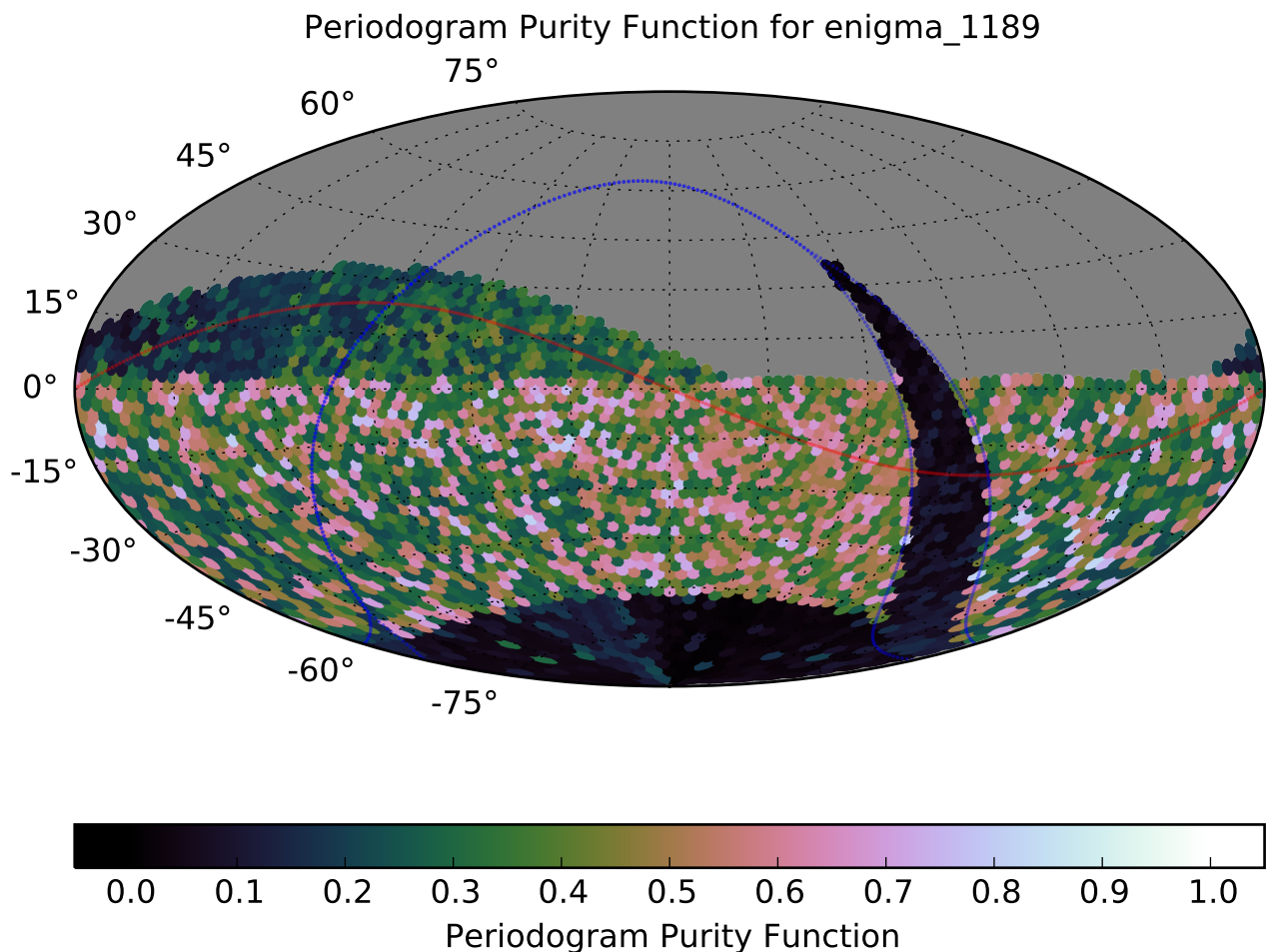


Figure 5.1: The value for the Periodogram Purity Function for candidate Baseline Cadence `minion_1016`. The Periodogram Purity Function provides a measure of the power lost due to aliasing.

Periodogram purity function (PeriodicMetric)

This metric calculates the Fourier power spectral window function of each field (Roberts et al. 1987) as a means of quantifying the completeness of phase coverage for a given periodic variable. The periodogram purity is defined as 1 minus the Fourier power spectral window function. in the

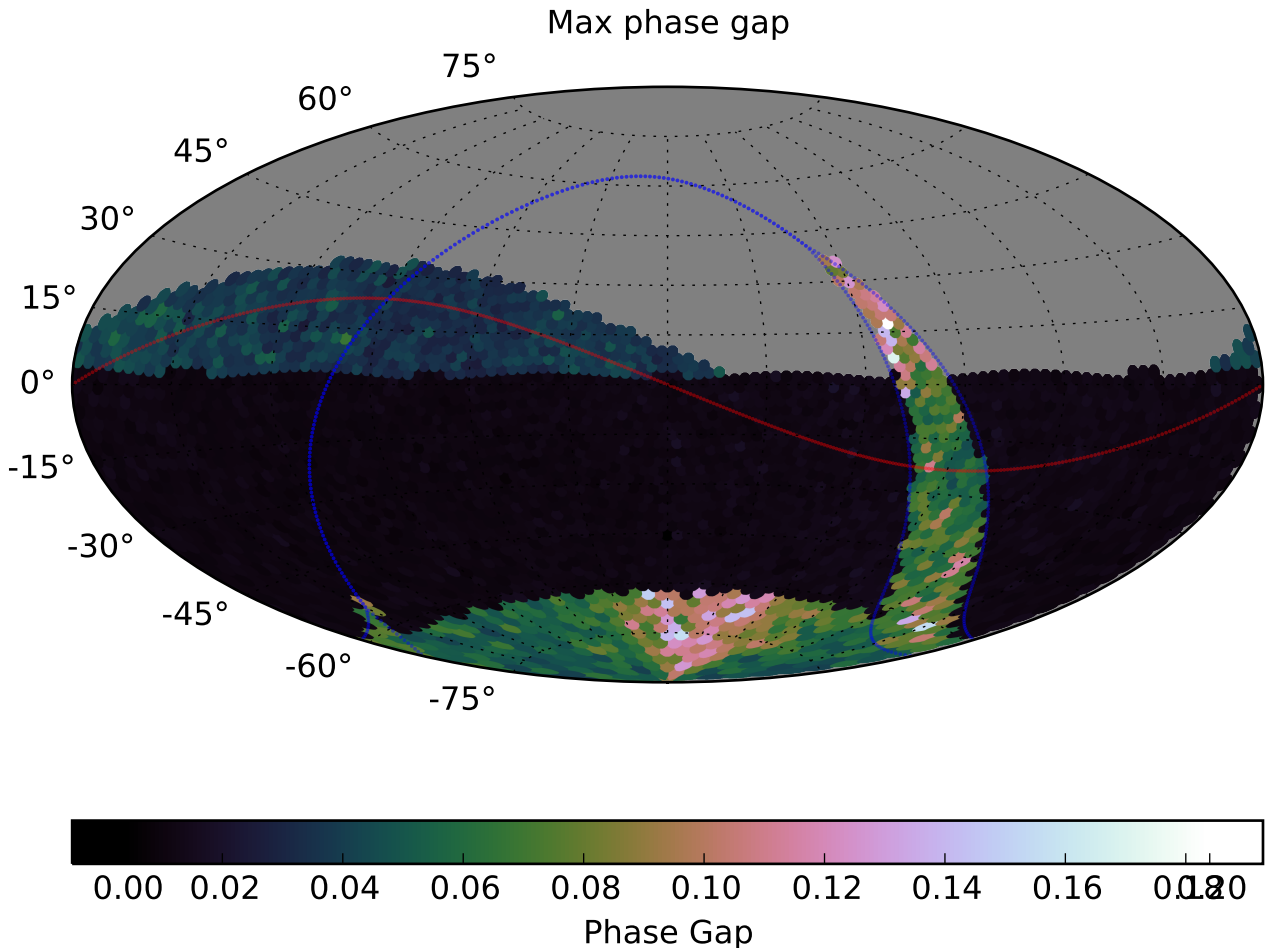


Figure 5.2: The median phase gap for candidate Baseline Cadence [minion_1016](#). The PhaseGapMetric looks at periods between 3 and 35 days by default.

perfect case, all power in the window function is concentrated in a delta function at zero, and is zero at all other frequencies. As power “leaks” away from the correct frequency as a consequence of discrete, non-ideal data sampling, the periodogram becomes more structured. For the purposes of MAF metrics, which are designed to quantify performance as a single number, the periodogram purity is quantified as the minimum value of the periodogram purity function at non-zero frequency shifts; the ideal case would be a periodogram purity metric value of 1.

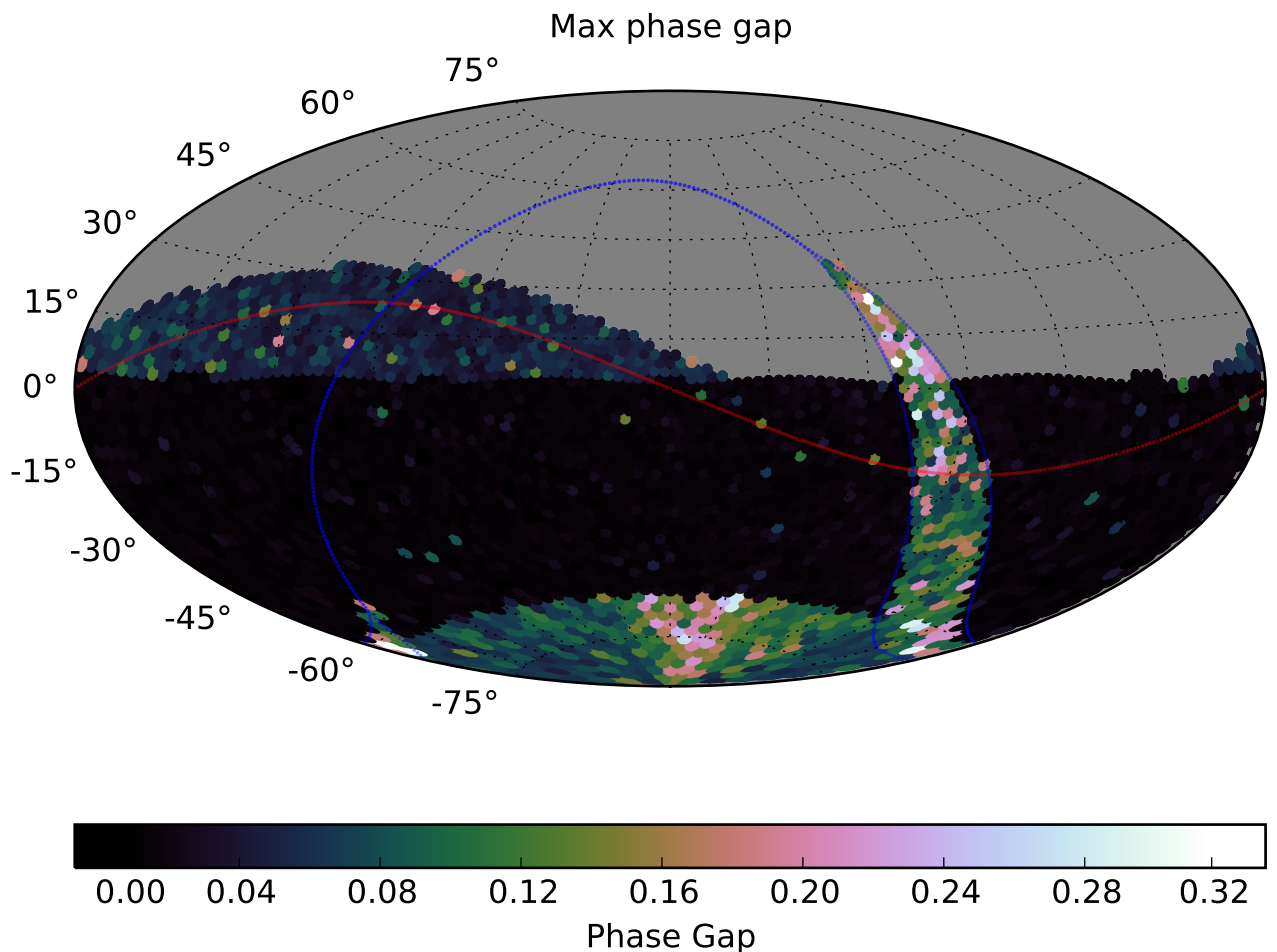


Figure 5.3: The maximum phase gap for candidate Baseline Cadence `minion_1016`. The PhaseGapMetric looks at periods between 3 and 35 days by default.

Phase Gap Metric (PhaseGapMetric)

The Phase Gap Metric is designed to examine the largest phase gaps in the observing schedule. For a given point in the sky, a series of periods are randomly selected (by default, 5 periods), with a default minimum of 3 days and maximum of 35 days. The largest phase gap for each period is calculated, and the metric plots the median (Figure 5.2) and maximum (Figure 5.3) of this subset of values that contains the maximum phase gap per period. The Phase Gap Metric is part of varMetrics.

Period Deviation Metric (PeriodDeviationMetric)

The Period Deviation Metric calculates the error in recovering the correct period of sinusoid using a given observing schedule and a Lomb-Scargle periodogram. For a given point in the sky, a series of periods are randomly selected (by default, 5 periods), and the metric returns the worst period deviation, and the period at which this occurred. The Period Deviation Metric is part of varMetrics.

5.3 Discovery of Multiperiodic, Short-Period Pulsating Variables

Keaton J. Bell

Most pulsating variable stars exhibit a superposition of multiple simultaneous pulsation modes. While these multiperiodic pulsators are observationally more complex than classical pulsators, they communicate a greater wealth of information about the stars. Global nonradial pulsations pass through and are affected by the interiors of stars, and the measured frequencies of photometric variability are eigenfrequencies of stars as physical systems. Therefore, the observation and study of photometric variability in multiperiodic pulsating stars is the most powerful method by which we can probe stellar interiors.

The current state and modern tools of the field of asteroseismology are thoroughly discussed by [Aerts et al. \(2010\)](#). The locations of the known classes of pulsating variable in the H-R Diagram are indicated in their Figure 1.12, and a summary of their general properties—including pulsation amplitudes and timescales—is provided in their Appendix A.

Sections 8.6 and 8.7 of the Science Book express the anticipated contributions that LSST will make to the study of pulsating variables. While the sparseness of observations (low duty cycle) over the LSST survey lifetime will make exact period solutions impossible for most multiperiodic, short-period pulsating variables, the Science Book correctly emphasizes that the photometric precision and multi-color information will yield detections of variability that can be treated statistically to determine the ensemble properties of different classes of pulsating star. The dependence of pulsational power on a star’s position in 5-color parameter space, as well as the relative pulsation amplitudes in different passbands, informs the least understood aspects of pulsation theory: mode selection and amplitude limiting mechanisms. A thorough statistical view of pulsating stars requires on the order of thousands of objects per type at a minimum, with robust detections of variability in multiple passbands.

5.3.1 The Case for ZZ Cetis

Of all the known classes of pulsating variable star, the ZZ Cetis (pulsating hydrogen-atmosphere white dwarfs) are the faintest, and among those with the lowest pulsation amplitudes. These will be the most difficult for LSST to detect and characterize, and they therefore provide an important benchmark for assessing the effectiveness of different proposed observing strategies for the study of pulsating stars. If LSST is well suited for ZZ Ceti science, it will be a useful tool for all classes of pulsator.

Most details of ZZ Ceti stars are not strictly relevant to this analysis, so we direct the interested reader to recent reviews by [Winget & Kepler \(2008\)](#), [Fontaine & Brassard \(2008\)](#), and [Althaus et al. \(2010\)](#).

As white dwarfs with atmospheres spectroscopically dominated by hydrogen cool to between 12,500 and 10,600 K, they are observed as the photometrically variable ZZ Cetis. The square root of the total observed pulsational power (intrinsic root-mean-squared signal) in these objects is on the order of 1% and the mean pulsation periods are ~ 10 min ([Mukadam et al. 2006](#)). Because the pulsation periods are \ll the typical LSST revisit time, the survey will sample the pulsations randomly in phase.

The ability to detect pulsations relies on the recognition that scatter in the flux measurements significantly exceeds what can be attributed to noise. LSST’s sensitivity to these pulsations depends on two things: the photometric precision and the total number of measurements. By affecting these survey characteristics, the choice of observing strategy impacts LSST’s success in its goal of exploring the variable universe. Strategies that maximize photometric precision and total number of visits in all filters optimize the survey toward this goal, but the tradeoffs between these dual requirements are complicated and must be explored in MAF to be understood.

While consideration of observations across all filters together provides the greatest sensitivity to detecting overall variability, the detection of pulsational power in individual filters serves the science needs for pulsating stars best. Since LSST will not measure the specific periods of complex, multi-periodic pulsating stars (at least not in the main survey), LSST’s potential to contribute significantly to this field lies in the ability to measure relative pulsation power across many passbands. For ZZ Cetis in particular, there is a strong dependence of the relative amplitudes measured in different filters on the geometry of the pulsations—specifically the spherical degrees, ℓ , of the spherical harmonic wave patterns associated with the pulsation modes. Determining the ℓ values associated with individual modes is essential for comparing measured pulsation frequencies with those calculated for asteroseismic stellar models. The difficulty in determining ℓ is currently the greatest limitation on white dwarf asteroseismology. LSST has the potential to statistically constrain the relative contributions of modes of different ℓ values to the overall photometric variations. The calculations by [Brassard et al. \(1995\)](#) of relative pulsation amplitudes in different filters show that measuring the amplitude in the u band is essential for gaining leverage on this problem.

5.3.2 Metrics

We have developed a custom MAF metric that calculates a “variability depth” for every point on the sky equal to the magnitude limit for detecting a population of photometric variables with a given root-mean-squared (r.m.s.) underlying signal to a desired level of completeness and contamination. The metric makes the simplifying assumptions that the typical revisit time for a field is longer than the pulsation periods (appropriate for many pulsators, including ZZ Cetis), and that the intrinsic variability takes the form of a Gaussian (which, for multi-periodic pulsators, is supported by the central limit theorem). The metric relies on the total number of visits and signal-to-noise per visit (scaled from the 5σ -depth, with Gaussian errors assumed) for the calculation, and is included in `sims_maf_contrib` as `VarDepth`.

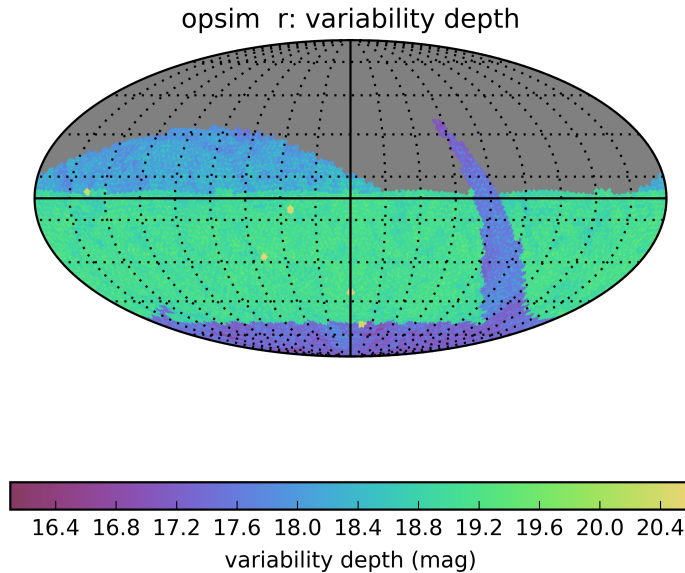


Figure 5.4: Example output of the `VarDepth` MAF metric run on the current baseline cadence, `minion_1016`, after 10 years of survey operations. Input parameters and SQL queries were set to calculate the magnitude limit for detecting 90% of pulsators with 1% r.m.s. variability from a cut on the measured variance in the *r* band (allowing 10% contamination from nonvariable sources).

We specialize this metric for the case of ZZ Ceti pulsators by including maps of the expected distribution of ZZ Cetis in the Galaxy. These maps were precomputed for the *u* and *r* filters by querying the CatSim database for white dwarfs with an SQL constraint to include only those with hydrogen atmospheres and with effective temperatures between 10,600 and 12,500 K (i.e., inside the ZZ Ceti instability strip). While the boundaries of the instability strip depend slightly on surface gravity, the width of the strip does not change much, so these temperature cuts yield representative counts. The white dwarf spectral energy distributions were calculated for CatSim by Pierre Bergeron et al.¹ The `ZZCetiCounts` metric calculates the number of ZZ Cetis that we expect to detect in each part of the sky, and the sum of the results gives the total number of ZZ Cetis with variability detected by LSST.

The measured r.m.s. scatter from pulsations in ZZ Cetis is typically of order $\sim 1\%$, with a mean value around 3% (Mukadam et al. 2006). Since we aim to statistically determine the ensemble amplitude properties in multiple filters for a large population of ZZ Cetis (particularly in the *u* filter), we adopt the following figure of merit for LSST’s ability to study pulsating stars: that significant variability should be detected in the *u* band for at least 1000 ZZ Cetis with r.m.s pulsational power of 1% by the end of the 10 yr survey operations.

¹<http://www.astro.umontreal.ca/~bergeron/CoolingModels/>

5.3.3 OpSim Analysis

For comparison purposes, we calculate the number of ZZ Cetis detected in both the u and r filters, assuming intrinsic r.m.s. variability of 1% for two of the currently available OpSim runs: `minion_1016`, the current baseline cadence, and `kraken_1045`, with doubled u -band exposure times. We require that 90% of ZZ Cetis with 1% r.m.s. variability are detected to the computed “variability depth,” with a tolerance for up to 10% of nonvariables with the same u and r magnitudes to yield false detections. The total number of ZZ Cetis detected for each of these analyses is provided in Table 5.1.

Table 5.1: ZZ Ceti Recovery for 1% R.M.S. Variability

OpSim Run	Filter	# ZZ Cetis
<code>minion_1016</code>	u	9
	r	127
<code>kraken_1045</code>	u	17
	r	123

Clearly LSST falls very short of the proposed figure of merit. The 1% level of variability assumed for ZZ Cetis in this treatment was chosen to ensure that the majority of lower-amplitude ZZ Cetis are detected by LSST. If we relax this constraint and repeat the analysis with ZZ Cetis modeled as 3% r.m.s. variables (the mean r.m.s. variation observed), we get the results shown in Table 5.2. This represents a minimum number of ZZ Cetis detected in total, allowing for incompleteness to low amplitude. While we still do not detect \sim 1000 ZZ Cetis in u , overall we see an increase in the total number of known ZZ Cetis by roughly an order of magnitude (in r).

Table 5.2: ZZ Ceti Recovery for 3% R.M.S. Variability

OpSim Run	Filter	# ZZ Cetis
<code>minion_1016</code>	u	197
	r	1601
<code>kraken_1045</code>	u	325
	r	1534

5.3.4 Discussion

We emphasize again that ZZ Cetis make up the most difficult class of pulsator to detect variability in, and that while other pulsators will be better served by LSST, the currently proposed cadences capture a less-than-complete census of pulsating variable stars. More sophisticated statistical techniques may come partially to the rescue here as our MAF metric simply treats every star on a case-by-case basis, rather than searching for increased scatter in a population of similar stars. Still, it appears that the science results for individual low-amplitude ZZ Cetis will be severely limited.

The situation for higher amplitude ZZ Cetis and other types of variable is better, and LSST observations of ZZ Cetis will certainly still be worthy on careful analysis. We note that the `kraken_1045` strategy with 60 s exposures in u does a much better job of measuring stellar variability at the expense of very few r -band detections. We argue that any observing strategy that increases the number of ZZ Cetis detected in the u band will improve LSST's scientific yield for *all* stellar pulsation studies.

Go to: • [the start of this section](#) • [the start of the chapter](#) • [the table of contents](#)

5.4 Discovery and Characterization of Young Stellar Populations

Patrick Hartigan, C. Johns-Krull, Peregrine McGehee

5.4.1 Introduction

All young stars exhibit some form of photometric variability, and these variations hold the key to understanding the diverse physical processes present at starbirth such as mass accretion events from circumstellar disks, presence of warps in envelopes, creation of new knots in stellar jets, evolution of stellar angular momenta, starspot longevity and cycles, and the frequency and strength of flares. With the proper cadences and filter choices, LSST will make a significant impact in our understanding of all these phenomena simply by providing large enough samples to allow us to relate these aspects of the young stars and their environments to stellar properties such as mass, age, binarity, and their location within their nascent dark clouds in a statistically significant manner.

Low-mass ($\lesssim 1.5M_{\odot}$) pre-main-sequence stars divide into two main categories, depending upon whether or not an optically thick dusty circumstellar disk exists in the system: young stars without dusty inner disks are known as ‘weak-lined T Tauri stars’ (wTTs), while those that have inner dusty disks are called ‘classical T Tauri stars’. Variability behavior differs between wTTs and cTTs. The wTTs variability is dominated by small-amplitude (typically ~ 0.1 mag) quasi-periodic variations that arise from cool star spots, though the active regions that generate X-rays in these objects undoubtedly produce flares as well. Additional variations occur among cTTs, primarily caused by unsteady mass infall from circumstellar disks onto their stars, and from periodic extinction events that unfold as dense clumps or disk warps circle the star in Keplerian orbits. At the extreme end of cTTs phenomena, rare massive outbursts of several magnitudes with decay times between several months to over a hundred years in pre-main-sequence stars (EX Ori’s and FU Ori’s) are of great interest to studies of disk accretion because they indicate the onset of a major instability. Only a handful of such systems have been found, and LSST will easily detect them along with similar, less-dramatic systems.

Obtaining rotation periods for large numbers of pre-main-sequence stars is the only way to quantify how the angular momenta of young stars vary with age. For both wTTs and cTTs, phase-coherence in the rotation periods defines the longevity of star spots, while the amplitude of the periodic component of the lightcurve constrains the spot coverage (and temperature if multiple filters are used). In cTTs, U-band fluxes rise during accretion events, which we can distinguish from extinction events if red magnitudes are also available. A large accretion event is a signal to observe the

system in the future with other instrumentation to look for evidence of a newly-created jet knot. Flaring activity is easiest to monitor at U, though the rapid decline of flares requires a rapid cadence to capture correctly.

LSST also provides a potential means to discover new young stars by way of their variability and colors. One of the challenges in this regard will be to distinguish young stars from other low-amplitude variable stars in the field. In that regard we expect that machine-learning techniques that incorporate knowledge of fluxes in other wavebands as well as the LSST lightcurves and colors will be an ongoing effort. It is possible that X-ray detections will be more reliable for detection of new young stars, but LSST will at minimum assist by identifying non-YSO X-ray sources, and should be a means for discovery for older pre-main-sequence stars (10 – 30 My range) that have had time to wander away from the well-known sites of star forming activity that are typical targets for deep, pointed X-ray surveys.

From the Milky Way science perspective:

LSST gives the opportunity to survey extensive areas around star formation regions in the Southern hemisphere. Among others, it would allow to study the Initial Mass Function down to the substellar limit across different environments. Young stars are efficiently identified by their variability.

Section 8.10.2 in the LSST Science Book (p298–299) provides a thorough scientific motivation for the characterization of young stars through variability, including discussion of the observational signatures of the diverse physical phenomena driving observed time variability. The general observable is strong, irregular flaring across the entire *ugrizy* bandpass of LSST. Flaring can last from minutes to years, and at amplitudes from a few tenths to several magnitudes.

The nature of the variability in young stars changes with evolutionary status. For the youngest stars still undergoing significant mass accretion, FU Orionis and related outbursts can occur due to circumstellar disk instabilities. As the natal environment dissipates and the accretion rates drops, the stars take on a Classical T Tauri appearance where the variability is primarily due to changes in the accretion flow and rotational modulation of hot spots resulting from accretion shocks on the protostellar photosphere. Also present are the signature of cool spots arising from strong magnetic fields. This cool spot rotational modulation is responsible for the variability in the disk-less, and older, weak-line T Tauri stars.

Of particular interest are the FUor and EXor variables, which are named after the prototype objects FU Orionis ([Hartmann & Kenyon 1996](#)) and EX Lupi ([Herbig et al. 2001](#)) respectively, and for which only a relatively small number of examples are known. In these pre-main sequence objects, eruptive outbursts of up to 6 magnitudes have been observed, with high state durations from years to decades. In addition to triggering follow-up observations, LSST should be able to set the first population constraints on the duration of high states, particularly for the short end of the timescale distribution for these eruptive variables.

5.4.2 Analysis

Target Regions

Young stars congregate in specific regions, so it is worthwhile to consider which of these areas will be the most fertile for studies with LSST. The closest star forming regions are all about 140 pc distant: Taurus-Auriga in the north and ρ Oph, Lupus, Cha I, and CrA in the south. However, these regions have only low-mass molecular clouds, and each contain only about 100 young stars. More massive molecular clouds produce both higher mass stars and more low mass stars. In Orion ($d = 414$ pc), the number of identified YSOs is ~ 3000 , and we expect $\gtrsim 30000$ pre-main-sequence stars in the famous southern star formation region in Carina (2.3 kpc). LSST will make its greatest impact when observing the more massive star formation regions, where the amount of young stars is much higher.

Owing to extinction in the dark clouds, source confusion will generally not be an issue (as evidenced by typical deep optical images of such regions), though the large fraction of pre-main-sequence binaries at all separations ensures that many lightcurves will be composites of the primaries and secondaries. More distant star-forming regions will suffer from enhanced foreground contamination, though it should be possible to eliminate most contaminating variable stars by combining close inspection of their lightcurves with colors.

Metrics:

A. Magnitude Limits, Filter Choices

To quantify YSO studies with LSST, we consider V 927 Tau, a rather faint, moderately-reddened $0.2 M_{\odot}$ young star in the Taurus cloud as a target goal. Extrapolating this star to the distance of Carina we have $u=24.0$, $g=23.0$, $r=20.8$, $i=19.4$, and $z=18.0$. For reference, a typical young star in the Carina X-ray catalog has an i -magnitude of 18. Objects that suffer larger extinctions along the line of sight will be easiest to observe in the red. The universal cadence option of 2×15 sec exposures will yield $\sigma = 0.02$ mag for $r=21.8$, a magnitude fainter than V 927 Tau would be in Carina. We show below that this photometric uncertainty suffices to recover a typical period from such an object. The mass function of young stars appears to peak around $0.3 M_{\odot}$, so LSST will determine periods below this mass peak with nominal r-band measurements for a region like Carina. Of course, several additional magnitudes of extinction will exist towards many embedded sources. For example, if we assume an additional five magnitudes of extinction at V for the V 927 Tau-like example above, then $r=25.2$ and $\sigma = 0.41$ mag per visit with universal cadence, so no usable lightcurve will be possible at r . However, $z=20.5$ in this case, where $\sigma < 0.01$ mag and precision lightcurves are again possible.

B. Period Recovery for wTTs

In order to assess how well LSST will recover periods, we created the following model for wTTs variability. Based on current surveys of wTTs, the periods are distributed approximately as a Poisson distribution with a mean of 3.5 days (? , Affer et al. (2013)). Amplitudes are typically 0.1 magnitude (? , (Grankin et al. 2008)), , so we adopt a Poisson distribution that has a mean amplitude of 0.05 mag, and then add 0.05 mag to ensure that the mean variability is 0.1 mag. Shapes of T-Tauri lightcurves can be sinusoidal, but many are ‘bowl-shaped’, influenced by the distribution of large dark starspots (? , (Alencar et al. 2010)). For the bowl lightcurves we assumed a Gaussian shape with a FWHM in a uniform distribution of extent between 0 and 0.75 in phase. Our simulations cover both of these shapes. Errors for each point were taken to be 0.02 magnitude, corresponding to about $r \sim 21.8$ for a universal cadence.

One set of simulations assumed a cadence of one observation every three days over the course of a year. If we define a successful period recovery to be better than a 1% error, then using the standard Scargle method (? , (Horne & Baliunas 1986)) we are able to find the correct period in 98% of the sinusoidal, and 86% of the bowl lightcurves, with the most difficult challenges being at the short end of the period distribution. If we change the cadence to once every 7 days, the ability to recover periods drops to 82% and 59% , respectively, for the two shapes. Interestingly, restricting the sample to the highest-amplitude sources ($\gtrsim 0.1$ magnitude) does little to aid period recovery. The main issue remains the short-period systems where $P \lesssim 2$ days.

Overall, standard cadences of once every few days should suffice to find most periodic T-Tauri stars that have periods $\gtrsim 3$ days. A dedicated campaign to observe star-forming regions at time intervals of an hour or less is required to capture the shorter-period systems. The r-filter should suffice for most objects, though some benefit will be had by going to z to allow the more heavily-extincted sources to be observed.

C. Period Recovery for cTTs

Complex irregular variations in cTTs lightcurves make it much more difficult, and in many cases impossible to recover periods in these systems. While sparse coverage of one observation every few days is adequate for identifying sudden changes from accretion events, these events to a large degree overwhelm low-amplitude periodic signatures. Even when period searches yield a low false-alarm probability, the results are not necessarily reliable. Results from Palomar Transient Factory surveys in the North American Nebula (? , (Findeisen et al. 2013)) and with Spitzer (? , (Cody et al. 2014)) reveal several types of both short- and long-term variations including both bursting and fading. These observations emphasize how important it will be to have some dense phase coverage as a reality check to ensure the reliability of any periods recovered from sparse data in these objects, as well as to follow the short-term variations that characterize accreting systems.

D. Discovery, Accretion and Extinction Events

As we indicated above, any cadence will uncover FU Ori and EX Ori events in all filters. Periodic extinction events follow the same restrictions and have the same requirements as rotational periods described in subsection B.

From the Milky Way science perspective:

In order to assess the ability of LSST to 1) identify and 2) classify Young Stellar Objects we need to quantify the variability timescales and amplitudes of both Class I/II (stars with disks, including Classical T Tauris) and Class III (Weak-line T Tauris). Inclusion of eruptive variables (FUor/EXor) is appropriate as well.

In brief, Weak-line T-Tauris are quasi-periodic with amplitudes of 0.1 to 0.3 mag and periods 1 to ~ 15 days, so their variability is comparable to that of γ Dor stars. Given the temporal evolution of cool spots, a period recovery analysis such as shown for RR Lyrae stars is likely difficult. The embedded systems and Classical T Tauris are irregular variables but have been shown to have distinctive colors due to extinction and the ultraviolet and blue excess arising from accretion shocks.

Table 5.3 shows a possible Figure of Merit for the recovery by LSST of the distribution of EXor high-state duration in outburst.

Figure of Merit for recovery of EXor high-state duration distribution

1. Produce ASCII lightcurve for eruptive outburst
2. Initialise large array to store the maps of fraction detected as a function of duration and amplitude.
2. for *duration T* in range {min, max}:
3. for *amplitude A* in range {min, max}:
4. run `mafContrib/transientAsciiMetric`
5. store the spatial map of the fraction detected for this (A, T) pair
6. Initialise master arrays to hold the run of duration distribution measurements.
7. Produce distribution of high-state durations and amplitudes from which the simulations will be drawn.
8. for *iDraw* in range {1, nDraws}:
9. construct model population with input duration distribution
10. Apply the stored metrics from 2-5 to measure fraction recovered
11. Characterize the duration distribution for this draw
12. Fill the *iDraw*'th entry in the master arrays.
13. **FoM 1:** Compute the median and variance of the upper/lower quintiles.
14. **FoM 2:** Evaluate the bias between recovered and input high-state duration.

Table 5.3: Steps for Figure of Merit recovering the distribution for the duration of EXor high states.

5.4.3 Summary and Recommendations

Performance for Nominal Cadences

Nominal cadences that return to a star-forming region every 3-4 days will suffice to determine rotation periods for $\sim 90\%$ of the young stars within the magnitude limits of LSST. These cadences are also adequate to detect major episodic accretion events like FU Ori's and EX Ori's.

The Need for Annual Dense Coverage of a Few Selected Regions

Occasional dense coverage of targeted regions is the only way to get quantitative information on short-term accretion and flare activity. Dense coverage also removes degeneracies for periodic variables that have periods less than a day, and is the only way to provide a sanity check on any periods recovered for cTTs, which have complex irregular light variations. Comparing longevities of starspots across the mass ranges of young stars requires two well-sampled lightcurves separated by large time intervals.

These goals can be accomplished by having a week every year where one or more selected fields are observed once every 30 minutes in u, r and z. A young star with a 2-day period sampled every 30 minutes provides a data point every 0.01 in phase. For the best-case scenario, observing for 7 nights and 10 hours per night would yield 140 photometric points in each filter. Depending on the period aliasing, this coverage should populate the phases well enough to identify most of the large starspots on the stellar photospheres.

At the beginning of LSST operations we argue that three targeted test fields be observed in this manner to illustrate what can be done with LSST in this mode. Combining a densely-packed short-interval dataset with a sparse but long baseline study maximizes the scientific return for both methods, and allows LSST to address all of the phenomena discussed in the Introduction.

From the Milky Way science perspective:

Galactic star formation regions are largely found at low Galactic latitudes or within the Gould Belt structure. As such study of young stars with LSST is closely tied to other science goals concerning the Milky Way Disk and is subject to the concerns of both crowded field photometry and the observing cadence along the Milky Way.

The embedded and Classical T Tauri stars also undergo significant and rapid color changes due to accretion processes. The ability of LSST to track these variations in color could be limited by the interval between filter changes.

Go to: • [the start of this section](#) • [the start of the chapter](#) • [the table of contents](#)

5.5 Future Work

In this section we provide a short compendium of science cases that are either still being developed, or that are deserving of quantitative MAF analysis at some point in the future.

5.5.1 Discovery of Periodic Pulsating Variables

Lucianne Walkowicz, Stephen Ridgway

Regular variables, such as Cepheids and RR Lyraes, are valuable tracers of Galactic structure and cosmic distance. In this case of these and other strictly (or nearly-strictly) periodic variables, data from different cycles of observation can be phase-folded to create a more fully sampled lightcurve as LSST visits will occur effectively at random phases. In a 10-year survey, most periodic stars of almost any period will benefit from excellent phase coverage in all filters (only a very small period range close to the sidereal day will be poorly observed). Therefore, most implementations of the LSST observing strategy will provide good sampling of periodic variables.

However, different implementations of the survey may result in different resulting sample sizes of these periodic variables, and may also affect the environments in which these stars are discovered. In this section, we create a framework for understanding how current implementations of the observing strategy influence (or even bias) the resultant sample size and environments where these important tracers may be identified.

Tracing Galactic Structure with RR Lyrae

RR Lyrae variables are crucial tracers of structure in the Galaxy and beyond into the Local Group. The incredible sample of RR Lyrae anticipated from LSST observations will enable discovery of Galactic tidal stream and neighboring dwarf galaxies throughout much of the Local Group ([Ivezic et al. 2008](#)). LSST also creates the possibility of detecting and studying RRL variables in the Magellenic Clouds; see Chapter [CHAPTER] for discussion.

[Oluseyi et al. \(2012\)](#) carried out an extensive simulation of period and lightcurve shape recovery of RR Lyrae variables using an early OpSim run opsim1_29. Correctly identifying the period aids in building the sample of interest, whereas fitting the lightcurve shape makes it possible to measure the metallicity of the star. In their simulation, they employed both a Fourier analysis and template matching to recover the lightcurve shape, finding that template matching yielded a more accurate lightcurve shape measurement in the presence of sparse data. The results of this simulation showed that the vast majority of RR Lyrae will be discovered by the baseline observing strategy (as deployed in opsim1_29) within 5 years of survey operations. Half of both RRLab and RRLc stars will be found out to \sim 600 kpc and \sim 250 kpc (respectively) by the end of the 10-year main survey, and template matching techniques for lightcurve shape recovery will provide metallicities to \sim 0.15dex.

The Cepheid Cosmic Distance Ladder

Classical cepheids remain an essential step in the cosmic distance ladder. Their calibration is based largely on LMC cepheids and known (assumed) distance of the LMC. The associated errors, while uncertain, are believed to be of \sim 7%. ([Madore, Barry F.; Freedman, Wendy L. \(2009\). "Concerning the Slope of the Cepheid Period-Luminosity Relation". The Astrophysical Journal 696 \(2\): 1498. arXiv:0902.3747. Bibcode:2009ApJ...696.1498M. doi:10.1088/0004-637X/696/2/1498.](#)) New developments in galactic studies are poised to support substantially improved descriptive information concerning nearby galactic cepheids, with possible substantial reductions in this error, by accurately securing the PL slope and zero point.

Cepheid calibration errors are associated in part with uncertainties in extinction, both interstellar and in some cases circumstellar, and in metallicity. At present, the direct, local calibration of cepheids is limited by the availability of a few direct distance measurements, obtained with HST, with errors \sim 10%. The GAIA mission is expected to return \sim 9000 Galactic cepheids, of all periods, colors and metallicities, with distance errors less than 10% (many of them much less) - [Windmark, F.; Lindegren, L.; Hobbs, D., 2011A&A...530A..76W](#). It is expected to deliver at least 1000 cepheids in the LMC with expected mean distance error \sim 7-8% ([Clementini \(2010\) - 011EAS....45..267C](#)). GAIA, as well as other methods, will also support determination of the 3-d map of galactic interstellar extinction - including possible variations in the extinction law. These rich data sets will be supported with direct measurements of cepheid diameters (A. Merand et al, A&A in press) and advances in stellar hydrodynamics ([Mundprecht et al. 2013](#)) which will provide theoretical and empirical basis for calibrations to reconcile known physics with observational correction factors.

Galactic cepheids will generally be too bright for LSST, but cepheids in the local group are sufficiently bright that LSST photometry will be limited by calibration errors rather than by brightness. This dataset will provide superb support for integration of GAIA-based galactic cepheid studies with extra-galactic cepheid studies.

GAIA will provide similar precision data with the potential to identify or support distance determinations from many other galactic star types. LSST photometric catalogs will represent a uniquely extensive and complete database for such investigations.

Metric Analysis

Several metrics currently exist in the MAF for evaluating how LSST survey strategy affect the recovery of periodic sources. For example, the PeriodicMetric makes use of the periodogram purity function, which effectively quantifies aliasing introduced into periodogram analysis from the sampling of the lightcurve. Similarly, the phase gap metric (PhaseGapMetric), evaluates the periodicity of the source lightcurve and its coverage in phase space (the latter being relevant for shape recovery).

Recreating the template matching results of the [Oluseyi et al. \(2012\)](#) simulation requires sampling specific input lightcurves and comparing with the library of available shapes; this necessarily requires a step outside of the MAF, but can easily be enabled using the lightcurve simulation tools under development.

Current simulations of the main survey show a broad uniformity of visits, with thorough randomization of visit phase per period, giving very good phase coverage with minimum phase gaps.

For periodic variable science, two cadence characteristics should be avoided:

- an exactly uniform spacing of visits (which is anyway virtually impossible);
- a very non-uniform distribution, such as most visits concentrated in a few survey years.

A metric for maximum phase gap will guard against the possibility that a very unusual cadence might compromise the random sampling of periodic variables.

In each case, it would help to jump-start science programs if some fraction of targets had more complete measurements early in the survey.

Go to: • [the start of this section](#) • [the start of the chapter](#) • [the table of contents](#)

5.5.2 Probing Planet Populations with LSST

Michael B. Lund, Avi Shporer

This section describes the unique discovery space for extrasolar planets with LSST, namely, planets in relatively unexplored environments.

A large number of exoplanets have been discovered over the past few decades, with over 1500 exoplanets now confirmed. These discoveries are primarily the result of two detection methods:

The radial velocity (RV) method where the planet's minimum mass is measured, and the transit method where the planet radius is measured and RV follow-up allows the measurement of the planet's mass and hence mean density. Other methods are currently being developed and used to discover an increasing number of planets, including the microlensing method and direct imaging. In addition, the Gaia mission is expected to discover a large number of planets using astrometry ([Perryman 2014](#)).

The *Kepler* mission has an additional almost 4000 planet candidates. While these planet candidates have not been confirmed, the sample is significant enough that planet characteristics can be studied statistically, including radius and period distributions and planet occurrence rates. LSST will extend previous transiting planet searches by observing stellar populations that have generally not been well-studied by previous transiting planet searches, including star clusters, the galactic bulge, red dwarfs, white dwarfs (see below), and the Magellanic clouds (see Section 7). Most known exoplanets have been found relatively nearby, as exoplanet systems with measured distances have a median distance of around 80 pc, and 80% of these systems are within 320 pc (exoplanets.org). LSST is able to recover transiting exoplanets at much larger distances, including in the galactic bulge and the Large Magellanic Cloud, allowing for measurements of planet occurrence rates in these other stellar environments ([Lund et al. 2015; Jacklin et al. 2015](#)). Red dwarfs have often been underrepresented in searches that have focused on solar-mass stars, however red dwarfs are plentiful, and better than 1 in 7 are expected to host earth-sized planets in the habitable zone ([Dressing & Charbonneau 2015](#)).

Another currently unexplored environment where LSST will be able to probe the exoplanet population is planets orbiting white dwarfs (WDs). Such systems teach us about the future evolution of planetary systems with main-sequence primaries, including that of the Solar System. When a WD is eclipsed by a planet (or any other faint low-mass object, including a brown dwarf or a small star) the radius and temperature ratios lead to a very deep eclipse, possibly a complete occultation, where during eclipse the target can drop below the detection threshold. The existence of planets orbiting WDs has been suggested observationally (e.g., [Farihi et al. 2009; Jura et al. 2009; Zuckerman et al. 2010; Debes et al. 2012](#)) and theoretically (e.g., [Nordhaus et al. 2010](#)). A few brown dwarf companions were already discovered (e.g., [Maxted et al. 2006; Casewell et al. 2012; Littlefair et al. 2006, 2014](#)), and [Vanderburg et al. \(2015\)](#) recently discovered a disintegrating planetary body orbiting a WD (see also [Croll et al. 2015; Gänsicke et al. 2016; Rappaport et al. 2016](#)).

While most of the sky that LSST will survey will be at much lower cadences than transiting planet searches employ, a sufficient understanding of the LSST efficiency for detecting planets combined with the large number of targets may still provide significant results. Additionally, the multiband nature of LSST provides an extra benefit, as exoplanet transits are achromatic while many potential astrophysical false positives, such as binary stars, are not.

5.5.3 Metrics

The detection of transiting planets will be dependent on having observations that will provide sufficient phase coverage for transiting planets, with periods that can range from less than one day up to tens of days. In order to address this range of periods, an initial metric that can be used

to address the detection of transiting planets is the Periodogram Purity Function, discussed more thoroughly in Section 5.2.1.

5.5.4 Discussion

In general, the detection of transiting exoplanets with LSST will rely on a small subset of potentially detectable planets that can be sufficiently separated from statistical noise, rather than a clear threshold in a planet's properties that would distinguish detectable planets vs. nondetectable planets. This will mean that the best calculation of planet yields will have to come from simulations of light curves for large numbers of stellar systems in order to characterize LSST. The computation time involved in this process is sufficiently prohibitive to prevent a metric being developed based directly on these simulated light curves, however future work may be able to map relationships between metric values for individual fields and the corresponding numbers of planets that can be detected.

Go to: • [the start of this section](#) • [the start of the chapter](#) • [the table of contents](#)

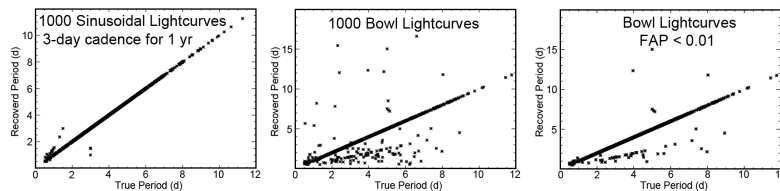


Figure 5.5: Recovered period vs. true period for a sample of sinusoidal (left), bowl-shaped (middle) and bowl-shaped with False Alarm Probability < 0.01 (right), assuming a 3-day cadence and one year of observing. What appears as a solid line are the individual points with periods that are recovered correctly. The bowl-shaped curves are more difficult to recover than the sinusoids, but the method is highly successful in both cases.

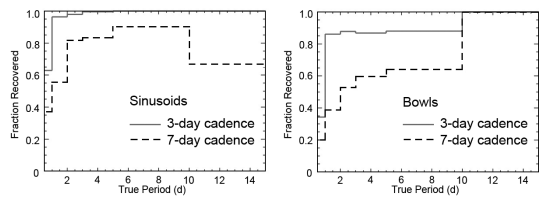


Figure 5.6: Fraction of periods recovered correctly for sinusoidal (left) and bowl light curves (right) for 3-day (solid line) and 7-day (dashed line) cadences over an observing period of one year. A 3-day cadence is significantly better than a 7-day one. Over 98% of sinusoidal, and 86% of bowl light curve periods are recovered successfully with the 3-day cadence. The percentages drop to about 82% and 59% respectively, for the 7-day cadence.

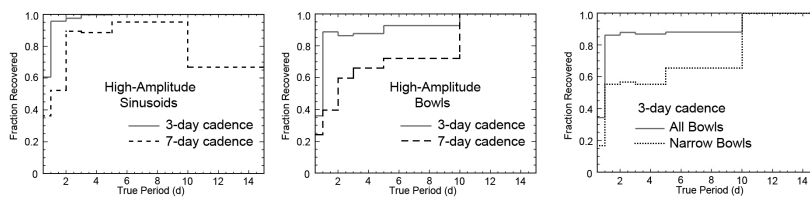


Figure 5.7: Left and center: Same as Fig 2 but restricting the sample to amplitudes greater than 0.1 mag. The method is only marginally more successful with the larger amplitude objects than it is with the entire sample. Right: The narrowest 278 bowls have a significantly higher error rate than the entire sample does.

6 Eruptive and Explosive Transients

Chapter editors: *Eric C. Bellm, Federica B. Bianco*

Contributing Authors:

Iair Arcavi, Laura Chomiuk, Zoheyr Doctor, Wen-fai Fong, Zoltan Haiman, Vassiliki Kalogera, Ashish Mahabal, Raffaella Margutti, ??, Stephen Ridgway, Ohad Shemmer, Nathan Smith, Paula Szkody, Virginia Trimble, Stefano Valenti, Bevin Ashley Zauderer

6.1 Introduction

Explosive and eruptive transients are physically and phenomenologically diverse. What these events share are rare, large-amplitude deviations from a quiescent state. These outbursts are typically unpredictable and of limited duration, and so their discovery and characterization are sensitive to the detailed observing strategy. Often, followup observations with other facilities can provide significant additional scientific value, but this creates a challenge to identify candidate events while they are still visible.

Transients such as novae, supernovae (SNe), and long gamma-ray bursts (GRBs) probe the final stages of stellar evolution. Tidal Disruption Events (TDEs), short GRBs, and Cataclysmic Variables (CVs) give us the opportunity to study compact and binary objects. Massive star eruptions allow us to understand mass loss mechanisms and chemical enrichment. The brightest transients (GRBs, TDEs, SNe) are light beams that can be seen over cosmic distances, and some transients—most notably Type Ia SNe—are cosmological tracers. In this chapter we focus on LSST’s potential to advance the astrophysics of eruptive and explosive transients; the use of SNe for cosmology is discussed in [Chapter 9](#). Transients in the Milky Way Disk are discussed in more detail in [Chapter 4](#).

Cadence choices will determine LSST’s ability to discover, classify, and characterize these events. However, due to their different time scales, different phenomena will benefit from different sampling strategies—sometimes significantly different, and at times orthogonal. Competing objectives described in this chapter are at the heart of LSST’s observing strategy and cadence design.

When evaluating a particular observation or series of observations in light of how they perform for a specific science case, it may be helpful to think of metrics as lying along a continuum between discovery and characterization. Discovery requires a minimum amount of information to recognize an event or object as a candidate of interest. It is particularly relevant for science cases that require triggering followup resources in real time from the live event stream.

Characterization, on the other hand, implies that basic properties of the event may be determined from the LSST observations, including but not limited to the classification of the event. It is particular relevant for science cases requiring analysis of large samples of completed lightcurves.

Characterization and classification of transient events benefits from substantial temporal sampling over the finite duration of the event along with color information (perhaps contemporaneous). Transient events slower than \sim weeks may be adequately sampled by a uniform LSST cadence. Obtaining adequate sampling for faster-evolving events may require special scheduling strategies. For some event types, LSST can only be expected to provide a discovery service, and followup will necessarily be performed elsewhere—so long as the cadence is sufficient to identify the event type. For some events, such as detecting electromagnetic counterparts to gravitational wave events (GWs), serendipitous discoveries are unlikely, but enabling a ToO program would provide the opportunity for LSST to contribute significantly to this science.

We consider a non-exhaustive set of “astronomical transients” in the paragraphs that follow. For a few of these transients, we quantify the ability of LSST cadences to produce data useful for various science goals. These case studies include SNe, GRBs, and GWs. For other transient families (Novae, LBVs, TDEs) we provide more general information in [Section 6.6](#), and we invite the community to further develop the ideas proposed here, as well as further other related goals, into quantified science cases.

6.1.1 Targets and Measurements

[Table 6.1](#) is a *non-exhaustive* list of phenomena to which we are referring as *Eruptive and Explosive transients* in this document.

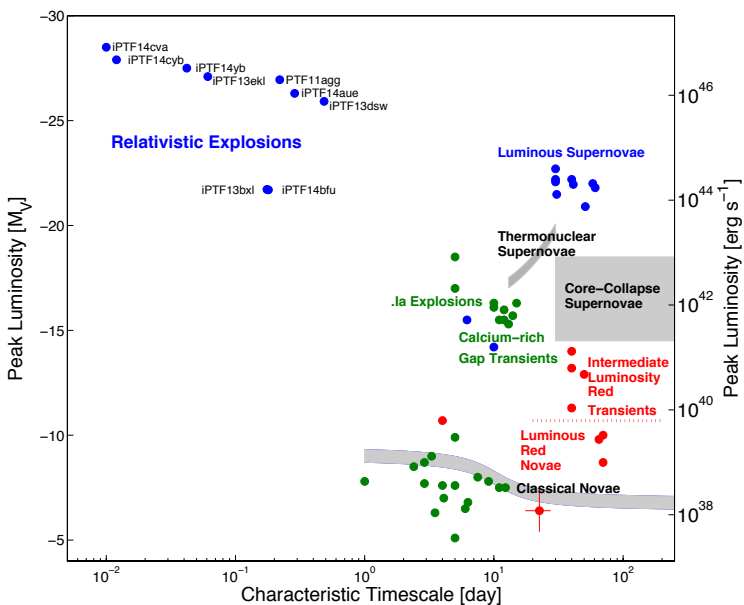


Figure 6.1: Peak luminosity-characteristic decay timescale plot for explosive transients (adapted from [Kasliwal 2011](#)).

Transient Type	Science drivers	Amplitude	Time Scale	Event Rate
Flare stars	Flare frequency, energy, stellar age, space weather	large	min	common
X-ray Novae	Interacting binaries, stellar evolution, SN progenitors, nuclear physics	large	weeks	rare
Cataclysmic variables (6.6.2)	Interacting binaries, stellar evolution, compact objects	large	min - days	common
LBV variability (6.6.3)	Late stages stellar evolution, Mass loss, SN progenitors	large	weeks-years	rare
Massive star eruptions (6.6.3)	Late stages stellar evolution, Mass loss, SN progenitors	extreme	weeks-years	rare
Supernovae (6.3)	stellar evolution, feedback, chemical enrichment, cosmology	extreme	days - months	very common
GRBs (6.4)	jet physics, SN connection, stellar evolution	extreme	min - days	rare
TDEs (6.6.1)	Massive BH demographics, accretion physics	large	weeks-months	very rare
LIGO detections (GW, 6.5)	EM characterization	unknown	unknown	rare
<i>Unknown</i>	Discovery	unknown	unknown	rare

Table 6.1: Overview of major types of optical transients.

6.1.2 Transient time scales

Optical transients display a wide range of intrinsic timescales ([Figure 6.1](#)), and even some long-lived events have short-duration features of interest.

For very short-lived phenomena (stellar flares, GRBs), the main function of LSST will be to provide discoveries and/or simple characterization. Followup to discovery/identification, if required, must take place elsewhere. This implies that the LSST observations must be sufficient to recognize in real time that an event is fast-evolving in order to trigger followup. However, assessing the rise slope is best done with a single filter, so prompt characterization also needs multiple epochs within a night, preferably separated by at least a few hours, in the same filter (we discuss this in detail in [Section 6.2](#)). That is, when observing with different filters it is very difficult to separate lightcurve evolution from color variations. Colors are informative when considering a statistical samples ([Section 6.3](#)): as long as the epoch of peak is reliably assessed, coadded light curves and color time series can be studied.

SNe fall in an intermediate time range. LSST will provide multiple visits in multiple filters during the typical SN duration (months). This sampling may still be insufficient for many science objectives, such as photometric classification of SN subtypes. However, moderate changes to LSST observing strategy may enhance the sampling for part of the sky part of the time, greatly improving the usefulness of SN observations. Metrics that assess the discovery rate of SN are included in [Chapter 9](#). Here we are interested in assessing the ability of LSST to discriminate SN from other transients, SN subtypes from one another, and to identify particularly interesting SNe: for example those that show signature of shock break-out, or companion interaction in the early light curve, and would be candidates for *flash spectroscopy* follow-up (e.g., [Gal-Yam et al. 2014](#)). In addition, metrics that quantify LSST's ability to constrain SN physics in a statistically large sample of SN are needed.

TDEs have only recently started to be characterized in the optical bands. The current sample of events show relatively long time-scales (rise and decline of the light curve is over months). We would like to assess - through metrics - how well TDEs can be distinguished from supernovae based on their light curve shape and color (in real-time so that followup observations can be triggered) and how well the LSST light curves themselves can be used to model the TDE emission and deduce the black hole properties.

Large amplitude flares from AGN may mimic explosive transients; they are discussed in [Chapter 8](#).

In addition we hope that LSST will provide a wealth of serendipitous discoveries of yet-to-be-observed transients. An ideal transient discovery survey would include balanced coverage of all time scales. LSST will cover longer time periods well, but will have to make some choices of emphasis in coverage of shorter time-scales.

In the sections that follow we will use several case studies to assess LSST's performance for a range of time-domain science:

- The ability of a given LSST cadence to discriminate truly young transients from those only first detected well after their explosion date ([Section 6.2](#)). This ability is a crucial input to follow-up strategy design. We identify a region of lightcurve slope that is characteristic of a variety of transients in their early phases and assess the ability of LSST's cadences to place

transients within this phase-space. More sophisticated classification algorithms will likely be necessary, but are beyond the scope of this whitepaper.

- The statistical constraints to a transient class that can be obtained over the course of the LSST survey, from the LSST survey data alone (assuming a successful classification). SN Ia early interaction signatures or IIb shock break-out ([Section 6.3](#)).
- The ability to identify in real-time a rapidly-evolving object of interest and trigger prompt follow-up observations. For this topic GRBs are used as a case study ([Section 6.4](#)).
- The value of triggered Target-of-Opportunity observations for following up very rare, fast-evolving events. Here the kilonova counterparts expected from Advanced LIGO triggers are used as a case study ([Section 6.5](#)).
- The insight that a cadence gives into single transient classes. We discuss CVs, massive star eruptions, and TDEs ([Section 6.6](#)).

6.1.3 Metrics

Two metrics were developed and are used in this chapter specifically for transient phenomena:

- `transientAsciiMetric`: accepts an ASCII file in input, so that realistic transient shapes can be used, with different shapes for different filters. The output can be the series of LSST observations (magnitude and error), or the fraction of transients detected (with user-specified constraints). This metric is used in [Section 6.3](#).
- `GRBTransientMetric`: calculates the fraction of GRB-like transients detected (with user-specified constraints) using an $F(t) \propto t^{-\alpha}$ lightcurve. This metric is used in [Section 6.4](#).

Additionally, the standard MAF metrics that quantify the gaps between consecutive visits to a field within a night and over multiple nights (`IntraNightGapsMetric` and `InterNightGapsMetric`) are of great value and are heavily used throughout this chapter, in [Section 6.2](#), [Section 6.3](#), and [Section 6.5](#) for example.

Further metrics relevant to transient science are discussed in [Chapter 4](#), [Chapter 9](#), and [Chapter 5](#).

Many science cases can be developed and tested with these metrics, and we encourage users to do so. In addition, we are collecting a library of representative transient lightcurves in a separate GitHub repository¹ and we encourage readers to contribute their transient models or observations.

6.1.4 OpSim Analysis

The current set of simulated cadences provide poor coverage in any one filter for transient events longer than a visit pair (\sim 30 minutes) and shorter than \sim weeks ([Figure 6.2](#) and [Figure 6.3](#); [Table 6.2](#)).

As discussed in the subsequent sections, this gap in the sampling hinders characterization of fast-evolving transients. A cadence with two visits separated by an hour or two rather than 20 minutes

¹https://github.com/LSSTTVS/LSST_TVS_RoadMap

FoM	Brief description	minion_1016	enigma_1281	kraken_1043	minion_1020	Notes
6.1-1	IntraNightGapsMetric, any filter	0.39	0.42	0.18	0.40	Median gap (hours) between consecutive observations of a field in any pair of filters in a single night.
6.1-2	IntraNightGapsMetric, <i>r</i> band	0.40	0.44	0.17	0.41	Median gap (hours) between consecutive <i>r</i> -band observations of a field in a single night.
6.1-3	InterNightGapsMetric, any filter	3.0	3.9	2.0	3.0	Median gap (days) between consecutive observations of a field in any pair of filters over multiple nights.
6.1-4	InterNightGapsMetric, <i>r</i> band	15.0	22.8	11.0	21.9	Median gap (days) between consecutive <i>r</i> -band observations of a field over multiple nights.

 Table 6.2: Inter- and intra-night revisit metrics in any filter and in *r*-band for several simulated surveys.

would provide better discrimination. A third visit in the same night in a different filter would provide color information valuable for realtime classification. If a subset of those third visits were in the same filter as the first two, it would improve the shape characterization of the fastest-evolving transients.

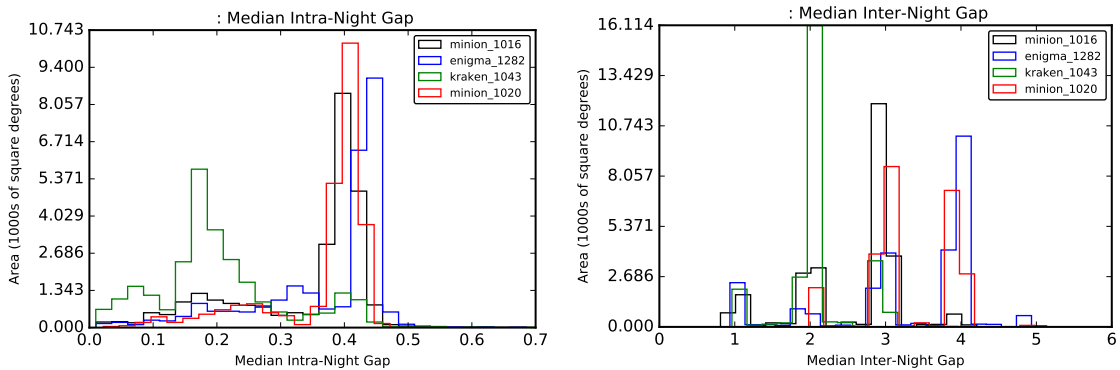


Figure 6.2: Histograms of median intra- (left) and inter- (right) night visit gaps for any band for several OpSim runs.

In fact, if the transient community were to design an optimal strategy for short and intermediate duration transients it would likely include 2 visits at a short time interval in different filter, and a third visit at a later time, but within the same night, with one of the two filters already used.

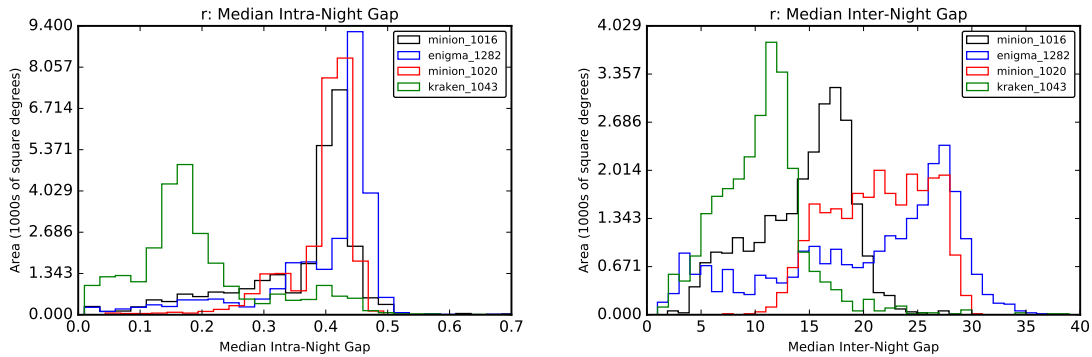


Figure 6.3: Histograms of median r -band intra- (left) and inter- (right) night visit gaps for several OpSim runs.

6.1.5 Discussion

LSST's currently simulated cadences have significant cadence gaps for timescales between nightly visit pairs and intra-night revisits. For many transient science cases, rolling-type cadences that improve the sampling of a subset of events may be helpful in maximizing the transient science that can be done with LSST: the minimum lightcurve sampling required to adequately discover or characterize them may still be larger than that provided by baseline cadences. However, even moderate adjustments (e.g., lengthening the visit pair spacing, or optimizing the deep drilling filter strategy) may yield improvements.

The metrics presented in these sections are initial efforts towards quantifying these goals, and they suggest specific directions for new OpSIM experiments. More detailed efforts to understand and model the challenging problem of transient classification with sparse lightcurves will be needed in order to best guide LSST's time-domain observing strategy.

6.2 Realtime Identification of Young Transients

Stefano Valenti, Federica B. Bianco

For many transients, the first few hours after event beginning reveal a tremendous amount of fundamental information. A large amount of resources in the transient community are devoted to the study of the very early phases of transients (e.g. SNe, GRBs). Since real-time discrimination is a very hard task, it is then important to be able to select, among the large number of transients discovered by LSST, the youngest objects, in order to devise follow-up plans and best distribute precious follow-up resources. In this section we investigate the feasibility of identification of young transients from the LSST data alone, using the intra-night visits.

The Baseline Cadence [minion_1016](#) predicts that, on average, fields in the main survey are revisited every ~ 3 days in any filter (Figure 2.7), and every ~ 15 days when using only r band visits (Figure 2.8). Hence, we are most likely to discover faint transients that are within 3 days of peak brightness. However, for the small subset of nearby events, we can hope to discover them within a few days of explosion. The challenge is to discriminate these truly young events from

newly-discovered SN that are near peak brightness. Within the [minion_1016](#) cadence, and most cadences realized thus far, the second intra-night visit occurs around 30 after the first visit (to maximize the Solar System moving objects recovery, [Chapter 3](#)). We want to understand ***how the intra-night gap enables, affects, and maximizes the identification of new transients as young***, where by young here we mean within a day of outburst/explosion.

To begin to answer this question, we limit our investigation to lightcurve shape alone, and specifically to what can be done in r band. We have selected a representative set of transients with good photometric coverage in the first week after the the outburst/explosion (left panel of [Figure 6.4](#)) and computed the light curve slope as a function of time in magnitudes per day (right panel of [Figure 6.4](#)). In [Figure 6.5](#) we report the change in r brightness between the first and the second visit for the same set of transients as function of phase.

Despite the heterogeneity in light curve shapes, most of the transients show a similar change in brightness on short time scales. This confirms that early classification of the transient sub-type is a major challenge. However, since in general young transients show a fast increase in brightness, it is much easier to assess whether a transients is *young*. Simply put, young transients will show a much larger brightness change between visits than old events. This discrimination is aided by a larger time gap between visits (e.g. 2 hours). Within 30 minutes the change, in brightness is of the order of 1%, or even less, for most transients even within the first ~ 3 days from the start of the outburst/explosion ([Figure 6.4](#), left). Thus a measurement of the change would require a $SNR \gtrsim 500$ on each measurement. Longer gaps give us more leverage: with a time gap of ~ 2 hours after the first visit, the change of brightness will increase to $\sim 5\%$. However the breadth of the gap is not unlimited: a gap of 24 hours imposes a significant delay in triggering follow up for these fast-evolving events.

A natural metric to compare cadences for this purpose is the median time difference between the first and last observations of a field each night. This differs from the `IntraNightGapsMetric`, as the latter only compares consecutive observations of a field and hence underestimates the nightly time baseline when there are three or more observations of a field in a night.

The classification of interesting transients, at an early stage, can be aided by using supplementary information, such as historical information from previous visits, and by color information about the transient. But to properly assess the color of an evolving transient, the gap between observations in different filters should not exceed a few hours ([Section 6.3](#)).

Finally, we stress that the quality and completeness of early multiwavelengh data available at this time is limited. The sample of astronomical transients used here is not comprehensive, and a uniform set of homogeneous data of different transients is still needed in order to further investigate the ideal separation between observations, the need for color information, and the tension between the two.

In the light of these considerations, we recommend the simulation of a cadence with three visits per field, per night, two in the same band, but spaced by two hours or more, and a third in a different band. This criteria could be limited to the observations above and below the ecliptic plane, where recovery of Solar System objects puts less strain on the cadence requirements.

Furthermore, we note that the currently envisioned deep drilling cadence prioritizes depth per visit at the expense of a higher cadence. One hour per night on a deep drilling field reaches a depth that not required for almost all transient science cases, and by cycling to a different field each night, the time between visits for a particular field is too long for many important science cases. Even with higher overhead, a more useful approach for nearly all transient science, that the deep drilling fields are designed to facilitate, would be to observe 3 or 4 of the available fields each night for 15 or 20 minutes.

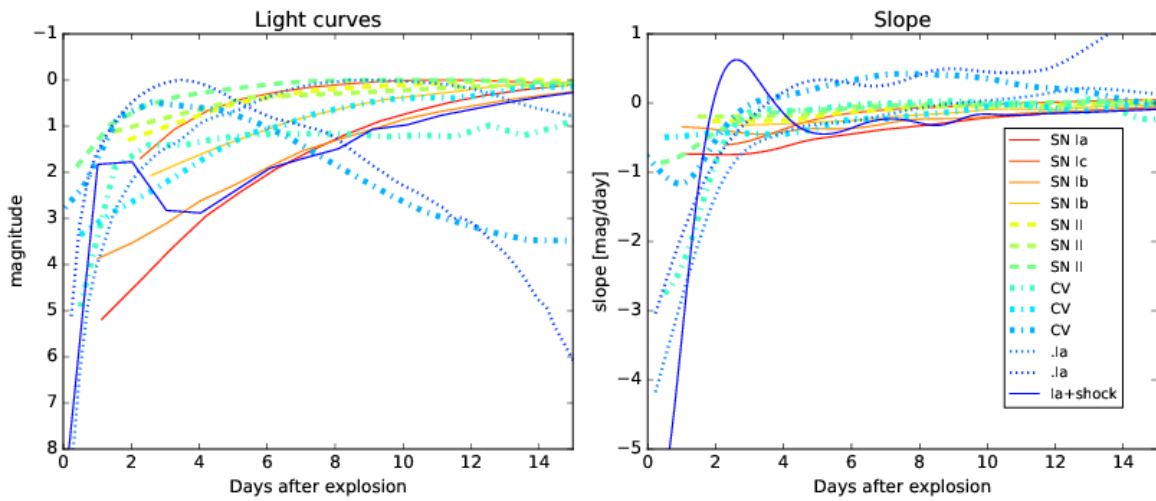


Figure 6.4: *Left:* r' -band light curve for representative transients as function of the phase from the beginning of the transient outburst/explosion for the first few days of the transient life. *Right:* slope of the transient evolution. Data from: SN Ia, Olling et al. (2015); SNII, Rubin et al. (2016); SN .Ia, Shen et al. (2010); SN Ib, Valenti et al. (2011), Cao et al. (2013); SN Ic, Mazzali et al. (2002); CV, Sokoloski et al. (2013), Finzell et al. (in prep), SN Ia+interaction (see Section 6.3)

6.3 Supernovae as Transients

Federica B. Bianco

Supernovae (SNe) represent the final dramatic stages of life of many stars. The term SN we covers a diverse set of phenomena: explosion of low mass stars in binary systems, thermonuclear SN or SN Ia (also discussed in Section 9.5), and explosion of high mass stars, Core collapse (CC) SNe, and even terminal explosions of more exotic systems, yet to be understood, like Super Luminous SNe (SLSNe). Phenomenologically, the observable of the explosion are themselves diverse. The transient duration ranges between weeks, months, even years. The electromagnetic energy radiated ranges between ~ 0.1 (faintest CC SNe), to ~ 1 (SN Ia) and ~ 100 (SLSNe) $\times 10^{49}$ erg, corresponding to absolute magnitudes at peak ranging between ~ -19 and ~ -22 .

LSST's contribution to SNe studies can be substantial. Synoptic surveys such as SDSS, SNLS, PTF, PanSTARRS have revolutionized our understanding of SN over and over again, exposing their

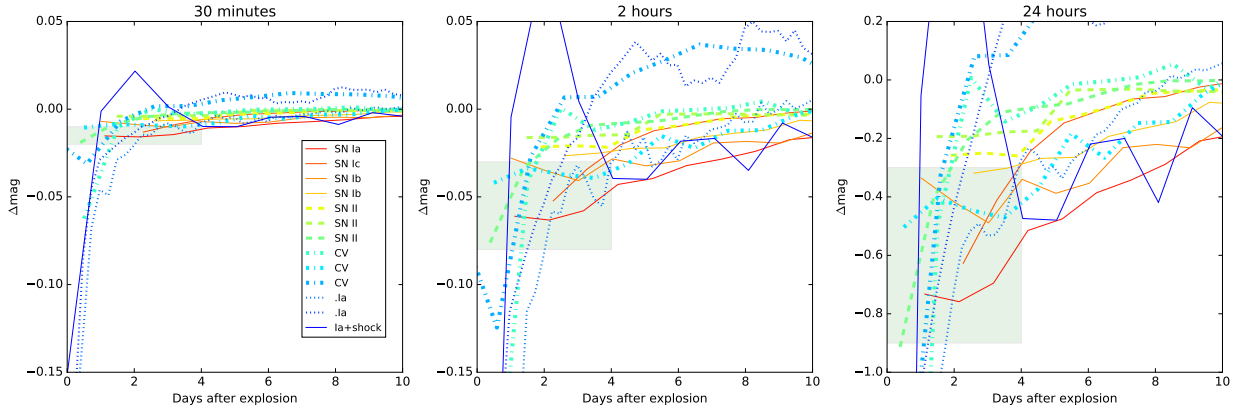


Figure 6.5: Observed magnitude change between two consecutive observations for a representative set of astronomical transients, as a function of the phase. We consider observation gaps of 30 minutes (left panel), 2 hours (central panel) and 24 hours (right panel).

diversity, and revealing different progenitor channels. LSST’s first crucial input will be discovery: the normal type Ia SN rate out to redshift $z = 1$ is estimated to be ~ 200 (sq.deg.) $^{-1}$ per year², and SN Ia represent only about 1/4 of all SN events (Li et al. 2011b): tens of millions of stars will explode within the LSST footprint every year. The key questions concerning LSST SN science are:

- LSST’s SN discovery power,
- LSST’s discrimination power,
- the quality of the statistical sample over time.

The first and second topic are *time sensitive*, while the latter is not, although it is interesting to understand the pace at which a science question can be advanced in the life time of LSST.

Discovery: the SN Ia discovery rate is a standard LSST time-domain metric: a fraction of $\sim 40\%$ SN Ia are expected to be discovered pre-peak luminosity within the standard LSST survey (e.g. [minion_1016](#) Figure 2.10). The topic of SNe discovery is discussed in further detail in 9.5.

The next step is then **discrimination**, and the question we need to answer, for SNe as well as for most other transients, is: will LSST photometry allow to distinguish SN from other transients, and to distinguish the different types of SN? And further: will this be achievable in time to appropriately direct follow-up efforts? This is particularly difficult considering that photometric classification schemes have only achieve modest performances in distinguishing, for example SN Ic from SN Ia. As mentioned earlier in this chapter, the issue of prompt classification is at the heart of the success of LSST transient science, but it is too complex to tackle in this chapter, while LSST’s ability to assess whether a new transient is young is discussed in [Section 6.2](#).

When a large statistical sample of SNe is generated, LSST’s photometry may allow to set constraints on the diversity of the sample, even as a standalone survey, without the aid of follow-up efforts. **Thus LSST alone can shed light on the diversity within the population of SN**,

²http://www.lsst.org/sites/default/files/docs/Wood-Vaisey_086.11.pdf

which in turn may constrain the genesis of the explosion.³ For SN Ia, where the exploding star is a Carbon-Oxygen (CO) White Dwarf (WD), outstanding questions that can be answered by an LSST photometric sample include, for example, what is the percentage of SN Ia that arise from a *double degenerate* (DD) progenitor system – a CO WD-WD binary –, from a *single degenerate* (SD) system – a WD-Main Sequence (MS) or WD-Red Giant (RG) binary–, or a *merger* – a WD-WD binary with a He and a CO WD. Answering this question would reduce the scatter in the Hubble diagram if SNe from different progenitors are shown to require different standardization ([Scolnic et al. 2014](#)). On the CC SN side: the diversity of SN sub-classes, and the relationship between them (is there a phenomenological continuum or actually distinct classes, e.g. between IIp and III, or Ib and IIb?) is yet to be understood. Exceptionally well studied objects may answer these questions: individual SN Ia with tight constraints on the progenitor system show, for example, that both single and double degenerate progenitors exist (e.g. SN 2011fe, [Li et al. 2011a](#), [Olling et al. 2015](#) and PTF 11kx, [Dilday et al. 2012](#)). However, a statistical sample is needed to set constraints on populations.

Thus the technical question to be answered is: how much detail can be sacrificed in favor of sample size without compromising diagnostic power? And the diagnostic power relies on color and sampling: thus what is the trade-off between cadence in the same filter, and observations in different filters. Specifically, transients can be distinguished early from two photometric characteristics: rise time and color. There is a tension between these observables, as discussed in Section 6.2. Obtaining colors relies of course on obtaining photometry in different bands as close as possible to *simultaneously*. However, assessing the rise slope is best done with a single filter, so prompt characterization also needs multiple epochs within a night, although separated by at least a few hours, in the same filter, as observing with different filters it is impossible (or very hard) to separate shape from color. Colors allow to learn a lot about the statistical sample: as long as the epoch of peak is reliably assessed coadded light curves can be studied, which is the goal of the analysis that follows.

6.3.1 Distinguishing progenitor scenarios

In this chapter we envision and design a SN related metric that works on a large sample (months, to years of LSST data) and assesses the ability to characterize the contribution of SNe with specific features to the global population: as a test case we will use the presence of an early blue excess for SN type Ia, signature of interaction with a companion, and thus of a SD progenitor. Equivalently, the presence of an early blue excess in CC SNe could be assessed, the signature of shock breakout, which directly measures the radius of the progenitor star. The *figure of merit* for this science case is the time within the survey required to achieve a sufficiently large sample of SNe satisfying proper quality criteria to enable us to distinguish populations with different contribution from DD and SD progenitors. To do this we rely on simulations of the observables of the population for different sample sizes, and on the `transientAsciiMetric` to determine the detectability of interacting, and non-interacting SNe. We are developing a metric (`colorGapMetric`) to assess the gap between detections in 2 filters. In the meantime we rely on the estimated of the gap between observations in a single filter, and in any filters (see [Sub-section 6.1.4](#)).

³Reliable typing of a SN and redshift determination would still require auxiliary data.

We simulate interacting SNe from the Nugent templates (Nugent et al. 2002) injecting the angle dependent effects of interaction with a companion as simulated by (Kasen 2010), for a $2 M_{\odot}$ and a $6 M_{\odot}$ MS companion stars, and a $1 M_{\odot}$ RG companion, following the procedure of (Bianco et al. 2011). We create synthetic progenitor populations with a fraction of single degenerate progenitor systems $0.05 \leq f_{SD} \leq 0.6$ in 0.05 intervals, and random lines of sight with respect to the binary's geometry. One such lightcurve, with maximal interaction effects, is shown in Figure 6.6, also indicating how it may be observed by LSST. For each population we simulate the observation of colors by selecting random epochs with a granularity of 1 day within the first 10 days after explosion, and subtracting the magnitude in different filters at the same epoch ± 1 day for each SN, and we include the effects of observational noise by generating datapoints from a draw within a Gaussian distribution centered at the color measured in the previous step and with standard deviation $\sigma_{pop} = 0.1, 0.3$, and 0.5 . We generate populations of $N_{pop} = 100, 1000, 10000$ $z = 0.5$ SNe, observed in $g' - r'$, as a representative case. Because the effect is heavily chromatic, and it dissipates becoming essentially negligible by r band, $u' - i'$ gives the most leverage. However g' and r' are the best observed LSST bands in most cadences. An extension of this work should then consider $g' - r'$, $u' - r'$, $g' - i'$, and $u' - i'$.

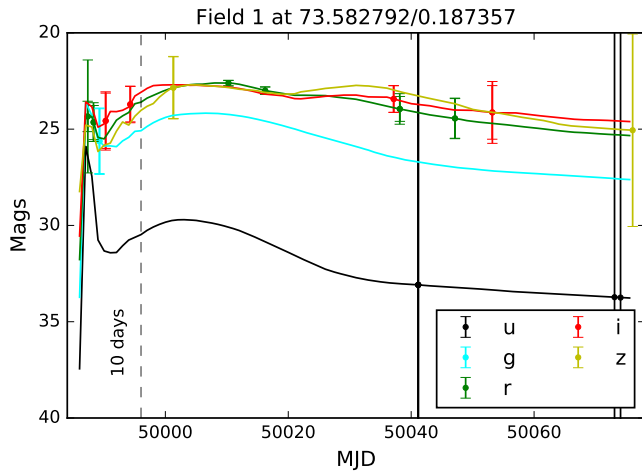


Figure 6.6: A normal SN Ia lightcurve at $z=0.5$ showing interaction with a RG companion as seen from the most favorable viewing angle: the effect of interaction as simulated by Kasen (2010) is added on top of a lightcurve simulated from the Nugent et al. 2002 templates. The data points represent one possible set of LSST observations of this transient, obtained by running the `transientAsciiMetric`. This particular event is detected in g' , r' , and i' within the first 10 days.

We perform Kolmogorov-Smirnoff (KS) and Anderson-Darling (AD) tests to evaluate, as a function of σ_{pop} and sample size N_{pop} , our diagnostic power. In Table 6.3 we report the ability to distinguish a population with a $f_{SD} > x$ from $f_{SD} = 0.05$; the number reported is the SN Ia fraction from SD progenitors that can be distinguished at a p -value ≤ 0.05 .

At this point we can evaluate how long it will take for a given LSST cadence to obtain a sufficient number of observations in the 2 desired bands, separated by less than 1 day, that pass the SNR requirements. This should be done in a full Monte Carlo simulation, injecting lightcurves with the proper lightcurve shape at the proper rate. Note that, because the early lightcurves of interacting SD SN Ia are brighter, they should be more easily detected. However at this stage we can take

$g - r$	$N_{\text{pop}} = 100$	$N_{\text{pop}} = 1,000$	$N_{\text{pop}} = 10,000$
$\sigma_{\text{pop}} = 0.5$	-	0.2	0.1
$\sigma_{\text{pop}} = 0.35$	-	0.2	0.1
$\sigma_{\text{pop}} = 0.1$	0.2	0.1	0.1

Table 6.3: Fraction of single degenerate (SD) SN Ia in a sample of $z = 0.5$ SNe that can be distinguished from a population with 95% double degenerate (DD) and 5% SD SNe Ia, for a given noise level (σ_{pop}) and number of observations (N).

some shortcuts. *First shortcut*: we evaluate the relative observability of SNe with excess, and SNe without excess at $z = 0.5$ and adjust the number of detections according to the injected ratio. The relative detectability can be assessed with the `transientAsciiMetric`, which allows us to see how OpSims recovers observations of transients with realistic shapes. We conclude that for RG-WD progenitors the detectability is enhanced by $\sim 50\%$ in g' compared to SD progenitors, and slightly less in r' .

Then we extract from the `transientAsciiMetric`, the number of *color observations*, i.e. observations in 2 bands within 1 day of each other, each fulfilling our SNR requirement for the color for 3-, 6-, and 12 months of survey in year 1. The SNR requirement is translated into a requirement on each observation of $\text{SNR} > \frac{1.0}{\sqrt{2.0} \sigma_{\text{pop}}}$.

With the goal of distinguishing a SD contribution of 10% to the SN Ia population to a three-sigma level (p -value ≤ 0.05), we need more than 1000 detections, in 2 filters within 1 day, and a $\sigma_{\text{pop}} < 0.35$ [Table 6.3](#). But the pairs of observations we recovered at the previous step are within the first 10 days but with any gap in time. *Second shortcut*: To include the constraint that the detections should be within 24 hours we refer to the `InterNightGapsMetric`, which is plotted in [Figure 2.7](#). For the `minion_1016` we estimate $\sim 10\%$ of the observations are revisited within a night. With the assumption that this is likely to happen in two different filters, which is *non-conservative*, but neglecting intra-night observations that may happen in the two different filters, which is a *conservative* assumption our numbers drop by a factor 10.

With all these assumptions standing, we find that that only 3 months of survey are sufficient to provide a useful, sufficiently large and high SNR sample for our purpose, and improve on the findings on this topic that were achieved with SDSS II ([Hayden et al. 2010](#)), and 3 years of SNLS data ([Bianco et al. 2011](#)) with `minion_1016`! With our assumptions, 3 month of survey are just enough to reach the goal for `enigma_1281`. Although the `enigma_1281` requires three visits, thus increasing the timeline for inter-night observations, it does not require the observations to be in any specific filters, and with the addition of the third visit within the same night, it increases the typical intra-night gap. It is possible that a detailed investigation of the true *inter-night gap between different filters*, or the addition of a requirement in the cadence that one of the night filter be different than the others (possibly requiring an increased gap between two of the three images to minimize filter changes) would provide valuable data for this kind of studies even faster.

This exercise demonstrates the power of LSST in collecting large high SNR samples of transients, but we must remind the reader that these conclusions, and generally large sample analysis, rely on having properly identified both the transient class (normal SN Ia) and the date of maximum!

FoM	Brief description		minion_1016	enigma_1281	Notes
6.3-1	SNIaprojenitorMetric, detections	1,000	3	6	Time to collect 1,000 relevant color observations in years in 3 month intervals.
6.3-2	SNIaprojenitorMetric, detections	10,000	> 12	> 12	Time to collect 10,000 relevant color observations in years in 3 month intervals.

Table 6.4: Figures-of-merit (FoMs) for statistical SN Ia progenitor studies to assess the contribution of SD progenitors to the SN Ia population.

This, once more, highlights the importance of prompt identification and classification: for SN Ia this likely will limit this work to objects that could be identified spectroscopically, enhancing the importance of follow-up.

Figure 6.7 shows the detection rate for SN Ia at $z = 0.5$ in absence of shock interaction as a function of SNR (obtained by summing in quadrature the errors on g' and r') for 3, 6 months, and a year of [minion_1016](#) and [enigma_1281](#).

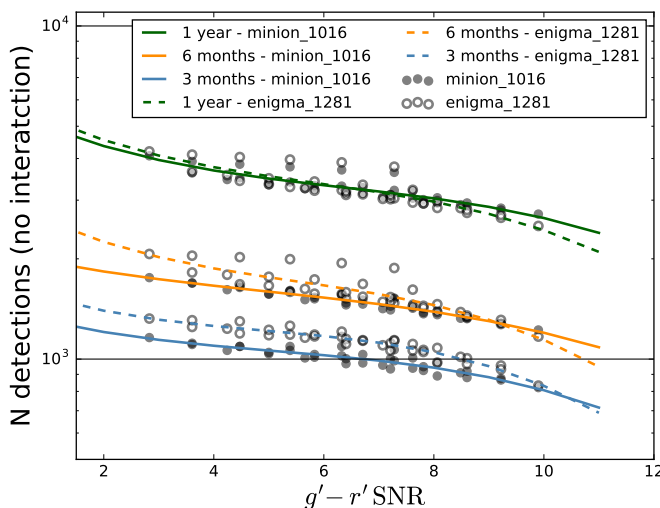


Figure 6.7: Normal SN Ia lightcurve at $z=0.5$ detected by the [minion_1016](#) cadence in 3 months, 6 months, and 1 year, that provide color information useful to constrain the progenitor distribution. Line are third-degree polynomial fits.

6.4 Gamma-Ray Burst Afterglows

Eric C. Bellm

Gamma-ray bursts (GRBs) are relativistic explosions typically classified by the temporal duration of their initial gamma-ray emission: Long GRBs, that mark the endpoint of the lives of some massive stars, and short GRBs, believed to originate from the merger of binary neutron stars. GRB emission is known to be beamed: the initial prompt gamma-ray emission is seen only for observers looking at the jet axis. The longer-wavelength X-ray, optical, and radio afterglow may be seen both by on- and off-axis observers. The latter case is known as an orphan afterglow, due to the absence of gamma-ray emission. On- and off-axis afterglows are predicted to have different temporal signatures in the optical: On-axis events decay as a power-law until a jet break, while off-axis events should be fainter and show an initial rise (Figure 6.8). Despite systematic searches, no convincing orphan afterglow candidates have yet been discovered, limiting our knowledge of the beaming fraction of GRBs and hence their true rates. Well-sampled orphan afterglow lightcurves would also permit study of the GRB jet structure.

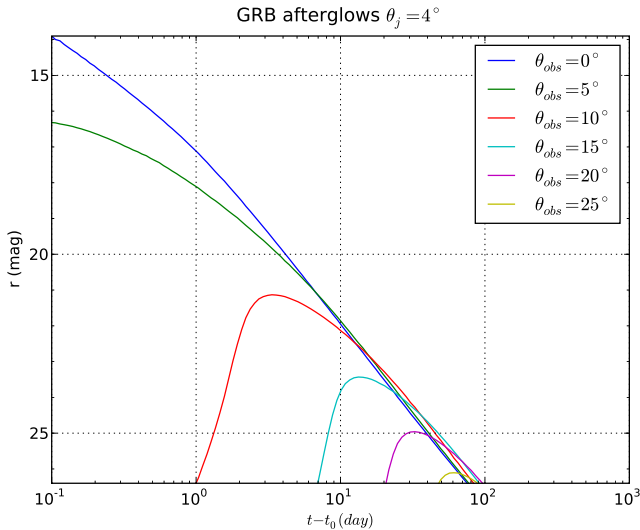


Figure 6.8: Predicted light curves of GRB afterglows by off-axis angle with respect to the jet axis θ_{obs} (Figure 8.8, LSST Science Collaboration et al. 2009). The forward shock model is derived from Totani & Panaiteescu (2002) and assumes a jet half opening angle $\theta_j = 4^\circ$, the isotropic equivalent energy of $E_{\text{iso}} = 5 \times 10^{53} \text{ erg}$, ambient medium density $n = 1 \text{ g cm}^{-3}$, and the slope of the electron energy distribution $p = 2.1$. The apparent AB r -band magnitudes assume a source redshift $z = 1$.

Because of their rarity, in all but one case (Cenko et al. 2015) to date GRBs have been discovered using their prompt emission by hard X-ray or gamma-ray all-sky monitors. This selection imposes biases on the population of relativistic explosions we observe. Baryon-loading in the GRB jet—a “dirty fireball” (Rhoads 2003)—can lead to on-axis events without gamma-ray emission. Only one plausible candidate has been identified to date (Cenko et al. 2013). Discovery of new dirty fireballs—if distinguished from off-axis events—would clarify the rates of these events and enhance our understanding of the diversity of stellar death.

LSST is the survey most capable of resolving these decades-old questions. Due to its large aperture and etendue, LSST can detect faint, fast-fading, and rare cosmological events, potentially enabling population studies of the high-redshift universe. [Ghirlanda et al. \(2015\)](#) estimated LSST could detect 50 orphan afterglows each year, more than any other planned survey.

The challenge of detecting and recognizing GRB afterglows in the LSST data in real time makes this science case a useful proxy for other fast transient science cases that benefit from $N > 2$ visits per night. In particular, this includes discovering supernovae soon after explosion for flash spectroscopy or shock breakout searches.

6.4.1 Target measurements and discoveries

GRB afterglow discovery is among the science cases that places the greatest stress on the LSST cadence. Because afterglows fade rapidly—dropping several magnitudes in the first few hours—high cadence observations are required to detect the fast fading. If an afterglow candidate can be recognized in real time, it will be possible to trigger TOO spectroscopy (to measure a redshift and confirm the event is cosmological), X-ray and radio observations (to detect a high-energy counterpart and the presence of a jet), and additional photometry (to characterize the lightcurve evolution). If there is no source at the location of the transient in the coadded reference image, two consecutive observations in the same filter separated by an hour or two are the minimum required to potentially trigger followup of a fast-fading event. However, a third observation within a night or two—ideally in the same filter—would improve the purity of the sample and reduce the reliance on triggered followup. Observations in other bands at high cadence are less useful because they require assumptions about the event’s SED and its evolution to determine if a source is truly fading.

Distinguishing orphan afterglows from on-axis events (whether conventional GRBs or dirty fireballs) will also require more than two detections. Orphan events may prove harder to recognize in real time, because they are intrinsically fainter than on-axis events and show an initial rise rather than a rapid decay (Figure 6.8). Additionally, because of relativistic time dilation, high redshift events are easier to detect, but these events will be fainter and more difficult to follow up. Accordingly, population studies of orphan afterglow candidates may by necessity be conducted with LSST photometry alone. Such studies may only be productive if LSST has sufficiently frequent revisits to a field in a single filter.

6.4.2 Metrics

The core figure of merit for GRB afterglows is simply the raw number of on- and off-axis events detectable in two, three, or more observations, preferably in a single filter.

The appropriate way to derive these detections is to conduct a Monte Carlo simulation of a cosmological population of GRBs and fold it through the LSST observing cadence (cf. [Japelj & Gomboc 2011](#)). We are developing this infrastructure for the MAF framework.

In the meantime, simplified metrics can give us a general idea of how well a given cadence can characterize fast-evolving transients such as GRBs. We have created a new metric, `GRBTransientMetric`,

FoM	Brief description	minion_1016	enigma_1281	kraken_1043	minion_1020	Notes
6.4-1	<code>GRBTransientMetric</code> , nPerFilter = 1	0.17	0.16	0.20	0.21	Fraction of GRB-like transients detected in at least one epoch.
6.4-2	<code>GRBTransientMetric</code> , nPerFilter = 2	0.12	0.10	0.09	0.14	Fraction of GRB-like transients detected in at least two epochs in any single filter.
6.4-3	<code>GRBTransientMetric</code> , nPerFilter = 3	0.05	0.08	0.04	0.04	Fraction of GRB-like transients detected in at least three epochs in any single filter.

Table 6.5: Mean figures-of-merit (FoMs) for on-axis Gamma-Ray Bursts for one, two, and three detections in a filter. The best value of each FoM is indicated in bold. The wider areal coverage of [minion_1020](#) improves its detection rate of GRBs in one and two epochs, while the triplet visits in [enigma_1281](#) naturally improve the three-detection efficiency.

that replaces the linearly rising and decaying lightcurve in `TransientMetric` with the $F \sim t^{-\alpha}$ decay characteristic of on-axis afterglows. (For the time being, we neglect the jet break that steepens the rate of decay; this implies that our detectability estimates are optimistic.)

We simulate random on-axis afterglows using the parameters of [Japelj & Gomboc \(2011\)](#): the R-band apparent magnitude at 1 minute after explosion is randomly drawn from a Gaussian with $\mu = 15.35$, $\sigma = 1.59$ and decays with $\alpha = 1.0$. For these estimates we simply assume zero color difference between in all LSST bands. There are roughly 300 on-axis GRBs per year with these parameters; we calculate the average fraction of these events which have at least one, two, or three detections in any single filter.

6.4.3 OpSim Analysis

We ran `GRBTransientMetric` on several OpSim v3.3.5 runs with a range of characteristics: [minion_1016](#), the baseline cadence; [enigma_1281](#), with three visits per WFD field; [kraken_1043](#), with no visit pairs; and [minion_1020](#), a PanSTARRS-like cadence.

[Table 6.5](#) lists the fraction of on-axis afterglows detected in at least one, two, and three visits in a single filter.

Because of its wider areal coverage, the PanSTARRS-like cadence of [minion_1020](#) maximizes the fraction of events detected in one and two epochs. Not surprisingly, the triplet-visit WFD cadence of [enigma_1281](#) maximizes the three-epoch detection rate.

6.4.4 Discussion

An LSST cadence purely designed for discovering GRB afterglows would include three or more visits to each field every night, with the visits separated by an hour or two. Moreover, it would be conducted in a single filter in order to best identify the lightcurve shape of off-axis events.

While the current surveys simulated are far from this ideal (usually just two closely spaced visits, with subsequent revisits days later), nonetheless an appreciable number of GRBs are detectable. `enigma_1281` would detect about 25 events each year in three epochs, already potentially the largest sample of untriggered afterglows.

However, some care is required in interpreting these values: while the GRB afterglow fades rapidly over the first day of the explosion (Figure 6.8), at later times a 30 minute visit separation is not enough to reveal significant evolution in the lightcurve. We intend to enhance our metric to require that detections are counted only if significant evolution is statistically distinguishable with 1% photometry.

In future work we intend to simulate cosmological populations of on- and off-axis in order to better determine how many events could be discovered in time to trigger real-time followup.

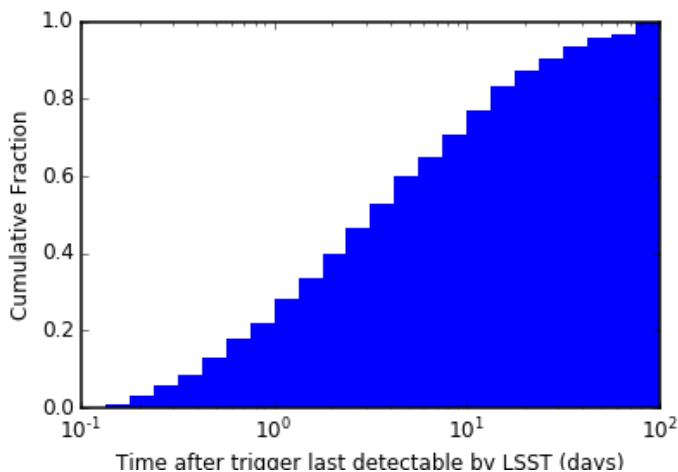


Figure 6.9: Cumulative fraction of GRB on-axis afterglows fainter than magnitude 24.7 at a given time after the burst. We use an $\alpha = 1$ decay with no jet breaks and the brightness parameters of [Japelj & Gomboc \(2011\)](#).

Thanks to LSST’s depth, GRBs can be visible for weeks (Figure 6.9). Accordingly, modest enhancements to the intra- and inter-night revisit rate with single-filter rolling cadences should substantially improve LSST’s discovery and characterization of relativistic explosions.

Go to: • [the start of this section](#) • [the start of the chapter](#) • [the table of contents](#)

6.5 Gravitational Wave Sources

[Raffaella Margutti](#), [Zoheyr Doctor](#), [Wen-fai Fong](#), [Zoltan Haiman](#), [Vassiliki Kalogera](#), [Virginia](#)

Trimble, Bevin Ashley Zauderer

The first detection of Gravitational Waves (GW) by the advanced LIGO/Virgo collaboration (Abbott et al. 2016a, 2009; Acernese 2008) has recently opened a new window of exploration into our Universe. The amount of information that can be revealed by the properties of the GW emission is immense and holds promises for revolutionary insights, including accurate masses and spins of neutron stars and black holes, tests of General Relativity and an accurate census of the neutron star (NS) and black hole (BH) populations that might challenge our current understanding of massive stellar evolution. However, GW events are poorly localized (10-100 deg² at the time of LSST operations). The identification of EM counterparts would provide precise localization and distance measurements, in addition to the necessary astrophysical context (e.g. host galaxy properties, connection to specific stellar populations) to fully exploit the revolutionary power of this new GW era.

6.5.1 Target measurements and discoveries

The first GW event was found to be associated with the merger of two black holes (Abbott et al. 2016a,b). Although no EM counterpart was expected to accompany a black-hole black-hole (BBH) merger, it seems now possible that even BBH mergers might produce short GRB-like EM emission (Connaughton et al. 2016; Loeb 2016; Zhang 2016; Perna et al. 2016; Stone et al. 2016). Indeed, in analogy with supermassive BH mergers, shocks might develop in the just-formed circumbinary accretion disk (if a disk forms), which can produce a bright afterglow following the BBH merger (e.g. Lippai et al. 2008; Corrales et al. 2010; Schnittman 2013). Albeit speculative in nature, it is advisable to keep an open mind about the possibility of EM counterparts to BBH mergers.

The most promising and better understood EM counterparts to GW events are “kilonovae” (Li & Paczyński 1998; Metzger et al. 2010; Metzger & Berger 2012; Kasen et al. 2013; Barnes & Kasen 2013). Kilonovae are short-lived (typical time scale of one week), apparently faint ($z \sim 21$ mag at peak at 120 Mpc), red ($i - z \approx 1$ mag), isotropic transients (Figure 6.10) due to the radioactive decay of r-process elements synthesized in the merger ejecta of a NS-NS or NS-BH system. These merging systems are the favored progenitors of short GRBs. Indeed, the signature of a kilonova emission has been recently found following the short GRB 130603B (Berger et al. 2013; Tanvir et al. 2013). The key piece of information that enabled the discovery of kilonova-like emission associated with this short GRB was its sub-arcsecond localization enabled by the detection of the optical afterglow, which allowed for an effective kilonova search with the Hubble Space Telescope (Figure 6.10). In contrast, the typical localization region of GW events in the LSST era is expected to be of the order of a few tens of square degrees (LIGO Scientific Collaboration et al. 2013). It is thus clear that the major challenges faced by the optical follow-up of GW events is represented by the combination of poor localizations with faint and fast evolving red electromagnetic counterparts.

The detection of an optical counterpart in conjunction with a GW event will significantly leverage the GW signal. LSST, with its wide FOV, wavelength coverage and exquisite sensitivity is uniquely poised to identify and characterize counterparts to GW events.

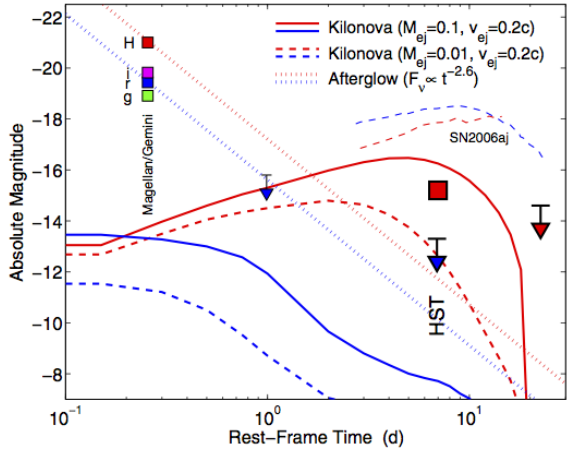


Figure 6.10: Kilonova signature in the short GRB 130603B as revealed by the Hubble Space Telescope (HST). The Magellan and Gemini telescopes sampled the optical afterglow of the GRB (dotted lines). The kilonova light starts to dominate the emission in the H band around a few days after the merger. Thick and dashed lines: theoretical kilonova models from Barnes & Kasen (2013) showing that kilonovae are fast-evolving, faint and red transients. The light-curve of the SN 2006aj associated with the long GRB 060218 is also shown for comparison. From Berger et al. (2013).

6.5.2 OpSim Analysis and Discussion

Effective follow up of GW triggers relies on the capability to sample a relatively large portion of the sky, repeatedly, over a time scale < 1 week, with different filters (Cowperthwaite & Berger 2015). In the optical band, the kilonova signature is expected to be more prominent in the i , z and y filters, which we identify as the most promising filters for the kilonova search. We emphasize however that another set of contemporaneous observations in a “bluer” filter is necessary to acquire color information and distinguish kilonovae from other fast-evolving transients.

We use the median inter-night gap for visits in the same filter derived from the candidate Baseline Cadence `minion_1016` to show that, in the absence of a Target of Opportunity (ToO) capability, it is *not* possible for LSST to play a major role in the identification of EM counterparts of GW triggers.

To identify kilonova candidates we need at least 2 observations acquired within ~ 1 week of the GW event (Cowperthwaite & Berger 2015). Using the inter-night gap distribution for visits in the y filter (which is the most promising filter for a kilonova search), the area of the sky covered with cadence $\Delta t < 7$ days at any given time, is $A_{sky} \sim 3000 \text{ deg}^2$ (including deep drilling fields). This is the area that can be searched for fast evolving transients. Two important considerations follow:

- (1) A_{sky} only covers $P \sim 7\%$ of the sky. The probability that the *entire* GW localization region is contained, by chance, within A_{sky} is thus very small.
- (2) Even if LSST is able to cover a meaningful portion of the GW region, we would still not have color information, and we would thus be unable to filter out contaminating transients.

We conclude that relying on the serendipitous alignment of the LSST fields with the GW localization map is not an effective strategy to follow up GW triggers and identify

their EM counterparts. We thus strongly recommend a ToO capability as part of the baseline LSST operations strategy.

Ideally, the ToO capability will allow for imaging of the GW localization map at least twice over $\Delta t \lesssim 1$ week with a “red” filter (i , z or y), and will include the possibility to designate a desired set of filters to obtain color information. By the time of LSST operation the typical size of the GW localization region is expected to be 10-100 deg², which would require a small number of LSST re-pointings. We thus do *not* anticipate a significantly disruptive impact on other LSST campaigns (especially if only the GW triggers with the best localizations in the southern sky are selected for LSST ToOs).

At the price of re-shuffling a reasonably small number of fields, *if* equipped with ToO capabilities, LSST can be the premier player in the era of EM follow up to GW sources.

Go to: • [the start of this section](#) • [the start of the chapter](#) • [the table of contents](#)

6.6 Future Work

In this section we provide a short compendium of science cases that are either still being developed, or that are deserving of quantitative MAF analysis at some point in the future.

6.6.1 Tidal Disruption Events

Iair Arcavi

A star passing close to a supermassive black hole (SMBH; $M \gtrsim 10^6 M_\odot$) will be torn apart by tidal forces. For certain ($\lesssim 10^8 M_\odot$) black hole masses, the disruption will occur outside the event horizon and will be accompanied by an observable flare (Hills 1975; Rees 1988). Such flares can be used to study inactive SMBHs, which are otherwise inaccessible beyond the nearby ($\lesssim 100$ Mpc) universe.

We are now building our understanding of how observational properties of TDEs are affected by the SMBH. Theory claims to provide such a connection (e.g. Lodato et al. 2009; Guillochon et al. 2014), but uncertainties in the physics of the disruption, subsequent accretion and emission mechanisms are currently topics of debate (e.g. Strubbe & Murray 2015; Guillochon et al. 2014; Roth et al. 2015), and new models are vigorously being developed (e.g. Piran et al. 2015; Hayasaki et al. 2015; Svirski et al. 2015; Bonnerot et al. 2015).

TDEs are rare ($\sim 10^{-5} - 10^{-4}$ events per galaxy per year; Wang & Merritt 2004; Stone & Metzger 2015), and until recently, TDE candidates were discovered mostly in archival data (e.g. Donley et al. 2002; Gezari et al. 2006; Esquej et al. 2007). Now, however, wide-field transient surveys have started discovering TDEs in real time.

Generally, two types of TDE candidates have been identified:

1. High energy TDEs - The prototype of which is Swift J1644 ([Bloom et al. 2011](#); [Burrows et al. 2011](#); [Levan et al. 2011](#); [Zauderer et al. 2011](#)), with two other events known ([Bradley Cenko et al. 2012](#); [Brown et al. 2015](#)). These events display emission in γ -rays and X-rays as well as in the radio, but are not detected in the optical.
2. Optical-UV TDEs - The prototype of which is PS1-10jh ([Gezari et al. 2012](#)). About 8 other events are known ([Chornock et al. 2014](#); [Arcavi et al. 2014](#); [Holien et al. 2014, 2015, 2016](#)). Some events were detected also in the X-rays and radio (in addition to the optical and UV), but the X-ray and radio signatures are different than those of the high energy TDE candidates.

It is still not clear whether both of these classes of transients are TDEs, and if so, why they are so different from each other. One option raised is that some TDEs may launch jets, which when directed towards us, appear as the high energy events, but otherwise appear as the optical-UV events. It is still not clear if this is indeed the case (e.g. [van Velzen et al. 2013](#)).

Here we focus on the second type of TDE candidates, which is the relevant class for LSST, since they can be discovered in the optical. However, multi-wavelength coordinated observations of optically-discovered events are required in order to better understand the connection between the two types of candidates.

The first well-sampled TDE of the optical+UV class was PS1-10jh (discovered by Pan-STARRS; [Gezari et al. 2012](#)). [Arcavi et al. \(2014\)](#) later presented three new TDE candidates from PTF and one discovered by ASAS-SN, all with similar properties as PS1-10jh. These events exhibit blue colors, broad light curves, peak absolute magnitudes of ~ -20 and a $\sim t^{-5/3}$ decay at late times. This decay law has been suggested as a unique signature of accretion-powered TDE light curves ([Rees 1988](#); [Evans & Kochanek 1989](#); [Phinney 1989](#)). Early-time deviations from the $t^{-5/3}$ rate can be used to constrain the density profile of the disrupted star ([Lodato et al. 2009](#); [Gezari et al. 2012](#)). Late-time deviations would test the accretion power-source hypothesis altogether.

The spectral signatures of these TDEs are still a puzzle. PS1-10jh displayed only He II emission lines, lacking any signs of H. Some of the [Arcavi et al. \(2014\)](#) sample, however, do display H emission. In fact, a continuum of H / He emission ratios for this class of transients is being revealed, and is now a focus of theoretical modelling ([Strubbe & Murray 2015](#); [Roth et al. 2015](#)).

The second recent discovery relating to this new sample concerns their host galaxies ([Arcavi et al. 2014](#); [French et al. 2016](#)), most of which are post-starburst galaxies. These galaxies show little or no signs of on-going star formation, but their significant A stellar populations indicate that star formation ceased abruptly a few hundred Myr to a Gyr ago ([Dressler & Gunn 1983](#)). Galaxies with these characteristics often show signs of recent galaxy-galaxy mergers ([Zabludoff et al. 1996](#)), which produced the starburst and evolved the bulge. Optical-UV TDEs are intrinsically over abundant in post-starburst galaxies by a factor of $\sim 30 - 200$ (depending on the characteristics of the galaxy; [French et al. 2016](#)). The reason for the strong preference of TDEs for post-starburst galaxies has still not been determined.

LSST's contribution to TDE studies will be substantial. [van Velzen et al. \(2011\)](#) estimate that LSST could discover approximately 4000 TDEs per year. The main drivers for studying TDEs with LSST are:

- Measuring black hole masses: This involves fitting models to TDE light curves. It is also relevant to correlate these measurements with host galaxy properties (mass, bulge/disk decomposition).
- Constraining galactic dynamics by measuring the TDE rates as functions of black hole mass and galaxy types.
- Characterizing TDE emission signatures.

A metric is required for measuring how well TDEs can be identified and distinguished from supernovae and active galactic nuclei. In general, we expect TDEs to:

- Be located in the center of their host.
- Display approximately constant blue (few 10^4 K) colors.
- Evolve slowly (weeks-months).
- Not show past AGN-like variability.
- Preferentially peak around mag -20.
- Preferentially be hosted in a post-starburst galaxy.

These criteria are based on our current knowledge of optical TDEs, which is still in its early stages. The field is rapidly evolving, and it is possible that new observations will change the current picture of TDE emission. This metric is probably best combined with those discussed in [Section 6.3](#) for identifying supernovae, though the luminosity function of TDEs (or what constitutes a “typical” TDE light curve) is not yet known.

A second metric is required to assess the accuracy with which the black hole mass can be constrained from the TDE light curves. This metric can be based on existing theoretical models to fit simulated TDE light curves (such as TDEFit; [Guillochon et al. 2014](#)).

6.6.2 Cataclysmic Variables

Paula Szkody, Federica B. Bianco

Cataclysmic Variables (CVs) encompass a broad group of objects including novae, dwarf novae, novalikes, and AM CVn systems, all with different amplitudes and rate of variability. The one thing they all have in common is active mass transfer from a late type companion to a white dwarf. The variability ranges from minutes (due to the flickering in dwarf novae and novalikes, the pulsations in accreting white dwarfs in the instability strip, or the orbital periods of AM CVn systems), to hours (for the orbital periods of novae, dwarf novae and novalikes) to days (for the normal outburst lengths of dwarf novae) to weeks (for the outburst length of superoutbursts in short orbital period dwarf novae and the outburst recurrence time of normal outbursts in short orbital period dwarf novae) to months (for the outburst recurrence time of longer period dwarf novae, various state changes in novalikes and the decline in novae) and, finally, to years (for the outburst recurrence timescales of the shortest period dwarf novae and the recurrence times in recurrent novae). The amplitudes range from tenths of mags for flickering and pulsations to 4 mags for normal dwarf

novae and changes in novalike states up to 9-15 mags for the largest amplitude dwarf novae and classical novae.

These large differences make correct classification with LSST difficult but necessary in order to reach goals of assessing the correct number of types of objects for population studies of the end points of binary evolution. Multiple filters (especially the blue u and g) along with amplitude and recurrence of variation provide the best discrimination, as all CVs are bluer during outburst and high states of accretion. Long term evenly sampled observations can provide indications of the low amplitude random variability and catch some of the more frequent outbursts but higher sampling is needed to determine whether an object has a normal or superoutburst, to catch a rise to outburst or to a different accretion state or to follow a nova. Novae typically have rise times of a few days while the decline time and shape provide information as to the mass, distance and composition. The time to decline by 2-3 magnitudes is correlated with composition, WD mass and location in the galaxy, thus enabling a study of Galactic chemical evolution. As with SN, the diagnostic power for all these systems rests on color and sampling.

The metrics rely on a given cadence to provide shape and recurrence time of large variations that will distinguish between new novae, dwarf novae outbursts and identify high vs low states, as well as available blue colors to distinguish low amplitude variability that would indicate new pulsators or novalikes. The population studies rely on the numbers of long orbital period (low amplitude, wide outbursts) vs short orbital period (patterns of short outbursts followed by larger, longer superoutbursts) dwarf novae at different places in the galaxy, as well as the numbers of recurrent (1-10 yrs) vs normal novae (10,000 yrs, about 35/galaxy/yr). Objects particularly worthy of discrimination for later followup are the numbers of CVs containing highly magnetic white dwarfs. These can be identified by a metric of 10 yrs of data on a large sample where the magnitude for a majority of the years is a faint (low) state and a small percentage of time is a bright (high) state, combined with a red color (due to cyclotron emission from the magnetic accretion column).

6.6.3 LBVs and related non-supernova transients

Nathan Smith

There is a large and diverse class of visible-wavelength transient sources recognized in nearby galaxies that appear to be distinct from traditional novae and from SNe, and have often been associated with the giant eruptions of luminous blue variables (LBV), such as the 19th century outburst of η Carinae. Broadly speaking, members of this class of transients share the common properties that they have peak luminosities below those of most core-collapse SNe and more luminous than novae and CVs (absolute magnitudes of roughly -9 to -15 mag). They also have H-rich spectra (usually) with relatively narrow lines that indicate modest bulk outflow velocities of 10^2 to 10^3 km s $^{-1}$ (although some have exhibited small amounts of material at faster speeds). They tend to evolve on fairly long timescales of weeks to years (although sometimes they exhibit a quick rise to peak similar to SNe II-P). This group of transients has gone by many names, such as LBV eruptions, SN impostors, Type V supernovae, intermediate-luminosity optical (or red) transients, as well as others that often include a physical interpretation. For brevity, these are often collectively referred to as “LBVs”, although many of them may not actually be LBVs. Carinae, however,

Observationally, these eruptions are understood to represent important and dramatic mass-loss episodes in the lives of massive stars, based on empirical estimates for the amount of ejected matter. These eruptions are expected to instigate mass loss that is comparable to or more important than metallicity-dependent winds of massive stars. This mode of mass loss, regardless of the mechanism, may be a very important ingredient in the evolution of massive stars that is currently not included in stellar evolution models. Correcting this is one of the key science drivers in trying to understand the physics these eruptions.

An important empirical discriminant of subgroups in this class comes from their progenitor stars. Some are indeed seen to be very luminous, blue supergiant stars consistent with traditional LBVs. Some, however, have somewhat less luminous, heavily dust-obscured progenitor stars that have been associated with either dust enshrouded blue or red supergiants, or alternatively, with super-AGB stars of $8\text{--}10 M_{\odot}$, with uncertainty . arises because when the objects are fully obscured by dust, one cannot actually measure the star's temperature, and the bolometric luminosities of super-AGB and red and blue supergiants overlap. Unfortunately, cases when we have strong constraints on the quiescent progenitor are rare, and once they reach their peak luminosity, there is a great deal of overlap in observed properties.

Theoretically, these eruptions are not understood. There are many ideas, but few if any confirmed mechanisms tied to observed objects. Some theoretical ideas involve (1) winds driven by super-Eddington instabilities (although the root cause for suddenly exceeding the Eddington limit remains unexplained), (2) hydrodynamic explosions caused by deep-seated energy deposition, such as unsteady nuclear burning, (3) accretion onto companion stars in binary systems (degenerate or not), (4) mergers in binary and triple systems, (5) electron-capture SNe, and (6) “failed SNe” associated with a weak explosion and envelope ejection that results from black hole formation during core collapse. Because of the relatively low total energy indicated by radiative luminosities and outflow speeds, these are usually discussed as non-terminal eruptions, however, the last two are terminal events that are less luminous and lower energy than normal SNe, and the last 3 should only occur once for a given source. Together with several well-studied examples that indicate repeating eruptions, there are indeed many cases where only one such transient has been seen at the same position, and some cases where late-time observations suggest that no source has survived with a luminosity comparable to its progenitor. All these theoretical mechanisms may lead to similar observed phenomena: weak explosions, moderate luminosities, slow expansion, dusty aftermath, but this class of objects may represent a mixed-bag of different mechanisms that get lumped together by default as “other” because they are not traditional SNe.

An area of recent interest is that eruptive non-terminal transients have been observed, in some cases, to precede much more powerful explosions that are seen as Type IIn supernovae. Detectability of SN precursors is discussed in [Chapter 4](#). Even if the pre-SN transients are not observed directly, pre-SN eruptive mass loss is inferred based on circumstellar interaction diagnostics of the SN. These SN precursors have observed or inferred properties that are very similar to LBVs and related transients, but then again, most of the LBVs and other SN impostors have been observed for decades and have not gone SN (yet). *Being able to distinguish which of these optical transients are SN precursors and which are not is a major science driver.* The amount of mass lost in a precursor eruption may dramatically alter the type of SN that is observed. There may also be a continuum of energies in pre-SN outbursts, extending down to more normal classes of core-collapse SNe, but these may often go unrecognized unless the SN is caught very early after explosion.

Rates for these LBV-like eruptions are very poorly constrained, largely because most previous SN and transient searches with small telescopes have been optimized for finding more luminous SNe in a larger volume. This field begun to change with recent surveys, and will be revolutionized with LSST. From discovered examples we have, numbers are very roughly consistent with a volumetric rate comparable to that of core-collapse SNe or larger. Rates of individual subclasses are not well constrained, and limited information often makes classification into various subgroups difficult or highly subjective. The “rate” also depends on how faint the lower limit of inclusions is; evidence suggests that the brightest events are more rare, and that numbers increase as one moves to lower luminosity. At the faint end, it becomes difficult to distinguish between eruptions and regular variability of LBVs, or between massive star eruptions and CVs. With deep LSST stacks identifying faint CV in quiescent states this will also change dramatically in the LSST age, with the unavailing of detailed progenitor information. Having deep, pre-eruption characterization of sources at the positions of these eruptive transients (as well as SN precursors) will likely be a major contribution of LSST.

In terms of timescales, many of the eruptive transients exhibit rise and decline timescales similar to normal SNe II-P or II-L, but with fainter peak luminosity. For these, observational cadence requirements will be the same as SNe. For some eruptive transients, however, the rise timescales can be very long (rising a few magnitudes in years). While LSST’s cadence will certainly be fast enough, being able to discover slowly rising transients that do not change much from night to night will be an important metric.

For the faster-rising transients, spectroscopic followup is needed to discriminate these from normal SNe, and also contextual information about the host galaxy (and hence, the absolute magnitude) is needed to differentiate these non-terminal eruptions from Type IIn supernovae (their spectra look similar, although LBVs do tend to have narrower lines). Spectral and color evolution, as well as information about the progenitor, is needed to distinguish among subgroups within the class. Multiwavelength followup is often extremely valuable or even essential; i.e. mid-IR tells us if an optically invisible source is cloaked in a dust shell but still quite luminous; Xrays and radio tell us if an expanding shock wave is the likely source of persistent luminosity. For these reasons, nearby cases will continue to be the most valuable in deciphering the physics of subclasses, whereas the increased volume in which LSST discovers these fainter transients will drastically improve our understanding of their rates. Armed with both a better understanding of their underlying physics and characterization, as well as their rates and duty cycles, these eruptive events can then be incorporated into stellar evolution models and population synthesis/feedback models.

7 The Magellanic Clouds

Chapter Editors: *David Nidever, Knut Olsen*

The Magellanic Clouds have always had outsized importance for astrophysics. They are critical steps in the cosmological distance ladder, they are a binary galaxy system with a unique interaction history, and they are laboratories for studying all manner of astrophysical phenomena. They are often used as jumping-off points for investigations of much larger scope and scale; examples are the searches for extragalactic supernova prompted by the explosion of SN1987A and the dark matter searches through the technique of gravitational microlensing. More than 17,000 papers in the NASA ADS include the words “Magellanic Clouds” in their abstracts or as part of their keywords, highlighting their importance for a wide variety of astronomical studies.

An LSST survey that did not include coverage of the Magellanic Clouds and their periphery would be tragically incomplete. LSST has a unique role to play in surveys of the Clouds. First, its large $A\Omega$ will allow us to probe the thousands of square degrees that comprise the extended periphery of the Magellanic Clouds with unprecedented completeness and depth, allowing us to detect and map their extended disks, stellar halos, and debris from interactions that we already have strong evidence must exist (REFS). Second, the ability of LSST to map the entire main bodies in only a few pointings will allow us to identify and classify their extensive variable source populations with unprecedented time and areal coverage, discovering, for example, extragalactic planets, rare variables and transients, and light echoes from explosive events that occurred thousands of years ago (REFS). Finally, the large number of observing opportunities that the LSST 10-year survey will provide will enable us to produce a static imaging mosaic of the main bodies of the Clouds with extraordinary image quality, an invaluable legacy product of LSST.

We have several important scientific questions:

1. What are the stellar and dark matter mass profiles of the Magellanic Clouds? Map extended disk, halo, debris, and streams. Use streams as probes of total mass profile. RR Lyrae give potential for three-dimensional stellar profile.
2. What is the satellite population of the Magellanic Clouds? Discovery of dwarfs by DES and other surveys illuminating for understanding distribution of dark matter subhalos and how galaxies form in them (REFS)
3. What are the internal dynamics of the Magellanic Clouds? Proper motions from HST and from the ground (REFS) have measured the bulk motions of the Clouds and have, in combination with spectroscopy, begun to unravel the three dimensional internal dynamics of the Clouds.

4. How do exoplanet statistics in the Magellanic Clouds compare to those in the Milky Way? Lund calculation shows can measure transits of Jupiter-like planets, Clouds are lower metallicity environment
5. Identify and characterize the variable star and transient population of the Clouds. Population studies, linking to star formation and chemical enrichment histories, etc, from Szkody et al. DD white paper.
6. Light echoes from supernovae and explosive events. Echoes can give view of such events unavailable by any other means, ref. papers by Rest et al.

These questions can be grouped into main overarching science themes:

1. **Galaxy formation evolution:** The study of the formation and evolution of the Large and Small Magellanic Clouds (LMC and SMC, respectively), especially their interaction with each other and the Milky Way. The Magellanic Clouds (MCs) are a unique local laboratory for studying the formation and evolution of dwarf galaxies in exquisite detail. LSST's large FOV will be able to map out the three-dimensional structure, metallicity and kinematics in great detail.
2. **Stellar astrophysics & Exoplanets:** The MCs have been used for decades to study stellar astrophysics, microlensing and other processes. The fact that the objects are effectively all at a single known distance makes it much easier to study them than in, for example, the Milky Way. LSST will extend these studies to fainter magnitudes, higher cadence, and larger area.

Many different types of objects and measurements with their own cadence “requirements” will fall into these two broad categories (with some overlap). These will be outlined in the next section.

A very important aspect of the “galaxy evolution” science theme is not just the cadence but also the sky coverage of the Magellanic Clouds “mini-survey”. A common misunderstanding is that the MCs only cover a few degrees on the sky. That is, however, just the central regions of the MCs akin to the thinking of the Milky Way as the just the bulge. The full galaxies are actually much larger with LMC stars detected at $\sim 21^\circ$ (~ 18 kpc) and SMC stars at $\sim 10^\circ$ (~ 11 kpc) from their respective centers. The extended stellar debris from their interaction likely extends to even larger distances. Therefore, to get a complete picture of the complex structure of the MCs will require a mini-survey that covers ~ 2000 deg 2 . At this point, it not entirely clear how to include this into the metrics. Note, that for the second science case this is not as much of an issue since the large majority of the relevant objects will be located in the high-density, central regions of the MCs.

[Below is a generic list of things we want to measure in the Magellanic Clouds.](#)

1. Deep Color Magnitude Diagrams
2. Proper Motions
3. Variable stars
4. Transients
5. Transiting Exoplanets
6. Light-echoes

-
7. Gyrochronology
 8. Interstellar scintillation

7.1 Future Work

In this section we provide a short compendium of science cases that are either still being developed, or that are deserving of quantitative MAF analysis at some point in the future.

7.1.1 The Proper Motion of the LMC and SMC

David Nidever, Knut Olsen

In the last decade work with *HST* has been able to measure the bulk tangential (in the plane of the sky) velocities (~ 300 km/s) of the Magellanic Clouds (Kallivayalil et al. 2016a,b,2013) and even the rotation of the LMC disk ([van der Marel & Kallivayalil 2014](#)). Gaia will measure precise proper motions of stars to ~ 20 th magnitude which will include the Magellanic red giant branch stars. LSST will be complementary to Gaia and measure proper motions of stars in the $\sim 20\text{--}24$ mag range that includes Magellanic main-sequence stars which are far more numerous than giants, and, therefore, more useful for mapping extended stellar structures. The LSST 10-year survey proper motion precision will be $\sim 0.3\text{--}0.4$ mas/yr at LMC main-sequence turnoff at $r \approx 22.5\text{--}23$. This will allow for accurate measurement of proper motions of *individual stars* at the $\sim 5\sigma$ level.

Besides measuring kinematics, the LSST proper motions can be used to produce clean samples of Magellanic stars. In addition, LSST proper motions can be used to improve star/galaxy separation which is quite significant for faint, blue Magellanic main-sequence stars.

Metrics

The natural Figure of Merit for this science case is the precision with which the proper motion of the Magellanic Clouds can be measured. This is likely to depend on the following diagnostic metrics:

- Single star proper motion precision, possibly quantified as. the significance level (σ -level) of the proper motion measurement of one Magellanic MSTO star ($r=23$ mag). We would expect this to take values of ~ 2.0 mas yr^{-1} / σ_{pm} .
- Another useful diagnostic metric would be the surface brightness limit of the Magellanic structures, using MSTO stars.
- A metric quantifying how much of the expected Magellanic debris/structure [Besla et al.](#) (from [2012](#)) model we can detect would allow the proper motion science case to be extended to peripheral structures. This would depend mostly on the area covered, but we could also use the surface brightness limit (calculated above) directly.

8 Active Galactic Nuclei

Chapter editors: *Ohad Shemmer, Timo Anguita*.

Contributing authors: *Vishal Kasliwal, Christina Peters, Niel Brandt, Gordon Richards, Scott Anderson, Robert Wagoner*

8.1 Introduction

This chapter discusses the potential effects of the LSST observing strategy on AGN science. In short, there appears to be a consensus among the AGN and galaxies communities that AGN science will benefit from the most uniform cadence in terms of even sampling for each band and uniform sky coverage. It is also expected that any reasonable perturbation to the nominal LSST observing strategy will not have a major effect on AGN science. This chapter attempts to identify all the areas of AGN science that may be affected by the observing strategy and to point out the metrics that can be used to quantify any potential effects. Since the total number of metrics that can be quantified is quite large, and the potential effects are not likely to be significant in most cases, the goal of this chapter is to identify potential “show stoppers” that may undermine key AGN research areas. For example, certain perturbations may reduce significantly the number of “interesting” AGNs, such as $z > 6$ quasars, lensed quasars, or transient AGNs. Another example is photometric reverberation mapping which is one of LSST’s greatest potential advantages for AGN research but is also very sensitive to the cadence; care must be taken to ensure that the observing strategy does not undermine the ability to make the best use of this method.

Note: Transient AGN and tidal disruption events are discussed in detail in the transients chapter ([Chapter 6](#)), while gravitationally-lensed AGN are covered in the cosmology chapter ([Section 9.6](#)).

8.2 AGN Selection and Census

Ohad Shemmer, Niel Brandt, Gordon Richards, Vishal Kasliwal, Scott Anderson

The primary goal for AGN science is to maximize the discovery of AGN with the LSST and construct the largest possible inventory of sources spanning the widest possible ranges in the redshift-luminosity parameter space. This, in turn, will provide tighter constraints within the context of various cosmological science cases, such as quasar clustering, $z > 6$ quasars and reionization, and strong gravitational lensing.

8.2.1 Target measurements and discoveries

It is expected that $\approx 10^7 - 10^8$ AGNs will be selected in the main LSST survey using a combination of criteria, split broadly into four categories: colors, astrometry, variability, and multiwavelength matching with other surveys. The LSST observing strategy will affect mostly the first three of these categories as described further below.

Colors: The LSST observing strategy will determine the depth in each band, as a function of position on the sky, and will thus affect the color selection of AGNs. Additionally, it will affect the reliability of the actual determination of the color, due to the non-negligible time gaps between observations using two different filters for a particular LSST field. This will eventually determine the AGN $L - z$ distribution and, in particular, may affect the identification of quasars at $z \gtrsim 6$ if, for example, Y -band exposures will not be sufficiently deep.

Variability: AGNs can be effectively distinguished from (variable) stars, and from quiescent galaxies, by exhibiting certain characteristic variability patterns (e.g., [Butler & Bloom 2011](#)). Picking the right cadence can increase the effectiveness of AGN selection. Ultimately, hybrid color and variability algorithms will be employed to enhance the selection process (e.g., [Peters et al. 2015](#)); this may be particularly important for selecting obscured sources which comprise a significant fraction of the entire AGN population.

Astrometry: In cases where selection by color and variability is insufficient for a reliable identification, AGNs can be further selected among sources having zero proper motion, within the uncertainties. The LSST cadence may affect the level of this uncertainty in each band, and may therefore affect the ability to identify (mostly fainter) AGN. Differential chromatic refraction (DCR), making use of the astrometric offset a source with emission lines has with respect to a source with a featureless power-law spectrum, can help in the selection of AGNs and in confirming their photometric redshifts ([Kaczmarszak et al. 2009](#)). The DCR effect is more pronounced at higher airmasses. Therefore, it could be advantageous to have at least one visit, per source, at airmass greater than about 1.4 (though of course there are trade-offs versus the additional extinction, for faint sources). AGN selection and photometric redshift confirmation may be affected since the LSST cadence will affect the airmass distribution, in each band, for each AGN candidate. The deep drilling fields (DDFs) will provide a truth table for determining the predictive power of the DCR method as a function of the airmass distribution of the observations.

The most critical measurement for the AGN census is having a reliable and precise redshift for each source, obtained both from a photometric and an astrometric redshift.

8.2.2 Metrics

The following are most important for the AGN census:

- 1) Determine the mean (averaged across the sky) **uncertainty on astrometric redshifts derived from DCR** as a function of airmass, image quality, and limiting magnitude. These uncertainties should be compared to the corresponding uncertainties on the photometric redshift.
- 2) Estimate the **number of quasars at $z > 6$ that LSST can discover** during a single visit, as well as in the entire survey, and verify that these numbers do not fall short of the original

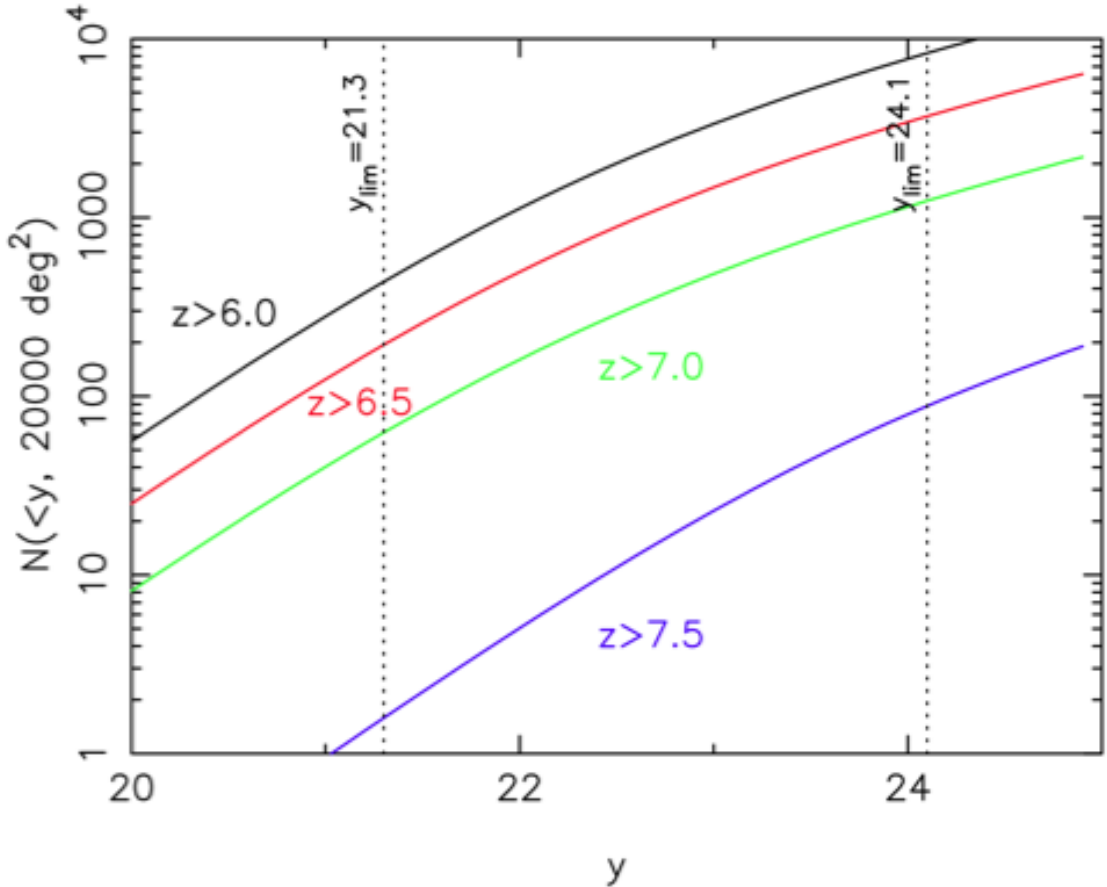


Figure 8.1: Number of quasars at $z > 6$ that LSST is expected to discover based on Y -band limiting magnitude in a single epoch (entire survey) marked by the first (second) dotted line from the left.

predictions. This requires computing the limiting Y -band magnitude, averaged across the sky for the nominal OpSim, as well as assessing the ability to reject L and T dwarfs via astrometry.

3) Assess the effect of **non-simultaneous colors on AGN selection**. First, the term color should be clearly defined. Potential definitions include the difference between the co-adds in two bands for the entire survey (or at a certain point in time during the survey), the difference between the median magnitude in each band during the survey, or the difference between observations in two bands that are closely spaced in time. Next, each source would be represented as an ellipse in color-color space. The aim is to assess the sizes of the ellipses and how these sizes could be minimized by perturbing the current cadence.

4) Assess how the sampling affects the selection of AGN by variability (e.g., interactions with red-noise power spectrum).

8.2.3 OpSim Analysis

For assessing the limitations of DCR on the $L - z$ plane of LSST AGNs, one needs to obtain from OpSim the current maximal airmasses for each band, and the associated image quality and limiting magnitude. The current maximal airmasses, per band, averaged across the sky are: 1.41, 1.50, 1.51, 1.51, 1.51, and 1.51 for u, g, r, i, z, Y , respectively. Need to convolve this with the seeing in each band to obtain the dependence on airmass and image quality. This output should be converted into the mean and spread of the uncertainty on the astrometric redshifts. The best way to obtain this is to fold the astrometric redshift estimation from DCR into MAF. Ultimately, one needs to check the implications of higher airmasses and limiting magnitudes on the ability to obtain more accurate and precise astrometric redshifts.

For predicting the number of detected $z > 6$ quasars the current enigma_1189 OpSim for the main, i.e., WFD survey, gives a single-visit 5σ -depth $Y = 21.51$ mag, and for the final co-added 5σ -depth the median is $Y = 24.36$. These limits are correspondingly deeper (i.e., better) than the original predictions (see Fig. 8.1).

As for general AGN selection, the effects of the sampling on variability selection should be assessed, and the amplitudes of the uncertainties in color-color space and how these depend on the cadence should be simulated.

Go to: • [the start of this section](#) • [the start of the chapter](#) • [the table of contents](#)

8.3 Disc Intrinsic AGN Variability

Ohad Shemmer, Vishal Kasliwal, Robert Wagoner

A variety of AGN variability studies will be enabled by LSST. These are intended to probe the physical properties of the unresolved inner regions of the central engine. Relations will be sought between variability amplitude and timescale vs. L , z , λ_{eff} , color, multiwavelength and spectroscopic properties, when available. For example, LSST AGNs exhibiting excess variability over that expected from their luminosities will be further scrutinized as candidates for lensed systems having unresolved images with the excess (extrinsic) variability being attributed mainly to microlensing.

Measuring time-delayed responses between variations in the continuum flux in one LSST band to the continuum flux in another, will be one of the main themes of AGN science in the LSST era (e.g., Chelouche 2013; Chelouche & Zucker 2013; Edelson et al. 2015; Fausnaugh et al. 2015). Such measurements can test accretion disk models in a robust manner for a considerably larger number of AGNs than is currently feasible with microlensing (see section 8.4).

Theories of the hierarchical merger of dark matter halos over cosmic time predict that galaxy-galaxy mergers should result in the formation of a large number of binary SMBHs. This population is predicted to be a strong, stochastic contributor to the overall gravitational wave background (Taylor et al. 2015). The inspiral of gravitationally bound pairs of SMBHs formed by a major merger may ‘stall’, reducing the gravitational wave signal (Colpi 2014). Potentially periodic AGN variability, leading to tentative discoveries of binary SMBHs (e.g., D’Orazio et al. 2015; Graham et al. 2015; Liu et al. 2015), may be feasible for LSST for periods ranging from a few days up to ~ 3 yr over

the entire survey. The fraction of close SMBHs, tentatively detected by LSST, may provide strong constraints on the strength of the gravitational wave signal expected from the inspiral.

In the deep-drilling fields (DDFs), the LSST sampling is expected to provide high-quality power spectral density (PSD) functions for $\approx 10^5 - 10^6$ AGNs across L , z , and λ_{eff} down to frequencies of $\sim 1 \text{ d}^{-1}$. These PSDs can enhance AGN selection, and can be used to constrain the SMBH mass and accretion rate/mode, as well as enable searching for periodic or quasi-periodic oscillations (QPOs).

The high-frequency QPO (HFQPO) periods expected from the inner accretion disk (which provide stable clocks located closer to the horizon as the BH spin increases) can be estimated from those of the fundamental g -mode, which agree with the observed HFQPO frequencies in stellar-mass BH binaries. Utilizing the theoretical upper bounds for BH spin and L/L_{Edd} , and the lower bound to the k - and bolometric correction $B_n(z)$, one obtains $\log P(\text{hr}) > 0.4(1 - m_n) + \log[(1 + z)D_{\text{L}}(z)^2]$ for magnitude m_n in a particular band n and luminosity distance $D_{\text{L}}(z)$. The k - and bolometric correction $B_n(z)$ is a decreasing function of BH mass, but an increasing function of BH spin. The Lyman-alpha forest limits the redshift range to $z < 2.7$ for g -band observations. The HFQPOs will be weaker within longer wavelength bands. For instance, for $m_g < 23$ and the optimal $z = 2.7$, the HFQPO period is $P > 4 \text{ hr}$. Searching for HFQPOs in the DDFs will be most effective if the sampling frequency in those fields for the u and g bands is at least nightly, i.e., $\gtrsim 3000$ visits, per band, during the entire survey. Given that the period of a typical HFQPO is related to the SMBH mass by $P(\text{hr}) \approx (1.1 - 4.0)(1 + z)(M/10^7 M_{\odot})$, LSST will be sensitive to probing SMBHs with $M < 10^7 M_{\odot}$ using HFQPOs.

8.3.1 Target measurements and discoveries

In the main survey, standard time-series analysis techniques will be used for measuring time delays between pairs of continuum bands and for detecting periodic AGNs. Correlation analyses will search for relations between AGN variability properties and their basic physical parameters. In the DDFs, such analyses will enable probing deeper and more frequently, resulting in higher-quality data that will provide stronger constraints; the only drawback is the relatively smaller number of sources available at the high-luminosity end.

A key measurement enabled by the DDFs is a high-quality PSD, in six bands, for the largest number of AGNs to date. These PSDs, which are rich in diagnostic power, will be used to search for ‘features’ such as QPOs and breaks, as well as power-law slopes, that can help constrain SMBH masses and accretion rates. Additionally, the PSDs can serve as selection tools, to more effectively distinguish AGNs from variable stars, as well as a basis to propose cadence perturbations to further enhance AGN selection.

A high-quality PSD, extending to high frequencies (reaching $\sim 1 \text{ min}$ timescales for stacked PSDs), can effectively distinguish AGNs from other variable sources, assuming AGN light curves are described by a particular continuous-time autoregressive moving average model (C-ARMA; [Kelly et al. \(2014\)](#)), i.e., C-ARMA(2,1), corresponding to a damped harmonic oscillator. Determination of the parameters that describe the PSD requires light curve sampling at least as frequent as $\sim 1 \text{ d}^{-1}$. Figure 8.2 shows the frequency dependence of the spectral index of the PSD for one particular AGN, Zw 229-15, observed with *Kepler*. The light curve of this source is well-described

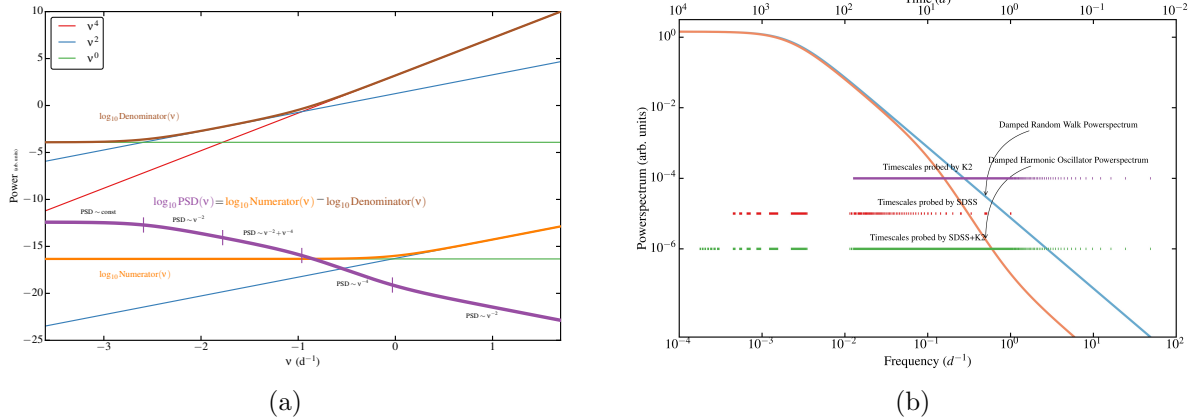


Figure 8.2: (a) shows the PSD of Zw 229-15 as a function of frequency, obtained from *Kepler* photometry. The PSD (purple) is the ratio of an even polynomial numerator (orange) to an even polynomial denominator (brown). This AGN is well-described by a C-ARMA(2,1) model; different powers of frequency dominate its PSD at different frequencies depending on the hyperparameters of this model. The wide frequency range enables detection of PSD spectral index variations ranging between 0 and 4. Clearly, the light curve of this AGN must be sampled on timescales *shorter* than 1 – 5 days in order to observe the ν^{-4} behavior characteristic of a higher order random walk. This is illustrated in (b) where we see the frequencies and time intervals probed by SDSS, Kepler and a light curve constructed by combining the two datasets (SDSS+K2). Each vertical dashed line corresponds to a pair of observations separated by the indicated δt (top axis). We plot (for illustration), two C-ARMA models with the same overall power – a damped random walk, i.e. a C-ARMA(1,0) process, and a damped harmonic oscillator, i.e. a C-ARMA(2,1) process. It is clear that SDSS (Kepler) cannot probe the highest (lowest) frequencies. However the combination of the two can cover the full frequency range. The LSST cadence should be chosen to provide similar temporal coverage in the DDFs.

by a C-ARMA(2,1) model. The C-ARMA(2,1) model is a higher order random walk than the damped random walk (DRW) model of Kelly et al. (2009), which corresponds to a C-ARMA(1,0) model. Recent variability studies indicate that the simple C-ARMA(1,0) model is insufficient to model AGN variability because the spectral index of its PSD is mathematically constrained to be 2 (Kelly et al. 2014; Kasliwal et al. 2015; Simm et al. 2015). Insufficient sampling of an AGN light curve (e.g., a few times a month), can therefore result in the erroneous conclusion that a DRW model adequately characterizes the variability.

Accurate recovery of the PSD parameters can be greatly enhanced by increasing the sampling frequency. To illustrate the effects of the cadence, Figure 8.3 shows how the inferred joint distribution of two hyperparameters of the C-ARMA(2,1) model, the oscillator timescale and the damping ratio, depend on the sampling frequency. Degrading the sampling frequency from $1/(30 \text{ min})$, corresponding to *Kepler* light curves, to $1/(3 \text{ d})$, corresponding to the nominal DDF cadence, changes both the size and the shape of the joint distribution, degrading both the accuracy and correlation of the inferred hyperparameters. Furthermore, the C-ARMA formalism may enable adjusting the cadence of the DDFs once the LSST survey begins to determine the sampling pattern in real time.

8.3.2 Metrics

While additional work is required for determining the optimal cadence in order to fully capture AGN accretion physics and to enhance AGN selection, it is clear that even the nominal DDF

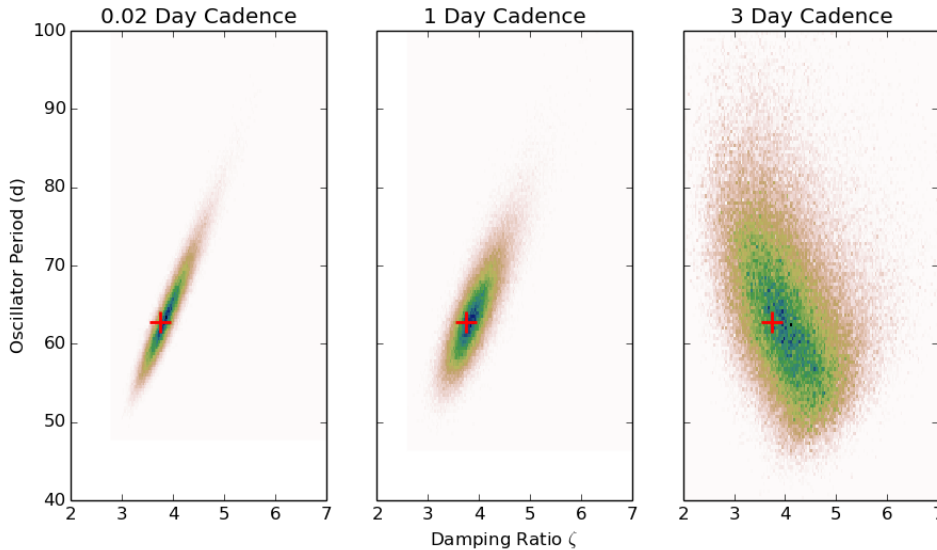


Figure 8.3: The effect of sampling frequency on hyperparameter estimation (courtesy of J. Moreno). Light curves were generated using a C-ARMA(2,1) model using the best-fit parameters for Zw 229-15, observed with *Kepler*, indicated by the red cross in each panel. The light curve was then down-sampled to simulate the effect of observational cadence. Constraints on the oscillator period and damping ratio begin to widen noticeably at 3-day sampling. At 1 week and longer cadence (not shown), one does not recover the correct model order. This strongly indicates the importance of further study to refine the cadence requirements for LSST.

sampling (in enigma_1189) is barely sufficient, and more frequent sampling would have been ideal. The ability to detect HFQPOs should also improve by increasing the sampling frequency, the amplitudes of such features are quite uncertain, as are the (short) duty cycles. Observations, theory and numerical simulations have only suggested that the fractional modulation should be small (less than a few percent). Thus it is not obvious how to choose a metric and observing strategy to maximize it, other than increasing the sampling frequency to at least nightly samplings in the g and u bands (i.e., increasing the sampling frequency in the DDFs at least by a factor of ~ 3).

Specific metrics include:

- 1) LSST can make a significant contribution using the C-ARMA formalism is the selection of low-luminosity AGN (LLAGN), i.e., sources with $L \lesssim 10^{42} \text{ erg s}^{-1}$, in the DDFs. Such sources are likely to be missed by traditional color-variability selection algorithms due to a strong host contribution. The metric to be developed should assess how the number of selected LLAGN depends on the sampling frequency in each band.
- 2) Assessing the standard deviation of the error in recovered time-lag between bands, τ , using a cross-correlation analysis. The goal is to minimize $\sigma_{\Delta\tau}$. Additionally, one should assess the worst case estimate of the time-lag between bands, i.e., minimizing $\max |\Delta\tau|$.
- 3) Determining the fractional error on the slopes and features of the PSD. Assuming that AGN variability is parametrized by a C-ARMA process with autoregressive roots $\{\rho_i : 1 \leq i \leq p\}$, the damping timescales and QPO centers are given by $\tau_i = 1/|\Re(\rho_i)|$ and $\text{QPO}_i = 2\pi/|\Im(\rho_i)|$,

respectively. One needs to investigate how well different sampling strategies recover each damping timescale and QPO center for a range of assumed models. The choice of appropriate models can be guided by using variability data from K2 observations of SDSS quasars.

8.3.3 Discussion

Overall, the key requirement is to increase the nominal sampling frequency in the DDFs by at least a factor of 3, i.e., having at least 3000 visits, per band, during the entire survey. Alternatively, if this sampling is not feasible for all the DDFs, it would be beneficial to identify a subset of “special” DDFs which would be sampled by this frequency. Such DDFs would also benefit from being circumpolar, e.g., the Magellanic Clouds, enabling a more uniform sampling to produce the highest quality PSDs.

Go to: • [the start of this section](#) • [the start of the chapter](#) • [the table of contents](#)

8.4 AGN Size and Structure with Microlensing

Timo Anguita

Microlensing due to stars projected on top of individual gravitationally-lensed quasar images produces additional magnification. Using the fact that the Einstein radii of stars in lensing galaxies closely match the scales of different emission regions in high-redshift AGNs (micro-arcseconds), analyzing microlensing induced flux variations statistically on individual systems allows us to measure “sizes” of AGN regions.

Assuming a thermal profile for accretion disks, sizes in different emission wavelengths will be probed and as such, placing constraints on the slope of this thermal profile. Given the sheer number of lensed systems that LSST is expected to discover (~ 8000), this will allow us to stack systems for better constraints and hopefully determine the *luminosity and redshift evolution of the disk size and profile*. Due to the typical relative velocities of lenses, microlenses, observers (Earth) and source AGN, the microlensing variation timescales are between months to a few decades.

8.4.1 Target measurements and discoveries

Analysis of microlensing induced variability will allow the measurement of accretion disk sizes R_λ and their thermal profile slope α . This needs to be done per system discovered. Assuming ~ 1000 lensed quasars with high quality light curves (i.e. that allow time delay measurements, see [Section 9.6](#)), a relationship between size, thermal profile slope, black hole mass and accretion disk luminosity will likely be derived.

How precisely are we going to be able to measure these parameters for a given survey strategy? This is not a simple question to answer due to the significant degeneracies that plague the phenomenon. This is what our MAF metric will quantify. Before we design this, we need to predict and statistically quantify the degeneracies and sensitivities.

The quasar microlensing optical depth is ~ 1 , so every lensed quasar should be affected by microlensing at any given point in time to a different extent. Note, however, that the larger the apparent magnification, the more stringent are the constraints on the geometric information that can be obtained of the source. [Mosquera & Kochanek \(2011\)](#) studied the expected microlensing timescales for all known lensed quasars at the time. They found that the median Einstein crossing time scales, which can statistically be interpreted as the time between high magnification events, in the observed *I*-band, is of the order of ~ 20 yr (with a distribution between 10 and 40 yr). Additionally, the source crossing time (duration of a high magnification event) is ~ 7.3 months (with a distribution tail up to 3 yr). This basically means that out of all the lensed quasar *images* (microlensing between images is completely uncorrelated) about half of them will be quiescent during the 10 yr baseline of LSST. However, since the typical number of lensed images is either two or four, this means that, statistically, in every system, one (for doubles) or two (for quads) high magnification events should be observed in 10 yr of LSST monitoring.

Note that, the important cadence parameter is the source crossing time. Ideally, high magnification events would need to be as uniformly sampled as possible. The ~ 7.3 months crossing time is the median for the observed *i*-band, but this time would be significantly shorter for bluer bands: for a thermal profile with slope α : $R_\lambda \propto \lambda^\alpha$ implies source crossing time $t_s \propto \lambda^{1/\alpha} \rightarrow t_u = t_i \times (\lambda_u / \lambda_i)^{1/\alpha}$. For a Shakura-Sunyaev slope of $\alpha = 0.75$ this would correspond to $\sim 7.3 \times (3600/8140)^{4/3}$ months which is ≈ 2.5 months in the *u*-band.

In terms of the cadence, at least three evenly sampled data points per band within two to three months would be preferred to be able to map the constraining high magnification event, and these would hopefully be uniformly spaced. Additionally, LSST can trigger imaging of high-magnification events with dedicated facilities to enhance these constraints. More frequent sampling (e.g., in the DDFs) would increase such constraints significantly. However, since lensed quasars are not that common, this smaller area would mean that only a modest number (< 100) of suitable systems will be monitored in the DDFs.

Regarding the season length, the “months” timescale of high magnification events very likely means that we can/will miss high magnification events in the season gaps, at least in the bluer bands.

“Show stopper”: observations spread on timescales larger than 3 months. This would likely miss the high magnification events. In those cases we could perhaps consider close consecutive photometric bands as equivalent accretion disk regions, however this would mean weaker constraints on the thermal profile.

Caveats: The above estimates correspond to those obtained by [Mosquera & Kochanek \(2011\)](#) for all *currently* known lensed quasars. It is important to take into consideration that the timescales directly depend on the projected velocities of the three-plane system: the redshifts of the lens and source as well as their respective peculiar velocities along the CMB dipole velocity in the direction towards the lensing galaxies (observer’s peculiar velocity). Therefore, every new system will have a different timescale. Furthermore, the discussion above is centered on high magnification events. Even though these produce the most valuable information, low magnification events or *no* magnification events can set constraints on the structure of high redshift AGN as well as the lensing galaxies (e.g. [Gil-Merino et al. 2005](#)). Finally, long timescale high accuracy multiband data as will be delivered by LSST have never been obtained to date for any lensed system. Coupling this fact

to a factor ~ 10 increase on the number of lensed quasars known, LSST will enable of totally new and unprecedented perspectives for microlensing studies.

Microlensing Aided Reverberation Mapping: Given that microlensing mostly affects continuum emission rather than BELR emission, microlensing can enable the disentangling of the BELR emission plus the continuum emission in single photometric bands, allowing the use of single broad band PRM measurements ([Sluse & Tewes 2014](#)). As with the two-band PRM method discussed above, the denser (and the longer) the sampling, the more accurate are the constraints that can be obtained for the time delays. This method allows constraining both the accretion disk structure as explained above and the BELR. The only additional requirement is one spectroscopic observation to constrain the “macro” magnification ratios from narrow emission lines.

8.4.2 Metrics

Metrics for these section need to be defined by using simulated light curves that take into account the several parameters that come into play in quasar microlensing. These include: the time gap between visits in the same band, projected CMB velocity, simulated peculiar velocities and redshifts of lenses and sources as well as “macro” lens model parameters (i.e., surface mass density and shear projected on top of lensed quasar images). Two metrics are currently in consideration:

High Magnification Events recovery metric: This metric will measure the number of high magnification events recovered/missed considering the cadence and season length in every LSST band and as the precision of the brightness measurement.

Accretion disk size and slope metric: This metric will do a full analysis of the “pure” microlensing light curves to recover these two physical AGN parameters. The figure of merit would be the accuracy of the measurement.

Since microlensing signal can only be obtained after time delays between images have been measured, both metrics need close interaction with time delay measurements. As such, the “Time Delays Challenges” (see [Section 9.6](#)) will include complete microlensing signal simulations which also take into account the aforementioned parameters. Note that given the dependence on individual filter cadence and season length as well as projected CMB velocities, every region on the sky needs to be considered independently. Time Delay Challenge submissions will thus include recovered “pure” microlensing light curves in addition to measured time-delays. By doing the reverse procedure, i.e. using these “pure” microlensing light curves to statistically re obtain the input accretion disk sizes and thermal slopes, we will be able to quantitatively measure the accuracy of the intrinsic accretion disk parameter estimations for a given survey strategy.

8.4.3 OpSim Analysis

Much like the cosmology with lensed quasar time delays, we expect a strong dependence of both proposed metrics with night-to-night cadence, uniformity and season length. Maximizing these will maximize the likelihood of recovering high magnification events, which in turn will provide the most stringent constraints on accretion disk structure. As mentioned above, since shorter

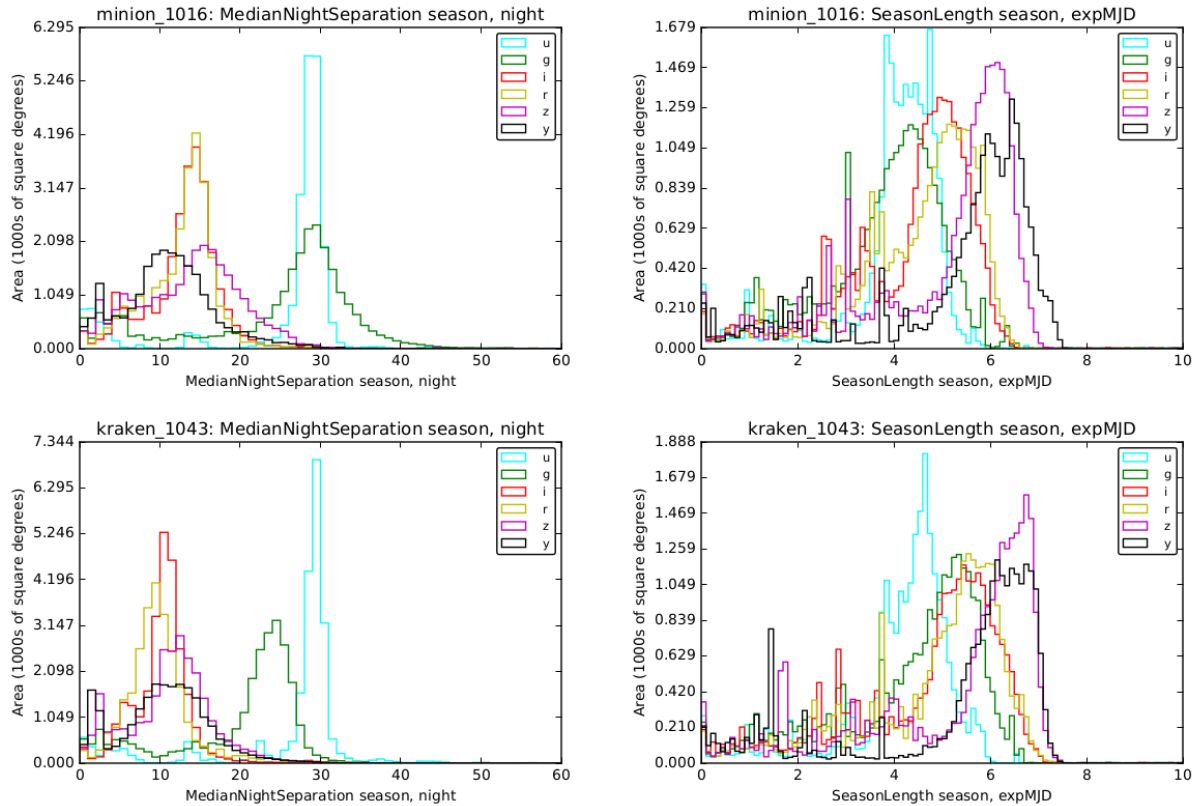


Figure 8.4: Median Night Separation in days (left) and median season length in months (right) for all bands in the current “Baseline Cadence” ([minion_1016](#), top) and “No Visit Pairs” ([kraken_1043](#), bottom) opsim outputs.

wavelengths show faster and stronger magnification events, in an ideal scenario, bluer bands would have tighter night-to-night cadence.

As shown in figure 8.4, it seems there is a slightly better prospect for the AGN structure with microlensing science case using the “No Visit Pairs” observing strategy in comparison to the baseline strategy due to the smaller inter-night gaps and longer season lengths in the g band. In both cases the night-to-night cadence in the longer wavebands are compatible with the detection of most microlensing events. On the other hand, in the u and g bands in both survey strategies it might compromise the results. Furthermore, in all LSST bands the spread in the night-to-night cadence (uniformity) and season length will likely dominate the uncertainties.

Go to: • [the start of this section](#) • [the start of the chapter](#) • [the table of contents](#)

8.5 Future Work

In this section we provide a short compendium of science cases that are either still being developed, or that are deserving of quantitative MAF analysis at some point in the future.

8.5.1 AGN Clustering

Ohad Shemmer

Measurements of the spatial clustering of AGNs with respect to those of quiescent galaxies can provide clues as to how galaxies form inside their dark-matter halos, and what causes the growth of their supermassive black holes (SMBHs). The impressive inventory of LSST AGNs will enable the clustering, and thus the host galaxy halo mass, to be determined over the widest ranges of cosmic epoch and accretion power.

We would consider the 2-point angular correlation function of AGN as our target measurement. The LSST cadence will not only affect the overall AGN census and its $L - z$ distribution, but also the depth in each band as a function of sky position that can directly affect the clustering signal.

Go to: • [the start of this section](#) • [the start of the chapter](#) • [the table of contents](#)

8.5.2 The Size and Structure of the Broad Emission Line Region

Ohad Shemmer

LSST may provide estimates of the size and structure of the broad emission line region (BELR) using the photometric reverberation mapping (PRM) method. This method enables one to measure the time-delayed response of the flux in one band to the flux in another by using cross-correlation techniques on AGN light curves (e.g., [Chelouche et al. 2014](#)). The main challenge of PRM is to detect, with high confidence, the time lag between the variations of a BELR line-rich band with respect to variations in a line-poor band, given the relatively small flux contributions ($\sim 10\%$) of BELR lines to each LSST band. Nevertheless, LSST is expected to deliver BELR line-continuum time delays in $\sim 10^5 - 10^6$ sources, which is unprecedented when compared to $\sim 60 - 80$ such measurements conducted, to date, via the traditional, yet much more expensive (per source) spectroscopic method. Sources in the DDFs will benefit from the highest quality PRM time-delay measurements given the factor of ~ 10 denser sampling ([Chelouche et al. 2014](#)).

Target measurements and discoveries

The PRM measurements will probe the size and structure of the BELR, in a statistical sense, and may provide improved SMBH mass estimates for sources that have at least single-epoch spectra. PRM will also be used to trigger follow-up spectrophotometric monitoring of “promising” cases depending on their variability properties. The goal is to obtain R_{BELR} measures for different BELR lines in certain luminosity and redshift bins; for example, PRM may provide mean R_{BELR} for Ly α in quasars at $2.1 \lesssim z \lesssim 2.2$ with $45 \lesssim \log L(\text{erg s}^{-1}) \lesssim 46$, or mean R_{BELR} for C IV $\lambda 1549$ in quasars at $1.6 \lesssim z \lesssim 1.7$ with $44 \lesssim \log L(\text{erg s}^{-1}) \lesssim 45$.

The PRM method is very sensitive to the sampling in each band, therefore the ability to derive reliable time delays can be affected significantly by the LSST cadence. The best results will be obtained by having the most uniform sampling equally for each band. Since the observed line-continuum lags scale with luminosity and redshift, PRM with the LSST will be limited by the

average time gaps between successive observations in a particular band. Additionally, there is a trade-off between the number of DDFs and the number of time delays that PRM can obtain (Chelouche et al. 2014). For example, an increase in the number of DDFs, with similarly dense sampling in each field, can yield a proportionately larger number of high-quality time delays, down to somewhat lower luminosities (to the extent that host-galaxy contamination can be neglected), but at the expense of far fewer time delays (for relatively high luminosity sources) in the main survey.

Metrics

The average and the dispersion in the number of visits, per band, across the sky for the nominal OpSim (during the entire survey) should be computed. Since PRM works best for uniform sampling, one should compare the distributions of the number of visits in each band, averaged across the sky, and identify ways to minimize any potential differences between these distributions. By running PRM simulations, one should identify the 1) minimum number of visits (in any band) that can yield any meaningful BELR-continuum lag estimates, and 2) the largest difference in the number of visits between two different bands that can yield any meaningful BELR-continuum lag estimates. These simulations should be repeated by doubling the nominal number of DDFs. Finally, the uncertainties on R_{BELR} values achieved with the nominal OpSim should be assessed, and potential perturbations to the cadence should be pointed out to reduce these uncertainties.

Another metric is the accuracy of the slope α , $\Delta\alpha$, in the $R_{\text{BELR}} \propto L^\alpha$ relation. Spectrophotometric monitoring typically yields $\alpha \simeq 0.50 \pm 0.05$.

Go to: • [the start of this section](#) • [the start of the chapter](#) • [the table of contents](#)

8.6 Discussion

The goals of this Chapter were 1) to define and quantify key metrics for AGN science that can be measured and tested using the current LSST observing strategy, and 2) to identify reasonable perturbations that may be beneficial for AGN science. Undoubtedly, additional work is required to refine many of these metrics and perform more rigorous tests and simulations. The following list identifies additional cadence-related aspects for further consideration. Together with the metrics discussed in this Chapter, this may be regarded as a road map for further investigations that should be performed during the planning stage.

- 1) Assuming a total of ten DDFs, it would be beneficial if one of those fields could be sampled more heavily than the others and would be visited nightly (or even more frequently, e.g., from ~ 1 to ~ 1000 min) per band. This can be justified by the fact that a) very few AGNs or transient AGNs have been monitored at these frequencies on such a long baseline, leaving room for discovery, and b) this may probe intermediate-mass black holes ($\sim 10^4 - 10^5 M_\odot$) via PRM or PSDs. Good candidate fields are the Magellanic Clouds and the Chandra Deep Field-South. An observational strategy should be developed and implemented either in a new OpSim, or during commissioning.

- 2) In order to have more informative metrics, accurate model light curves are needed that can reproduce fiducial light curves in different bands, at different inherent luminosities, and at different redshifts. This may be developed together with the Strong Lensing Science Collaboration.
- 3) There is a need to compare the science content in this Chapter with the AGN chapter in the LSST Science Book as well as with the Ivezic et al. overview paper (<http://arxiv.org/pdf/0805.2366v4.pdf>) to ensure that no key science aspect is overlooked or compromised by the nominal cadence.
- 4) It is worth checking whether any aspect of blazar science might be compromised by the nominal cadence, or would benefit from a specific cadence requirement.
- 5) The effects of the cadence on the overall LSST astrometry accuracy and precision should be assessed in terms of potential effects on AGN selection. For example, AGN selection may benefit from very good depth at least in the 1st and 10th year of the survey.

Go to: • [the start of this section](#) • [the start of the chapter](#) • [the table of contents](#)

9 Accurate Cosmological Measurements on the Largest Scales

Chapter editors: [Eric Gawiser](#), [Michelle Lochner](#).

Contributing authors: [Timo Anguita](#), [Humna Awan](#), [Rahul Biswas](#), [??](#), [Phil Marshall](#), [Josh Meyers](#), [Jeonghee Rho](#).

9.1 Introduction

Cosmology is one of the key science themes for which LSST was designed. Our goal is to measure cosmological parameters, such as the equation of state of dark energy, or departures from General Relativity, with sufficient accuracy to distinguish one model from another, and hence drive our theoretical understanding of how the universe works, as a whole. To do this will necessarily involve a variety of different measurements, that can act as cross-checks of each other, and break parameter degeneracies in any single one.

The Dark Energy Science Collaboration (DESC) has identified five different cosmological probes enabled by the LSST: weak lensing (WL), large scale structure (LSS), type Ia supernovae (SN), strong lensing (SL), and clusters of galaxies (CL). In all cases, the primary concern is residual systematic error: the shapes and photometric redshifts of galaxies, and the properties of supernova and lensed quasar light curves, will all need to be measured with extraordinary accuracy in order for LSST’s high statistical power to be properly harnessed. This accuracy will come from the abundance and heterogeneity of the individual measurements made, and the degree to which they can be modeled and understood. This latter point implies a need for uniformity in the survey, which enables powerful simplifying assumptions to be made when calibrating on the largest, cosmologically most important scales. The need for heterogeneity also implies uniformity, in the sense that the nuisance parameters that describe the systematic effects need to be sampled over as wide a range as possible (examples include the need to sample a wide range of roll angles to minimize shape error, and observing conditions to understand photometric errors due to the changing atmosphere).

In this chapter we look at some of the key measurements planned by the Dark Energy Science Collaboration, and how they depend on the Observing Strategy.

9.2 Large Scale Structure: Testing Dithering Patterns and Timescales to Improve Survey Uniformity

Humna Awan, Eric Gawiser ??, Lynne Jones

Three of the key cosmology probes available with LSST represent “static science” insensitive to time-domain concerns. These are Weak Lensing, Large-Scale Structure, and Galaxy Clusters. Nonetheless, due to the need to track and correct for the survey “window function” in all of these probes, cosmology with LSST will benefit greatly from achieving survey depth as uniform as possible over the WFD area. OpSim tiles the sky in hexagons inscribed within the nearly-circular LSST field-of-view. It has been shown in Carroll et al. (2014) that the default LSST survey strategy implemented in OpSim runs leads to a strongly non-uniform “honeycomb” pattern due to overlapping regions on the edges of these hexagons receiving double the observing time. A pattern of large dithers proves sufficient to greatly reduce these overlaps, leading to an increase in median survey depth in each filter of 0.08 magnitudes.

In this section, we report results from an investigation by Awan et al. (in preparation) of several geometrical patterns for dithers performed on timescales varying from once per observing season to once per night to every visit.

9.2.1 Dithering Patterns and Timescales

9.2.2 Metrics

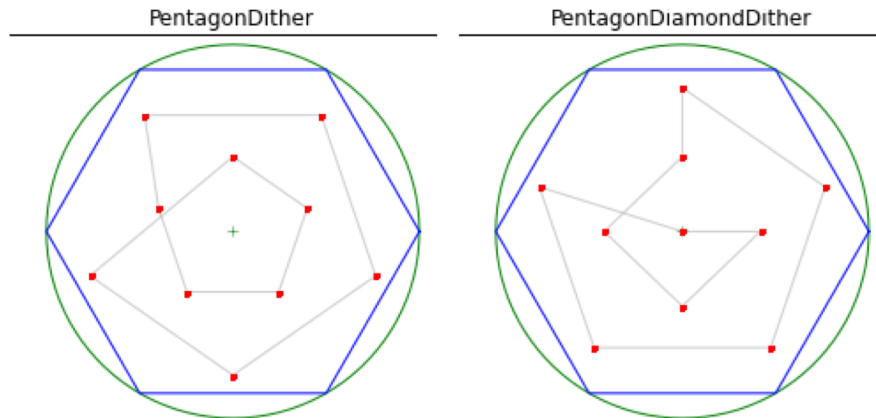
Our primary metric is the total uncertainty in the derived window function over relevant angular scales, modeled via variations in the angular power spectrum of fake galaxy fluctuations between *gri* bands. Intermediate metrics include the number of galaxies in each pixel, fluctuations in this number, total power in the angular power spectrum of a skymap of those fluctuations, and residual power that angular power spectrum after subtracting a smooth fit to it.

9.2.3 OpSim Analysis

In this section we present our ongoing OPSIM/ MAF analysis, as we try to answer the question “what dithering strategies produce acceptable variations in survey uniformity, and which appears optimal?”

What we show here are selected highlights from the paper by Awan et al (2015).

Go to: • [the start of this section](#) • [the start of the chapter](#) • [the table of contents](#)



: Fig. 1.— Geometries for by season dithering strategies.

Figure 9.1:

9.3 Weak Lensing

Stephen Ridgway, Josh Meyers.

Much of LSST cosmology may be limited by systematic errors rather than photon signal-to-noise. This is especially true of weak gravitational lensing, which relies on very accurate (i.e. low bias), but very low signal-to-noise, measurements of the shapes of galaxies, and high signal-to-noise measurements of PSF calibration stars.

9.3.1 Target Measurements

It is expected that even after maximal optimization of camera optics and electronics, that systematic image shape errors will be associated with the orientation of the camera focal plane. How big are these errors likely to be? We don't know.

They will be able to be partially reduced by randomization of the orientation of the camera with respect to the sky. This is represented by the parameter RotSkyPos: we can construct diagnostic metrics that quantify the uniformity of its distribution at each sky position.

Similarly, the telescope optics may harbor systematic aberrations, and these also could be mitigated by recording images with varying parallactic angle. Another relevant parameter, RotTelPos, is indicative of the projected angle of the telescope optics on the sky.

Uniformity of depth is expected to be essential. How essential? We don't yet know.

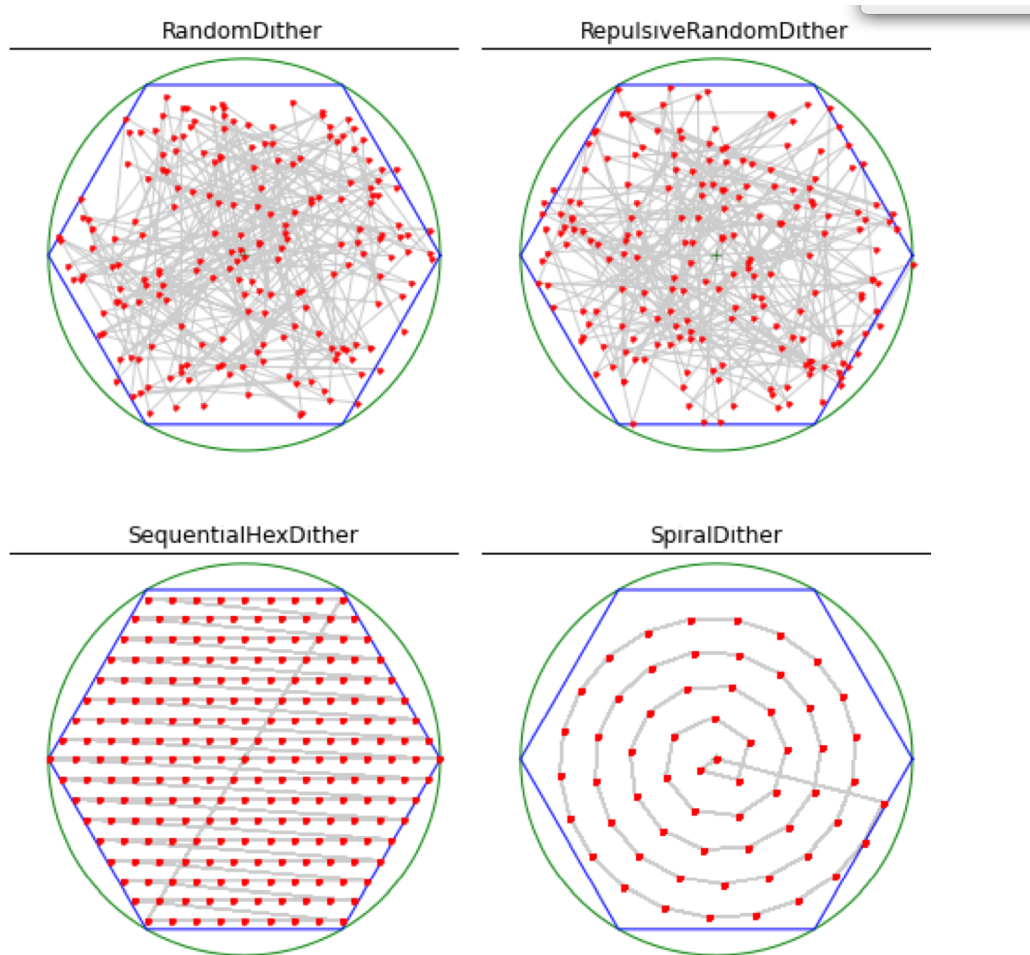


Fig. 2.— Geometries for by visit and by night dithering strategies.

Figure 9.2:

9.3.2 Metrics

Our figure of merit for weak lensing is σ_{sys} , the residual shear systematic error. This is related to the uniformity of the sky survey in ways not yet derived, but for now we can prepare by calculating some low-level diagnostic metrics.

A metric is available for RotSkyPos. The metric computes, for any selected filter and simulation, a histogram of the distribution of rms values of RotSkyPos computed per field. It also computes basic statistics of these distributions.

9.3.3 OpSim Analysis

The distribution of rms values by filter is shown in [Figure 9.6](#) for the current candidate baseline simulation, enigma_1189. As shown, the rms values cluster around the value 1 radian, with typical

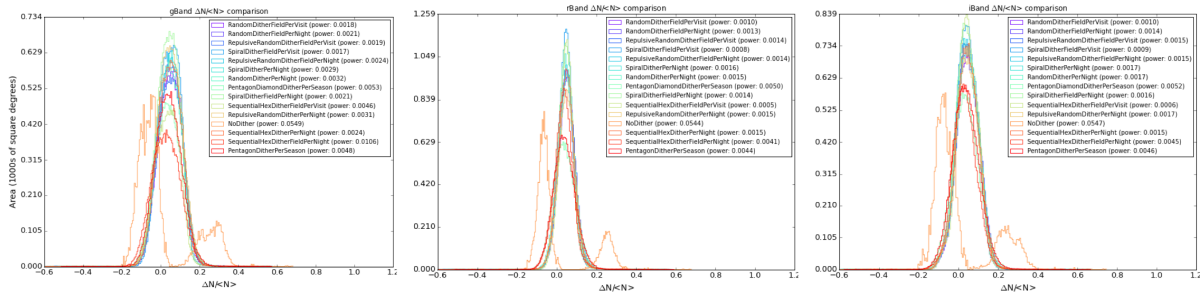


Fig. 4.— Histograms for artificial fluctuations in galaxy counts in gri bands for various dithering strategies.

Figure 9.3:

values 1 ± 0.3 radian. This compares to a completely uniform distribution over the half circle with an rms of 1.14.

9.3.4 Discussion

The RotSkyPos metric analysis shows that the majority of fields have a good randomization of detector angles projected on the sky.

There are several limitations to this observation.

First, we do not have at present a quantitative requirement for randomization of this parameter. In future development of weak lensing analysis, a criterion should be developed.

Second, a significant fraction of fields have median values that are lower or higher than expected for a random distribution, with some far from uniformly distributed. Regardless of the *perfield* criterion, it is desirable to avoid the incidence of individual discrepant fields.

The recommended criterion for randomization of RotSkyPos is not the behavior of the majority of the fields, but of the minority with the least random behavior. The number of non-random fields should be minimized. A recommended metric is the count of fields with median RMS less than 0.8 or greater than 1.5 radians (these values to be reviewed again as additional experience is gained with additional OpSim schedule simulations and weak lensing analysis.)

It is certain that actively controlling the statistics of RotSkyPos will require additional slewing of the camera rotator. At present, the operations plan is to only slew when necessary to prepare for a filter change - that could be estimated at the equivalent of $\simeq 3$ complete rotations per day. Figure 9.6 shows that to render the distribution completely uniform would require moving all observing angles an average of $\simeq 30$ degrees, or 300 complete rotations per night. The timing of this has not been considered. Whether or not this uniformity could be achieved with less slew time if implemented in scheduling remains to be demonstrated.

A similar metric for RotTelPos should be developed.

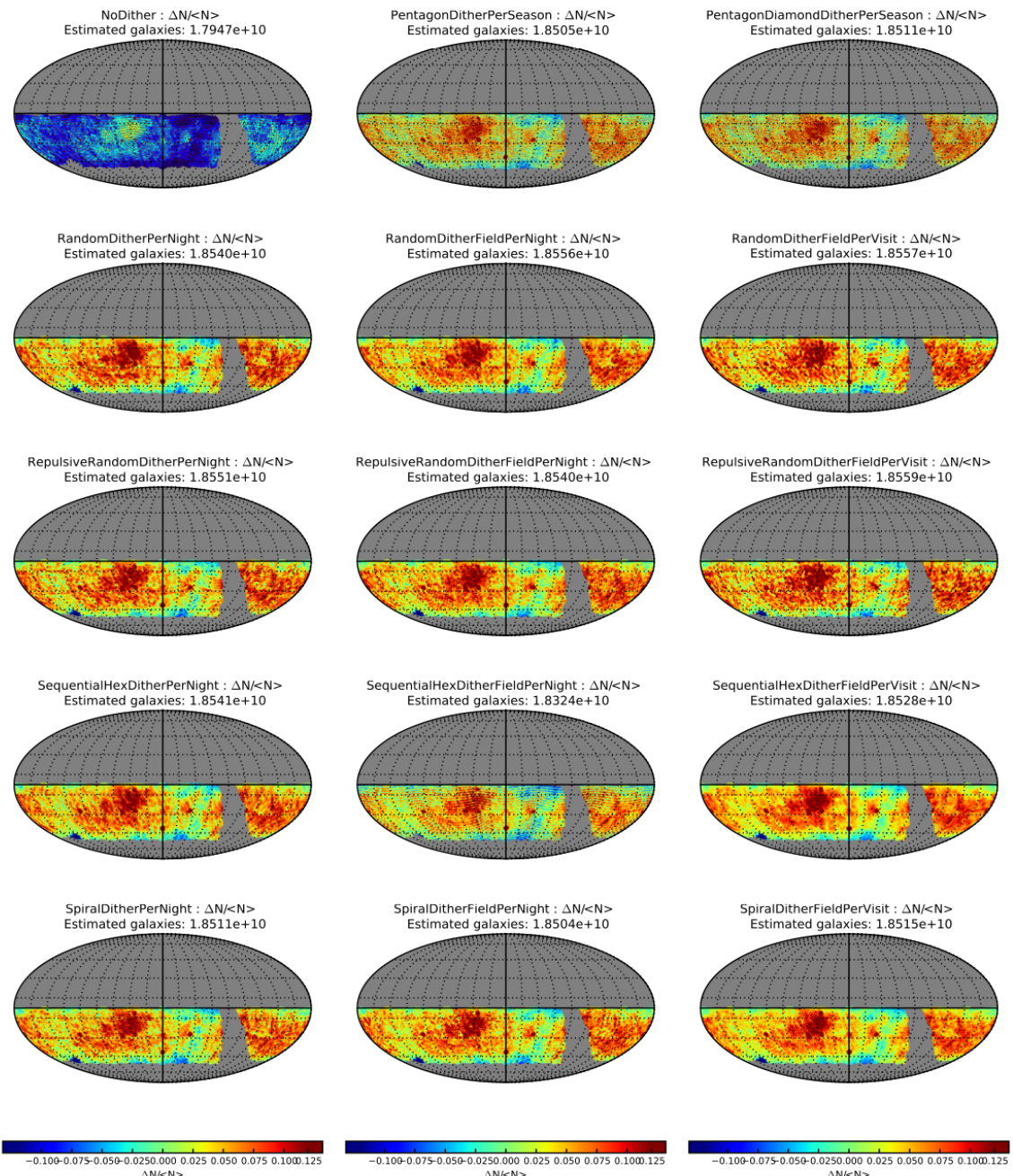


Fig. 5.— Skymaps for r-band differential galaxy counts from various dithering strategies.

Figure 9.4:

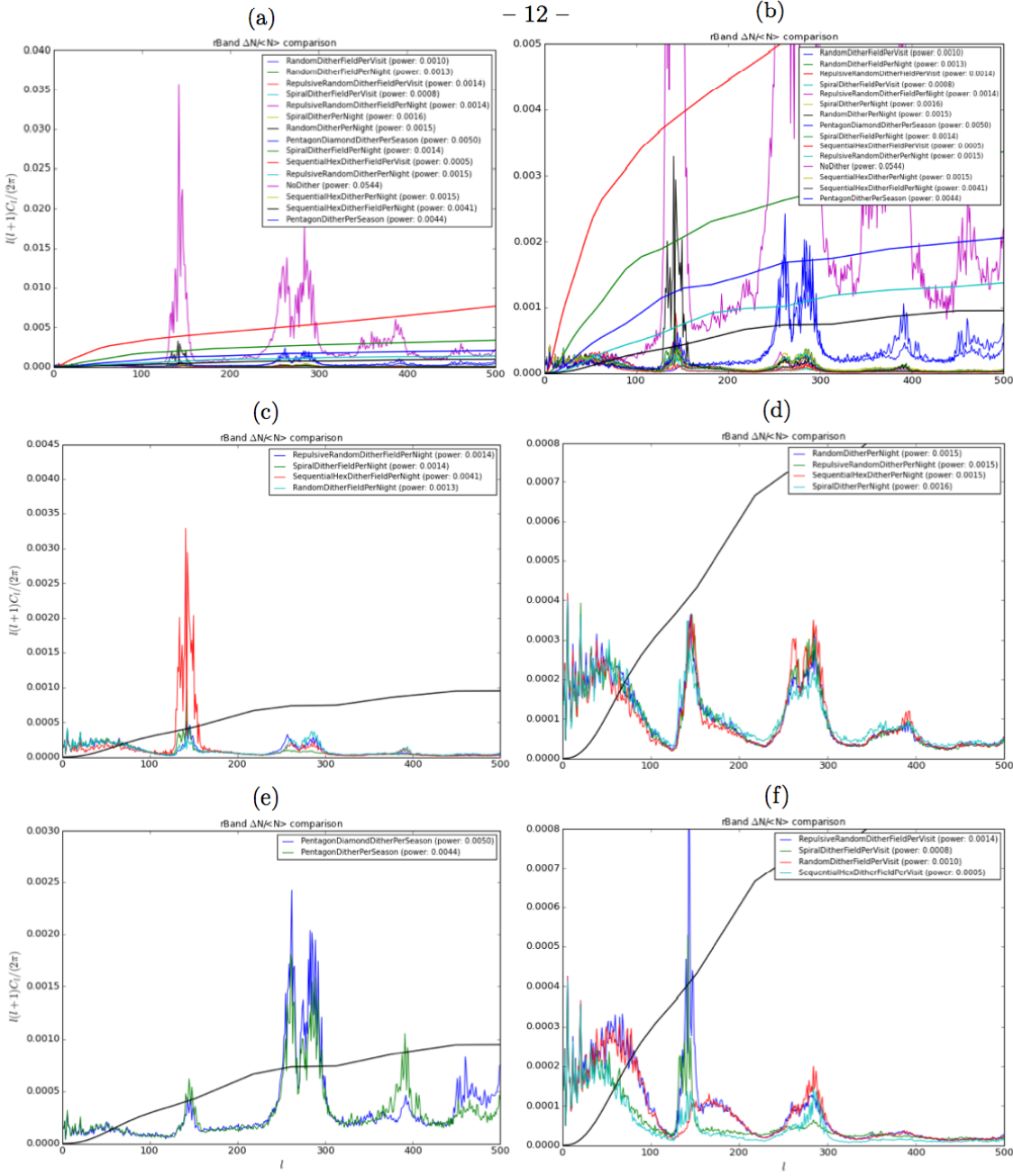


Fig. 6.— Angular power spectra for artificial fluctuations in r-band galaxy counts from various strategies. Panel (a) includes the spectra for all strategies, with its zoomed version shown in Panel (b). Panel (c) includes those for FieldPerNight strategies, Panel (d) for PerNight, Panel (e) for PerSeason, and Panel (f) for FieldPerVisit strategies. Thick curves are an example BAO signals, where the red one is for $0.15 < z < 0.37$, green for $0.37 < z < 0.66$, blue for $0.66 < z < 1$, cyan for $1 < z < 1.5$, and black for $1.5 < z < 2$.

Figure 9.5:

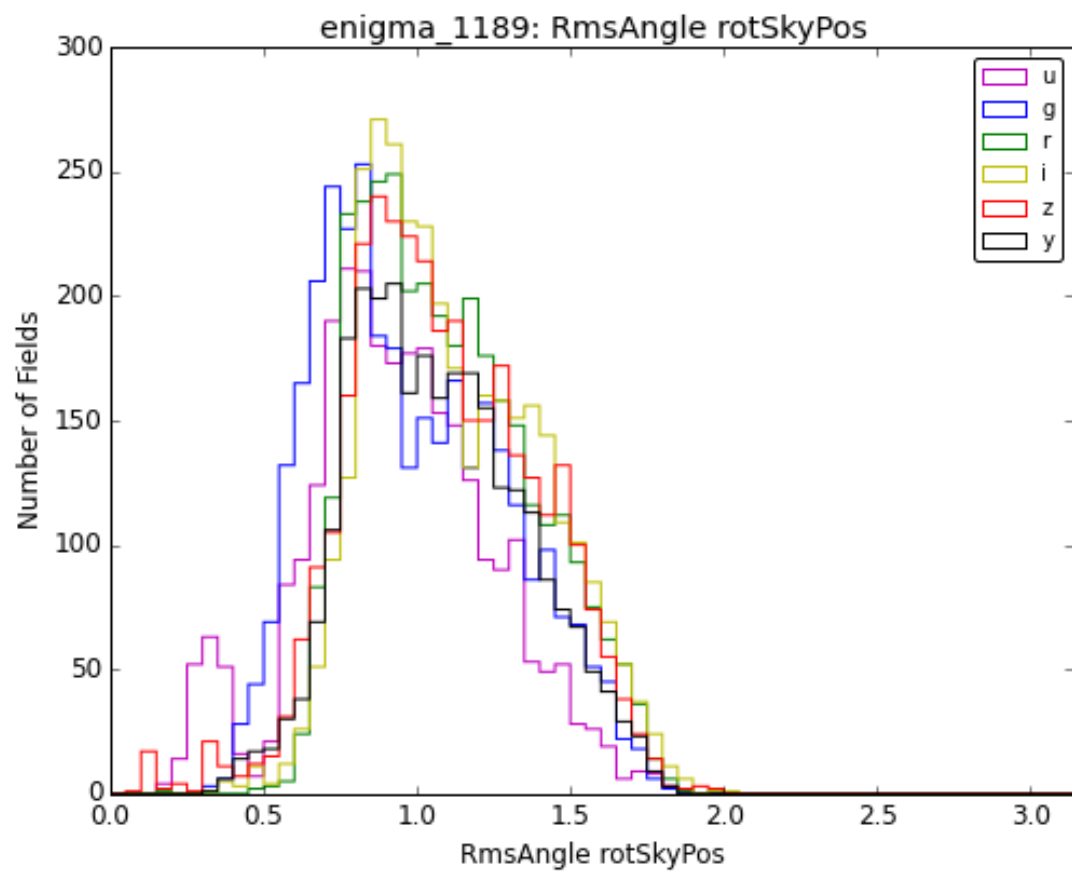


Figure 9.6: The relative angle of the detector plane with respect to the sky, RotSkyPos, as a histogram showing the number of fields vs. rms of the parameter.

9.4 Photometric Redshifts

Melissa L. Graham, Samuel Schmidt, Andy Connolly, Željko Ivezić

9.4.1 Introduction

Photometric redshifts are an essential part of every cosmology probe within LSST. The principal concern for LSST photo- z performance is to meet the stringent requirements on redshift uncertainty, bias, and catastrophic outlier rate as laid out in the Science Requirements document. Photo- z 's are dependent on precise measurements of galaxy colors, thus cadence and depth variations must be examined as a function of all six LSST filter bandpasses. Overall image depth and signal-to-noise is our primary concern. For studies of Large Scale Structure, Weak Lensing, Clusters, and Supernova host galaxies, survey uniformity is desired for the full depth survey, while the temporal details of how we reach full depth are not as important as uniformity both as a function of sky position and observing conditions. However, as we desire science-grade photometric redshifts after one year of operations, two years, and so forth, the cadence must meet some basic requirements for the six-band system at least on the timescales of the yearly data releases.

Specifications. The Science Requirements Document (SRD) defines the minimum statistical specifications for photometric redshifts for an $i < 25$, magnitude-limited sample of 4×10^9 galaxies from $0.3 < z < 3.0$ as: (1) the root-mean-square (σ) error in photo- z , divided by $1 + z$, must be $\sigma < 0.02$; (2) the fraction of “catastrophic” outliers (defined as those with errors exceeding the larger of 0.06 or 3σ) must be $< 10\%$; and (3) the average bias must be $\overline{z_{\text{true}} - z_{\text{phot}}} < 0.003$. With this in mind, we are developing software to show that our photo- z algorithms can meet specifications for LSST baseline parameters and to simulate the impact of deviations from the 10-year baseline plan on photo- z statistics.

Planned Experiments. This software is designed to allow the user to modify LSST baseline parameters, simulate a set of test galaxy observations (i.e., magnitudes with errors appropriate for the given LSST parameters) from a training catalog with “true” magnitudes and redshifts and a realistic intrinsic dispersion in color, magnitude, and redshift, run a photometric redshift algorithm on the test galaxies (i.e., matching in color-space to the training catalog), and output statistics for analysis. Modifiable LSST input parameters will include: the limiting magnitude applied to the galaxy catalogs (e.g., $i < 25$); the number of visits per filter; the number of years of LSST observations that have passed (this can be a fraction of a year); systematic offsets to the magnitudes in each filter (default = 0); and coefficients for the magnitude uncertainties in each filter (default = 1). Output for user analysis will include catalogs of z_{true} vs. z_{phot} and the aforementioned statistics on the photo- z in any desired redshift range. For example, we will be able to vary the total number of u -band visits and examine how this affects the fraction of outliers at 1, 5, and 10-years of the survey. In this software, parameters of the photo- z algorithm itself will also be modifiable, allowing us to test options in the algorithms against various LSST observing strategies.

Currently implemented photo- z algorithm. We draw N_{test} “test” galaxies from the training catalog, determine their magnitude uncertainties as appropriate for the LSST parameters, randomly scatter their magnitudes to induce an observational error, and calculate the associated

colors and color errors. We calculate the Mahalanobis distance in color space between each test galaxy and all training catalog galaxies, and identify a color-matched subset using a threshold defined by the χ^2 percentage point function at 95%. We draw a random color-matched training galaxy and use its redshift as the photo- z for that test galaxy. We then calculate our statistical metrics on the photometric redshifts for the test sample, using each test galaxy’s original catalog redshift as the “true” redshift. This process is open to substituting alternate photometric redshift algorithms, a variety of galaxy catalogs, and/or adding priors based on e.g., apparent magnitude.

9.4.2 Metrics

The primary metrics we will use to evaluate LSST observing strategies with respect to the SRD photo- z specifications are the standard deviation, bias, and fraction of outliers. For all test galaxies we calculate $\Delta z = (z_{\text{true}} - z_{\text{phot}})/(1 + z_{\text{true}})$, and identify galaxies in the interquartile range of Δz . For these interquartile galaxies we determine the standard deviation, σ , of the Δz distribution, and the bias as the median value of Δz . The interquartile range is used to exclude outliers from influencing these statistics; in other words, they represent the standard deviation and bias for the subset of “good” photo- z ’s. The “catastrophic” outliers are identified as those with Δz exceeding the larger of 0.06 or 3σ .

9.4.3 Initial Results

To demonstrate this software with a preliminary analysis, we apply the currently implemented photo- z algorithm to a catalog of galaxies that was originally created as an accurate cosmological simulation for Euclid. We first cull the catalog to galaxies with i -band magnitude < 25.3 , and then randomly draw training and test galaxy samples (with at least a $4\times$ more galaxies in the training sample than the test sample). For this demonstration we show how the photo- z metrics evolve with respect to two of the basic LSST parameters: the year of the survey, and the number of u -band visits. When we simulate results in a given year of LSST, we assume uniform progression in all filters (i.e., the total number of visits per filter, [56, 80, 184, 184, 160, 160] in [u,g,r,i,z,y], is distributed evenly over all years). When we simulate the LSST 10-year results for a given number of u -band visits, the visits removed/added to u -band are added/subtracted evenly to/from the other five filters. The results of these tests are presented in Figure 9.7 and 9.8. For example, in this demonstration we can see that the u -band is necessary to limit scatter at $z < 0.5$ and $z > 2.0$.

9.4.4 Discussion

Additional considerations for observing strategy. As mentioned above, overall image depth and signal-to-noise is our primary concern, so we are not testing changes in e.g., the inter-night gap time or the exposure time of individual visits. Our software is instead focused on modifying other LSST parameters such as systematic offsets to the magnitudes in each filter and/or coefficients for the magnitude uncertainties in each filter in order to simulate improvements or degradations the system throughput, sky background brightness, and other such factors. We also aim to test airmass distributions (i.e., changes to the effective filter functions), different progression rates for filters (e.g., a scenario in which we complete all u -band by year 2), scenarios in which some areas

of sky have better/worse coverage at any given time, and so forth. In all respects we are open to suggestions from the community.

Considerations for building the real training catalog. All photometric redshift algorithms require training set data consisting of objects with secure spectroscopic redshifts. For LSST, many of these will be contained in a small number of training/calibration fields (e.g. COSMOS, VVDS). Imaging these fields to full depth in all six bands early in the survey (but under the range of observing conditions expected for the ten year survey) will be key to characterizing performance. Inclusion of these patches of full-depth imaging must be included in any cadence design. Future simulations of photo- z results can include varying the quality of the training catalog obtained by LSST.

Integration with MAF. One way to extend our program to be able to evaluate observing strategies simulated with OPSim could be to use the MAF to enable us to simulate representative samples of galaxies across the mock LSST sky, and compute the metrics we have defined. It may be possible to avoid such a large computation by first defining some intermediate diagnostic metrics, such as the u -band coverage, and working out how our higher level metrics depend on them, using some approximate interpolation formulae.

Connecting to the Dark Energy Figure of Merit. The metrics we have defined here should be able to be related to the DETF Figure of Merit, but because photo-zs affect all of the LSS, WL and CL cosmological probes, this step may need to wait until a joint Figure of Merit MAF metric is developed.

Go to: • [the start of this section](#) • [the start of the chapter](#) • [the table of contents](#)

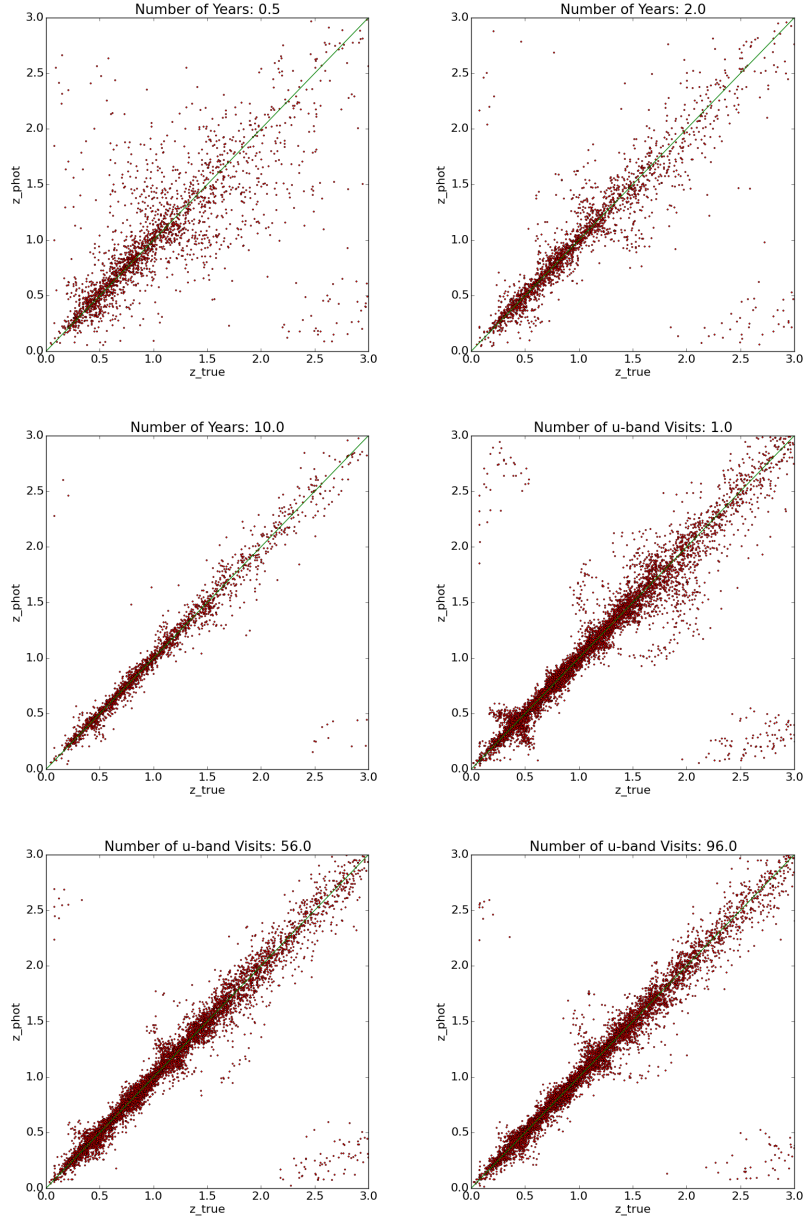


Figure 9.7: Photometric vs. spectroscopic (i.e., catalog truth) redshifts for our preliminary simulations. Across the top row we show results from 0.5, 2.0 and 10.0 years of the LSST survey using catalogs with 2500 test and 10000 training galaxies. The photo-z's clearly improve with time as the survey progresses. Across the bottom row we show results for 1, 56 (baseline), and 96 u -band visits using catalogs with 10000 test and 40000 training galaxies. Between the left-most and middle plot of the bottom row, representing 1 and 56 (baseline) u -band visits respectively, we see that u -band data is necessary to limit scatter in the photo-z's, especially at $z < 0.5$ and $z > 2.0$.

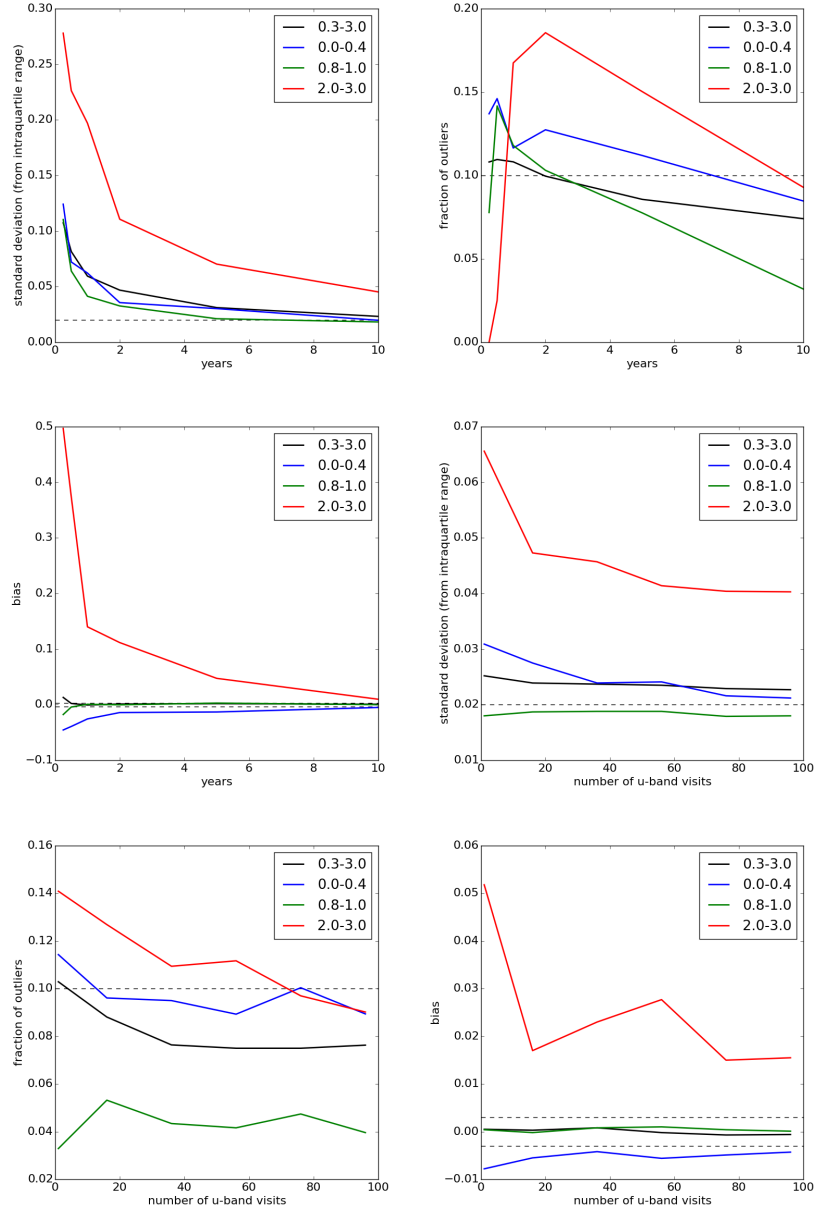


Figure 9.8: Three photo- z metrics as a function of LSST parameters. From left to right, the y-axis is the standard deviation, the fraction of outliers, and the bias. The top row shows these statistics as a function of the number of years of LSST survey, and the bottom row shows them as a function of the number of u -band visits. Colors show these relations for four bins in redshift: 0.3–3.0 (black), 0.0–0.4 (blue), 0.8–1.0 (green), and 2.0–3.0 (red). Dashed lines mark the SRD specification for each metric. The fraction of catastrophic outliers appears erroneously low early in the LSST survey (top middle plot) when the dispersion in $z_{\text{spec}} - z_{\text{phot}}$ is too large to adequately identify outliers (e.g., see top left plot of Figure 9.7).

9.5 Supernova Cosmology and Physics

Jeonghee Rho, Michelle Lochner, Rahul Biswas, Seth Digel.

This section is concerned with the detection and characterization of supernovae (SNe) over time with LSST and their various scientific applications. A crucial application is the use of supernovae type Ia (SNIa) and potentially some core-collapse SN (like type IIP) to trace the recent expansion history of the universe, and confront models of the physics driving the late time accelerated expansion of the universe.

LSST will improve on past surveys by observing a substantial number of well-characterized supernovae, at high redshift. This large sample is not necessarily tied to the large area of LSST and can rather be obtained from a relatively small spatio-temporal region with larger numbers of well-measured light curves.

On the other hand, the WFD aspect will make the LSST survey the first to scan a very large area of the entire Southern sky for SNe. SNe that are detected and well characterized by LSST can trace large scale structure in a novel way, and include estimates of radial distances, as well as their own redshift estimates that may be used in conjunction with host galaxy redshift information. Due to these properties, they can probe the isotropy of the late time universe.

In addition, this large sample will enable further sharpening of our understanding of the properties of the SN population of different types (see [Section 6.3](#)). This last point is extremely important for SN cosmology goals as the success of SNIa cosmology has always been based on the empirical model that intrinsic peak brightnesses are related to the certain observable characteristics of SNe. The WFD SNIa sample will dramatically increase the size of the sample available to train such an empirical model, as well as understand the probability of deviations and scatter from this model. Aside from issues like calibration which need to be addressed separately, a larger sample of such well measured SNe is probably the only way to address ‘systematics’ due to deviations from the empirical model. The anticipated sample can be thought of as consisting of two components: the low-redshift sample which is more likely to be complete, and the higher-redshift sample that will be able to constrain evolution.

9.5.1 Target measurements and discoveries

SNe of different types are visible over time scales of about a few weeks (e.g., type Ia) to nearly a year (type IIP). During the full ten-year survey, LSST will scan the entire southern sky repeatedly with a WFD cadence, and certain specific locations of the sky called the Deep Drilling Fields (DDF) with special enhanced cadence.

This spatio-temporal window should contain millions of SNe, that will have apparent magnitudes brighter than the single exposure limiting magnitude of LSST. However, the actual sequence of observations by LSST, defined by the series of field pointing as a function of time in filter bands (along with weather conditions), will determine the extent to which each SN can be detected and characterized well. Characterization of the SNe is at the core of a number of science programs that use them as bright, abundant objects with empirically determined intrinsic brightnesses.

For LSST, this goal entails:

- a. The detection of SNe
- b. Photometric classification
- c. Estimation of photometric redshifts of SNe (or identifying host galaxies and obtaining their redshifts from photometry or follow-up spectroscopy)
- d. Estimation of intrinsic brightnesses of the SNe
- e. Constructing a Hubble diagram with this data for cosmological inference

The efficacy of photometric typing, redshifts and estimation of intrinsic brightnesses are all dependent on the amount of information available in the observed light curves of SNe. While these steps are not necessarily independent, it is useful to think of the requirements on some of these steps separately; it is not unlikely that combinations of some of the steps would still be affected by similar requirements. Ultimately, any cosmological figure of merit (the $w_0 - w_a$ figure of merit described in [Albrecht et al. \(2006\)](#) for example) will depend on intermediate metrics describing each of these steps in turn. Here we focus on steps **a**, **b** and **d**, leaving steps **c** and **e** for future work.

Supernova detection

Supernova light curves consisting of flux measurements at different times are built through photometry at specific locations on each of the observed images. A finite list of such specific locations is constructed through a transient detection pipeline studying difference images. In brief, this process consists of studying subtractions between a ‘template’ image (coadded over time so that a supernova flux averages to a small value) and single visit images called ‘science images’ at different times, after correcting for differences in resolution, observing conditions and pixel registration. In such difference images, one expects to obtain non zero pixel values at locations of transients including supernovae, and pixel values at other locations (including locations of static astrophysical sources) to be consistent with zero aside from a noise. The efficiency of detecting a supernova in a single exposure depends on a number of factors, the most significant of which is the signal (brightness of the supernova in the science image compared to the template) to sky noise in the relevant image.

Supernova classification

Because LSST will discover significantly more SNe than can be spectroscopically confirmed, automated classification of supernova type from multi-band light curves is crucial. While cosmology with a photometric SNe sample with contamination from core collapse SNe is possible (see for example [Kunz et al. \(2007\)](#); [Newling et al. \(2011\)](#); [Hlozek et al. \(2012\)](#); [Knights et al. \(2013\)](#); [Bernstein et al. \(2012\)](#); [Campbell et al. \(2013\)](#); [Rubin et al. \(2015\)](#)), these methods still benefit from accurate class probabilities from classification algorithms. To investigate the effect of observing strategy on SNe classification, we use the multi-faceted machine learning pipeline developed in [Lochner et al. \(2016\)](#).

Estimating intrinsic supernova brightness

The ultimate goal of using SNe (type SNIa or SNIIP) for cosmology requires estimating the intrinsic brightness of each SN. The first (and sometimes only, depending on the light curve model) step is fitting the calibrated fluxes to a light curve model with a set of parameters. According to the ansatz used in SN cosmology, the intrinsic brightness of SNe is largely determined by the parameters of the light curve model; hence the uncertainties on the inferred parameters largely determine the

uncertainties on the inferred peak intrinsic brightness or distance moduli of the SNe. This means the error on the fitted distance modulus parameter is a useful proxy for the quality of the light curve and the accuracy of the resulting cosmological inference.

9.5.2 Metrics

Since the steps described above are all necessary for the determination of SN intrinsic brightnesses, a metric for supernova cosmology must quantify the ability to perform these steps on each supernova of the sample. To connect this to the output of OpSim, we propose the following strategy:

- Study the sequences of observations in small spatial regions of the sky so that the sequences of observations relate to positions of astrophysical objects like supernovae. This capability is already built into MAF with multiple slicers like the `OpSimFieldSlicer` or the `Healpixslicer`. For example, in [Figure 9.9](#), we show such a sequence for a WFD and DDF field for a single year.
- On each such spatial region, we look at sliding time windows, each time window of size about 70 days (corresponding roughly to a supernova Type Ia lifetime starting 20 days before peak and extending to about 50 days after peak). As an example, we choose a time window around the night=570, which has an MJD value of 49923 for both the fields (fieldID: 744 and 309) shown in [Figure 9.9](#) and show the time window in [Figure 9.10](#).
- We assign a metric value that we call **perSNMetric** PM to each of these time windows to estimate the quality of observations for a supernova whose rough lifetime matches that time window. The prescription for assigning these values to each time window defines our metric and should quantify the success of the steps mentioned above. We would expect this value to be a function of the properties of the sequence of observations and the properties of the transients (SN) being studied.

$$PM = PM(\text{observationSequence}, \text{SNproperties})$$

- We add up the **perSNMetric** for the time windows to estimate the metric values M for the spatial region of the sky surveyed.

$$M = \sum_i PM_i.$$

This gives us our final metric M .

To define the metric M , we need to define the perSNMetric. Two different approaches to defining the perSNMetric for a given OpSim run are possible: a) Use a simulated supernovae Type Ia with specific parameters, observed with the sequence of observations in the above time window, and evaluate the success of each step. b) Study heuristics of the observation sequences by using large simulations with randomized parameter values.

Here we will discuss the simpler approach (a). The SN metric in a spatial region reflects the contribution of the sample of SNe observed in that spatial region towards inferring the cosmological parameters. Let us consider a case where each SN observed with conditions better than a certain

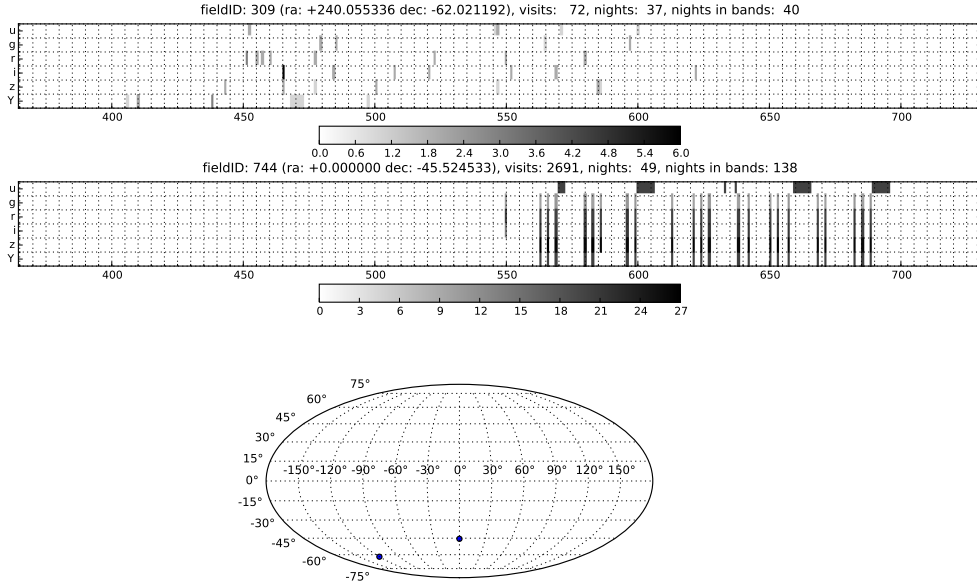


Figure 9.9: Example of the cadence in the 2nd season in a WFD Field (fieldID 309) (top-panel) and a Deep Drilling Field (fieldID 744) (middle panel) and the spatial location of these two fields shown on a map. The cadence plots show a heatmap of the number of observations per night during the second season in each filter u, g, r, i, z, y. The header shows the fieldID and location of the field, the total number of visits during that period, the number of distinct nights on which observations are taken, and the number of distinct observations (where observations are considered indistinct if they are on the same night and use the same band).

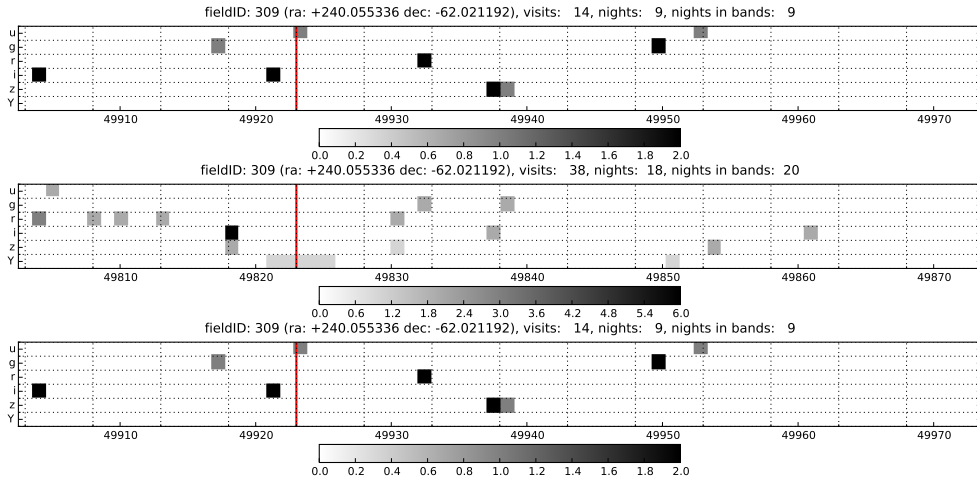


Figure 9.10: Example of a time window in a WFD Field (fieldID 309) (top-panel) and a second time window (middle panel) on the same field, and a Deep Drilling Field (fieldID 744) (bottom panel) all extending -20 days before and 50 days after a chosen night or MJD. For the Deep Drilling Field in the bottom panel, and the WFD field in the top panel, the chosen date around which the time window is constructed is the MJD of 49923, which is also 570 nights into the survey and marked by a red vertical line (which can be used to compare the location to Figure 9.9). The middle panel shows a window in Field 309 centered around an MJD of 49823 or a night of 470 which may also be compared to Figure 9.9. The plots again show the heatmap of observations in each filter in each night as in the cadence plots of Figure 9.9.

Metric	Description
I. SN discovery	Given the observations in a time window corresponding to the lifetime of a supernova, evaluate the probability of detecting a transient
II. SN classification	Given the observations in a time window corresponding to the lifetime of a supernova, evaluate the probability of accurately classifying the transient
III. SN light curve characterization quality	Given the observations in a time window corresponding to the lifetime of a supernova, evaluate the quality of characterization

Table 9.1: Components of the perSNMetric

threshold contributes equally to the inference. Then the relevant metric would be a function of the number of SN in the sample passing such selection criteria. More generally, when the quality of all the supernovae are not similar, the metric should be thought of as the weighted sum of supernovae, with the weights being related to the inverse of the effective variance of the distance modulus:

$$M \sim \sum_i w_i, \quad w_i \sim 1.0/\sigma_\mu^2. \quad (9.1)$$

By comparing with the form of the perSNMetric, we see that the perSNMetric should be a proxy for $1.0/\sigma_\mu^2$, where σ_μ^2 is the effective variance on the distance modulus of the supernova, as determined by fitting an empirical model to the supernova light curve.

Steps in the PerSNMetric

As described before, the measurement of the distance modulus is the result of several steps. Therefore, we expect the perSNMetric to be a product of metrics in each of the steps:

$$PM_i = \prod_{\text{steps}} PM_i^{\text{steps}} \quad (9.2)$$

These components of perSNMetric constructed in different steps are described in [Table 9.1](#).

I. Discovery Metric

This metric is designed to gauge the performance of detection of SNe discussed in [Sub-section 9.5.1](#). This metric is a proxy for the probability that a supernova will be detected during its lifetime by the set of images taken in different bands by LSST. A larger number of images taken at a time when the supernova is bright enough increases the probability of detection. Assuming that a single detection in any of the images containing the supernova is sufficient to trigger photometry at the location, one can find the probability of detection from an SNR vs. efficiency of detection curve. The signal-to-noise ratio (SNR) can be determined given properties of a supernova (redshift,

intrinsic brightness etc.) and the five sigma depth provided in OpSim. While such a SNR-efficiency curve does not yet exist for the LSST pipeline, one can use such a curve from previous surveys, in particular a SNR-efficiency curve constructed during a stage of the Dark Energy Survey for g, r, i, z bands of DES, and provided by R. Kessler, priv. communication. This is shown in [Figure 9.11](#).

Using this information, one can compute the value of the probability that a SN with given properties will be discovered if it occurs with the spatio-temporal window of LSST. We use this as the value for the supernova discovery metric (SNDM). While very high redshift (and thus faint) supernovae will not be discovered, it is potentially possible to discover many supernovae whose light curves will in turn not be well characterized or hard to classify.

II. Classification Metric

Separating supernovae from other detected transients is being considered in [Chapter 6](#). Here we concern ourselves with problem of classifying subclasses of SNe. Multiple techniques have been proposed to solve this problem and it is not yet clear how the relative success of these techniques are affected by observing strategy. We thus use the multifaceted, machine learning pipeline developed in [Lochner et al. \(2016\)](#) to compare alternative observing strategies. The exact metric used to determine the efficacy of the classification depends on the exact problem at hand. For producing a general purpose, well-classified set of all types of supernovae (for example, to study supernova population statistics), one could use the AUC metric defined in [Lochner et al. \(2016\)](#), which is a good balance between purity and completeness. Alternatively, if one only considers supernova cosmology, a simpler metric might be the percentage supernova detected if a purity of (for example) 95% is demanded from the final sample. Work is still ongoing to apply the full classification pipeline to multiple OpSim runs and incorporate a metric into MAF, combining it with the other components of the perSNMetric.

III. Quality Metric

We construct the quality metric for the perSNMetric by obtaining the light curve of the SN in the time window described above. We fit the light curve, using the SALT2 model ([Guy et al. 2007](#)), and approximately estimate the uncertainty in distance from the light curve fit alone. Of course, as is well known, luminosity distance estimates of supernova Type Ia also show an intrinsic scatter of around 0.1 in previous surveys, which may be expected to decrease with better training samples and understanding of underlying correlations of SNIa properties and their environments. We compute a quality metric for each SNIa as the ratio of the square of the uncertainty of the distance indicator from the supernova to the square of the intrinsic dispersion. When added up over SN to obtain a value QM , the uncertainty on cosmological parameters may be expected to scale as $\sim \sqrt{1.0 + \sum QM}$.

9.5.3 OpSim Analysis

The scientific goal of characterizing SNe is to a large extent dependent on how well the light curves of individual SNe are sampled in time and filters. To study this, we re-index the OpSim output on spatial locations rather than use the temporal index. Here we first illustrate in terms the cadence in two example LSST fields.

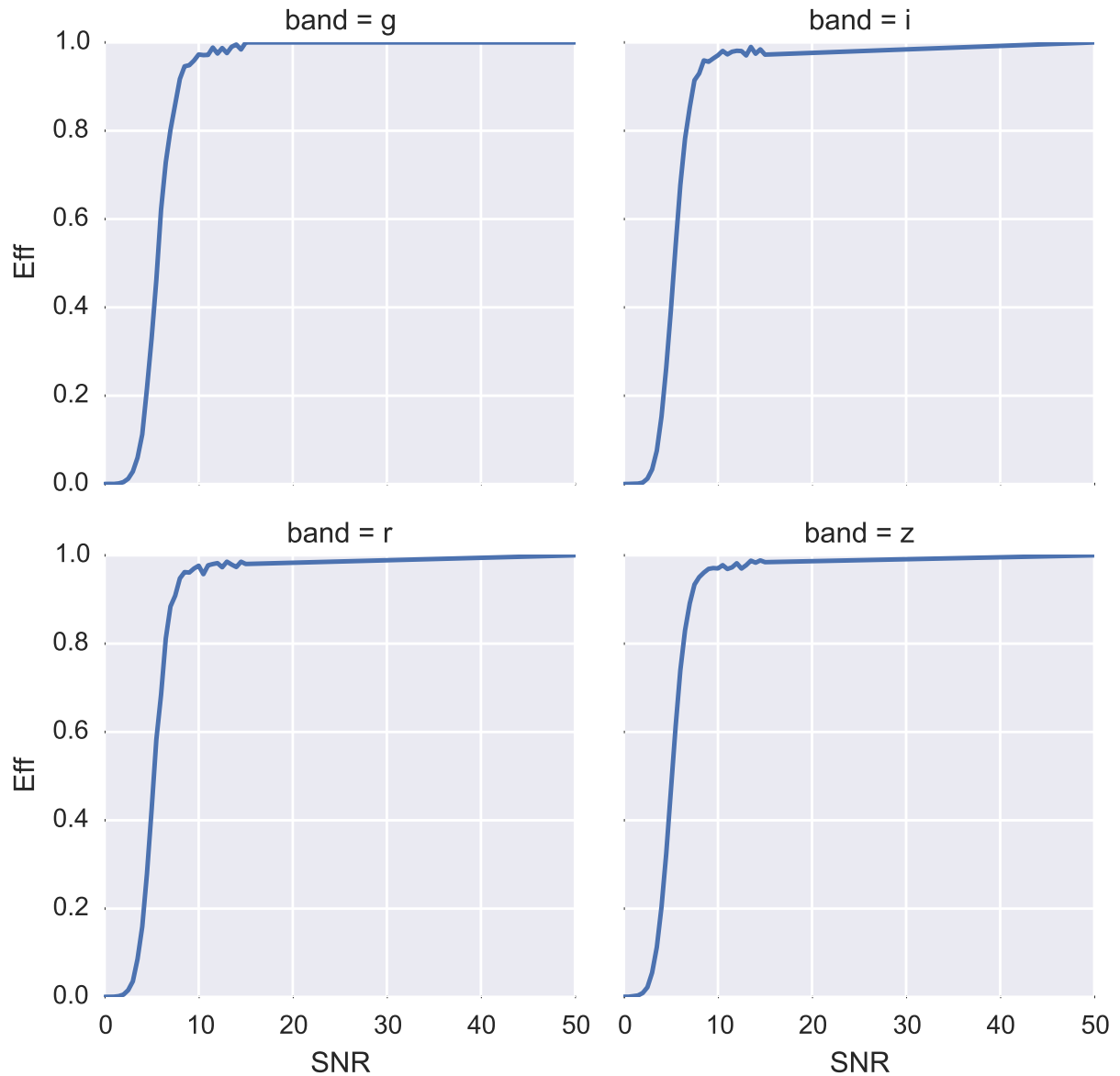


Figure 9.11: Probability of detecting a transient from a single difference image in different bands as a function of the signal-to-noise as obtained from Dark Energy Survey, (from R. Kessler). It shows, that for high SNR greater than ~ 10 , a single exposure used in difference imaging may be sufficient to detect the SN, while for lower SNR several such image differences may be necessary to have a high probability of detection.

We analyzed the OpSim output of the Baseline Observing Strategy, `enigma_1189.sqlite.db`¹ which includes Deep Drilling Fields (DDF) and the main survey (WFD). Using the OpSim output `enigma_1189`, we generated light curves for a type Ia supernova with a redshift of $z=0.5$ at a few different locations. A date in MJD is chosen where the LSST simulated data are reasonably well populated. We used the SALT2-extended model with x_0 , x_1 and c set so that the SNIa would have a specific magnitude of -19.3 in the rest frame BessellB band. This was performed using a version of `SNCosmo` to interpolate the SALT2 surfaces, and the LSST catalog simulation package to calculate the flux for LSST bandpasses.

[Figure 9.12](#) shows the light curve in different filters in a deep drilling field. The number of visits for 50 days (which is the period of the simulated SNIa light curve in rest-frame, which translates to 75 days at $z=0.5$) is 53 per filter. For this light curves, the supernova quality metric (SNQM) and the discovery metric (SNDM), are both equal to 1. SNDM=1 indicates that this object is a transient that will be definitely discovered, and SNQM=1 indicates that the light curves will be of high quality enough to contribute extremely well to the inference of cosmological parameters. The light curves and quantified metric demonstrate that data from Deep Drilling Fields would generate high quality light curves, allowing a high rate of supernova discovery.

In contrast, [Figure 9.13](#) shows a light curve from the WFD survey. This light curve is generated in Field 290 and has an average number of data points in the light curve of 2 per filter. Using these light curves, the probability (SNDM) of detecting this supernova is less than 0.1. [Figure 9.14](#) directly compares the light curves and cadences of the two fields considered, from the DDF and WFD.

To further study the quality of light curves across the survey, we simulate the same type Ia supernova in 16 different fields, including DDF 290 already studied, from the `enigma_1189` OpSim run and record the average number of visits per 50 day time window ([Table 9.2](#)). A well-known rule of thumb for good quality SN light curves is to demand 7-10 epochs per light curve spread over 50 days or so for more than one filter. Although the averages in [Table 9.2](#) are only approximations because the cadence is non-uniform, they give a clear indication that with the `enigma_1189` observing strategy, the WFD will be largely useless for SNe studies. This motivates our proposal of a rolling cadence strategy to improve the sampling of SNe over a much larger area than the DDFs.

9.5.4 Discussion

For the current baseline observing strategy, the DDF fields will produce an exquisite sample of well-characterized SNe for cosmology and astrophysics studies. Further analysis is required to determine exactly how many (useful) supernovae will be detected and what the resulting cosmological constraints will be, but in this section we have discussed and motivated several important intermediate metrics.

¹<http://ops2.tuc.noao.edu/runs/>

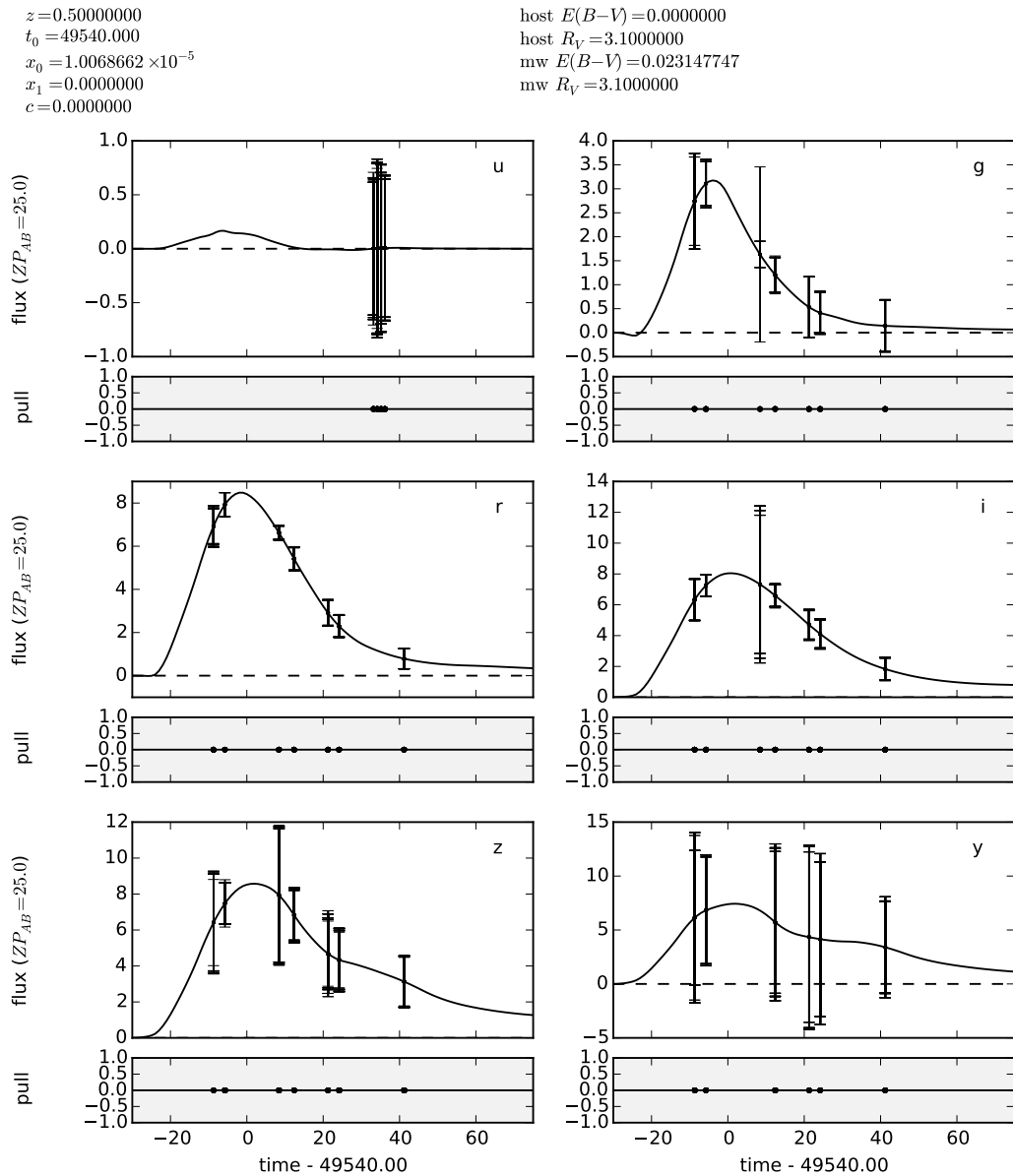


Figure 9.12: An example of light curve of SN Type Ia using Deep-Drilling Survey of the LSST Baseline OpSim run.

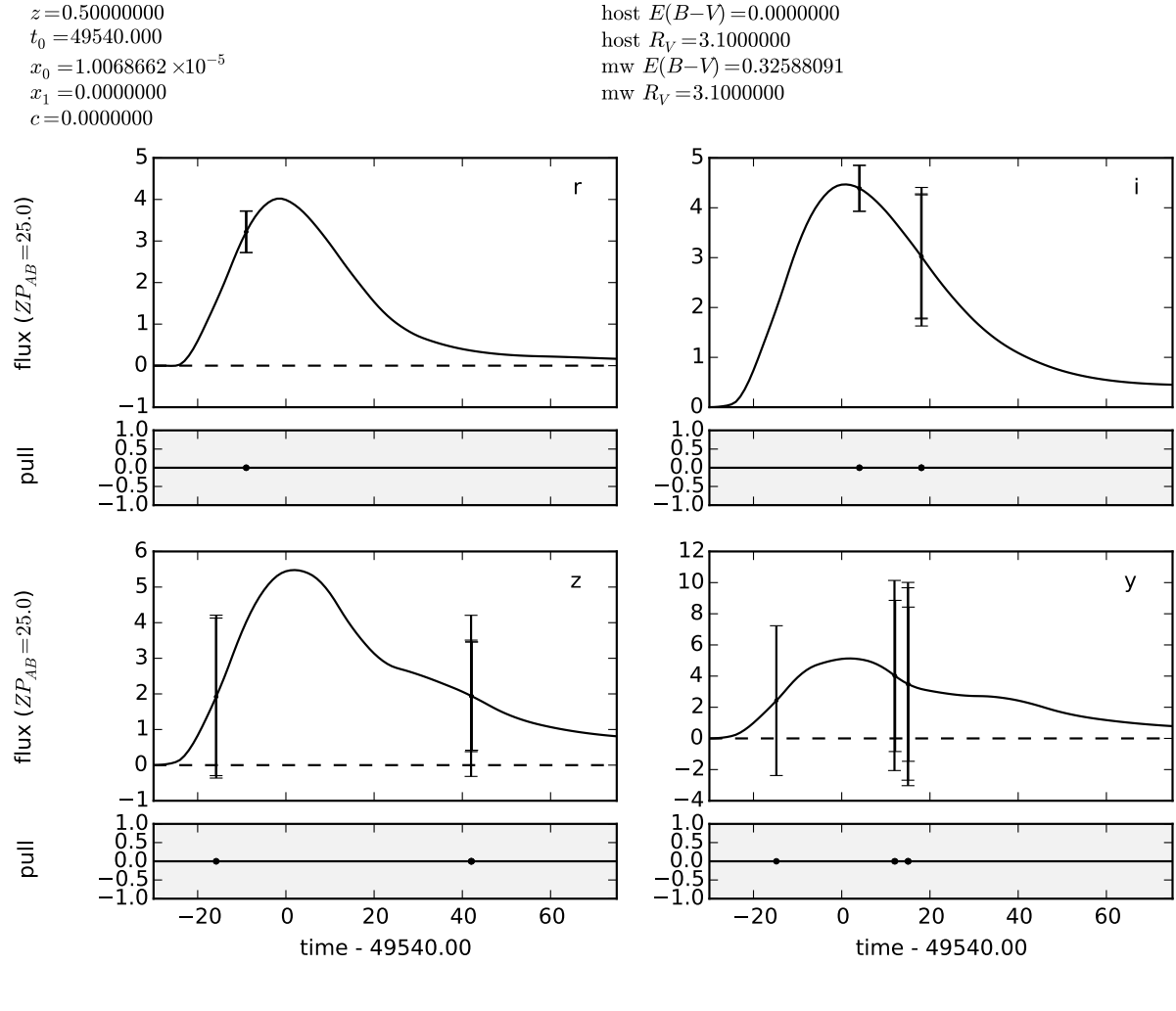


Figure 9.13: An example of light curve of SN Type Ia using the Main Survey of the LSST Baseline OPSIM run.

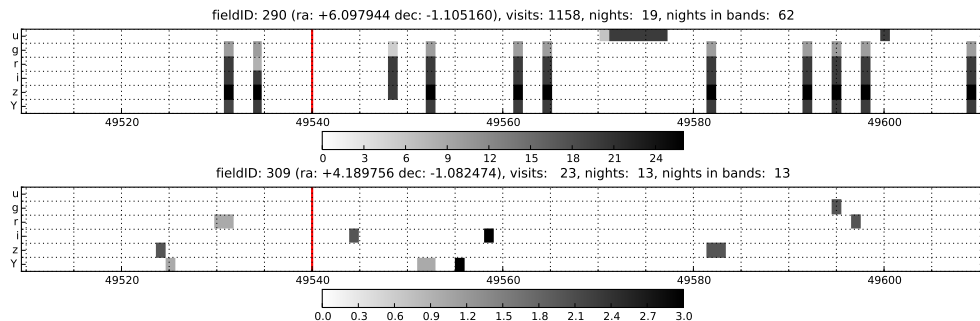


Figure 9.14: Cadence of Observations in the timewindow of a representative supernova at redshift of $z=0.5$ in a DDF (top) field (fieldID: 290) and a WFD (bottom) field (fieldID: 309). The red lines show the date of explosion, and the shades show the number of observations in a night in a distinct filter.

Field or No.	(RA,Dec)	No. of LSST visits per year (u,g,r,i,z,y)	Avg. No.
290 DDF	(349.386,-63.321)	2363 (398,229,402,414, 522,396)	53
1	(190,-83)	239 (38,41,41,44,33,42)	5.3
2	(20,-83)	252 (52,56,40,21,37,44)	5.7
3	(116,-66)	220 (36,38,37,32,44,33)	5.0
4	(240.05,-62.02)	101 (2,5,11,19,19,45)	2.2
5	(120,-50)	80 (4,7,9,18,24,18)	1.8
6	(80,-40)	96 (5,8,15,17,27,24)	2.2
7	(280,-40)	86 (4,2,6,4,24,18)	2.0
8	(30,-20)	86 (3,4,10,21,27,21)	1.96
9	(100,-20)	58 (4,2,6,4,24,18)	1.3
309	(6.097, -1.105)	80 (4,7,9,18,24,18)	1.83
11	(50,+1.5)	72 (3,6,10,12,22,19)	1.64
12	(320, +5)	7 (0,0,2,0,4,0)	0.15
13	(60,+5)	66 (0,7,11,20,28,0)	1.5
14	(60,+20)	72 (0,8,13,22,29,0)	1.64
15	(60,+30)	44 (0,5,6,15,18,0)	1.0

Table 9.2: Table of 16 fields in the OpSim `enigma_1189`. The first column is simply an index, with the special example fields of the DDF field 290 and WFD field 309 indicated. The position of the fields is shown in column 2. The third column contains the total and per filter band number of visits per year and this is averaged per filter per 50 day time window in column 4. It can be seen that with this observing strategy, only the deep drilling fields are suitable for supernova cosmology, where 7-9 data points per filter band is considered adequate quality.

Scientific Motivation for Rolling Cadence

It is clear from the above analysis, that the WFD component of the LSST survey will not be useful for supernova cosmology. However, with some changes to the observing strategy, it is likely that a large part of the WFD can be leveraged by implementing a rolling cadence strategy. The idea is to sample a particular field with much higher cadence, at the expense of other fields, for a period of time (such as 50-100 days) and change fields throughout the survey to preserve uniformity by the end of the 10 year period. Ideally, we would propose changing the filter every day, and trebling the average WFD cadence in these smaller fields. This would achieve our goal of 7-9 points per light curve over a 50 day period and in addition, the variety of filters would result in extremely well-characterized SNe in several bands that will thus be also be more easily classified.

Go to: • [the start of this section](#) • [the start of the chapter](#) • [the table of contents](#)

9.6 Strong Gravitational Lens Time Delays

Phil Marshall, Lynne Jones, Timo Anguita

The multiple images of strongly lensed quasars and supernovae have delayed arrival times: variability in the first image will be observed in the second image some time later, as the photons take different paths around the deflector galaxy, and through different depths of gravitational potential. If the lens mass distribution can be modeled independently, using a combination of high resolution imaging of the distorted quasar/SN host galaxy and stellar dynamics in the lens galaxy, the measured time delays can be used to infer the “time delay distance” in the system. This distance enables a direct measurement of the Hubble constant, independent of the distance ladder.

9.6.1 Target measurements and discoveries

For this cosmological probe to be competitive with LSST’s others, the time delays of several hundred systems (which will be distributed uniformly over the extragalactic sky) will need to be measured with bias below the sub-percent level, while the precision required is a few percent per lens. In galaxy-scale lenses, the kind that are most accurately modeled, these time delays are typically between several days and several weeks long, and so are measurable in monitoring campaigns having night-to-night cadence of between one and a few days, and seasons lasting several months or more.

To obtain accurate as well as precise lensed quasar time delays, several monitoring seasons are required. Lensed supernova time delays have not yet been measured, but their transient nature means that their time delay measurements may be more sensitive to cadence than season or campaign length.

Rung	Mean Cadence (days)	Cadence Dispersion (days)	Season (months)	Campaign (years)	Length (epochs)
0	3.0	1.0	8.0	5	400
1	3.0	1.0	4.0	10	400
2	3.0	0.0	4.0	5	200
3	3.0	1.0	4.0	5	200
4	6.0	1.0	4.0	10	200

Table 9.3: The observing parameters for the five rungs of the Time Delay Challenge. Reproduced from [Liao et al. \(2015\)](#).

9.6.2 Metrics

Anticipating that the time delay accuracy would depend on night-to-night cadence, season length, and campaign length, we carried out a large scale simulation and measurement program that coarsely sampled these schedule properties. In [Liao et al. \(2015\)](#), we simulated 5 different light curve datasets, each containing 1000 lenses, and presented them to the strong lensing community in a “Time Delay Challenge.” These 5 challenge “rungs” differed by their schedule properties, in the ways shown in [Table 9.3](#). Focusing on the best challenge submissions made by the community, we derived a simple power law model for the variation of each of the time delay accuracy, time delay precision, and useable sample fraction, with the schedule properties cadence, season length and campaign length. These models are shown in [Figure 9.15](#), reproduced from [Liao et al. \(2015\)](#), and are given by the following equations:

$$\begin{aligned} |A|_{\text{model}} &\approx 0.06\% \left(\frac{\text{cad}}{3\text{days}} \right)^{0.0} \left(\frac{\text{sea}}{4\text{months}} \right)^{-1.0} \left(\frac{\text{camp}}{5\text{years}} \right)^{-1.1} \\ P_{\text{model}} &\approx 4.0\% \left(\frac{\text{cad}}{3\text{days}} \right)^{0.7} \left(\frac{\text{sea}}{4\text{months}} \right)^{-0.3} \left(\frac{\text{camp}}{5\text{years}} \right)^{-0.6} \\ f_{\text{model}} &\approx 30\% \left(\frac{\text{cad}}{3\text{days}} \right)^{-0.4} \left(\frac{\text{sea}}{4\text{months}} \right)^{0.8} \left(\frac{\text{camp}}{5\text{years}} \right)^{-0.2} \end{aligned}$$

All three of these metrics would, in an ideal world, be optimized: this could be achieved by decreasing the night-to-night cadence (to better sample the light curves), extending the observing season length (to maximize the chances of capturing a strong variation and its echo), and extending the campaign length (to increase the number of effective time delay measurements). A combined figure of merit should therefore be readily available.

The quantity of greatest scientific interest is the *accuracy in cosmological parameters*: this could be computed as follows. Setting a required accuracy threshold defines the available number of lenses, which in turns gives us the mean precision per lens there. Combining the whole sample, we would get the error on the weighted mean time delay, and can equate that to the statistical uncertainty on the Hubble constant. The Figure of merit would be the final precision on H_0 , as a way to sum up the sample size and time delay measurability (at fixed accuracy requirement).

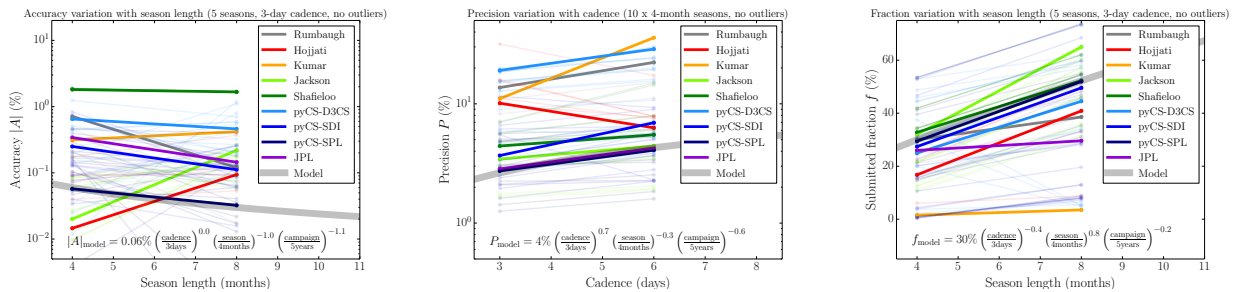


Figure 9.15: Examples of changes in accuracy A (left), precision P (center) and success fraction f (right) with schedule properties, as seen in the different TDC submissions. The gray approximate power law model was derived by visual inspection of the pyCS-SPL results; the signs of the indices were pre-determined according to our expectations. Reproduced from Liao et al. (2015).

9.6.3 OPSim Analysis

In this section we present the results of our ongoing OPsim/MAF analysis, as we try to answer the question “how good would the proposed observing strategies be, for time delay lens cosmography?”

We used the `SeasonStacker` to work with seasons, rather than calendar years. We used `ops2_1075` OPsim run for most of our tests, but plan to re-run on `minion_1016` and `kraken_1043`, in order to assess the new baseline cadence and compare it against a simulated observing strategy where the visit pair requirement is relaxed.

Figure 9.16 shows the results of our MAF analysis of one OPsim database, `ops2_1075`, where we have assumed that all filters were able to be used in the light curve analysis (as was implicitly assumed when applying the results of Liao et al.). These sky maps show that, over the main (WDF) survey area, the time delay accuracy, time delay precision and time delay lens success fraction are consistently maintained, indicating that the global average values of these metrics could conceivably be used as higher level metrics or even figure of merit.

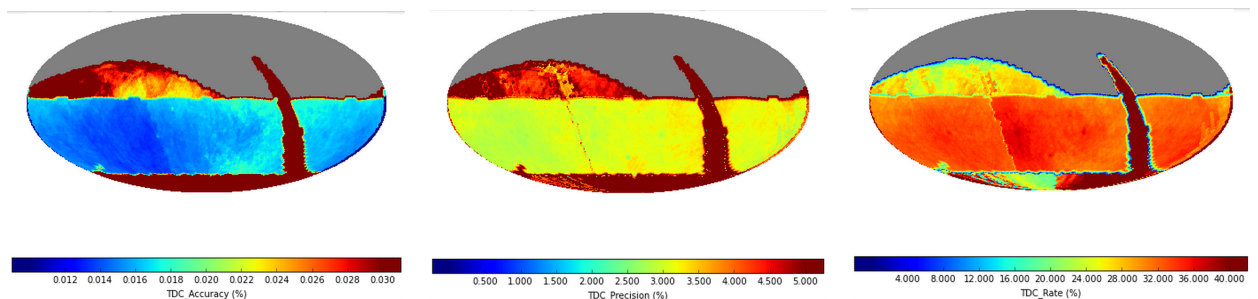


Figure 9.16: Sky maps of the accuracy A (left), precision P (center) and success fraction f (right) metrics, for the `ops2_1075` OPsim database and assuming all filters (`ugrizy`) are used in the analysis according to the assumptions described in the text.

9.6.4 Discussion

The main risk involved with this science case is that the multi-filter light curve analysis will not be well approximated by the real-life combination of all 6 filters together. The second time delay challenge (TDC2) will help answer this question. For now, just using 2 filters gives a lower limit on the overall precision we should expect.

We would expect the relaxation of the visit pairs requirement to increase the night to night cadence by a factor of two, if the visits are redistributed randomly in time. If OPSIM is not being as liberal as this, we may not see much improvement over the baseline cadence: efficiency maximization could be preventing visits being fully split. We are interested in any changes to the WFD survey time sampling that reduce the inter-night gaps: these would include rolling cadence schemes.

Go to: • [the start of this section](#) • [the start of the chapter](#) • [the table of contents](#)

10 Special Surveys

Chapter editors: *David Nidever, Knut Olsen.*

10.1 Introduction

The four main LSST science themes, as defined by the Science Book, drive the design of LSST’s main Wide-Fast-Deep survey. However, it has always been recognized that many important scientific projects, including some that are highly relevant to LSST’s main science themes, are not well served by the areal coverage and/or cadence constraints placed on the WFD survey. To this end, the LSST Project set aside a nominal 10% of the observing time to serve what are collectively called “special surveys”.

Projects that will certainly make use of this 10% time (that is not dedicated to the WFD survey) include the Deep Drilling fields and the Galactic Plane surveys, as well as any survey wishing to observe at declinations below -60° , such as the Magellanic Clouds. These special programs have the potential to heavily oversubscribe the nominal 10% of time assigned to them. It is of thus critical importance for these programs to define compelling science cases, clearly justify their observing requirements, and derive metrics to quantify the performance of a given schedule for the program. This chapter provides a venue for such investigations.

10.2 Solar System mini-surveys

David Trilling, Lynne Jones.

There are several populations of Near Earth Objects (Solar System bodies whose orbits bring them close to the Earth’s orbit) that, because of their orbital properties, would not be easily detected in the wide-fast-deep survey. These populations are very interesting for both scientific and sociological purposes, though, due to their close proximity to the Earth, and in fact their potential for impacting the Earth. LSST will have the capability to carry out surveys for these populations by using a small amount of time in “mini-surveys.” Two of these mini-surveys have pointings that fall within the nominal wide-fast-deep plan, and simply require a modification of the cadence. The third program is a twilight program, with a special cadence (though all twilight programs are likely to have special cadences). These three programs are listed here and described below. The three mini-surveys are the following:

- A mini-survey to look for mini-moons, which are temporarily captured satellites of the Earth;

- A mini-survey to find meter-sized impactors up to two weeks prior to impact. This would allow telescopic characterization of these impactors, which could be compared to laboratory measurements of the meteorites derived from the impactor. Advanced warning of an impactor also allows detailed study of impact physics by being on location when the impact occurs;
- A mini-survey to observe the “sweetspot” in twilight fields to look for NEOs in very Earth-like orbits that would otherwise not be found in opposition fields.

These surveys will support two important scientific investigations:

1. What are the properties of the population of objects that is nearest to the Earth?
2. What is the impact risk from NEOs in populations that have not yet been well characterized (mini-moons, sweetspot objects)?
3. How do the telescopic properties of an impactor relate to the laboratory-measured properties of the ensuing meteorites?

Many different types of objects and measurements with their own cadence “requirements” will fall into these two broad categories (with some overlap). These will be outlined in the next section.

10.2.1 Target measurements and discoveries

Special cadences

Each of the three Solar System mini-surveys requires a special cadence. These cadences are described here.

- **Mini-moons** Mini-moons are objects that are temporary satellites of the Earth. Therefore, they have orbital motions similar to the Earth’s moon, and much faster than other Solar System populations. Therefore, a special cadence is required to detect these objects enough times to link objects, create tracklets, and determine orbits. A suggested cadence for a mini-moon survey is a series of 3 second exposures, with each pointing visited at least twice per night. Such a survey would cover essentially all of the opposition sky each night. The opposition sky should be re-observed several nights in a row in order to link objects from night to night and determine their orbits. xxx need to work on these details; a bit sketchy right now xxx
- **Impactors** The Earth is struck by meter-sized impactors about once a month xxx confirm xxx. On two occasions, impacting asteroids have been discovered some hours before impact, but there are no existing surveys that are dedicated to finding impactors. Impactors generally have small apparent motions on the sky (because their orbits are not too different than the Earth’s). The single exposure depth of LSST images suggests that a meter-sized NEO could be discovered perhaps a week before impact (given the typical Earth-relative velocity of such a body). A suggested cadence for an impactor survey would be to survey the opposition patch four times per night. This is more visits than in the nominal cadence, and would allow high fidelity linking of observations to find orbits. The nominal wide-fast-deep cadence (twice per night, three times during a lunation) has a latency of orbit determination of up to two weeks, which is not acceptable for the impactor survey, as an impact would occur in a timescale of

just a few days from discovery. The cadence of four observations/night should be repeated roughly every three days, so that an object on an inbound trajectory could be observed at least once, and possibly twice, before impact. Note that this cadence is compatible with the wide-fast-deep survey, in that the fields and exposure times are nominal; the only difference is that each field is visited four times in a night, and that the fields are revisited every few nights. The overall impact of this mini-survey on the wide-fast-deep survey is likely to be small, and possibly negligible.

- **Twilight/sweetspot survey**

NEOs on very Earth-like orbits are relatively unlikely to come to opposition, and therefore are relatively unlikely to appear in data obtained in the wide-fast-deep survey. These objects are particularly interesting since, having very Earth-like orbits, they are the most likely objects to be Earth impactors. These objects are most likely to be detected in a twilight survey that looks at the “sweetspot” — a location at around 60 degrees Solar elongation that is only visible at twilight. Because these sweetspot fields are only visible for a small amount of time in a night, a special cadence is required to find and link these objects to determine their orbits. These observations would be best carried out in the z filter (because the observations are made in twilight, when the sky is still relatively bright). Fields should be revisited at 15 minute intervals, and each field should be revisited every other night during this experiment, so that observations can be linked. (A long interval between observations prohibits linking.) The total experiment should last roughly one week, so that each object would have a tracklet on four nights (nights 1,3,5,7). During twilight, some 25 pointings could be visited before the fields have set. Because these observations are made during twilight, there may be no significant impact on the nominal wide-fast-deep survey.

Measurements

For each of these three programs, the most important measurement to be made is the position of any object as a function of time. In other words, the usual measurements of moving objects from LSST images is also the requirement for the source detections for these mini-surveys. As usual for Solar System surveys, there is a trade-off of sensitivity (Solar System objects are most easily detected in r band) against characterization (observing a given object in multiple filters yields an estimate of composition). For these three cases, discovery and good orbit determination is probably more important than immediate characterization from LSST measurements, so the nominal expectation is that all these mini-surveys would be carried out in r band.

10.2.2 Metrics

The metrics to be used to determine the efficacy of LSST at scientific success of these mini-surveys are identical to those employed in [Chapter 3](#). The most important of these metrics include the completeness as a function of size; the number of detections over a given length of time (for instance, the one week approach timescale of impactors); and the quality of the derived orbit. These metrics are defined in more detail in [Chapter 3](#). The important question is: how much value do the mini-surveys add?

10.2.3 OpSim Analysis

The current default observing strategy does not include any of these mini-surveys. Therefore, the scientific yield, at this default, is zero. Both the mini-moons and impactor surveys are relatively small experiments, on the scale of the LSST project, at something like 10–20 hours total per instance of the experiment. (The impactor experiment, for example, might be carried out one or several times a year, both to build up statistics and to identify further potential impactors.) Furthermore, the impactors survey cadence is different from the nominal wide-fast-deep survey, but could be a simple modification of the nominal wide-fast-deep survey cadence.

The twilight/sweetspot survey is also not included in the nominal OpSim strategy, and the overall discussion of twilight observations is deferred to a later discussion.

Go to: • [the start of this section](#) • [the start of the chapter](#) • [the table of contents](#)

10.3 Short Exposure Surveying

Christopher Stubbs

The current LSST requirements stipulate a minimum exposure time of 5 seconds, with an expected default exposure time of 15 seconds. This document advocates for decreasing the minimum exposure time requirement from 5 to 0.1 seconds. This would increase the dynamic range for bright sources (compared to the default 15 sec time) by about 5 magnitudes, to a total of 13 astronomical magnitudes (where dynamic range is the difference between the brightest unsaturated source and the faintest point source detectable at 5 sigma). This is a large factor, and would enable a wide range of science goals, outlined below. One interesting aspect of this is that it would allow us to operate the LSST system during twilight times that would otherwise saturate the array due to background sky brightness. This would allow a number of the goals described below to be carried out without impacting the primary survey by conducting observations during twilight sky conditions that would saturate the array at longer exposure times.

10.3.1 Introduction

Since the twilight sky brightness is an important factor discussed below, we provide here a very brief outline of the temporal evolution of the background sky brightness.

Tyson & Gal (1993) provide a simple framework that serves our purposes well. They provide observational data as well as a simple model for the evolution of twilight sky brightness. Figure 1 from that paper is included below, as [Figure 10.1](#). They show that a good model for the sky brightness evolution is given by an exponential with $\log_{10}(S) = (k/\tau)t + C$, where S is the sky brightness in electrons per pixel per second, C is the dark sky background, $k = (10.6 \text{ minutes})^{-1}$ is a universal (band-independent) timescale during which the sky's surface brightness changes by a factor of ten (at latitude –30 degrees), and τ is a season-dependent factor that ranges from 1.0 at the equinox to 1.07 in austral winter and 1.20 in austral summer. So the rule of thumb is that

we should expect it to take 4.25 minutes for the sky background to change by one magnitude per square arc sec. (In what follows we'll ignore the increased twilight time in summer and winter.)

For current generation typical astronomical camera systems that take over a minute to read out, this 4.2 minute time scale means that only a handful of images can be obtained during twilight time. But for the LSST camera with a 2 second readout time, we can obtain hundreds of short exposures during twilight. Even if we are limited to a 15 second cadence due to thermal stability or data transfer limitations there is a large amount of time opened up that we can use.

What do we stand to gain in operational time with shorter exposures? If the standard survey terminates taking 15 second exposures due to some sky brightness criterion, by shifting to 0.1 sec images at that point we will have changed the sky flux per pixel by $2.5 \log_{10}(150) = 5.4$ magnitudes. This brings us back into a high dynamic range regime, as described below.

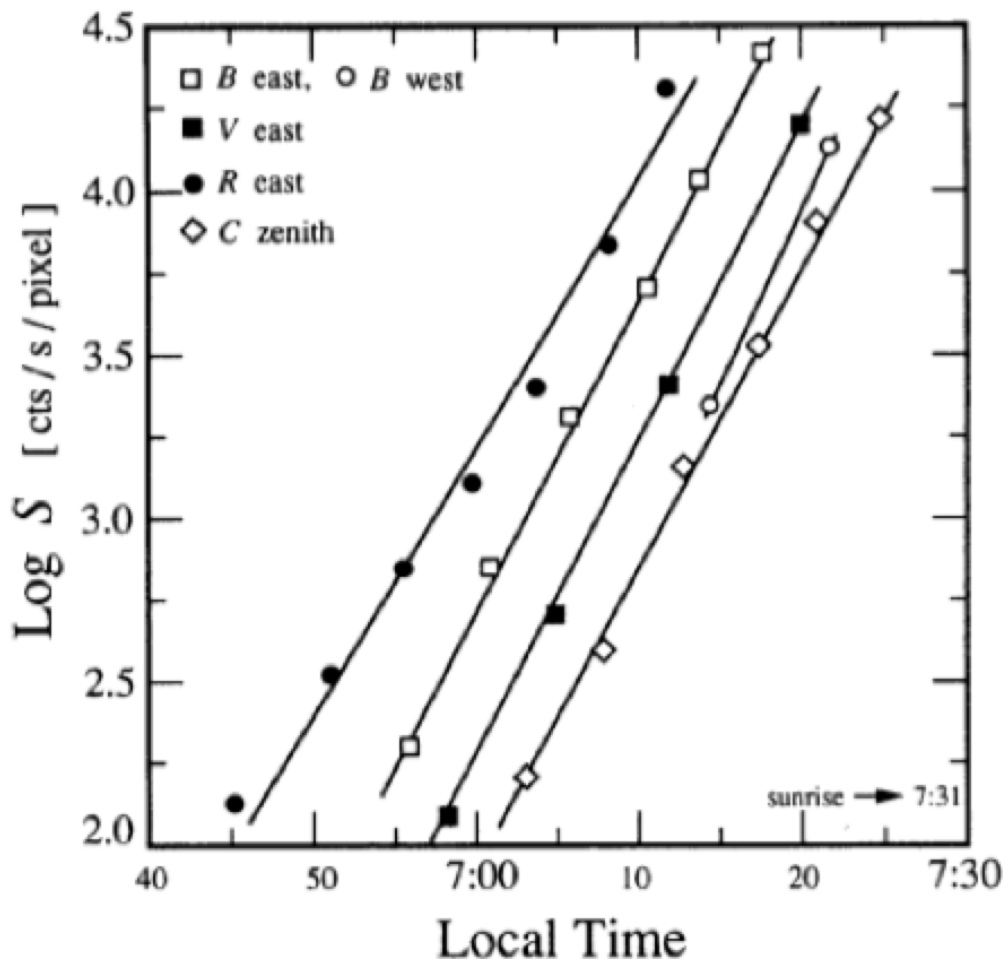


Figure 10.1: (reproduced from Tyson et al, 1993). This plot shows the twilight sky surface brightness as a function of local time for four broadband filters (C, B, V and R) and different pointing directions. The surface brightness changes by one magnitude in a 4.2 minute interval, essentially independently of the passband and pointing.

Figure 10.2 illustrates the principles that underpin this proposal. LSST is a unique combination

of hardware and software, that will deliver reliable catalogs of both the static and the dynamic sky. By pushing towards shorter integration times we can greatly expand the scientific reach of the system.

The dynamic range in magnitudes that we can achieve for a given integration time depends on the sky background, the read noise, and the full well depth per pixel. We will adopt a typical value of 100Ke for the full well depth, but the arguments presented below are essentially independent of this value. The dynamic range in magnitudes is limited on the bright end by the point source whose PSF peak exceeds full well, and on the faint end by the 5σ point source sensitivity, which depends on sky brightness per pixel. So we are squeezed between the two parameters of full well depth and sky background.

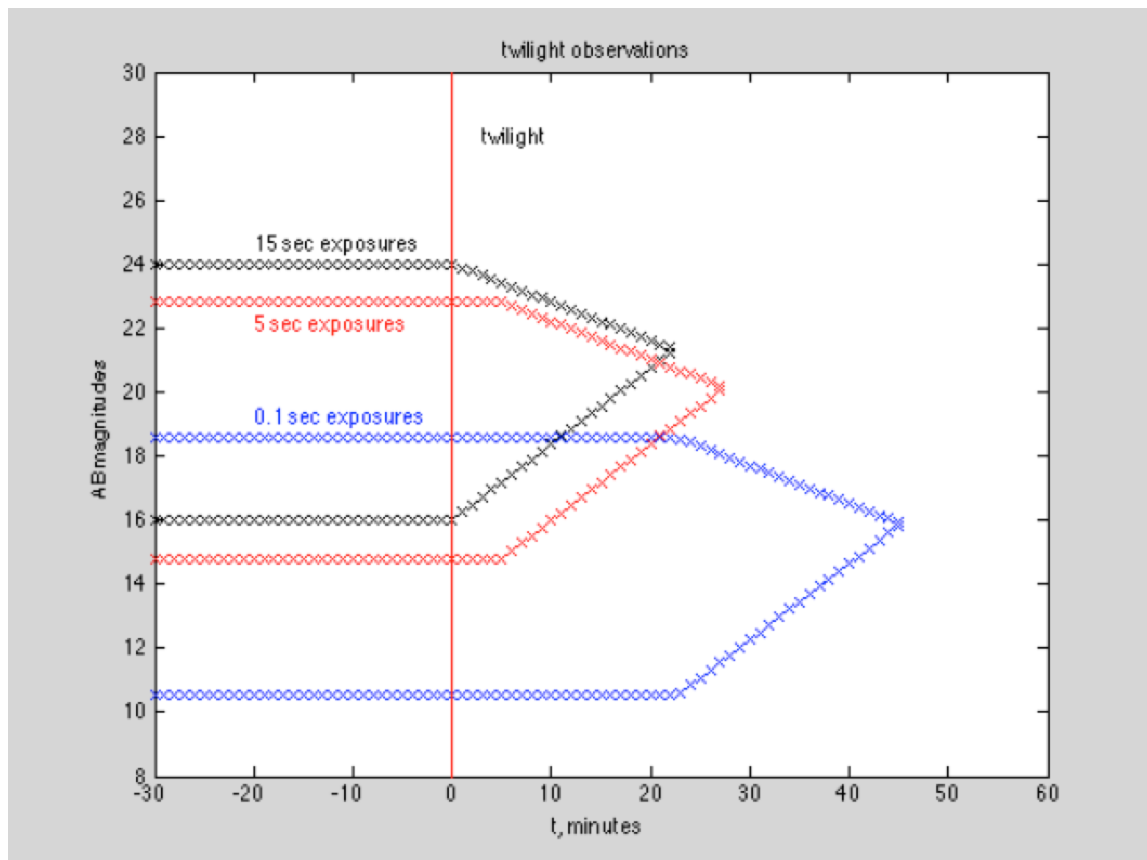


Figure 10.2: Twilight dynamic range. As we enter morning twilight time, the increasing sky brightness requires brighter sources for 5 sigma detection, and also limits unsaturated objects to increasingly fainter sources. Eventually the gap between these goes to zero. But operating at shorter exposure times allows us to push useful survey operations into brighter twilight time, and also to increase the dynamic range of the LSST survey products. The black lines correspond to 15 second integrations (nominally in the r band), the red lines to 5 second exposures, and the blue curves to 0.1 second exposures. The upper lines in each case represent the 5 sigma point source detection threshold while the lower line corresponds to the source brightness that produces saturation in the peak pixel of the PSF. Adding shorter exposure times increases our dynamic range in flux, and adds valuable observing time.

The 5-sigma limiting flux scales as the square root of the sky brightness, while the saturation flux decreases linearly as sky brightness increases. So the two curves in Figure 10.2 have slopes that

differ by a factor of two. Operating during bright-sky time with short exposures adds about 20 minutes of observing per twilight, or 40 minutes per night. This is a non-trivial resource!

[Figure 10.2](#) shows one reason why it is not advantageous to go below 0.1 second exposures- we would lose the overlap between a twilight survey and the standard LSST object catalog.

10.3.2 Science Drivers for Shorter Exposures

Having set the stage for the opportunity to operate at shorter exposure times either during dark sky time, or during twilight, or both, we now describe some of the scientific motivations for doing so.

Discovery space at short time scales.

LSST is a time domain discovery machine. It is hard to anticipate the importance of being able to detect astronomical variability on short time scales. By extending the time domain sensitivity to phenomena with a characteristic time of less than 5 seconds, we will have added 1.5 orders of magnitude in time domain sensitivity.

Taking short exposures does not necessarily imply a requirement on fast image cadence. Periodic variability can be readily detected and characterized with a succession of short images that do not satisfy the Nyquist criterion, as long as we know the time associated with each data point to adequate accuracy. But it does seem appropriate to investigate the maximum possible rapid-fire imaging rate for LSST, presumably limited by either data transfer bottlenecks or by thermal issues within the camera.

Distances to Nearby SN Ia- an essential ingredient in using supernovae to probe dark energy.

The determination of the equation of state parameter of the Dark Energy using type Ia supernovae entails measuring the redshift dependence of the luminosity distances to objects over a range of redshifts. The low end of this redshift range is limited by peculiar velocities to considering supernovae at redshifts $z > 0.01$. At this distance (distance modulus of $\mu = 33$) the peak brightness of a type Ia supernova is $r=15$ and exceeds the expected LSST point source saturation limit.

Moreover, the rate on the sky of these bright nearby supernovae is so low that in the standard cadence we don't expect to obtain well-sampled multiband light curves for them. But we will discover many of them on the rise. Using twilight time with short exposures to obtain appropriate temporal and passband coverage will allow us to extend the LSST SN Hubble diagram across the entire redshift range of 0.01 to 1.

It is vitally important that we obtain these nearby-SN light curves on the same photometric system, reduced with the same data reduction pipeline, as the distant sample. This means we really must use the LSST instrument and software in order to avoid systematic errors arising from differences in photometric systems or algorithmic issues.

We stress that this twilight SN followup campaign can be accomplished without impacting the main survey, during the roughly 20 minutes per night of twilight that would otherwise unusable at the default exposure time. We would use the brighter twilight time to obtain pointed observations on nearby supernovae, motivated by the importance of photometric uniformity described above.

A Bright Star Survey for Galactic Science.

We could also use the added twilight time to conduct a bright star survey, and the precise astrometry and photometry from LSST can then be used in conjunction with archived data ranging from 11th to 27th AB magnitudes. This short-exposure domain would extend the LSST dynamic range in fluxes by two orders of magnitude, towards the bright end. Moreover, obtaining precise positions, fluxes and variability at these brighter magnitudes would greatly increase the overlap with the historical archive of astronomical information, including from digitized plate data. We would be able to obtain astrometric and color information to high precision, as well time series for variability studies.

An example of an application to Milky Way structure studies comes from RR Lyrae variable stars. With a saturation magnitude of around 16th in the standard LSST survey, RR Lyrae closer than 20 kpc will be saturated in the standard LSST images. So we will lose nearly all Galactic RR Lyrae. Extending the survey's bright limit to 11th magnitude will allow us to collect light curves for RR Lyrae beyond ~ 100 parsecs, collecting essentially all Southern hemisphere Galactic RR Lyrae.

Another application for stellar population studies is measuring the fraction of binary stars as a function of stellar type, metallicity, age and environment. By conducting a variability survey in the 11-18 magnitude range we can capitalize on temperature and metallicity data already in hand for many of these objects.

Another application of a bright star survey would be to search for planetary transits in the magnitude range appropriate for radial velocity followup observations using 30 meter class telescopes. For high dispersion spectrographs at the 4m aperture class, most targets are currently around 8th magnitude, so we should expect 30m telescopes to attain similar radial velocity precisions for sources of magnitude $8 + 5\log(30/4) = 12$. By going to shorter exposures we obtain almost an hour's additional observing time per night when these sources don't saturate, whereas they are far beyond saturation in the default 15 second LSST survey images.

A typical ($r-K$) color between SDSS and 2MASS is $r-K=3$. The 2MASS catalog is complete down to $K \sim 14$ which corresponds to $r \sim 17$. So most 2MASS stars will be saturated in the standard LSST 15 second observations. A bright star survey will allow a multiband match to the 2MASS data, as well as an astrometric comparison between the two catalogs.

Finally, the apparent magnitude of solar system objects depends on their distance from us and from the sun, as well as illumination and observation geometry. Extending the bright limit will allow us to track asteroid positions as they approach opposition.

10.3.3 Counterarguments

What About Scintillation Effects?

Short exposure times suffer from scintillation effects. An estimate for uncertainty due to scintillation is provided by <http://astro.corlan.net/gcx/scint.txt>. For a 0.1 second integration we expect a fractional flux uncertainty of 0.15 at 2 airmasses and 0.043 at 1 airmass, for a 10 cm aperture. Scaling this up to the 8.5m aperture of LSST by a factor $D^{2/3}$ predicts fractional flux variations of below one percent, even at two airmasses, for a 0.1 second exposure. So scintillation should not impact our ability to make precision measurements of flux and position.

What about just doing this with smaller telescopes?

A possible counter-argument to the proposal of allowing for shorter exposure times is that much of this can be done with smaller telescopes. But it's important to bear in mind that LSST is a system, and the data reduction and dissemination tools are as important as the hardware. We intend to deliver accessible, high-quality, well-calibrated photometry on a common photometric system and correspondingly good positions. If we do so from a co-added point source depth of 27th to the short-exposure bright limit of 11th magnitude we will span over six decades in flux on a well-calibrated flux scale. We would also have the ability to study astrophysical variability on time scales from 0.1 second to 10 years, which is nine decades in the time domain. This combination of temporal and flux dynamic range would be a truly remarkable achievement, and would yield science benefits far beyond the illustrative examples provided above. Much of this discovery space is enabled by going to shorter exposures.

10.3.4 Proposed Implementation and Impacts

The implementation of this would simply entail taking short-exposure images during twilight time that would otherwise go unused. The data rate would go up, and the number of shutter cycles per night would also increase.

10.4 A Mini-Survey of the Old Open Cluster M67

Suzanne Hawley, Ruth Angus, Derek Buzasi, James Davenport, Mark Giampapa, Vinay Kashyap, Søren Meibom.

10.4.1 Introduction

As coeval, equidistant, and chemically homogeneous collections of stars, open star clusters are ideal for studying the dependence of astrophysical phenomena on the most fundamental stellar parameters - age and mass. Indeed, there are few fields in astronomy that do not rely on results from cluster studies, and clusters play a central role in establishing how stellar rotation and magnetic

activity can be used to constrain the ages of stars and stellar populations. From an observational perspective, because of their angular extent they are accessible to efficient surveys in both imaging and multi-object spectroscopy. A selection of clusters representing a sequence in age can be used to establish critical empirical relationships such as the dependence of activity on rotation, the relationships between activity, rotation and stellar age, the evolution of activity cycles, and the nature and evolution of flare activity—an urgent area of investigation in view of the potential impacts on the structure and evolution of exoplanet atmospheres in systems with late-type host stars.

Unfortunately for observers, open clusters dissipate on timescales which are generally comparable to stellar evolution timescales on the lower main sequence, so older clusters are relatively rare. In addition, most clusters lie close to the galactic plane, where determining membership is significantly complicated by the large numbers of foreground and background stars. In this document, we suggest an LSST survey of M67, an open cluster whose relative compactness, age, and location above the galactic plane combine to make it the ideal cluster for a closer look.

10.4.2 Science Case

The evolution of the rotation rate and magnetic activity in solar-type stars are intimately connected. Stellar rotation drives a magnetic dynamo, producing a surface magnetic field and magnetic activity which manifests as starspots, chromospheric (Ca II HK, H α) and coronal (X-ray) emission, and flares. The magnetic field also drives a stellar wind causing angular momentum loss (“magnetic braking”) which in turn slows the rotation rate over time, leading to decreased magnetic activity. More magnetically active stars (larger spots, stronger Ca II HK, H α and X-ray emission, more flares) therefore tend to be younger and to rotate faster. The rotation-age relationship is known as gyrochronology, and the correlation between rotation, age and magnetic activity for solar-type stars was first codified by Skumanich (1972). However, the decrease in rotation rate and magnetic field strength over long time-scales is poorly understood and, in some cases, hotly contested (Angus et al. 2015, Van Saders et al. 2016). Recent asteroseismic data from the Kepler spacecraft have revealed that magnetic braking may cease at around solar Rossby number, implying that gyrochronology is not applicable to older stars (Van Saders 2016).

In addition, the rotational behavior of lower mass stars is largely unknown due to the faintness of mid-late type M dwarfs. There is reason to believe that M dwarfs cooler than spectral type M4 may behave differently from the G, K and early M stars, since that spectral type marks the boundary where the star becomes fully convective, and a solar-type shell dynamo (which requires an interface region between the convective envelope and radiative core of the star) can no longer operate. Using chromospheric H α emission as a proxy, West et al. (2008) studied a large sample of M dwarfs from SDSS and showed that magnetic activity in mid-late M dwarfs lasts much longer than in the earlier type stars.

The difficulties inherent in understanding the evolution of stellar rotation and activity on the lower main sequence are further increased by our inability to obtain accurate ages for field stars with ages comparable to that of the Sun, which appears to be just the range of ages for which our understanding of the phenomena are most suspect. While asteroseismology can address this

situation with exquisite precision, it can only do so for the brighter stars accessible to space missions such as Kepler. Making use of older open clusters is a way to fill this gap.

The solar-age and solar-metallicity open cluster, M67, is a benchmark cluster for understanding stellar evolution and the nature of late-type stars at solar age. M67 is unique due to its solar chemical composition, the fact that it is relatively nearby (~ 900 pc), and its relatively low extinction due to its location above the galactic plane. Extensive proper motion, radial velocity and photometric surveys have been carried out (e.g., Girard et al. 1989, Montgomery et al. 1993, Yadav et al. 2008, Geller et al. 2015), while Giampapa et al. (2006) conducted a survey of chromospheric activity in the solar-type members of M67 which yielded interesting insights on the range of magnetic activity on sun-like stars in comparison with the range exhibited by the Sun during the sunspot cycle. nehag et al. (2011) find that solar twins in M67 have photospheric spectra that are virtually indistinguishable from the Sun's at echelle resolutions.

Located in the sky at approximately RA = 9h and Dec = $+12^\circ$, M67 is an exceptionally meritorious and accessible candidate for an LSST mini-survey, which would also enable productive follow-up observations by an array of OIR facilities. LSST observations of M67 would yield data on the rotation periods and variability of its members at high precisions, particularly for dwarfs later than about K0 ($V > 16$). Little is known about the nature of variability on short and long time scales for low-mass dwarfs at solar age. For example, the frequency of ‘superflaring’ at solar age could be investigated for the first time. Furthermore, the combination of LSST observations and OIR synoptic datasets for M67 would enable the characterization of the conditions of the habitable zones in late-type stars at solar age.

In addition to sun-like stars, M67 includes an array of interesting objects such as blue stragglers (Shetrone & Sandquist 2000), an AM Her star (Gilliland et al. 1991, Pasquini et al. 1994), a red straggler, two subgiants (Mathieu et al. 2003), and detected X-ray sources due to stellar coronal emission (e.g., Pasquini & Belloni 1998). Davenport & Sandquist (2010) found a minimum binary fraction of 45% in the cluster. Other investigations include studies of the white dwarf cooling sequence (Richer et al. 1998), angular momentum evolution near the turnoff (Melo et al. 2001), and the behavior of key light elements such as lithium and beryllium (e.g., Randich et al. 2007).

10.4.3 Observing Plans

Performing the mini-survey of M67 which we advocate would require two modifications to the baseline LSST operations mode. LSST does not plan to observe as far north as Dec = $+12^\circ$ in its main survey, but the M67 field should certainly be accessible for a mini-survey as a single pointing. Since imaging the entire cluster would require less than a single LSST field, we view this additional pointing as being of minimal inconvenience relative to the expected scientific gain. As we anticipate rotation periods ranging from \sim days up to several months, we would require sampling over all of these timescales, though it need not be continuous.

A second potential complication is that the cluster is relatively bright. While dwarfs below about spectral K0 in M67 are fainter than the LSST bright limit of ~ 16 , the cluster G dwarfs will saturate the LSST detectors in a 15-second integration. We suggest two alternative approaches to address this issue. First, if the short exposure surveying mode suggested elsewhere in this document (Section 10.3) is adopted, then the new LSST minimum exposure time of 0.1 seconds

would easily accommodate the entire M67 main sequence. Alternatively, or if the short exposure mode is not adopted, we note that work with the Kepler mission (e.g., Haas et al. 2011) has shown success using custom pixel masks to accurately perform photometry on stars as much as 6 magnitudes brighter than the saturation level. Similar techniques applied to the LSST fields should enable photometry for the G dwarfs, particularly those in less-crowded portions of the field.

Go to: • [the start of this section](#) • [the start of the chapter](#) • [the table of contents](#)

Go to: • [the start of this section](#) • [the start of the chapter](#) • [the table of contents](#)

11 Synergy with WFIRST

Chapter editor: *Jason Rhodes*.

Contributing authors: *David Rubin, David Bennett, Matthew T. Penny, Rachel Street*.

11.1 Introduction

The Wide Field Infrared Survey Telescope (WFIRST) is a NASA mission that entered Phase A in February 2016. WFIRST was the highest recommendation for large space missions in the 2010 New Worlds New Horizons Decadal Survey. That recommendation envisioned a wide-field observatory with near infrared (NIR) capabilities to complement LSST's optical capabilities; the Decadal Survey recognized the obvious synergy between WFIRST and LSST. WFIRST's design has evolved since 2010 and the design being pursued for a mid-2020s launch uses an existing 2.4m telescope donated to NASA, giving WFIRST capabilities not envisioned by the Decadal Survey. WFIRST has 3 primary science objectives:

- Determine the nature of the dark energy that is driving the current accelerating expansion of the universe using a combination of weak lensing, galaxy clustering (including Baryon Acoustic Oscillations and Redshift Space Distortions), and supernovae type Ia (SN).
- Study exoplanets through a statistical microlensing survey and via direct imaging and spectroscopy with a coronagraph.
- Perform NIR surveys of the galactic and extragalactic sky via a Guest Observer program.

WFIRST will be at L2 to enable the thermal stability needed for the precise astrometric, photometric, and morphological measurements required for these science goals. The baseline WFIRST mission architecture is described in detail in the final report of the WFIRST Science Definition Team (arxiv/1503.03757). The WFIRST Wide Field Instrument(WFI) has a NIR focal plane with a ~ 0.28 square degree field of view made up 18 4k \times 4k Teledyne H4RG NIR detectors and will have imaging capabilities from 0.7 – 2 microns and grism spectroscopy capabilities from 1.35 – 1.89 microns with $R \sim 461\lambda$. The WFI also contains an Integral Field Channel (IFC) spectrometer with $R \sim 100$ resolution over the range 0.6 – 2 microns for SN follow up. The exoplanet coronagraph will have imaging (0.43 – 0.97 microns) and spectroscopic (0.6 – 0.97 microns) capabilities with a contrast ratio of 1 part in a billion.

WFIRST's 6 year primary mission is envisioned to have 2 years dedicated to a ~ 2200 square degree High Latitude Survey (HLS) for weak lensing and galaxy clustering, 1 year of microlensing observations divided into 6 seasons, 0.6 years of SN search and follow-up, one year dedicated to the coronagraph and 1.4 years dedicated to competitively selected Guest Observer observations.

WFIRST has no expendables that would prevent an extended mission of 10 years or longer, and an extended mission will likely be given over entirely to Guest Observer observations.

The synergy with LSST is very promising indeed. In this chapter we aim to lay out three specific projects in the three main WFIRST science areas, and test the simulated LSST Observing Strategies for their performance in each case. Then, we use these results to design a suite of modified LSST Observing Strategies, which we propose as new OPSIM simulation runs.

11.2 Cosmology with the WFIRST HLS and LSST

Jason Rhodes

WFIRST's High Latitude Survey (HLS) will cover 2200 square degrees in 4 NIR photometric filters (3 of which will be sufficiently sampled for weak lensing shape measurements) and NIR grism spectroscopy. The benefits of overlapping spectroscopic and photometric surveys for dark energy constraints and systematics mitigation are strong. The primary scientific driver of the photometric portion of the WFIRST HLS is weak gravitational lensing, but there is a wide range of ancillary science that will be possible with the publicly available WFIRST HLS data (see for instance, the SDT report mentioned above). However, the requirements on the HLS are largely set by constraints from weak lensing measurements. Each galaxy in the WFIRST weak lensing survey needs to have an accurate photometric redshift. This requires optical photometry that reaches the depth of the NIR photometry WFIRST will acquire (J 27AB). *Thus, the WFIRST weak lensing survey will require the full 10-year LSST depth in 4 optical bands for optimal photometric redshift determination.*

There is strong benefit not just to WFIRST, but to LSST, in coordinating observations of the WFIRST HLS survey field. The combination of full-depth LSST data and WFIRST HLS NIR data will provide the gold standard in photo-zs. Furthermore, WFIRST grism observations over the same area will provide many millions of high quality slitless spectra and WFIRST's IFC can be run in parallel with WFI observations to provide many more very accurate spectroscopic redshifts in the survey area. Thus, the WFIRST photometric data will help to provide better LSST photo-zs and WFIRST will also provide many of the spectra needed as a training set to calibrate the photo-zs for both missions. A further benefit to LSST might be the reduced need for LSST observations at the reddest end of the LSST wavelength range (the z and y filters), where both the atmosphere and the physics of CCDs make ground-based observations less efficient than what WFIRST can achieve. Further work is needed to quantify this benefit, especially as the WFIRST proposed filter set is evolving. Finally, the joint processing of LSST and WFIRST data will provide better object deblending parameters than LSST can achieve alone; WFIRST will be able to provide a morphological prior for the deblending of LSST images.

11.2.1 Measuring Dark Energy Parameters

The goal in this science project would be to measure Dark Energy parameters from various weak lensing probes, capitalizing on the improved photometric redshifts that a joint analysis of LSST and WFIRST photometry would provide. A useful Figure of Merit is the usual Dark Energy Task

Force figure of merit, quantifying the available precision on the equation of state parameters w_0 and w_a . For example, we are interested in improvements in the weak lensing DE FoM as the LSST photometric redshifts and galaxy shapes are improved over the whole LSST survey area via joint analysis with WFIRST. We are also interested in increasing the WFIRST DE FoM as quickly as possible. Indeed, the basic problem we face is one of timing: being able to combine the WFIRST data with the LSST sooner will accelerate the production of cosmological results.

Therefore, we propose an acceleration of the LSST survey over about 10% of the LSST survey area (the ~ 2200 WFIRST HLS) such that the full LSST ten years survey depth is reached on a timescale that maximizes the joint usefulness of LSST and WFIRST data on that area. Assuming the two year WFIRST HLS is taken in the first four years of a WFIRST mission that launches in 2024, this would require reaching full LSST depth over that area in ~ 2028 rather than ~ 2032 . Since the HLS area is roughly 1/8 as large as the LSST “Main Survey” region, this could be achieved by devoting 1.25 years of LSST observations to the HLS area, assuming that it covers a wide enough range of Right Ascension. More practically, it could be achieved by devoting 25% of LSST observing time to this area during each of the first 5 years of the LSST survey, which doubles the time it would naturally be observed during those years at a modest reduction in coverage of the rest of the Main Survey area during that time period. Given existing plans to speed up the LSST cadence over small sub-areas of the LSST survey, this may only require coordination of the locations of the accelerated LSST area and the WFIRST HLS. As LSST and WFIRST progress, there is a mutual benefit in continuing discussions about the optimal joint observation schedule.

A simple, first order diagnostic metric would be the amount of LSST/WFIRST overlapping survey area that reaches the full LSST depth when the WFIRST HLS is completed. Such a metric is straightforward, but not able to be meaningfully encoded until the 2020s, when the WFIRST launch date and survey plan is more definite. Strawman survey plans could, however, be evaluated to help with LSST schedule planning. A slightly more complicated metric could include the pace at which the overlapping LSST/WFIRST survey areas are both taken to full depth, since this would make each data set maximally useful to the US community (or anyone with immediate access to both WFIRST and LSST data). WFIRST data is unlikely to have any proprietary period. Current plans call for the WFIRST HLS to be conducted in multiple passes, but the exact survey pattern is still undecided, so this metric is also not quantifiable yet.

There may be some reduced need for the the LSST reddest bands in the WFIRST HLS overlap area, which should also be folded into the metric. We note that the default survey strategy would only achieve the full LSST photometric depth over the WFIRST HLS after 10 years of survey (~ 2032).

11.2.2 Discussion

Increasing the cadence of the LSST survey over $\sim 10\%$ of the LSST survey has science benefits that go far beyond the LSST/WFIRST synergy described here: an observing strategy that met the joint WFIRST/LSST cosmology goals could also provide the kind of “rolling cadence” favored by other science teams. There are benefits to certain aspects of time-domain science. Every effort should be made to coordinate all discussions of increased survey cadence (resulting in full LSST depth well before 10 years) over sub-areas of the LSST survey footprint. Specific attention should be paid to

whether the accelerated portions of the LSST survey can completely overlap the WFIRST HLS, and whether the position of the WFIRST HLS can be determined, in part, by other science drivers within LSST. This will require close LSST and WFIRST coordination at the Project levels.

Go to: • [the start of this section](#) • [the start of the chapter](#) • [the table of contents](#)

11.3 Supernova Cosmology with WFIRST and LSST

David Rubin

The WFIRST SN survey seeks to measure thousands of SNe Ia with excellent systematics control over a two-year period. The Science Definition Team (SDT) outlined a three-tiered cadenced imaging survey: wide to $z = 0.4$ (27.44 square degrees), medium to $z = 0.8$ (8.96 square degrees), deep to $z = 1.7$ (5.04 square degrees). SNe discovered in the imaging would be followed with IFU spectrophotometry, helping to monitor changes in SN physical parameters and the extinction distribution with redshift. However, due to the slew time (now believed to be higher than was used in the SDT survey), and high read noise in short exposures, the wide survey was very inefficient, spending a bit more than half of its time on slews, while the medium survey would spend a significant fraction of its time slewing. However, the LSST DDFs offer a path to high signal-to-noise, well calibrated, multi-band optical imaging over an even larger area than WFIRST can survey. If the wide and medium tiers are replaced with LSST DDF discoveries, then WFIRST can offer spectrophotometry (with good host-galaxy subtraction) for $\sim 2,000$ LSST SNe, with screening spectra for $\sim 1\text{-}2,000$ more. As the WFI and IFU operate in parallel, this survey could provide sparsely sampled NIR imaging for $\sim 5,000$ SNe up to $z = 1$ at the same time as the spectroscopy. The joint survey would thus provide systematics control (almost certainly better than either survey alone), as well as a cross-check of LSST photometric typing and host-galaxy-only redshift assignment.

11.3.1 Target measurements and discoveries

The targets of the measurements are related to those enumerated in Section 9.5.1. The SNe must be detected ~ 10 observer-frame days before maximum light, so that there is time for a shallow screening spectrum before deeper spectrophotometry around maximum. There should be enough visits per filter so that some photometric screening can be done before WFIRST triggers any spectroscopy. There should be an identification of the host galaxy (if seen), so that joint WFIRST/LSST photometric redshifts can be used to provide a distance-limited sample (minimizing selection effects). Finally, the light curve should continue after the SN has been sent to WFIRST, so that important light-curve parameters (date of maximum, rise time and decline time, etc.) can be measured.

11.3.2 Metrics

The primary metrics are based on constraining cosmological parameters; the DETF FoM is standard (although other cosmological FoMs can be constructed using eigenmode constraints). For the

joint observations proposed here, we anticipate an increase in the FoM of about 20% (WFIRST is still working to optimize the WFIRST side of the joint survey for the best possible constraints).

The cosmological metric will essentially depend on the number of SNe meeting the above targets. It will degrade if CC SNe mistakenly sent to WFIRST for followup, if SNe Ia are sent to WFIRST but the LC is lost due to weather gaps, or if the cadence and depth simply do not allow the measurement of light curve parameters. These metrics will be strongly related to those in Section 9.5.2, but with more emphasis on the rising portion of the light curve.

Go to: • [the start of this section](#) • [the start of the chapter](#) • [the table of contents](#)

11.4 Exoplanetary Microlensing with WFIRST and LSST

David Bennett, Matthew T. Penny, Rachel Street.

Perhaps the most exciting discovery to come out of gravitational microlensing surveys is the discovery of a large population of “rogue” planets by the MOA Collaboration (Sumi et al. 2011). These planets are isolated in the sense that no host star can be detected by microlensing. Depending on the peak magnification and light curve coverage, this can imply that a host must be > 10 AU or > 100 AU, and Bennett et al. (2012) have argued that the median separation of possible host stars is likely to be > 30 AU. Further observations by both the MOA and OGLE collaborations provide a qualitative confirmation of this result, as dozens of additional short timescale events have been discovered by the MOA and OGLE alert systems, but we await details of the implied rogue planet populations that will come from detailed analyses of both the MOA and OGLE samples.

A major weakness with the microlensing data that indicates this large population of rogue planets is that, thus far, the properties of this population have only been inferred by their Einstein radius crossing time, t_E , distribution. But, the Einstein radius crossing time depends not only on the lens mass, but also on its distance and transverse velocity. As a result, we cannot directly infer the mass or distance distribution of the rogue planet sample.

Our understanding of the rogue planet distribution can be greatly improved by measuring the microlensing parallax effect (Gould et al. 1992; Alcock et al. 1995). The microlensing parallax effect can be described by the transverse relative lens-source velocity, \mathbf{v}_\perp , projected to the position of the observer,

$$\tilde{\mathbf{v}} = \mathbf{v}_\perp D_S / (D_S - D_L) , \quad (11.1)$$

where D_L and D_S are the lens and source distances, respectively. Typically, microlensing parallax is measured using the orbital motion of the Earth, but it can also be measured using light curve observations from telescopes at different locations in the Solar System (Dong et al. 2007; Calchi Novati et al. 2015) or even different locations on Earth (Gould et al. 2009). However, in the case of microlensing by planetary mass objects, the event durations are too short to allow a significant light curve change due to the Earth’s orbital motion, but the near simultaneous observations from Earth and a satellite orbiting at the Earth-Sun L2 point (where WFIRST will orbit) does allow the measurement of microlensing parallax signals due to planetary mass lenses (Gould, Gaudi & Han, 2003).

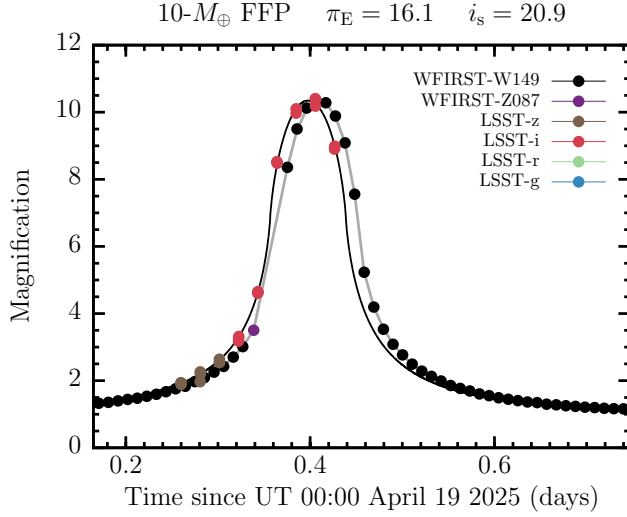


Figure 11.1: The light curve of a $10M_{\oplus}$ planet with a microlensing parallax mass measurement from simultaneous WFIRST and LSST observations.

When a microlensing parallax signal is measured, the \tilde{v} value can generally distinguish between bulge and disk lenses, as \tilde{v} generally points in the direction of the Galactic disk rotation and has a magnitude of $\tilde{v} \lesssim 200$ km/sec for a lens in the disk, while for a lens in the bulge, the magnitude of the projected velocity is $\tilde{v} \gtrsim 200$ km/sec. A microlensing parallax measurement also yields a mass distance relationship,

$$M_L = \frac{\tilde{v}^2 t_E^2 c^2}{4G} \frac{D_S - D_L}{D_L D_S} . \quad (11.2)$$

Because the \tilde{v} value places a fairly strong constraint on D_L and the source is very likely to be in the bulge, equation 11.2 generally provides a good constraint on the lens mass. But, for some events, we can do even better. For high magnification events or events with low-mass lenses, the finite angular size of the source star is resolved, and the light curve provides a measurement of the source radius crossing time, t_* . This allows the angular Einstein radius to be determined, $\theta_E = t_E \theta_*/t_*$, where the angular source radius, θ_* can be determined from the color and brightness of the source star (Boyajian et al. 2014). When both \tilde{v} and θ_E , the mass of the lens is measured to be

$$M_L = \frac{c^2}{4G} \tilde{v} t_E \theta_E = \frac{\theta_E \tilde{v} t_E}{(8.1439 \text{ mas AU})} M_{\odot} . \quad (11.3)$$

Figure 11.1 shows an example of the light curves for one of the rogue planets with a mass determined by simultaneous WFIRST and LSST observations.

We propose simultaneous high cadence observations of the WFIRST microlensing fields (which should be covered by a single LSST pointing) by LSST during each of the six 72-day WFIRST exoplanet microlensing survey sessions. These will allow microlensing parallax measurements to determine the distances and masses of a representative sub-sample of the rogue planets found by the WFIRST microlensing survey. These measurements will be crucial for the interpretation of WFIRST’s rogue planet discoveries, and they cannot be obtained by another method.

We also propose continuous monitoring of the WFIRST microlensing fields at a cadence of one observation per day starting a year before and ending a year after the WFIRST microlensing.

days	Observations
Feb 10-16	3
Feb 17-23	4
Feb 24-Mar 1	5
Mar 2-8	6
Mar 9-14	7
Mar 15-21	8
Mar 22-28	9
Mar 29-Apr 4	10
Apr 5-10	11
Apr 11-17	12
Apr 18-24	13
Apr 25-28	14

Table 11.1: Observations per night at 30 minute cadence for a Spring WFIRST microlensing survey.

This will allow us to search for microlensing signals of possible host stars for the detected rogue planet candidates. Such signals will appear as separate microlensing signals long before or after the apparent rogue planetary signals. They cannot be detected by WFIRST due to the limited 72 day WFIRST observing windows.

11.4.1 Target measurements and discoveries

We will point at a single field, centered on the WFIRST microlensing fields, and this should cover all 10 WFIRST microlensing fields.

For our preliminary estimates of the high cadence observing, we assume that the bulge is observed every 30 minutes when the bulge is at an airmass of < 2.5 for 76-day observing runs (each 72-day WFIRST observing season plus 2 days on either side). Each visit consists of 3 exposures, one 2 sec exposure followed by two 15 sec exposures. With a 2 sec readout and 1 sec for the shutter to open and close, this comes to 42 sec on target per visit (since the final readout can be done while slewing). If we assume a 30 deg slew in Azimuth before and after each ML pointing, the slews to and from the target should take 22 sec, which is 12 sec above the average. So, each observation will take 66 sec out of the regular observing sequence. The number of observations per night, assuming a 30 minute cadence, for a Spring, 2025 observing session are given in [Table 11.1](#). We will require that these observations be taken in the *riz* or *y* filters with at least 3 (or 0) observations in each filter per night. The total number of observations with this observing plan is 649 or 11.9 hour per 72-day observing session or 3894 observations and 71.4 hours for all the high cadence observations that we propose.

The low-cadence (1 observation per day) observations taken when WFIRST is not observing, would consist of 1270 observations if we assume that the observations are not taken during the time when

Category	$100 M_{\oplus}$	$10 M_{\oplus}$	$1 M_{\oplus}$	Total
WFIRST-events	417	127	33	577
$i \leq 23$	88	30	13	131
π_E measured	22	8.2	2.7	32.9
M_L measured	5.9	3.4	1.5	10.8

Table 11.2: Number of rogue planets of the given mass detected, assuming one such planet per main sequence star.

the u filter is on the telescope (this is assumed to be 1/6 of the time). The low-cadence off-season observations then total 23.3 hours, for a grand total of 95.7 hours over 8 years.

These observing plans can be altered by changing the cadence of the high cadence observations from once every 30 minutes to once every 15, 60, or 120 minutes, or we could change the number of WFIRST microlensing observing seasons that were covered. We have not yet simulated the different observing cadences, however.

11.4.2 Metrics

Table 11.2 shows the results of our simulations of the combined WFIRST-LSST observing program. We assume that there is 1 planet per main sequence star at each of $1 M_{\oplus}$, $10 M_{\oplus}$, and $100 M_{\oplus}$. This is the $1-\sigma$ lower limit found by Sumi et al. (2011) at $M_L \approx 300 M_{\oplus}$, and the rogue planet mass function is thought to increase toward lower masses, so this is a conservative assumption. The first row gives the number of events that will be observed by WFIRST. The second row gives the number of these events with SDSS- $i \leq 23$, which were the only events included in the LSST simulations. The third and fourth rows give the number of these events with LSST-WFIRST microlensing parallax measurements and the number with full mass measurements. It is these rows that indicate the value of the LSST observations.

We can see from the final column that the LSST observations should yield more than 30 rogue planet microlensing parallax measurements and more than 10 rogue planet mass measurements. These are measurements that cannot be made by other methods. **THE PREVIOUS SENTENCE NEEDS MORE JUSTIFICATION.** In addition, this program would also yield masses for a somewhat larger number of bound planets (Gould, Gaudi & Han 2003), although many of these will have their masses determined by other means as well.

For a figure of merit, we select the product of the number of π_E and M_L , which is 355 for our straw man program.

Go to: • [the start of this section](#) • [the start of the chapter](#) • [the table of contents](#)

Go to: • [the start of this section](#) • [the start of the chapter](#) • [the table of contents](#)

12 Tensions and Trade-offs

Chapter editors: *Stephen Ridgway, Phil Marshall*

12.1 Introduction

The LSST survey will be carried out with physical and operational constraints that will impact all science objectives. These include design limitations, such as the aperture of the telescope, or the limited number of filter changes that can be supported during the lifetime of the survey. They include natural constraints, such as the quantity of useful observing time in 10 years. They include practical constraints such as the detector noise and readout time.

The LSST observing schedule can be designed, to some extent, to minimize the impact that these limitations have on any one or few science objectives. As the science objectives become more numerous and more complex, the optimization becomes more difficult and the chances increase that significant compromises may be required.

In chapters 3-9 of this report, science objectives are described, and for each, metrics, and in some cases merit functions, are designed to represent quantitatively the interests of that topic in a schedule optimization. Not all of these metric sets are fully worked out, and in most cases they are provisional pending further analysis and community review and input. They do suffice to bring attention to many special requirements.

The design of the LSST scheduler, and of the algorithms that will select the visit sequences, has a considerable distance to go before hard cadence questions must be confronted and resolved. However, it is already possible to survey the reach of science needs, and to identify areas of competition which may become candidates for careful trades and decisions in the years before the survey begins.

In this chapter, we review the possible tensions that are now evident, and where tradeoffs may become necessary.

Most potential tensions within the main survey concern temporal sampling for variable targets. Tensions among static science objectives, and between static science and variable science may be less likely and mild.

The strongest point of tension may prove to be between mini-surveys and the main survey.

12.2 Variable Targets - Where Is The Tension?

Strictly periodic targets are relatively neutral to cadence speed, since successive periods can be combined to improve phase coverage steadily through the survey. The only odd cases are ultra-short (< 1 minute) and ultra long (>10 years) periods, and periods very, very close to one sidereal day. However, with precision measurements over a long term, some of the very interesting results for periodic variables will be in period drifts or slight deviations from periodicity. Furthermore, even periodic targets benefit from an early interval of higher frequency sampling, at least in some sky regions, as this can accelerate the ramp up of the science.

By far the majority of variables and transients, stellar and galactic, are not periodic. For these, study will be greatly simplified (or may absolutely require) sufficient sampling within an interval that depends on the target type. One would like to satisfy the sampling theorem, with visits at twice the frequency of the highest frequency content, but this is only a conceptual guide - knowledge of, and experience with, the targets and the science objectives can provide practical criteria.

A truly uniform cadence provides a revisit rate of one visit pair every 16 days (in r or i filters), or every 3.7 days (in any filter) - assuming a 5 month observing season. This is a sparse sample rate for many variable types. Achieving higher sample rates requires (possibly very strong) deviations from complete uniformity. Thus the obvious - rapid cadences cannot apply everywhere all the time. Rapid cadences must be designed, executed selectively, are bounded by the number of visits available, and must be coordinated with all other such cadences as well as more general survey requirements.

12.2.1 Examples

Several examples will illustrate the diversity of cadences that are represented in the science programs described in this white paper.

QSO variability tends to be “red”. A uniform distribution of the LSST visits, with minimal seasonal gaps, provides fairly good support for identifying QSOs from variability pattern.

For a SN, sufficient sampling must be acquired during the life of the event. A good cadence in at least one filter is required to support classification, and multicolors to support photometric redshift determination. A uniform LSST cadence, even with large seasonal gaps, does not provide a sufficient sampling rate for SN science - an enhancement of 2X or greater is strongly requested.

To determine the rotational period of stars with spots, sampling must resolve light variations sufficiently to constrain periodicity within the spot lifetime (weeks). This cadence is much more rapid than provided by a uniformly distributed WFD visit pattern.

Flaring stars and interacting binaries may show dramatic flux changes in minutes to hours, and correct identification of such events may require several data points, and possibly more than one filter, on a similar time scale.

The solar system small body case is particularly complex. The science is one of the main LSST drivers. Detection of PHAs has a non-scientific and even political component. Asteroid confusion can interfere with transient discovery. The density of targets is a strong function of position

on the sky. Characterization of solar system objects, by determination of orbits, requires visit patterns on short timescale (\approx hour return) and intermediate time scale (\approx 2 weeks) - long timescale confirmation occurs naturally later in the survey. The number and pattern of rapid revisits required for positive identification depends strongly on the false positive rate, which cannot yet be predicted with confidence.

12.2.2 How to provide a range of cadence speeds

The problem of sampling diverse events was of course recognized very early in survey planning. Previous cadence development has explored the following special cadence options:

Rapid revisits - this feature was introduced for study of solar system bodies and most schedule simulations give high priority to acquiring visits in pairs with 30 minute separation. Experiments have been done with triples, in case that should prove necessary for asteroid characterization. The possibility of using a different revisit pattern in different parts of the sky (e.g. less frequent away from the ecliptic) has been mentioned. Different patterns for different filters (e.g. not using pairs for u-filter visits) has been suggested, but not yet investigated. The use of visit pairs is clearly a very large impact decision, for practical purposes reducing by 2X the effective revisit rate for other targets. However, rapid pairs is very effective for measuring brightness gradients for rapidly varying objects, and thus particularly valuable for the difficult problem of characterizing blank sky transients.

Mini-surveys - Mini-surveys can include special cadences. The deep drilling concept utilizes rapid visit sequences to achieve greater depth without saturation of detector wells, giving sky-limited true time series with \approx 30 second sampling steps. The possibilities for mini-surveys are limitless, but of course they are bounded by the amount of time available outside the main survey. The trade between mini-surveys and the main survey is discussed below.

Rolling cadence - a rolling cadence allows for the possibility of re-deploying visits within the main survey so as to respond to special cadence demands without compromising main survey goals (or, perhaps in principle, trading against main survey goals in a measured and optimum way). Rolling cadences are discussed in Chapter 2. As an example, the average 9 visit pairs per year in the r filter, which would be distributed over a season in a uniform survey, could be distributed over 2 months, 1 month, 1 week, or 1 day, in a rolling cadence (leaving no visits in r for the rest of the season). Or, more conservatively for the main survey, half (4-5 visit pairs) could be spent in an enhanced visit rate, reserving the other half to maintain visit pairs in the rest of the season. Also, a rolling cadence can concern any number of filters - for example, one filter could be used to provide short bursts of rapid sampling, while other filters could maintain a uniform distribution. Different rolling cadences can be used in different parts of the sky, or at different times during the survey. There is an immense range of possibilities for rolling cadence, and the surface has barely been scratched.

Commissioning survey - the highest priority of the commissioning schedule is - of course - commissioning. A second objective is to demonstrate telescope operation in the planned survey mode - presumably including main survey, deep drilling, rolling cadences, etc. There have been ambitious suggestions, going beyond these basics, such as integrating some fields to the full survey depth, or

acquiring some special cadences. However, there is no assurance that any of these will be possible, as they have lower priority than the formal commissioning objectives.

12.2.3 Other options for special cadences

Pre-survey options - there are a number of survey instruments (CTIO, CFHT, Subaru) that can easily reach the single visit depth of LSST. These resources could be used to explore limited sky regions ($\approx 1\%$ of the LSST sky) with cadences that are planned for LSST (or cadences that are not planned for LSST), providing touchstone datasets especially for the more common target types that will dominate the survey.

Twilight survey - chapter 10 describes a concept for twilight data acquisition, using short exposures to tolerate bright sky. This time is not required for current LSST science, and in principle could be allocated to z,y filters in short bursts (20 minutes) of fast cadence (< 15 seconds) imagery, within the sensitivity limits of the twilight sky.

Follow-up - LSST is, in large part, a variable discovery tool. It is not realistic to expect LSST to provide its own follow-up for all possible target types and characteristics. Fortunately, many of the most useful discoveries will be bright enough to follow-up with smaller, more accessible apertures. Follow-up can be far more customized to the science needs than a general purpose LSST cadence. Faint targets of sufficient value may likewise merit followup with exceptional ground and space-based resources.

Post-survey options - will LSST operate for more than 10 years? It's possible, maybe even probable, but at present too speculative to plan around.

12.2.4 Frequency of filter changes

Multi-color visits are a very special case for LSST. Moving the large (huge) optical filters involves substantial structure and mechanisms. While filter change time is not fully characterized, it will be slow enough that filter change frequency competes directly with efficiency. Furthermore, the mechanisms have a finite lifetime and are not designed to allow an indefinite number of changes. These are practical limitations of the facility. Combined, they ensure that “rapid” multi-color sequences will be the exception rather than the rule. Science objectives which need near-simultaneous multi-color photometry will be in competition for a limited resource.

With a limited number of filter changes per night, it is possible for visit pairs to be acquired (sometimes) in different filters. Deep drilling fields which have multiple filters in a single visit will be close in time (all exposures in one filter will be obtained, then the filter changed and all the exposures in the next filter obtained). Other exceptional targets, e.g. certain ToO observations, might be planned with rapid multi-filter sequences.

For periodic variables, simultaneous multi-color photometry is a convenience. For non-periodic or transient targets, it is desirable. It is important to identify when and if rapid filter changes are essential.

12.2.5 Tension between rapid and slow cadences

In summary, we can readily identify competing demands for very different cadences, including fast cadences in multiple ranges. For characteristic times ranging from $<\approx 1$ minute to ≈ 1 month, a uniform visit distribution cannot be fully satisfactory, and in some cases it may be concluded to be totally unsatisfactory. A number of concepts for alternate cadences are available. None can provide rapid cadence all the time over all the sky. It may be possible to provide cadences matched to most requirements over part of the sky all of the time, and over all of the sky at some time. For transient targets, a complex survey cadence may obtain limited duration but “appropriate” sampling of a fraction of the actual events, with the fraction TBD, but inevitably significantly less than one.

The tension in scheduling is, first and foremost, not between competing science objectives, but between science objectives and limited scheduling flexibility. The confrontation between science requirements and schedule performance leans on the metrics and merit functions that are the major goal of this white paper. It should be clear from the 10 foregoing chapters that the difficult goal of metrics analysis is not in describing sampling for the science, which is “easy”. The more difficult part is in determining the number of science targets for which adequate sampling can be provided by a simulation, and perhaps the greatest challenge is determining how many such targets with the specified sampling are required for a science objective. It is only when this step has been accomplished for a large part of the science that competition between the science objectives can become a quantitative process.

12.3 Static Target Science - Is There Any Tension?

The needs of static target science appear to have fewer points of potential tension among them than variable targets. The major cadence-related concerns are:

Photometry - the best photometric performance will be achieved after the calibration has been closed around the sky with superior image quality and superior photometric quality visits to every field. While this is probable due to randomization of conditions over 10 years, the sooner that it is achieved during the survey, the sooner high quality photometry will be available. This could be a target of active schedule control, with corresponding decreasing flexibility in some other schedule variables.

Astrometry - both proper motions and parallaxes are served by any schedule that spreads visits well over the duration of the survey. Parallaxes benefit from observing at a range of hour angles, which is slightly in competition with the preference to observe at small airmass for best image quality, but typical simulated schedules show good astrometric performance. A rolling cadence that moved a significant fraction of visits from one time period of the survey to another could impact the astrometric performance (either for better or for worse), though as long as the fraction of visits concerned was small, the effect would correspondingly be small.

Homogeneity - an example of required homogeneity is image quality. Just as the atmosphere allows a range of image quality during a night and from night to night, each point on the sky will be observed with a range of image quality. To enable understanding of selection effects, and to compare

sky regions on an even playing field, it is desirable that for each filter, all parts of the sky should be observed with a similar distribution of image quality, and in particular with similar best image quality. Achieving homogeneity of conditions actively could be quite challenging, but simulations show that with a large number of independent visits, it occurs naturally to good approximation. Any cadence that relied on concentrated bursts of visits in a short interval would tend to reduce the spread of conditions observed. However, such an extreme has not been proposed or studied.

Randomization - closely related to homogeneity, randomization is means of achieving homogeneity in some observing parameters. Examples are the projected angles of camera and telescope optics on the sky. These are less random than sky conditions, as they depend on instrument setup and schedule history. Simulations show that optics angles are well randomized passively (i.e. without scheduler optimization) for most points on the sky, but not for all. Randomization could be improved, for example by actively running the camera rotator when advancing from one sky position to the next, in order to populate under represented camera angles. The rotation takes time, and could reduce the overall efficiency of the survey. Only simulations can explore the impact of these additional mechanical motions.

Dithering - dithering of visits is a powerful method of improving homogeneity of sky coverage passively. Few compromises have been identified with dithering thus far. Dithering for small regions has a price. Imagine the loss in depth due to large dithers with a single FOV, e.g. a deep drilling field (this has not been proposed). Due to this effect, certain rolling cadences can have a potential small loss of efficiency or efficacy when implemented with dithering.

The foregoing shows that within the static science domain, there are few and mild points of tension and potential competition.

12.4 Tension Between Static And Variable Science

For the most part, the tensions between static science and variable science are modest and easily understood. A variable-driven cadence that requires special timing of visits may result in loss of efficiency due to increased slew times, or observing under less optimum conditions (larger airmass). Special cadences are likely to reduce randomization and homogenization to a small degree. However, except for very aggressive cadence implementations, these are second-order effects. Furthermore, they are measurable with simple metrics - the impact of variable science schedule considerations on static science should be small, and it can be readily quantified.

12.5 Mini-surveys and Main Survey - Tension for Sure

The LSST proposal and current plan allow a fraction of the total survey time for mini-survey. These may cover special sky regions or cadences. The fraction 10% has been carried for mini-surveys. This is not necessarily a sacred number. In Chapter 2, current scheduling experience has shown that the main survey program, to design depth, can be accomplished in $\approx 85\%$ of the available time. However, improvements in simulations could move this estimate up or down. Adequacy of

the design depths could be reconsidered. And of course the execution of the survey could encounter unprecedented circumstances.

Proposals for mini-surveys include deep drilling fields, the northern ecliptic, and the Magellanic clouds. Notional suggestions for deep drilling fields alone would exceed 10%. Most schedule simulations have allocated a limited number of visits to the galactic plane (based on the expectation that crowding would limit the useful stacked depth). However, as detailed in Chapter 4, many areas of galactic science could benefit from a more aggressive visit plan, perhaps similar to the main survey.

At present there is no evidence that the trade between main and mini-surveys will require difficult compromises. But it is a natural area of tension, and since is subject to weather experience (not to mention the evolution of the science) it is likely to be with us through the life of the survey.

12.6 Summary and Conclusion

The likely points of technical and scientific tension in scheduling are apparent from the schedule simulation experience (Chapter 2) and the science objectives and metrics (Chapters 3-10). Static science has relatively few and mild points of concern. Variable science has little and moderate tension with static science. Variable science has many points of tension between different variable science objectives, owing to the wide range of time scales. These lead to contrasting technical demands. They may or may not prove to be areas of scientific competition.

It goes without saying that in essentially all cases, “more is better”. That is however not a sufficient characterization for schedule planning.

The essential information needed to clarify tensions is the determination, for each science objective, of three things.

- The cadence requirements
- For a simulated schedule, the number of instances of targets satisfactorily observed
- The number of such targets required for the science

This information is the key to calibrating the metrics in terms of absolute and relative sufficiency.

References

- Abbott, B. P., Abbott, R., Abbott, T. D., Abernathy, M. R., Acernese, F., Ackley, K., Adams, C., Adams, T., Addesso, P., Adhikari, R. X., & et al. 2016a, Physical Review Letters, 116, 131102
—. 2016b, ArXiv e-prints
- Abbott, B. P., Abbott, R., Adhikari, R., Ajith, P., Allen, B., Allen, G., Amin, R. S., Anderson, S. B., Anderson, W. G., Arai, M. A., & et al. 2009, *Phys. Rev. D*, 80, 102001
- Acernese, F. e. a. 2008, *Phys. Rev. D*, 26
- Adams, S. M., Kochanek, C. S., Beacom, J. F., Vagins, M. R., & Stanek, K. Z. 2013, *ApJ*, 778, 164
- Aerts, C., Christensen-Dalsgaard, J., & Kurtz, D. W. 2010, Asteroseismology
- A'Hearn, M. F., Feaga, L. M., Keller, H. U., Kawakita, H., Hampton, D. L., Kissel, J., Klaasen, K. P., McFadden, L. A., Meech, K. J., Schultz, P. H., Sunshine, J. M., Thomas, P. C., Veverka, J., Yeomans, D. K., Besse, S., Bodewits, D., Farnham, T. L., Groussin, O., Kelley, M. S., Lisse, C. M., Merlin, F., Protopapa, S., & Wellnitz, D. D. 2012, *ApJ*, 758, 29
- A'Hearn, M. F., Millis, R. L., Schleicher, D. G., Osip, D. J., & Birch, P. V. 1995, *Icarus*, 118, 223
- Albrecht, A., Bernstein, G., Cahn, R., Freedman, W. L., Hewitt, J., Hu, W., Huth, J., Kamionkowski, M., Kolb, E. W., Knox, L., Mather, J. C., Staggs, S., & Suntzeff, N. B. 2006, ArXiv Astrophysics e-prints
- Althaus, L. G., Córscico, A. H., Isern, J., & García-Berro, E. 2010, A&ARv, 18, 471
- Arcavi, I., Gal-Yam, A., Sullivan, M., Pan, Y.-C., Cenko, S. B., Horesh, A., Ofek, E. O., De Cia, A., Yan, L., Yang, C.-W., Howell, D. A., Tal, D., Kulkarni, S. R., Tendulkar, S. P., Tang, S., Xu, D., Sternberg, A., Cohen, J. G., Bloom, J. S., Nugent, P. E., Kasliwal, M. M., Perley, D. A., Quimby, R. M., Miller, A. A., Theissen, C. A., & Laher, R. R. 2014, The Astrophysical Journal, 793, 38
- Baker, M. & Willman, B. 2015, *AJ*, 150, 160
- Barnes, J. & Kasen, D. 2013, *ApJ*, 775, 18
- Berger, E., Fong, W., & Chornock, R. 2013, *ApJL*, 774, L23
- Bernstein, J. P., Kessler, R., Kuhlmann, S., Biswas, R., Kovacs, E., Aldering, G., Crane, I., D'Andrea, C. B., Finley, D. A., Frieman, J. A., Hufford, T., Jarvis, M. J., Kim, A. G., Marriner, J., Mukherjee, P., Nichol, R. C., Nugent, P., Parkinson, D., Reis, R. R. R., Sako, M., Spinka, H., & Sullivan, M. 2012, *ApJ*, 753, 152
- Besla, G., Kallivayalil, N., Hernquist, L., van der Marel, R. P., Cox, T. J., & Kereš, D. 2012, *MNRAS*, 421, 2109
- Bhardwaj, A., Kanbur, S. M., Singh, H. P., Macri, L. M., & Ngeow, C.-C. 2015, *MNRAS*, 447, 3342
- Bhardwaj, A., Kanbur, S. M., Singh, H. P., & Ngeow, C.-C. 2014, *MNRAS*, 445, 2655
- Bianco, F. B., Howell, D. A., Sullivan, M., Conley, A., Kasen, D., González-Gaitán, S., Guy, J., Astier, P., Balland, C., Carlberg, R. G., Fouchez, D., Fourmanoit, N., Hardin, D., Hook, I., Lidman, C., Pain, R., Palanque-Delabrouille, N., Perlmutter, S., Perrett, K. M., Pritchett, C. J., Regnault, N., Rich, J., & Ruhlmann-Kleider, V. 2011, *ApJ*, 741, 20
- Bloom, J. S., Giannios, D., Metzger, B. D., Cenko, S. B., Perley, D. A., Butler, N. R., Tanvir, N. R., Levan, A. J., O'Brien, P. T., Strubbe, L. E., De Colle, F., Ramirez-Ruiz, E., Lee, W. H., Nayakshin, S., Quataert, E., King, A. R., Cucchiara, A., Guillochon, J., Bower, G. C., Fruchter, A. S., Morgan, A. N., & van der Horst, A. J. 2011, Science (New York, N.Y.), 333, 203
- Bonnerot, C., Rossi, E. M., Lodato, G., & Price, D. J. 2015, Monthly Notices of the Royal Astronomical Society, 455, 2253
- Bono, G., Castellani, V., & Marconi, M. 2000, *ApJ*, 529, 293
- Bradley Cenko, S., Krimm, H. A., Horesh, A., Rau, A., Frail, D. A., Kennea, J. A., Levan, A. J., Holland, S. T., Butler, N. R., Quimby, R. M., Bloom, J. S., Filippenko, A. V., Gal-Yam, A., Greiner, J., Kulkarni, S. R., Ofek, E. O., Olivares E., F., Schady, P., Silverman, J. M., Tanvir, N. R., & Xu, D. 2012, The Astrophysical Journal, 753, 77
- Brassard, P., Fontaine, G., & Wesemael, F. 1995, *ApJS*, 96, 545
- Britt, C. T., Maccarone, T., Pretorius, M. L., Hynes, R. I., Jonker, P. G., Torres, M. A. P., Knigge, C., Johnson, C. O., Heinke, C. B., Steeghs, D., Greiss, S., & Nelemans, G. 2015, *MNRAS*, 448, 3455

- Brocato, E. & Castellani, V. 1992, *A&A*, 258, 397
- Brown, G. C., Levan, A. J., Stanway, E. R., Tanvir, N. R., Cenko, S. B., Berger, E., Chornock, R., & Cucchiaria, A. 2015, Monthly Notices of the Royal Astronomical Society, 452, 4297
- Burrows, D. N., Kennea, J. A., Ghisellini, G., Mangano, V., Zhang, B., Page, K. L., Eracleous, M., Romano, P., Sakamoto, T., Falcone, A. D., Osborne, J. P., Campana, S., Beardmore, A. P., Breeveld, A. A., Chester, M. M., Corbet, R., Covino, S., Cummings, J. R., D'Avanzo, P., D'Elia, V., Esposito, P., Evans, P. A., Fugazza, D., Gelbord, J. M., Hiroi, K., Holland, S. T., Huang, K. Y., Im, M., Israel, G., Jeon, Y., Jeon, Y.-B., Jun, H. D., Kawai, N., Kim, J. H., Krimm, H. A., Marshall, F. E., P Mészáros, Negoro, H., Omodei, N., Park, W.-K., Perkins, J. S., Sugizaki, M., Sung, H.-I., Tagliaferri, G., Troja, E., Ueda, Y., Urata, Y., Usui, R., Antonelli, L. A., Barthelmy, S. D., Cusumano, G., Giommi, P., Melandri, A., Perri, M., Racusin, J. L., Sbarufatti, B., Siegel, M. H., & Gehrels, N. 2011, *Nature*, 476, 421
- Butler, N. R. & Bloom, J. S. 2011, *AJ*, 141, 93
- Cáceres, C. & Catelan, M. 2008, *ApJS*, 179, 242
- Campbell, H., D'Andrea, C. B., Nichol, R. C., Sako, M., Smith, M., Lampeitl, H., Olmstead, M. D., Bassett, B., Biswas, R., Brown, P., Cinabro, D., Dawson, K. S., Dilday, B., Foley, R. J., Frieman, J. A., Garnavich, P., Hlozek, R., Jha, S. W., Kuhlmann, S., Kunz, M., Marriner, J., Miquel, R., Richmond, M., Riess, A., Schneider, D. P., Sollerman, J., Taylor, M., & Zhao, G.-B. 2013, *ApJ*, 763, 88
- Cantrell, A. G., Bailyn, C. D., Orosz, J. A., McClintock, J. E., Remillard, R. A., Froning, C. S., Neilsen, J., Gelino, D. M., & Gou, L. 2010, *ApJ*, 710, 1127
- Cao, Y., Kasliwal, M. M., Arcavi, I., Horesh, A., Hancock, P., Valenti, S., Cenko, S. B., Kulkarni, S. R., Gal-Yam, A., Gorbikov, E., Ofek, E. O., Sand, D., Yaron, O., Graham, M., Silverman, J. M., Wheeler, J. C., Marion, G. H., Walker, E. S., Mazzali, P., Howell, D. A., Li, K. L., Kong, A. K. H., Bloom, J. S., Nugent, P. E., Surace, J., Masci, F., Carpenter, J., Degenaar, N., & Gelino, C. R. 2013, *ApJL*, 775, L7
- Carlin, J. L., Majewski, S. R., Casetti-Dinescu, D. I., Law, D. R., Girard, T. M., & Patterson, R. J. 2012, *ApJ*, 744, 25
- Carroll, C. M., Gawiser, E., Kurczynski, P. L., Bailey, R. A., Biswas, R., Cinabro, D., Jha, S. W., Jones, R. L., Krughoff, K. S., Sonawalla, A., & Wood-Vasey, W. M. 2014, in Society of Photo-Optical Instrumentation Engineers (SPIE) Conference Series, Vol. 9149, Society of Photo-Optical Instrumentation Engineers (SPIE) Conference Series, 0
- Casetti-Dinescu, D. I., Nusdeo, D. A., Girard, T. M., Korchagin, V. I., & van Altena, W. F. 2015, *ApJL*, 810, L4
- Casewell, S. L., Burleigh, M. R., Wynn, G. A., Alexander, R. D., Napiwotzki, R., Lawrie, K. A., Dobbie, P. D., Jameson, R. F., & Hodgkin, S. T. 2012, *ApJL*, 759, L34
- Cenko, S. B., Kulkarni, S. R., Horesh, A., Corsi, A., Fox, D. B., Carpenter, J., Frail, D. A., Nugent, P. E., Perley, D. A., Gruber, D., Gal-Yam, A., Groot, P. J., Hallinan, G., Ofek, E. O., Rau, A., MacLeod, C. L., Miller, A. A., Bloom, J. S., Filippenko, A. V., Kasliwal, M. M., Law, N. M., Morgan, A. N., Polishook, D., Poznanski, D., Quimby, R. M., Sesar, B., Shen, K. J., Silverman, J. M., & Sternberg, A. 2013, *ApJ*, 769, 130
- Cenko, S. B., Urban, A. L., Perley, D. A., Horesh, A., Corsi, A., Fox, D. B., Cao, Y., Kasliwal, M. M., Lien, A., Arcavi, I., Bloom, J. S., Butler, N. R., Cucchiara, A., de Diego, J. A., Filippenko, A. V., Gal-Yam, A., Gehrels, N., Georgiev, L., Jesús González, J., Graham, J. F., Greiner, J., Kann, D. A., Klein, C. R., Knust, F., Kulkarni, S. R., Kuttyrev, A., Laher, R., Lee, W. H., Nugent, P. E., Prochaska, J. X., Ramirez-Ruiz, E., Richer, M. G., Rubin, A., Urata, Y., Varela, K., Watson, A. M., & Wozniak, P. R. 2015, *ApJL*, 803, L24
- Chelouche, D. 2013, *ApJ*, 772, 9
- Chelouche, D., Shemmer, O., Cotlier, G. I., Barth, A. J., & Rafter, S. E. 2014, *ApJ*, 785, 140
- Chelouche, D. & Zucker, S. 2013, *ApJ*, 769, 124
- Chomiuk, L., Soderberg, A. M., Chevalier, R. A., Bruzewski, S., Foley, R. J., Parrent, J., Strader, J., Badenes, C., Fransson, C., Kamble, A., Margutti, R., Rupen, M. P., & Simon, J. D. 2015, ArXiv e-prints
- Chornock, R., Berger, E., Gezari, S., Zauderer, B. A., Rest, A., Chomiuk, L., Kamble, A., Soderberg, A. M., Czekala, I., Dittmann, J., Drout, M., Foley, R. J., Fong, W., Huber, M. E., Kirshner, R. P., Lawrence, A., Lunyan, R., Marion, G. H., Narayan, G., Riess, A. G., Roth, K. C., Sanders, N. E., Scolnic, D., Smartt, S. J., Smith, K., Stubbs, C. W., Tonry, J. L., Burgett, W. S., Chambers, K. C., Flewelling, H., Hodapp, K. W., Kaiser, N., Magnier, E. A., Martin, D. C., Neill, J. D., Price, P. A., & Wainscoat, R. 2014, *The Astrophysical Journal*, 780, 44
- Colpi, M. 2014, *Space Science Reviews*, 183, 189
- Connaughton, V., Burns, E., Goldstein, A., Briggs, M. S., Zhang, B.-B., Hui, C. M., Jenke, P., Racusin, J., Wilson-Hodge, C. A., Bhat, P. N., Bissaldi, E., Cleveland, W., Fitzpatrick, G., Giles, M. M., Gibby, M. H., Greiner, J., von Kienlin, A., Kippen, R. M., McBreen, S., Mailyan, B., Meegan, C. A., Paciesas, W. S., Preece, R. D., Roberts, O., Sparke, L., Stanbro, M., Toelge, K., Veres, P., Yu, H.-F., & authors, o. 2016, ArXiv e-prints

- Corral-Santana, J. M., Casares, J., Munoz-Darias, T., Bauer, F. E., Martinez-Pais, I. G., & Russell, D. M. 2015, ArXiv e-prints
- Corrales, L. R., Haiman, Z., & MacFadyen, A. 2010, *MNRAS*, 404, 947
- Cowperthwaite, P. S. & Berger, E. 2015, *ApJ*, 814, 25
- Croll, B., Dalba, P. A., Vanderburg, A., Eastman, J., Rappaport, S., DeVore, J., Bieryla, A., Muirhead, P. S., Han, E., Latham, D. W., Beatty, T. G., Wittenmyer, R. A., Wright, J. T., Johnson, J. A., & McCrady, N. 2015, ArXiv e-prints
- Debes, J. H., Walsh, K. J., & Stark, C. 2012, *ApJ*, 747, 148
- Dilday, B., Howell, D. A., Cenko, S. B., Silverman, J. M., Nugent, P. E., Sullivan, M., Ben-Ami, S., Bildsten, L., Bolte, M., Endl, M., Filippenko, A. V., Gnat, O., Horesh, A., Hsiao, E., Kasliwal, M. M., Kirkman, D., Maguire, K., Marcy, G. W., Moore, K., Pan, Y., Parrent, J. T., Podsiadlowski, P., Quimby, R. M., Sternberg, A., Suzuki, N., Tytler, D. R., Xu, D., Bloom, J. S., Gal-Yam, A., Hook, I. M., Kulkarni, S. R., Law, N. M., Ofek, E. O., Polishook, D., & Poznanski, D. 2012, *Science*, 337, 942
- Donley, J. L., Brandt, W. N., Eracleous, M., & Boller, T. 2002, *The Astronomical Journal*, 124, 1308
- D’Orazio, D. J., Haiman, Z., & Schiminovich, D. 2015, *Nature*, 525, 351
- Drake, A. J., Catelan, M., Djorgovski, S. G., Torrealba, G., Graham, M. J., Belokurov, V., Koposov, S. E., Mahabal, A., Prieto, J. L., Donalek, C., Williams, R., Larson, S., Christensen, E., & Beshore, E. 2013a, *ApJ*, 763, 32
- Drake, A. J., Catelan, M., Djorgovski, S. G., Torrealba, G., Graham, M. J., Mahabal, A., Prieto, J. L., Donalek, C., Williams, R., Larson, S., Christensen, E., & Beshore, E. 2013b, *ApJ*, 765, 154
- Dressing, C. D. & Charbonneau, D. 2015, *ApJ*, 807, 45
- Dressler, A. & Gunn, J. E. 1983, *The Astrophysical Journal*, 270, 7
- Durech, J., Scheirich, P., Kaasalainen, M., Grav, T., Jedicke, R., & Denneau, L. 2007, in *IAU Symposium*, Vol. 236, Near Earth Objects, our Celestial Neighbors: Opportunity and Risk, ed. G. B. Valsecchi, D. Vokrouhlický, & A. Milani, 191–200
- Edelson, R., Gelbord, J. M., Horne, K., McHardy, I. M., Peterson, B. M., Arévalo, P., Breeveld, A. A., De Rosa, G., Evans, P. A., Goad, M. R., Kriss, G. A., Brandt, W. N., Gehrels, N., Grupe, D., Kennea, J. A., Kochanek, C. S., Nousek, J. A., Papadakis, I., Siegel, M., Starkey, D., Uttley, P., Vaughan, S., Young, S., Barth, A. J., Bentz, M. C., Brewer, B. J., Crenshaw, D. M., Dalla Bontà, E., De Lorenzo-Cáceres, A., Denney, K. D., Dietrich, M., Ely, J., Fausnaugh, M. M., Grier, C. J., Hall, P. B., Kaastra, J., Kelly, B. C., Korista, K. T., Lira, P., Mathur, S., Netzer, H., Pancoast, A., Pei, L., Pogge, R. W., Schimoia, J. S., Treu, T., Vestergaard, M., Villforth, C., Yan, H., & Zu, Y. 2015, *ApJ*, 806, 129
- Esquej, P., Saxton, R. D., Freyberg, M. J., Read, A. M., Altieri, B., Sanchez-Portal, M., & Hasinger, G. 2007, *Astronomy and Astrophysics*, 462, L49
- Evans, C. R. & Kochanek, C. S. 1989, *The Astrophysical Journal*, 346, L13
- Farihi, J., Jura, M., & Zuckerman, B. 2009, *ApJ*, 694, 805
- Fausnaugh, M. M., Denney, K. D., Barth, A. J., Bentz, M. C., Bottorff, M. C., Carini, M. T., Croxall, K. V., De Rosa, G., Goad, M. R., Horne, K., Joner, M. D., Kaspi, S., Kim, M., Klimanov, S. A., Kochanek, C. S., Leonard, D. C., Netzer, H., Peterson, B. M., Schnulle, K., Sergeev, S. G., Vestergaard, M., Zheng, W.-K., Anderson, M. D., Arevalo, P., Bazhaw, C., Borman, G. A., Boroson, T. A., Brandt, W. N., Breeveld, A. A., Brewer, B. J., Cackett, E. M., Crenshaw, D. M., Dalla Bonta, E., De Lorenzo-Cáceres, A., Dietrich, M., Edelson, R., Efimova, N. V., Ely, J., Evans, P. A., Filippenko, A. V., Flatland, K., Gehrels, N., Geier, S., Gelbord, J. M., Gonzalez, L., Gorjian, V., Grier, C. J., Grupe, D., Hall, P. B., Hicks, S., Horenstein, D., Hutchison, T., Im, M., Jensen, J. J., Jones, J., Kaastra, J., Kelly, B. C., Kennea, J. A., Kim, S. C., Korista, K. T., Kriss, G. A., Larionov, V. M., Lee, J. C., Lira, P., MacInnis, F., Manne-Nicholas, E. R., Mathur, S., McHardy, I. M., Montouri, C., Musso, R., Nazarov, S. V., Norris, R. P., Nousek, J. A., Okhmat, D. N., Pancoast, A., Papadakis, I., Parks, J. R., Pei, L., Pogge, R. W., Pott, J.-U., Rafter, S. E., Rix, H.-W., Saylor, D. A., Schimoia, J. S., Siegel, M., Spencer, M., Starkey, D., Sung, H.-I., Teems, K. G., Treu, T., Turner, C. S., Uttley, P., Villforth, C., Weiss, Y., Woo, J.-H., Yan, H., Young, S., & Zu, Y. 2015, ArXiv e-prints
- Fontaine, G. & Brassard, P. 2008, *PASP*, 120, 1043
- French, K. D., Arcavi, I., & Zabludoff, A. 2016, *The Astrophysical Journal*, 818, L21
- Gal-Yam, A., Arcavi, I., Ofek, E. O., Ben-Ami, S., Cenko, S. B., Kasliwal, M. M., Cao, Y., Yaron, O., Tal, D., Silverman, J. M., Horesh, A., De Cia, A., Taddia, F., Sollerman, J., Perley, D., Vreeswijk, P. M., Kulkarni, S. R., Nugent, P. E., Filippenko, A. V., & Wheeler, J. C. 2014, *Nature*, 509, 471
- Gänsicke, B. T., Aungwerojwit, A., Marsh, T. R., Dhillon, V. S., Sahman, D. I., Veras, D., Farihi, J., Chote, P., Ashley, R., Arjyotha, S., Rattanasoon, S., Littlefair, S. P., Pollacco, D., & Burleigh, M. R. 2016, *ApJL*, 818, L7
- Gezari, S., Chornock, R., Rest, A., Huber, M. E., Forster, K., Berger, E., Challis, P. J., Neill, J. D., Martin, D. C.,

- Heckman, T., Lawrence, A., Norman, C., Narayan, G., Foley, R. J., Marion, G. H., Scolnic, D., Chomiuk, L., Soderberg, A., Smith, K., Kirshner, R. P., Riess, A. G., Smartt, S. J., Stubbs, C. W., Tonry, J. L., Wood-Vasey, W. M., Burgett, W. S., Chambers, K. C., Grav, T., Heasley, J. N., Kaiser, N., Kudritzki, R.-P., Magnier, E. A., Morgan, J. S., & Price, P. A. 2012, *Nature*, 485, 217
- Gezari, S., Martin, D. C., Milliard, B., Basa, S., Halpern, J. P., Forster, K., Friedman, P. G., Morrissey, P., Neff, S. G., Schiminovich, D., Seibert, M., Small, T., & Wyder, T. K. 2006, *The Astrophysical Journal*, 653, L25
- Ghirlanda, G., Salvaterra, R., Campana, S., Vergani, S. D., Japelj, J., Bernardini, M. G., Burlon, D., D'Avanzo, P., Melandri, A., Gomboc, A., Nappo, F., Paladini, R., Pescalli, A., Salafia, O. S., & Tagliaferri, G. 2015, *A&A*, 578, A71
- Gil-Merino, R., Wambsganss, J., Goicoechea, L. J., & Lewis, G. F. 2005, *A&A*, 432, 83
- Gould, A. 2013a, ArXiv e-prints
- . 2013b, ArXiv e-prints
- Graham, M. J., Djorgovski, S. G., Stern, D., Glikman, E., Drake, A. J., Mahabal, A. A., Donalek, C., Larson, S., & Christensen, E. 2015, *Nature*, 518, 74
- Green, G. M., Schlafly, E. F., Finkbeiner, D. P., Rix, H.-W., Martin, N., Burgett, W., Draper, P. W., Flewelling, H., Hodapp, K., Kaiser, N., Kudritzki, R. P., Magnier, E., Metcalfe, N., Price, P., Tonry, J., & Wainscoat, R. 2015, *ApJ*, 810, 25
- Guillochon, J., Manukian, H., & Ramirez-Ruiz, E. 2014, *The Astrophysical Journal*, 783, 23
- Guy, J., Astier, P., Baumont, S., Hardin, D., Pain, R., Regnault, N., Basa, S., Carlberg, R. G., Conley, A., Fabbro, S., Fouchez, D., Hook, I. M., Howell, D. A., Perrett, K., Pritchett, C. J., Rich, J., Sullivan, M., Antilogus, P., Aubourg, E., Bazin, G., Brioner, J., Filoli, M., Palanque-Delabrouille, N., Ripoche, P., & Ruhlmann-Kleider, V. 2007, *A&A*, 466, 11
- Hartmann, L. & Kenyon, S. J. 1996, *ARAA*, 34, 207
- Hayasaki, K., Stone, N. C., & Loeb, A. 2015, eprint arXiv:1501.05207
- Hayden, B. T., Garnavich, P. M., Kasen, D., Dilday, B., Frieman, J. A., Jha, S. W., Lampeitl, H., Nichol, R. C., Sako, M., Schneider, D. P., Smith, M., Sollerman, J., & Wheeler, J. C. 2010, *ApJ*, 722, 1691
- Herbig, G. H., Aspin, C., Gilmore, A. C., Imhoff, C. L., & Jones, A. F. 2001, *PASP*, 113, 1547
- Hills, J. G. 1975, *Nature*, 254, 295
- Hlozek, R., Kunz, M., Bassett, B., Smith, M., Newling, J., Varughese, M., Kessler, R., Bernstein, J. P., Campbell, H., Dilday, B., Falck, B., Frieman, J., Kuhlmann, S., Lampeitl, H., Marriner, J., Nichol, R. C., Riess, A. G., Sako, M., & Schneider, D. P. 2012, *ApJ*, 752, 79
- Holoien, T. W.-S., Kochanek, C. S., Prieto, J. L., Grupe, D., Chen, P., Godoy-Rivera, D., Stanek, K. Z., Shappee, B. J., Dong, S., Brown, J. S., Basu, U., Beacom, J. F., Bersier, D., Brimacombe, J., Carlson, E. K., Falco, E., Johnston, E., Madore, B. F., Pojmanski, G., & Seibert, M. 2016, eprint arXiv:1602.01088
- Holoien, T. W.-S., Kochanek, C. S., Prieto, J. L., Stanek, K. Z., Dong, S., Shappee, B. J., Grupe, D., Brown, J. S., Basu, U., Beacom, J. F., Bersier, D., Brimacombe, J., Danilet, A. B., Falco, E., Guo, Z., Jose, J., Herczeg, G. J., Long, F., Pojmanski, G., Simonian, G. V., Szczygieł, D. M., Thompson, T. A., Thorstensen, J. R., Wagner, R. M., & Woźniak, P. R. 2015, *Monthly Notices of the Royal Astronomical Society*, 455, 2918
- Holoien, T. W.-S., Prieto, J. L., Bersier, D., Kochanek, C. S., Stanek, K. Z., Shappee, B. J., Grupe, D., Basu, U., Beacom, J. F., Brimacombe, J., Brown, J. S., Davis, A. B., Jencson, J., Pojmanski, G., & Szczygieł, D. M. 2014, *Monthly Notices of the Royal Astronomical Society*, 445, 3263
- Ivezić, Ž., Sesar, B., Jurić, M., Bond, N., Dalcanion, J., Rockosi, C. M., Yanny, B., Newberg, H. J., Beers, T. C., Allende Prieto, C., Wilhelm, R., Lee, Y. S., Sivarani, T., Norris, J. E., Bailer-Jones, C. A. L., Re Fiorentin, P., Schlegel, D., Uomoto, A., Lupton, R. H., Knapp, G. R., Gunn, J. E., Covey, K. R., Allyn Smith, J., Miknaitis, G., Doi, M., Tanaka, M., Fukugita, M., Kent, S., Finkbeiner, D., Munn, J. A., Pier, J. R., Quinn, T., Hawley, S., Anderson, S., Kiuchi, F., Chen, A., Bushong, J., Sohi, H., Haggard, D., Kimball, A., Barentine, J., Brewington, H., Harvanek, M., Kleinman, S., Krzesinski, J., Long, D., Nitta, A., Snedden, S., Lee, B., Harris, H., Brinkmann, J., Schneider, D. P., & York, D. G. 2008, *ApJ*, 684, 287
- Ivezic, Z., Tyson, J. A., Allsman, R., Andrew, J., Angel, R., & for the LSST Collaboration. 2008, ArXiv e-prints
- Jacklin, S., Lund, M. B., Pepper, J., & Stassun, K. G. 2015, *AJ*, 150, 34
- Japelj, J. & Gomboc, A. 2011, *PASP*, 123, 1034
- Jewitt, D. 2012, *AJ*, 143, 66
- Jura, M., Farihi, J., & Zuckerman, B. 2009, *AJ*, 137, 3191
- Kaczmarszczik, M. C., Richards, G. T., Mehta, S. S., & Schlegel, D. J. 2009, *AJ*, 138, 19
- Kasen, D. 2010, *ApJ*, 708, 1025
- Kasen, D., Badnell, N. R., & Barnes, J. 2013, *ApJ*, 774, 25

- Kasliwal, M. M. 2011, PhD thesis, California Institute of Technology
- Kasliwal, V. P., Vogeley, M. S., & Richards, G. T. 2015, *MNRAS*, 451, 4328
- Kelly, B. C., Bechtold, J., & Siemiginowska, A. 2009, *ApJ*, 698, 895
- Kelly, B. C., Becker, A. C., Sobolewska, M., Siemiginowska, A., & Uttley, P. 2014, *ApJ*, 788, 33
- Kiel, P. D. & Hurley, J. R. 2006, *MNRAS*, 369, 1152
- Knights, M., Bassett, B. A., Varughese, M., Hlozek, R., Kunz, M., Smith, M., & Newling, J. 2013, *JCAP*, 1, 39
- Kunz, M., Bassett, B. A., & Hlozek, R. A. 2007, *Phys. Rev. D*, 75, 103508
- Levan, A. J., Tanvir, N. R., Cenko, S. B., Perley, D. A., Wiersema, K., Bloom, J. S., Fruchter, A. S., Postigo, A. d. U., O'Brien, P. T., Butler, N., van der Horst, A. J., Leloudas, G., Morgan, A. N., Misra, K., Bower, G. C., Farihi, J., Tunnicliffe, R. L., Modjaz, M., Silverman, J. M., Hjorth, J., Thöne, C., Cucchiara, A., Cerón, J. M. C., Castro-Tirado, A. J., Arnold, J. A., Bremer, M., Brodie, J. P., Carroll, T., Cooper, M. C., Curran, P. A., Cutri, R. M., Ehle, J., Forbes, D., Fynbo, J., Gorosabel, J., Graham, J., Hoffman, D. I., Guziy, S., Jakobsson, P., Kamble, A., Kerr, T., Kasliwal, M. M., Kouveliotou, C., Kocevski, D., Law, N. M., Nugent, P. E., Ofek, E. O., Poznanski, D., Quimby, R. M., Rol, E., Romanowsky, A. J., Sánchez-Ramírez, R., Schulze, S., Singh, N., van Spaandonk, L., Starling, R. L. C., Strom, R. G., Tello, J. C., Vaduvescu, O., Wheatley, P. J., Wijers, R. A. M. J., Winters, J. M., & Xu, D. 2011, *Science* (New York, N.Y.), 333, 199
- Li, L.-X. & Paczyński, B. 1998, *ApJL*, 507, L59
- Li, W., Bloom, J. S., Podsiadlowski, P., Miller, A. A., Cenko, S. B., Jha, S. W., Sullivan, M., Howell, D. A., Nugent, P. E., Butler, N. R., Ofek, E. O., Kasliwal, M. M., Richards, J. W., Stockton, A., Shih, H.-Y., Bildsten, L., Shara, M. M., Bibby, J., Filippenko, A. V., Ganeshalingam, M., Silverman, J. M., Kulkarni, S. R., Law, N. M., Poznanski, D., Quimby, R. M., McCully, C., Patel, B., Maguire, K., & Shen, K. J. 2011a, *Nature*, 480, 348
- Li, W., Leaman, J., Chornock, R., Filippenko, A. V., Poznanski, D., Ganeshalingam, M., Wang, X., Modjaz, M., Jha, S., Foley, R. J., & Smith, N. 2011b, *MNRAS*, 412, 1441
- Liao, K., Treu, T., Marshall, P., Fassnacht, C. D., Rumbaugh, N., Dobler, G., Aghamousa, A., Bonvin, V., Courbin, F., Hojjati, A., Jackson, N., Kashyap, V., Rathna Kumar, S., Linder, E., Mandel, K., Meng, X.-L., Meylan, G., Moustakas, L. A., Prabhu, T. P., Romero-Wolf, A., Shafieloo, A., Siemiginowska, A., Stalin, C. S., Tak, H., Tewes, M., & van Dyk, D. 2015, *ApJ*, 800, 11
- LIGO Scientific Collaboration, Virgo Collaboration, Aasi, J., Abadie, J., Abbott, B. P., Abbott, R., Abbott, T. D., Abernathy, M., Accadia, T., Acernese, F., & et al. 2013, ArXiv e-prints
- Lippai, Z., Frei, Z., & Haiman, Z. 2008, *ApJL*, 676, L5
- Littlefair, S. P., Casewell, S. L., Parsons, S. G., Dhillon, V. S., Marsh, T. R., Gänsicke, B. T., Bloemen, S., Catalan, S., Irawati, P., Hardy, L. K., Mcallister, M., Bours, M. C. P., Richichi, A., Burleigh, M. R., Birmingham, B., Breedt, E., & Kerry, P. 2014, *MNRAS*, 445, 2106
- Littlefair, S. P., Dhillon, V. S., Marsh, T. R., Gänsicke, B. T., Southworth, J., & Watson, C. A. 2006, *Science*, 314, 1578
- Liu, T., Gezari, S., Heinis, S., Magnier, E. A., Burgett, W. S., Chambers, K., Flewelling, H., Huber, M., Hodapp, K. W., Kaiser, N., Kudritzki, R.-P., Tonry, J. L., Wainscoat, R. J., & Waters, C. 2015, *ApJL*, 803, L16
- Lochner, M., McEwen, J. D., Peiris, H. V., Lahav, O., & Winter, M. K. 2016, ArXiv e-prints
- Lodato, G., King, A. R., & Pringle, J. E. 2009, *Monthly Notices of the Royal Astronomical Society*, 392, 332
- Loeb, A. 2016, *ApJL*, 819, L21
- LSST Science Collaboration, Abell, P. A., Allison, J., Anderson, S. F., Andrew, J. R., Angel, J. R. P., Armus, L., Arnett, D., Asztalos, S. J., Axelrod, T. S., & et al. 2009, ArXiv e-prints
- Lund, M. B., Pepper, J., & Stassun, K. G. 2015, *AJ*, 149, 16
- Lund, M. B., Siverd, R. J., Pepper, J. A., & Stassun, K. G. 2016, *PASP*, 128, 025002
- Marconi, M., Molinaro, R., Bono, G., Pietrzyński, G., Gieren, W., Pilecki, B., Stellingwerf, R. F., Graczyk, D., Smolec, R., Konorski, P., Suchomska, K., Górska, M., & Karczmarek, P. 2013, *ApJL*, 768, L6
- Maxted, P. F. L., Napiwotzki, R., Dobbie, P. D., & Burleigh, M. R. 2006, *Nature*, 442, 543
- Mazzali, P. A., Deng, J., Maeda, K., Nomoto, K., Umeda, H., Hatano, K., Iwamoto, K., Yoshii, Y., Kobayashi, Y., Minezaki, T., Doi, M., Enya, K., Tomita, H., Smartt, S. J., Kinugasa, K., Kawakita, H., Ayani, K., Kawabata, T., Yamaoka, H., Qiu, Y. L., Motohara, K., Gerardy, C. L., Fesen, R., Kawabata, K. S., Iye, M., Kashikawa, N., Kosugi, G., Ohyama, Y., Takada-Hidai, M., Zhao, G., Chornock, R., Filippenko, A. V., Benetti, S., & Turatto, M. 2002, *ApJL*, 572, L61
- McGehee, P. M., West, A. A., Smith, J. A., Anderson, K. S. J., & Brinkmann, J. 2005, *AJ*, 130, 1752
- Metzger, B. D. & Berger, E. 2012, *ApJ*, 746, 48
- Metzger, B. D., Martínez-Pinedo, G., Darbha, S., Quataert, E., Arcones, A., Kasen, D., Thomas, R., Nugent, P., Panov, I. V., & Zinner, N. T. 2010, *MNRAS*, 406, 2650

- Mosquera, A. M. & Kochanek, C. S. 2011, *ApJ*, 738, 96
- Mukadam, A. S., Montgomery, M. H., Winget, D. E., Kepler, S. O., & Clemens, J. C. 2006, *ApJ*, 640, 956
- Mundprecht, E., Muthsam, H. J., & Kupka, F. 2013, *MNRAS*, 435, 3191
- Newling, J., Bassett, B. A., Hlozek, R., Kunz, M., Smith, M., & Varughese, M. 2011, ArXiv e-prints
- Nordhaus, J., Spiegel, D. S., Ibgui, L., Goodman, J., & Burrows, A. 2010, *MNRAS*, 408, 631
- Nugent, P., Kim, A., & Perlmutter, S. 2002, *PASP*, 114, 803
- Ofek, E. O., Sullivan, M., Cenko, S. B., Kasliwal, M. M., Gal-Yam, A., Kulkarni, S. R., Arcavi, I., Bildsten, L., Bloom, J. S., Horesh, A., Howell, D. A., Filippenko, A. V., Laher, R., Murray, D., Nakar, E., Nugent, P. E., Silverman, J. M., Shaviv, N. J., Surace, J., & Yaron, O. 2013, *Nature*, 494, 65
- Olling, R. P., Mushotzky, R., Shaya, E. J., Rest, A., Garnavich, P. M., Tucker, B. E., Kasen, D., Margheim, S., & Filippenko, A. V. 2015, *Nature*, 521, 332
- Oluseyi, H. M., Becker, A. C., Culliton, C., Furqan, M., Hoadley, K. L., Regencia, P., Wells, A. J., Ivezić, Ž., Jones, R. L., Krughoff, K. S., Sesar, B., Jacoby, S., & Allison, I. J. 2012, *AJ*, 144, 9
- Parker, A., Ivezić, Ž., Jurić, M., Lupton, R., Sekora, M. D., & Kowalski, A. 2008, *Icarus*, 198, 138
- Peixinho, N., Delsanti, A., & Doressoundiram, A. 2015, *A&A*, 577, A35
- Perna, R., Lazzati, D., & Giacomazzo, B. 2016, *ApJL*, 821, L18
- Perryman, M. 2014, The Exoplanet Handbook
- Peters, C. M., Richards, G. T., Myers, A. D., Strauss, M. A., Schmidt, K. B., Ivezić, Ž., Ross, N. P., MacLeod, C. L., & Riegel, R. 2015, *ApJ*, 811, 95
- Pfahl, E., Rappaport, S., & Podsiadlowski, P. 2003, *ApJ*, 597, 1036
- Phinney, E. S. 1989, The Center of the Galaxy: Proceedings of the 136th Symposium of the International Astronomical Union
- Piran, T., Svirski, G., Krolik, J., Cheng, R. M., & Shiokawa, H. 2015, The Astrophysical Journal, 806, 164
- Rappaport, S., Gary, B. L., Kaye, T., Vanderburg, A., Croll, B., Benni, P., & Foote, J. 2016, *MNRAS*, 458, 3904
- Rees, M. J. 1988, *Nature*, 333, 523
- Rhoads, J. E. 2003, *ApJ*, 591, 1097
- Roberts, D. H., Lehar, J., & Dreher, J. W. 1987, *AJ*, 93, 968
- Roth, N., Kasen, D., Guillochon, J., & Ramirez-Ruiz, E. 2015, eprint arXiv:1510.08454
- Rubin, A., Gal-Yam, A., De Cia, A., Horesh, A., Khazov, D., Ofek, E. O., Kulkarni, S. R., Arcavi, I., Manulis, I., Yaron, O., Vreeswijk, P., Kasliwal, M. M., Ben-Ami, S., Perley, D. A., Cao, Y., Cenko, S. B., Rebbapragada, U. D., Woźniak, P. R., Filippenko, A. V., Clubb, K. I., Nugent, P. E., Pan, Y.-C., Badenes, C., Howell, D. A., Valenti, S., Sand, D., Sollerman, J., Johansson, J., Leonard, D. C., Horst, J. C., Armen, S. F., Fedrow, J. M., Quimby, R. M., Mazzali, P., Pian, E., Sternberg, A., Matheson, T., Sullivan, M., Maguire, K., & Lazarevic, S. 2016, *ApJ*, 820, 33
- Rubin, D., Aldering, G., Barbary, K., Boone, K., Chappell, G., Currie, M., Deustua, S., Fagrelius, P., Fruchter, A., Hayden, B., Lidman, C., Nordin, J., Perlmutter, S., Saunders, C., Sofiatti, C., & Supernova Cosmology Project, T. 2015, *ApJ*, 813, 137
- Schlafly, E. F., Green, G., Finkbeiner, D. P., Jurić, M., Rix, H.-W., Martin, N. F., Burgett, W. S., Chambers, K. C., Draper, P. W., Hodapp, K. W., Kaiser, N., Kudritzki, R.-P., Magnier, E. A., Metcalfe, N., Morgan, J. S., Price, P. A., Stubbs, C. W., Tonry, J. L., Wainscoat, R. J., & Waters, C. 2014, *ApJ*, 789, 15
- Schnittman, J. D. 2013, Classical and Quantum Gravity, 30, 244007
- Scolnic, D., Rest, A., Riess, A., Huber, M. E., Foley, R. J., Brout, D., Chornock, R., Narayan, G., Tonry, J. L., Berger, E., Soderberg, A. M., Stubbs, C. W., Kirshner, R. P., Rodney, S., Smartt, S. J., Schlafly, E., Botticella, M. T., Challis, P., Czekala, I., Drout, M., Hudson, M. J., Kotak, R., Leibler, C., Lunnan, R., Marion, G. H., McCrum, M., Milisavljevic, D., Pastorello, A., Sanders, N. E., Smith, K., Stafford, E., Thilker, D., Valenti, S., Wood-Vasey, W. M., Zheng, Z., Burgett, W. S., Chambers, K. C., Denneau, L., Draper, P. W., Flewelling, H., Hodapp, K. W., Kaiser, N., Kudritzki, R.-P., Magnier, E. A., Metcalfe, N., Price, P. A., Sweeney, W., Wainscoat, R., & Waters, C. 2014, *ApJ*, 795, 45
- Sesar, B., Banholzer, S. R., Cohen, J. G., Martin, N. F., Grillmair, C. J., Levitan, D., Laher, R. R., Ofek, E. O., Surace, J. A., Kulkarni, S. R., Prince, T. A., & Rix, H.-W. 2014, *ApJ*, 793, 135
- Shafter, A. W., Curtin, C., Pritchett, C. J., Bode, M. F., & Darnley, M. J. 2014, in Astronomical Society of the Pacific Conference Series, Vol. 490, Stell Novae: Past and Future Decades, ed. P. A. Woudt & V. A. R. M. Ribeiro, 77
- Shen, K. J., Kasen, D., Weinberg, N. N., Bildsten, L., & Scannapieco, E. 2010, *ApJ*, 715, 767
- Simm, T., Salvato, M., Saglia, R., Ponti, G., Lanzuisi, G., Nandra, K., & Bender, R. 2015, ArXiv e-prints
- Sluse, D. & Tewes, M. 2014, *A&A*, 571, A60

- Sokoloski, J. L., Croots, A. P. S., Lawrence, S., & Uthas, H. 2013, *ApJL*, 770, L33
- Solontoi, M. 2010, PhD thesis, University of Washington
- Stone, N. C. & Metzger, B. D. 2015, Monthly Notices of the Royal Astronomical Society, 455, 859
- Stone, N. C., Metzger, B. D., & Haiman, Z. 2016, ArXiv e-prints
- Strubbe, L. E. & Murray, N. 2015, Monthly Notices of the Royal Astronomical Society, 454, 2321
- Svirski, G., Piran, T., & Krolik, J. 2015, eprint arXiv:1508.02389
- Tanvir, N. R., Levan, A. J., Fruchter, A. S., Hjorth, J., Hounsell, R. A., Wiersema, K., & Tunnicliffe, R. L. 2013, *Nature*, 500, 547
- Taylor, S. R., Vallisneri, M., Ellis, J. A., Mingarelli, C. M. F., Lazio, T. J. W., & van Haasteren, R. 2015, ArXiv e-prints
- Torrealba, G., Catelan, M., Drake, A. J., Djorgovski, S. G., McNaught, R. H., Belokurov, V., Koposov, S., Graham, M. J., Mahabal, A., Larson, S., & Christensen, E. 2015, *MNRAS*, 446, 2251
- Totani, T. & Panaiteescu, A. 2002, *ApJ*, 576, 120
- Tyson, N. D. & Gal, R. R. 1993, *AJ*, 105, 1206
- Đurech, J., Hanuš, J., Oszkiewicz, D., & Vančo, R. 2016, *A&A*, 587, A48
- Valenti, S., Fraser, M., Benetti, S., Pignata, G., Sollerman, J., Inserra, C., Cappellaro, E., Pastorello, A., Smartt, S. J., Ergon, M., Botticella, M. T., Brimacombe, J., Bufano, F., Crockett, M., Eder, I., Fugazza, D., Haislip, J. B., Hamuy, M., Harutyunyan, A., Ivarsen, K. M., Kankare, E., Kotak, R., LaCluyze, A. P., Magill, L., Mattila, S., Maza, J., Mazzali, P. A., Reichart, D. E., Taubenberger, S., Turatto, M., & Zampieri, L. 2011, *MNRAS*, 416, 3138
- van der Marel, R. P. & Kallivayalil, N. 2014, *ApJ*, 781, 121
- van Haaften, L. M., Nelemans, G., Voss, R., van der Sluys, M. V., & Toonen, S. 2015, *A&A*, 579, A33
- van Velzen, S., Farrar, G. R., Gezari, S., Morrell, N., Zaritsky, D., Östman, L., Smith, M., Gelfand, J., & Drake, A. J. 2011, *The Astrophysical Journal*, 741, 73
- van Velzen, S., Frail, D. A., Körding, E., & Falcke, H. 2013, *Astronomy & Astrophysics*, 552, A5
- Vanderburg, A., Johnson, J. A., Rappaport, S., Bieryla, A., Irwin, J., Lewis, J. A., Kipping, D., Brown, W. R., Dufour, P., Ciardi, D. R., Angus, R., Schaefer, L., Latham, D. W., Charbonneau, D., Beichman, C., Eastman, J., McCrady, N., Wittenmyer, R. A., & Wright, J. T. 2015, *Nature*, 526, 546
- VanderPlas, J. T. & Ivezić, Ž. 2015, *ApJ*, 812, 18
- Vivas, A. K., Olsen, K., Blum, R., Nidever, D. L., Walker, A. R., Martin, N. F., Besla, G., Gallart, C., van der Marel, R. P., Majewski, S. R., Kaleida, C. C., Muñoz, R. R., Saha, A., Conn, B. C., & Jin, S. 2016, *AJ*, 151, 118
- Wang, J. & Merritt, D. 2004, *The Astrophysical Journal*, 600, 149
- Winget, D. E. & Kepler, S. O. 2008, *ARA&A*, 46, 157
- Zabludoff, A. I., Zaritsky, D., Lin, H., Tucker, D., Hashimoto, Y., Shectman, S. A., Oemler, A., & Kirshner, R. P. 1996, *The Astrophysical Journal*, 466, 104
- Zauderer, B. A., Berger, E., Soderberg, A. M., Loeb, A., Narayan, R., Frail, D. A., Petitpas, G. R., Brunthaler, A., Chornock, R., Carpenter, J. M., Pooley, G. G., Mooley, K., Kulkarni, S. R., Margutti, R., Fox, D. B., Nakar, E., Patel, N. A., Volgenau, N. H., Culverhouse, T. L., Bietenholz, M. F., Rupen, M. P., Max-Moerbeck, W., Readhead, A. C. S., Richards, J., Shepherd, M., Storm, S., & Hull, C. L. H. 2011, *Nature*, 476, 425
- Zhang, B. 2016, ArXiv e-prints
- Zinn, R., Horowitz, B., Vivas, A. K., Baltay, C., Ellman, N., Hadjiyska, E., Rabinowitz, D., & Miller, L. 2014, *ApJ*, 781, 22
- Zuckerman, B., Melis, C., Klein, B., Koester, D., & Jura, M. 2010, *ApJ*, 722, 725